

AFRL-IF-RS-TR-2005-143
Final Technical Report
April 2005



QUANTITATIVE UNCERTAINTY ASSESSMENT AND NUMERICAL SIMULATION OF MICRO- FLUID SYSTEMS

Johns Hopkins University

Sponsored by
Defense Advanced Research Projects Agency
DARPA Order No. J406

APPROVED FOR PUBLIC RELEASE; DISTRIBUTION UNLIMITED.

The views and conclusions contained in this document are those of the authors and should not be interpreted as necessarily representing the official policies, either expressed or implied, of the Defense Advanced Research Projects Agency or the U.S. Government.

AIR FORCE RESEARCH LABORATORY
INFORMATION DIRECTORATE
ROME RESEARCH SITE
ROME, NEW YORK

STINFO FINAL REPORT

This report has been reviewed by the Air Force Research Laboratory, Information Directorate, Public Affairs Office (IFOIPA) and is releasable to the National Technical Information Service (NTIS). At NTIS it will be releasable to the general public, including foreign nations.

AFRL-IF-RS-TR-2005-143 has been reviewed and is approved for publication

APPROVED:

/s/
CLARE D. THIEM
Project Engineer

FOR THE DIRECTOR:

/s/
JAMES A. COLLINS, Acting Chief
Advanced Computing Division
Information Directorate

REPORT DOCUMENTATION PAGE			Form Approved OMB No. 074-0188	
Public reporting burden for this collection of information is estimated to average 1 hour per response, including the time for reviewing instructions, searching existing data sources, gathering and maintaining the data needed, and completing and reviewing this collection of information. Send comments regarding this burden estimate or any other aspect of this collection of information, including suggestions for reducing this burden to Washington Headquarters Services, Directorate for Information Operations and Reports, 1215 Jefferson Davis Highway, Suite 1204, Arlington, VA 22202-4302, and to the Office of Management and Budget, Paperwork Reduction Project (0704-0188), Washington, DC 20503				
1. AGENCY USE ONLY (Leave blank)		2. REPORT DATE April 2005	3. REPORT TYPE AND DATES COVERED Final Jun 00 – Dec 03	
4. TITLE AND SUBTITLE QUANTITATIVE UNCERTAINTY ASSESSMENT AND NUMERICAL SIMULATION OF MICRO-FLUID SYSTEMS			5. FUNDING NUMBERS G - F30602-00-2-0612 PE - 61101E PR - E117 TA - 00 WU - 63	
6. AUTHOR(S) Omar M. Knio, Roger G. Ghanem, Alain Matta – Johns Hopkins University Habib N. Najm, Bert Debusschere – Sandia National Laboratories Olivier P. LeMaitre – Univeriste d'Evry Val d'Essonne				
7. PERFORMING ORGANIZATION NAME(S) AND ADDRESS(ES) Johns Hopkins University, 3400 N. Charles Street, Baltimore MD 21218-2686 Sandia National Laboratories, 7011 East Avenue, Livermore CA 94550 Univeriste d'Evry Val d'Essonne, 91020 Evry cedex, France			8. PERFORMING ORGANIZATION REPORT NUMBER N/A	
9. SPONSORING / MONITORING AGENCY NAME(S) AND ADDRESS(ES) Defense Advanced Research Projects Agency AFRL/IFTC 3701 N. Fairfax Drive 26 Electronic Parkway Arlington VA 22203-1714 Rome NY 13441-4514			10. SPONSORING / MONITORING AGENCY REPORT NUMBER AFRL-IF-RS-TR-2005-143	
11. SUPPLEMENTARY NOTES AFRL Project Engineer: Clare D. Thiem/IFTC/(315) 330-4893 Clare.Thiem@rl.af.mil				
12a. DISTRIBUTION / AVAILABILITY STATEMENT APPROVED FOR PUBLIC RELEASE; DISTRIBUTION UNLIMITED.				12b. DISTRIBUTION CODE
13. ABSTRACT (Maximum 200 Words) A stochastic multidimensional code is constructed for the simulation of a multi-component reacting mixture in pressure and electrokinetically-driven microchannel flows. The code is based on a detailed physical formulation that incorporates realistic models for the dependence of mixture properties on local species concentrations, the variation of the zeta-potential with local mixture conditions, and buffer behavior. The stochastic formulation relies on a spectral representation of uncertain quantities, and thus enables propagation and quantification of uncertainty in model parameters and/or operating conditions. Polynomial Chaos (PC) decompositions are used for this purpose, and are used in conjunction with a Galerkin methodology. The new modeling and decision-support capabilities resulting from the combination of a detailed physical model with accurate and efficient uncertainty quantification formalism are demonstrated, in particular, through application of the stochastic code to transient computations of protein-labeling reactions in two-dimensional electrochemical microchannel flow. Thus, this project has established highly efficient uncertainty quantification schemes that are ideally suited for micro-fluidic flows that arise, in particular, in bio-sensing and detection. By adopting a flexible computational methodology, the presently developed UQ tools may be readily adapted to assist in design, evaluation and/or deployment of a wide class of flow devices. Consequently, the impact of the present effort naturally extends well beyond the scope of its immediate applications.				
14. SUBJECT TERMS Microfluid flow, uncertainty qualification, polynomial chaos, simulation				15. NUMBER OF PAGES 175
				16. PRICE CODE
17. SECURITY CLASSIFICATION OF REPORT UNCLASSIFIED	18. SECURITY CLASSIFICATION OF THIS PAGE UNCLASSIFIED	19. SECURITY CLASSIFICATION OF ABSTRACT UNCLASSIFIED	20. LIMITATION OF ABSTRACT UL	

Contents

List of Figures	ii
Acknowledgments	v
Summary	1
1 Introduction	3
1.1 General	3
1.2 Motivation	3
1.3 Objectives	4
2 Approach	6
2.1 Random Variables and Processes	6
2.2 Polynomial Chaos Decomposition	7
2.3 Application to the Incompressible NS Equations	9
3 Results and Discussion	12
3.1 Physical Formulation	13
3.2 Stochastic Electrochemical Microchannel Flow Code	18
3.3 Applications and Demonstrations	25
4 Conclusions	42
References	43
Appendices	46
A Personnel	46
B List of Publications and Presentations	47
B.1 Journal Papers	47
B.2 Proceedings	47
B.3 Theses	48
B.4 Conference Presentations	49
B.5 Invited Lectures	50
C Copies of Selected Publications	52

List of Figures

1	Dependence of the CPU time on the number of modes P in SPM computations of internal, gravity-driven flow under stochastic temperature boundary conditions. The spatial discretization is on a staggered, finite-difference grid, with conservative second-order differences. Results with first, second, and third-order PC expansions are reported, respectively $N_o = 1, 2$, and 3 . Adapted from [12].	11
2	Empirical data and curve fit for the ζ potential of a fused silica capillary versus pH in an aqueous solution of KCl at various molarities. Adapted with permission from [16], Copyright 1992 American Chemical Society.	14
3	Schematic illustration of the modular nature of the stochastic electrochemical microchannel flow code.	19
4	Schematic illustration of the computational grid, showing the discretization scheme for primary variables.	20
5	Time evolution of U and L concentrations in a homogeneous protein labeling reaction. The uncertainty in these concentrations, due to a 1 % uncertainty in the labeling reaction rate parameters, is indicated by $\pm 3\sigma$ “error bars”.	26
6	PDF of the unlabeled protein concentration at different mean values. As the unlabeled protein reacts away, its PDF becomes narrower and more skewed.	27
7	A plug of protein U and dye D are introduced in a rectangular microchannel and react to form a labeled protein L.	28
8	Mean concentrations of proteins U, L, and dye D at $t = 0.12$ s. U and D just met and L is produced at their interface. The values of the contour levels go linearly from 0 (blue) to 1.3×10^{-4} mol/l (red). In this figure, as well as in all subsequent contour plots, the full physical domain is shown, from 0 to 1 cm in x and from 0 to 1 mm in y	29
9	Standard deviation of the protein and dye concentrations at $t = 0.12$ s. The values of the contour levels go linearly from 0 (blue) to 1.1×10^{-5} mol/l (red). The largest uncertainties are found in the reaction zone.	30
10	Major contributions of individual input parameters to the overall standard deviation in $[L]$ in the area around the reaction zone at $t = 0.12$ s, $y = 0.5$ mm. The uncertainty in the applied voltage potential “ ΔV ” has the most dominant contribution to the overall standard deviation in $[L]$	31
11	Mean (top) and standard deviation (bottom) of the labeled protein concentration L at $t = 0.50$ s. The initially flat profiles are now severely distorted. The values of the contour levels go linearly from 0 (blue) to 3.2×10^{-4} mol/l (red) in the top plot and from 0 (blue) to 10^{-4} mol/l (red) in the bottom plot.	32

12	Mean (top) and standard deviation (bottom) of the electrical conductivity of the electrolyte solution at $t = 0.50$ s. Annihilation of ions in the labeling reaction results in a significantly lower mean electrical conductivity near the L plug. The values of the contour levels go linearly from 7.1×10^{-3} S/m (blue) to 1.3×10^{-2} S/m (red) in the top plot and from 0 (blue) to 1.5×10^{-3} S/m (red) in the bottom plot.	32
13	Mean (top) and standard deviation (bottom) of the electrical field strength in the x -direction at $t = 0.50$ s. Near the L plug, the mean streamwise electrical field strength is about 40 % higher than in the undisturbed flow. The values of the contour levels go linearly from 91.4 kV/m (blue) to 146 kV/m (red) in the top plot and from 0.20 kV/m (blue) to 13 kV/m (red) in the bottom plot.	33
14	Mean (top) and standard deviation (bottom) of the electrical field strength in the y -direction at $t = 0.50$ s. The magnitude of the mean of this field strength is up to 15 % of the initial field strength in the x -direction. The values of the contour levels go linearly from -16.3 kV/m (blue) to 16.3 kV/m (red) in the top plot and from 0 (blue) to 5.8 kV/m (red) in the bottom plot.	33
15	Mean (top) and standard deviation (bottom) of the streamwise velocity at $t = 0.50$ s. The local increase in the electroosmotic wall velocity leads to recirculation zones near the L plug. The largest uncertainties are found near the wall. The values of the contour levels go linearly from 6.8 mm/s (blue) to 9.1 mm/s (red) in the top plot and from 5.6×10^{-3} mm/s (blue) to 0.59 mm/s (red) in the bottom plot.	34
16	Mean (top) and standard deviation (bottom) of the wall-normal velocity at $t = 0.50$ s. The mean of this velocity has a magnitude of up to 6 % of the initial streamwise velocity. The values of the contour levels go linearly from -0.56 mm/s (blue) to 0.56 mm/s (red) in the top plot and from 0 (blue) to 0.26 mm/s (red) in the bottom plot.	34
17	Overlay of the mean a) and Standard Deviation b) of the labeled protein concentration [L] at times $t = 0.24$ s and $t = 0.72$ s. The profiles spread out as they move downstream (to the right), especially along the top wall, which has the non-uniform ζ -potential. The maximum value for the mean of [L] is 1.5×10^{-6} mol/l and the maximum standard deviation is 5.4×10^{-7} mol/l.	35
18	Filled contour plots of several fields at time $t = 0.72$ s. a) Mean electrical conductivity, ranging from 0.0121 to 0.0124 S/m; b) Mean electrostatic field strength in x , ranging from 991 to 1011 V/cm; c) Mean streamwise velocity field, ranging from 7.4 to 7.6 mm/s; d) Standard deviation in streamwise velocity field, ranging from 0 to 0.7 mm/s	36
19	Effect of non-uniform electrostatic field strength on hydrodynamic dispersion of an analyte plug. A local increase of the electroosmotic wall velocity creates local accelerations in the flow that induce pressure gradients elsewhere in the channel. The resulting non-uniform velocity profile distorts the analyte plugs and increases dispersion.	37

20	Time evolution of $\langle \delta^2 \rangle$ for a random ζ -potential variability with $L_C = 50$ channel depths. Effective diffusion coefficient (scaled by the molecular diffusivity D_{mol}) for COV= 0.10: 47, COV=0.20: 181, COV=0.30: 397. . . .	39
21	Ratio of effective over molecular diffusion coefficient as a function of COV. .	39
22	Time evolution of $\langle \delta^2 \rangle$ for a random ζ -potential variability with $COV = 0.10$. Effective diffusion coefficient (scaled by the molecular diffusivity D_{mol}) for $L_C = 25$: 54, $L_C = 50$: 47, $L_C = 100$: 32.	40
23	Standard deviation profile of the streamwise standard deviation velocity σ_u in cases with $L_C = 25L_y$ (dashed) and $L_C = 100L_y$ (solid) at $x = 3$ mm on the left and $x = 6$ mm on the right.	40
24	Variation of the effective diffusivity D_{eff} with respect to the velocity gradient.	41
25	Probability density function for the location (left) and spatial variance δ^2 (right) of the U profile at $t = 0.45$ in a case with $L_C = 25L_y$ and COV = 0.1.	41

Acknowledgments

This work was supported by the Defense Advanced Research Projects Agency (DARPA) and Air Force Research Laboratory, Air Force Materiel Command, USAF, under agreement number F30602-00-2-0612. The authors also acknowledge collaborative efforts and useful discussions with:

- Prof. Juan Santiago of Stanford University and Prof. Tamal Mukherjee of Carnegie Mellon University. These collaborations provided research results and key insights obtained from SIMBIOSYS tasks at these institutions.
- Dr. Matthew Reagan of Sandia National Laboratories. These interactions provided important synergies with a research program on uncertainty quantification in reacting flow at Sandia, that was supported by the Laboratory Directed Research and Development program, and by the Dept. of Energy, Office of Basic Energy Sciences (BES), Division of Chemical Sciences, Geosciences and Biosciences.

The U.S. government is authorized to reproduce and distribute reprints for Governmental purposes notwithstanding any copyright annotation thereon. Computations were performed at the National Center for Supercomputer Applications.

Summary

The research program involved a collaborative effort between the Johns Hopkins University (JHU, prime contractor) and Sandia National Laboratories (SNL, subcontractor) that specifically aimed at:

1. Construction of uncertainty quantification (UQ) methods for microfluid applications involving transport and kinetics;
2. Development of computational techniques that implement these methods;
3. Assembly of uncertainty modules in a computational code that simulates a multicomponent reacting mixture; and,
4. Demonstration of UQ schemes and decision support capabilities.

A novel probabilistic approach to UQ in a detailed electrochemical microchannel flow was adopted. The key concept in this approach is to consider the uncertainty as generating a new dimension, and to regard the solution as being dependent on this dimension. A convergent expansion along the new dimension is then sought in terms of the Polynomial Chaos (PC) system, and the coefficients in this representation are determined through a weighted residual formalism. Solution of the resulting stochastic governing equations is then used to efficiently obtain accurate predictions of the mean solution and to quantify uncertainty around the mean.

Consistent with the program objectives, the PC-based UQ approach was applied to a detailed physical model of electrochemical microchannel flow. The physical formulation incorporates realistic models for the dependence of mixture properties on local species concentrations, the variation of the ζ -potential with local mixture conditions, and buffer behavior. It also relies on a specially-tailored, mixed differential-algebraic construction that efficiently accommodates both fast electrolyte buffer chemistry and slow bio-reaction kinetics.

A modular approach to code design was adopted. The code consisted of three main modules, each incorporating optimized numerical constructions for the solution of: (a) the transient flow field, (b) the species concentrations, and (c) the electrostatic field. One of the advantages of this modular construction is that it efficiently accommodates different bio-reactions, buffer solutions as well as operating and boundary conditions. The computational code constructed relies on finite-difference discretization of the stochastic model equations. Solution of the momentum equations is accomplished using a stochastic projection method (SPM) which was developed during the course of the project. The construction of SPM exploits the decoupled nature of stochastic divergence constraints and results in an efficient solution algorithm which scales linearly with the number of stochastic degrees of freedom. Numerical tests also demonstrate that stochastic modeling errors decay exponentially with increasing refinement in the stochastic dimensions. Thus, the scheme exhibits substantial computational advantages over Monte-Carlo (MC) techniques.

Meanwhile, integration of the species concentration equations is performed using a specially-tailored operator-split discretization that is combined with an upwind stochastic discretization of the transport terms. Coupled with the differential-algebraic chemistry formulation, the construction defeats the stiffness of the governing equations due to disparity between chemical and diffusion timescales. Solution of the non-linear algebraic constraints associated with fast buffer kinetics is performed using an adapted Newton solver. Non-linear operations on stochastic quantities are computed using the UQ toolkit, a software library that was also developed during the project. The utility of this toolkit was demonstrated during the construction of the stochastic code as well as in combination with simplified CAD models. In the former area, the UQ toolkit resulted in an elegant code formulation which resulted from an efficient generalization of the deterministic base formulation. In the latter case, the UQ toolkit enabled incorporation of UQ and decision-support capabilities into CAD models.

Construction of the stochastic code was completed by combining momentum and species concentration modules with a multigrid module for the solution of the electrostatic field. The stochastic multigrid module inverts the non-separable elliptic equations for the stochastic electrostatic field. The multigrid construction combines generalized multi-dimensional coarsening and refinement iterations with a one-dimensional line relaxation scheme. This combination results in an efficient construction which defeats the spatial complexity due to the large aspect ratios encountered in microchannel domains.

The combined physical modeling, UQ and decision-support capabilities achieved through the development of the stochastic code were demonstrated through applications of the code to transient computations of protein-labeling reactions in two-dimensional electrochemical microchannel flow.

1 Introduction

1.1 General

This final report highlights research activities conducted under a research program entitled, "Quantitative Uncertainty Assessment and Numerical Simulation of Micro-Fluid Flows." The research effort was supported by the Defense Advanced Research Projects Agency (DARPA) and Air Force Research Laboratory, Air Force Materiel Command, USAF, under agreement number F30602-00-2-0612. The period of performance was June 28, 2000 - December 31, 2003.

The research program involved a collaborative effort between the Johns Hopkins University (JHU, prime contractor) and Sandia National Laboratories (SNL, subcontractor). The Principal Investigators (PIs) at JHU were Profs. Omar Knio of the Mechanical Engineering Department and Roger Ghanem of the Department of Civil Engineering; the PI at SNL was Dr. Habib Najm of the Combustion Research Facility. The project also involved collaborative effort with Prof. Olivier Le Maitre of the Universite d'Evry. Prof. Le Maitre's involvement was made possible through several summer visits that were directly supported by this research program. During the academic year, Prof. Le Maitre also contributed to this program through efforts supported in part by CNRS, through affiliation with the Laboratoire d'Informatique pour la Mecanique et les Sciences de l'Ingenieur, Orsay, France. A summary of personnel involved in the project is provided in Appendix A.

1.2 Motivation

The design of micro-fluidic systems for biological or chemical sensing depends critically on the ability to accurately predict complex transport and reaction phenomena that inherently depend on a multitude of length- and time-scales. In many situations, this task is complicated due to uncertainties that arise from diverse sources. These include inexact knowledge of system forcing, initial and boundary conditions, as well as parametric uncertainties in the physical model and in physical properties of the medium. These properties may exhibit a random component with significant spatial or temporal fluctuations, or may be known in an approximate fashion. A prominent example concerns chemical or biological systems, whose modeling involves complex kinetic mechanisms which may include dozens of species - each characterized by thermodynamic and transport properties - and hundreds of elementary reactions - specified in terms of rate parameters. Transport properties and rate parameters exhibit nontrivial dependence on the thermodynamic state and this dependence must also be parameterized. Thus, micro-fluidic devices are described by complex physical models having a large number of parameters that are known in an approximate fashion only. Several factors, including measurement error and simplified calculations/approximate estimates, contribute to this parametric uncertainty. In some situations involving biological systems, this difficulty is further compounded by incomplete or partial knowledge of the relevant reactions. Consequently, in order to become effective tools, it is essential for simulation-based design approaches to include a rational assessment of uncertainty.

Quantitative uncertainty propagation is also a crucial step in the evaluation of system performance, which may be affected for instance by environmental parameters that are difficult to observe in a laboratory setting. Thus, it is also essential to predict the impact of various combinations of external parameters and to quantify “off-design” behavior. This issue is of prime importance for micro-fluidic detection devices, whose susceptibility to false positives and false negatives must be carefully assessed in order to avoid potentially disastrous consequences. Performance analysis should also address the vulnerability of the system to changes in environmental conditions, such as temperature, humidity, and airborne chemicals. These conditions may significantly alter system behavior, and it is crucial to develop an understanding of these changes so that adequate design and deployment strategies can be formulated. It is also essential to conduct such analyses during the design stages, so as to avoid or minimize costly field trials. Managing uncertainty and mitigating its consequences is crucial for controlling the confidence in the predictions of computer simulations of microfluidic devices, as it provides a rational coupling between prediction error control and available or required data.

1.3 Objectives

Microfluidic simulation and design tools existing at the start of the program generally lacked the necessary capabilities for quantitative uncertainty assessment. This project aimed at addressing this need, namely by developing computational uncertainty propagation and management methods that are ideally-suited for incorporation into microfluidic system simulation and design tools. The general objectives of the project were:

1. Construct uncertainty quantification (UQ) methods for microfluid applications involving transport and kinetics;
2. Develop computational techniques that implement these methods;
3. Assemble uncertainty modules in a parallel code that simulates a multicomponent reacting mixture;
4. Demonstrate application of uncertainty quantification schemes and decision support capabilities.

As further described in section 2, the uncertainty representation and quantification approach was based on a spectral Galerkin method. The key concept in this approach is to consider the uncertainty as generating a new dimension, and to regard the solution as being dependent on this dimension. A convergent expansion along the new dimension is then sought in terms of the Polynomial Chaos system, and the coefficients in this representation can be determined through a weighted residual formalism. The proposed approach naturally results in an efficient uncertainty propagation scheme and consequently avoids the prohibitive costs of Monte-Carlo-type approaches. A second major advantage of the proposed approach is that it efficiently yields quantitative estimates of the sensitivity of the solution to uncertainties

in input parameters, and in initial and boundary conditions. Moreover, it can adequately accommodate correlated inputs, probe the dependence of specific observables on particular components of the input data, and quantify the sensitivity of the parameters with respect to the solution at various spatial locations (inverse problem). This quantitative information is in a format that permits it to be readily used in designing experiments to better calibrate and test the validity of postulated models, or in assessing “off-design” performance.

2 Approach

As mentioned in the introduction, our approach towards the representation of random input data and solution variables is based on the so-called Polynomial Chaos decompositions [1, 2]. PC methods rely on a probabilistic framework [3], which distinguishes them from alternative approaches in uncertainty assessment including fuzzy set theories, interval analysis, convex analysis, as well as linearization and perturbation methods. The fundamental concept on which PC decompositions are based is to regard uncertainty as generating a new dimension and the solution as being dependent on this dimension. A convergent expansion along the new dimension is then sought in terms of a set of orthogonal basis functions, whose coefficients can be used to quantify and characterize the uncertainty. The motivation behind PC approaches includes its suitability to models expressed in terms of partial differential equations, the ability to deal with situations exhibiting steep non-linear dependence of the solution on random model data, and the promise of obtaining efficient and accurate estimates of uncertainty. In addition, such information is provided in a format that permits it to be readily used to probe the dependence of specific observables on particular components of the input data, to design experiments in order to better calibrate or test the validity of postulated models.

With the probabilistic framework of PC decompositions, a random variable is viewed as a function of a single variable that refers to the space of elementary events. Similarly, a stochastic process or field is then a function of $n + 1$ variables where n is the physical dimension of the space over which each realization of the process is defined.

Contrary to Monte-Carlo (MC) simulation, which can be viewed as a collocation method in the space of random variables, PC decompositions are based on coupling Hilbert space concepts—specifically projections of random functions—directly with models of computational mechanics. Random variables, defined as measurable functions from the set of basic events onto the real line, provide the mechanism for achieving such coupling, and the solution to the problem will be identified with its projection on a set of appropriately chosen basis functions. This approach is thus consistent with the identification of the space of second-order random variables* as a Hilbert space with the inner product on it defined as the mathematical expectation operation [4]. This Hilbert space structure is very convenient as it forms the foundation of many methods of deterministic numerical analysis; in addition, projections on subspaces as well as convergent approximations can now be unambiguously defined, quantified, and refined as necessary.

2.1 Random Variables and Processes

For brevity, we shall restrict our attention in this section to the case of Gaussian random variables and processes. Recall that a Gaussian process, $E(\mathbf{x}, \theta)$, can be characterized by its covariance function $R_{EE}(\mathbf{x}, \mathbf{y})$. Here, \mathbf{x} and \mathbf{y} are used to denote spatial coordinates, while

*Second-order random variables are those random variables with finite variance, they are mathematically similar to deterministic functions with finite energy.

θ is used to denote the random nature of the corresponding quantity. Being symmetrical and positive definite, R_{EE} has all its eigenfunctions mutually orthogonal, and they form a complete set spanning the function space to which E belongs. It can be shown that if this set of deterministic eigenfunctions is used to represent E , then the random coefficients appearing in the expansion are also orthogonal. The represents can be expressed in terms of the well-known Karhunen-Loève (KL) expansion [4]:

$$E(\mathbf{x}, \theta) = \overline{E}(\mathbf{x}) + \sum_{i=1}^{\infty} \sqrt{\lambda_i} \xi_i(\theta) \phi_i(\mathbf{x}), \quad (1)$$

where $\overline{E}(\mathbf{x})$ is the mean of the stochastic process, $\xi_i(\theta)$ are orthogonal random variables, while $\phi_i(\mathbf{x})$ and λ_i are the eigenfunctions and eigenvalues of the covariance kernel, respectively. $\phi_i(\mathbf{x})$ and λ_i are the solution of the following integral equation:

$$\int_D R_{EE}(\mathbf{x}, \mathbf{y}) \phi_i(\mathbf{y}) d\mathbf{y} = \lambda_i \phi_i(\mathbf{x}), \quad (2)$$

where D denotes the domain over which $E(\mathbf{x}, \theta)$ is defined.

Note that the KL expansion is mean-square convergent irrespective of the probabilistic structure of the process being expanded, provided it has finite variance [4]. The closer a process is to white noise, the more terms are required in the expansion. Conversely, a Gaussian random variable, α , be represented by a single term, i.e. the KL expansion can be reduced to:

$$\alpha = \bar{\alpha} + \sigma_{\alpha} \xi \quad (3)$$

where $\bar{\alpha}$ is the mean, σ_{α} is the standard deviation, and ξ is normalized Gaussian with unit standard deviation.

2.2 Polynomial Chaos Decomposition

The covariance function of the solution process is not known *a priori*, and hence the KL expansion may not be used to approximate it. Furthermore, even when the problem specification only involves Gaussian parameters or processes, the solution process is not necessarily Gaussian, so that the KL representation may not be a suitable approximation even when much is known about the covariance function of the solution. Thus, an alternative representation means is needed, and the PC decomposition addresses this need.

Since the solution process, u , is a function of the random data, it is natural to seek to represent it as a non-linear functional of the ξ_i 's that are used to represent the random data. It can be shown [2] that this functional dependence can be expressed in terms of polynomial functions of the ξ_i , known as polynomial chaoses, according to:

$$u = a_0 \Gamma_0 + \sum_{i_1=1}^{\infty} a_{i_1} \Gamma_1(\xi_{i_1}) + \sum_{i_1=1}^{\infty} \sum_{i_2=1}^{\infty} a_{i_1 i_2} \Gamma_2(\xi_{i_1}, \xi_{i_2}) + \dots \quad (4)$$

where $\Gamma_n(\xi_{i_1}, \dots, \xi_{i_n})$ denotes the Polynomial Chaos [1,5] of order n in the variables $(\xi_{i_1}, \dots, \xi_{i_n})$. The polynomial chaoses are usually generalized multidimensional Hermite polynomials of

independent variables that are measurable functions with respect to the Wiener measure. In particular, when the independent variables are identified as the Gaussian vector $\boldsymbol{\xi} = (\xi_1, \xi_2, \dots, \xi_n)$, one recovers the familiar expression of the expectation:

$$\langle f \rangle = \frac{1}{(2\pi)^{n/2}} \int_{-\infty}^{\infty} f(\boldsymbol{\xi}) \exp\left(-\frac{|\boldsymbol{\xi}|^2}{2}\right) d\boldsymbol{\xi} \quad (5)$$

where $|\boldsymbol{\xi}|^2 = \sum_{i=1}^n \xi_i^2$.

The zero, first, and second-order polynomials are given by [6]:

$$\Gamma_0 = 1, \quad \Gamma_1(|xi_i) = \xi_i, \quad \Gamma_2(\xi_i, \xi_j) = \xi_i \xi_j \delta_{ij} \quad (6)$$

where δ_{ij} is the Kronecker delta. For computational purposes, the “generic” PC representation (4) must be suitably truncated, and this is typically performed by retaining polynomials of order $\leq p$, where p is a prescribed value. It is also convenient (section 3) to introduce a one-to-one mapping between the set of indices appearing in the truncated sum corresponding to (4) and a set of ordered indices, and rewrite the truncated sum in (4) in single-index form according to:

$$u \simeq \sum_{j=0}^P u_j \Psi_j \quad (7)$$

where the Ψ_j denote the polynomial chaoses in single-index notation, while $P+1$ is the total number of polynomial chaoses of order $\leq p$. Note that for the one-dimensional case, $P = p$, while in a space with n stochastic dimensions [7],

$$P = \frac{(p+n)!}{p!n!} - 1. \quad (8)$$

Note that the polynomials are mutually orthogonal, in the sense that the inner product $\langle \Psi_i \Psi_j \rangle = 0$ when $i \neq j$. Moreover, the set $\{\Psi_j\}_{j=1}^{\infty}$ can be shown to form a complete basis in the space of second-order random variables. Specifically, any second-order process u has a mean-square convergent expansion given in equation (4) where $\Gamma_p(\cdot)$ is the Polynomial Chaos of order p [2]. Also note that the PC expansion can be used to represent, in addition to the solution process, both Gaussian and non-Gaussian model data. One can verify this by observing that the first summation in an expansion of the form given by Eq. (4) represents a Gaussian component; thus, for a Gaussian function, expansion (4) reduces to a single summation, the coefficients a_{i_1} being the coefficients in the Karhunen-Loève expansion of the function [6,8]. Accordingly, the additional summations in the expansion are immediately identified as representing the non-Gaussian behavior of the function in terms of a non-linear, (polynomial) functional dependence on the independent Gaussian variables.

In order to obtain a complete probabilistic characterization of the solution process, u , it is sufficient to determine the “deterministic” coefficients u_j appearing in Eq. (7). Due to the orthogonality of the Ψ ’s, the coefficients of the PC expansion of u satisfy:

$$u_j = \frac{\langle u \Psi_j \rangle}{\langle \Psi_j^2 \rangle}, \quad (9)$$

for $j = 0, \dots, P$. As mentioned in the introduction, we shall primarily focus on determination of the u_j 's using a Galerkin approach, and the latter is initially outlined for a generic stochastic process, u , governed by:

$$\mathcal{O}(u(\boldsymbol{\xi}), \boldsymbol{\xi}) = 0, \quad (10)$$

where \mathcal{O} is a non-linear operator. The Galerkin scheme is based on introducing the expansion (7) into (10) and taking orthogonal projections onto the truncated basis, which results in the following system for the basis function coefficients:

$$\left\langle \mathcal{O} \left(\sum_i u_i \Psi_i(\boldsymbol{\xi}), \boldsymbol{\xi} \right), \Psi_j \right\rangle = 0, \quad j = 0, \dots, P. \quad (11)$$

Solution of the above coupled system then yields the desired coefficients. Below, we focus on implementation of this approach to the incompressible NS equations.

2.3 Application to the Incompressible Navier Stokes (NS) Equations

Application of the PC decomposition above is illustrated by outlining the construction of the stochastic projection method (SPM) as originally introduced in [9] (Appendix C). The SPM focuses on the numerical solution of the incompressible NS equations:

$$\frac{\partial \mathbf{u}}{\partial t} + (\mathbf{u} \cdot \nabla) \mathbf{u} = -\nabla p + \nu \nabla^2 \mathbf{u} \quad (12)$$

$$\nabla \cdot \mathbf{u} = 0 \quad (13)$$

where $\mathbf{u} = (u, v)$ is the velocity vector, t is time, p is the pressure, and ν the kinematic viscosity. For brevity, we focus on the solution of Eqs. (12-13) in a 2D domain, D , with specified velocity boundary conditions on ∂D satisfying:

$$\int_{\Gamma} \mathbf{u}_n dA = 0 \quad (14)$$

where $\Gamma = \partial D$ is the boundary of D , \mathbf{u}_n is the component of \mathbf{u} normal to Γ , and dA is the surface element along Γ . We also restrict our attention to the case of a single parameter, and illustrate the case of a Gaussian initial condition:

$$\mathbf{u}(\mathbf{x}, t = 0) = \bar{\mathbf{u}}(\mathbf{x}) + \xi \mathbf{u}'(\mathbf{x}) \quad (15)$$

where ξ is a Gaussian variable with unit variance, and $\bar{\mathbf{u}}(\mathbf{x})$ and $\mathbf{u}'(\mathbf{x})$ are given quantities. Note that in the present case $\bar{\mathbf{u}}$ and \mathbf{u}' represent the mean and standard deviation of the initial velocity field, respectively. One can immediately verify this claim from the definitions of mean and variance applied to each of the velocity components. For instance, for the u component, we have:

$$\langle u(\mathbf{x}, t = 0) \rangle \equiv \langle \bar{u}(\mathbf{x}) + \xi u'(\mathbf{x}) \rangle = \bar{u}(\mathbf{x}), \quad \text{and} \quad (16)$$

$$\sigma_{u(\mathbf{x}, t=0)} \equiv \langle (u(\mathbf{x}, t = 0) - \langle u(\mathbf{x}, t = 0) \rangle)^2 \rangle = |u'(\mathbf{x})|. \quad (17)$$

The development of the SPM is based on inserting the PC decompositions of all stochastic quantities into the NS equations, and applying the Galerkin procedure to derive governing equations for the individual modes appearing in these expansions. This results in a system of the form:

$$\frac{\partial \mathbf{u}_k}{\partial t} + \sum_{i=0}^P \sum_{j=0}^P \mathcal{M}_{ijk}(\mathbf{u} \cdot \nabla) \mathbf{u} = -\nabla p_k + \nu \nabla^2 \mathbf{u}_k \quad (18)$$

$$\nabla \cdot \mathbf{u}_k = 0 \quad (19)$$

for $k = 0, \dots, P$. Note that the quadratic term involves a convolution sum involving the multiplication tensor:

$$\mathcal{M}_{ijk} \equiv \frac{\langle \Psi_i \Psi_j \Psi_k \rangle}{\langle \Psi_k^2 \rangle} \quad (20)$$

Boundary and initial conditions are also decomposed in a similar fasion. In particular, for the latter we have: $\mathbf{u}_0(\mathbf{x}, t = 0) = \bar{\mathbf{u}}(\mathbf{x})$, $\mathbf{u}_1(\mathbf{x}, t = 0) = \mathbf{u}'(\mathbf{x})$, and $\mathbf{u}_k(\mathbf{x}, t = 0) = 0$ for $k = 2, \dots, P$.

SPM relies a fractional step projection scheme in order to integrate the evolution equations of the stochastic modes. In a first fractional step, we integrate the coupled advection-diffusion equations:

$$\frac{\partial \mathbf{u}_k}{\partial t} + \sum_{i=0}^P \sum_{j=0}^P \mathcal{M}_{ijk}(\mathbf{u}_i \cdot \nabla) \mathbf{u}_j = \nu \nabla^2 \mathbf{u}_k \quad (21)$$

for $k = 0, \dots, P$. An explicit multistep scheme may be used for this purpose. For instance, for a second-order Adams-Bashforth scheme we have:

$$\frac{\mathbf{u}_k^* - \mathbf{u}_k^n}{\Delta t} = \frac{3}{2} \mathbf{H}_k^n - \frac{1}{2} \mathbf{H}_k^{n-1} \quad k = 0, \dots, P \quad (22)$$

where \mathbf{u}_k^* are the predicted velocity modes, Δt is the time step,

$$\mathbf{H}_k \equiv \nu \nabla^2 \mathbf{u}_k - \sum_{i=0}^P \sum_{j=0}^P \mathcal{M}_{ijk}(\mathbf{u}_i \cdot \nabla) \mathbf{u}_j, \quad (23)$$

and the superscripts refer to the time level. In the second fractional step, a pressure correction is performed in order to the divergence constraints on the velocity modes. We have:

$$\frac{\mathbf{u}_k^{n+1} - \mathbf{u}_k^*}{\Delta t} = -\nabla p_k \quad k = 0, \dots, P \quad (24)$$

where the pressure fields p_k are determined so that the fields \mathbf{u}_k^{n+1} satisfy the divergence constraints in (19), i.e.

$$\nabla \cdot \mathbf{u}_k^{n+1} = 0 \quad (25)$$

Combining equations (24) and (25) results in the following system of *decoupled* Poisson equations:

$$\nabla^2 p_k = -\frac{1}{\Delta t} \nabla \cdot \mathbf{u}_k^* \quad k = 0, \dots, P \quad (26)$$

Similar to the original projection method [10], the above Poisson equations are solved, independently, subject to Neumann conditions that are obtained by projecting equation (24) in the direction normal to the domain boundary [10, 11].

One of the key advantages of SPM is that the numerical formulation effectively exploits the fact that the velocity divergence constraints are *decoupled*, which results in a set of $P + 1$ decoupled pressure projection steps. Since these steps typically account for the bulk of the computational effort in incompressible flow simulations, the solution of the stochastic system can be at essentially a cost of $P + 1$ deterministic solutions. Coupled with the spectral nature of the stochastic representation, this leads to a highly efficient stochastic solver, as illustrated in Fig. 1 below.

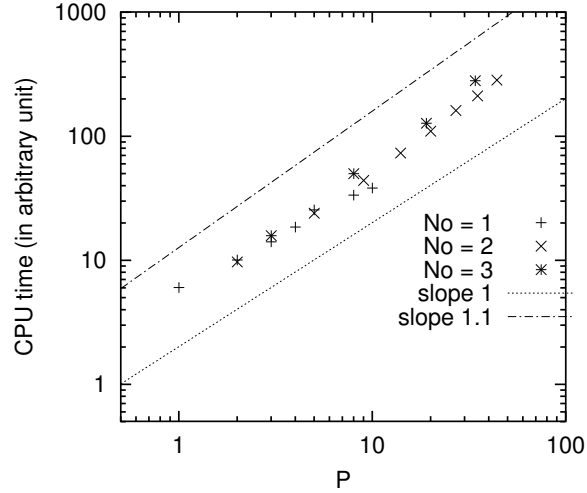


Figure 1: Dependence of the CPU time on the number of modes P in SPM computations of internal, gravity-driven flow under stochastic temperature boundary conditions. The spatial discretization is on a staggered, finite-difference grid, with conservative second-order differences. Results with first, second, and third-order PC expansions are reported, respectively $N_o = 1, 2$, and 3 . Adapted from [12].

3 Results and Discussion

As mentioned in the Introduction, a central objective of the present project consisted of the design and implementation of a stochastic solver suitable for accurate and efficient simulation of a reacting multicomponent mixture in pressure- and electrokinetically-driven microchannels, and for propagating and quantifying uncertainty in model predictions. In other words, this task required generalization of the SPM outlined in section 2.3 to a detailed physical model of electrochemical microchannel flow. In pursuing this objective, our effort addressed several fundamental difficulties, due in large part to the disparate length- and time-scales that characterize electrochemical microchannel flows. These difficulties include:

1. disparity between the timescales of bio-reactions between species in the mixture and characteristic timescales of the buffer. The latter are typically orders of magnitude smaller than the former, which results in a severe scale complexity and a stiff computational system.
2. disparity between timescales characterizing species diffusion and momentum diffusion. Specifically, relevant flow conditions have low Reynolds number but high Peclet numbers, which results in computational challenges in the treatment of transport terms.
3. slender computational domains, having large ratios between channel length and channel height. This generally results in high-aspect-ratio computational grids, and further compounds difficulties in the treatment of transport and diffusion.
4. variable-mixture properties and the non-linear dependence of chemical reaction rates and buffer chemistry on species concentrations. These result in additional challenges in the treatment of stochastic terms which, unlike the example above, are no-longer limited to quadratic products.

In order to overcome the difficulties above, we formulated a computational model that judiciously combines:

- a detailed physical formulation that incorporates realistic models for buffer behavior and the dependence of mixture properties on local composition;
- a mixed differential-algebraic formulation that defeats the chemical stiffness of the equations of motion;
- an operator-split integration scheme that efficiently handles the time-scale disparity between species and momentum diffusion;
- an efficient pseudo-spectral approach for the estimation of non-linear operations on stochastic quantities; and,
- a specially-tailored stochastic multigrid method for the efficient solution of non-separable, stochastic, elliptic equations in slender domains.

This section discusses the development of the stochastic, electrochemical microchannel flow, and applications to that were performed to demonstrate the resulting capabilities. An outline of the physical model for electrochemical microchannel flow first is provided in section 3.1. Section 3.2 then summarizes the development of the computational code. Highlights from selected applications are finally provided in section 3.3

3.1 Physical Formulation

A detailed model was developed of both electroosmotic and pressure-driven flow in a microchannel filled with an electrolyte buffer and model protein analyte samples. The construction considers the fully coupled momentum, species transport, and electrostatic field equations, including a model for the dependence of the ζ -potential on pH and buffer molarity. A mixed finite-rate, partial-equilibrium formulation is applied for the chemical reactions. In particular, “fast” electrolyte reactions are described by associated equilibrium constraints, while the remaining “slow” protein labeling reactions are modeled with finite-rate kinetics. As outlined below, the formulation involves coupled systems of equations that govern: (a) momentum transport, (b) species transport, and (c) electrostatic potential.

Momentum

The continuity and momentum equations for a two-dimensional flow field in the (x, y) plane, with uniform density and viscosity are given by [13]

$$\nabla \cdot \mathbf{u} = 0 \quad (27)$$

$$\frac{\partial \mathbf{u}}{\partial t} + \mathbf{u} \cdot \nabla \mathbf{u} = -\nabla p + \nu \nabla^2 \mathbf{u} \quad (28)$$

where \mathbf{u} is the velocity, p is the pressure normalized by density, and ν is the kinematic viscosity.

Without loss of generality, we assume that the microchannel flows are electroosmotically driven with an applied electrostatic field in the x -direction. Assuming a double layer that is thin with respect to the channel size, the effect of wall electrostatic forces can be represented in terms of a wall slip velocity u_w , using the Helmholtz-Smoluchowski relationship [13]

$$u_w = \frac{\epsilon \zeta}{\mu} \nabla_t \phi_w \quad (29)$$

where ϵ is the permittivity of the fluid, ζ is the zeta potential, ϕ_w is the electrostatic field potential at the wall, and μ is the dynamic viscosity. Since both the electrostatic field and the ζ potential depend on the fluid composition, equation (29) represents a major coupling between the flow velocity and the species transport.

The ζ potential is a function of the wall material and fluid characteristics [14,15]. In this work, a relationship for ζ as a function of the local pH and buffer molarity was obtained

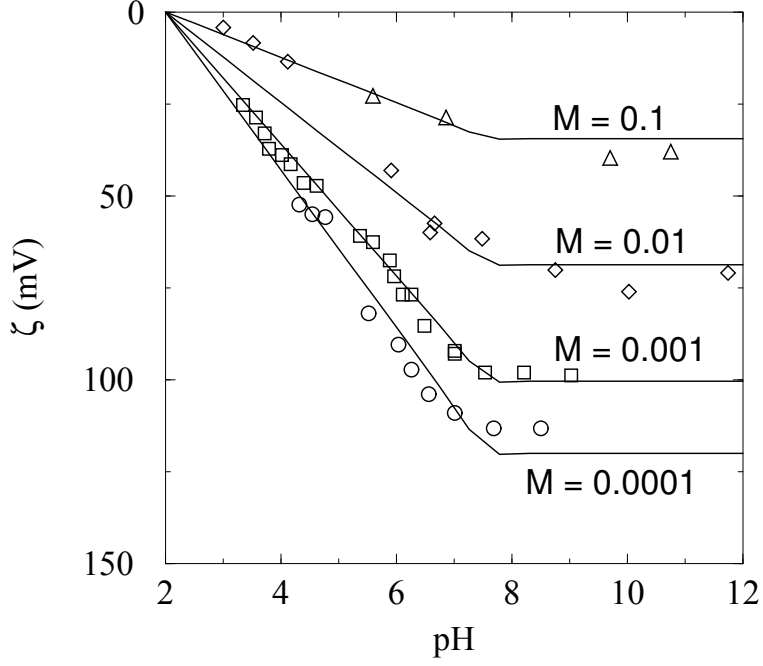


Figure 2: Empirical data and curve fit for the ζ potential of a fused silica capillary versus pH in an aqueous solution of KCl at various molarities. Adapted with permission from [16], Copyright 1992 American Chemical Society.

from empirical data for the zeta potential of a fused silica capillary in an aqueous solution of KCl, as shown in Fig. 2 [16]. This data was curve-fitted into the following relationship:

$$\zeta(\text{pH}, \mathcal{M}) = \left\{ -(\text{pH} - 2) + \left(\frac{1}{2} + \frac{1}{2} \tanh(5(\text{pH} - 7.5)) \right) (\text{pH} - 7.6) \right\} \times (-2.7 \ln(\mathcal{M} + 2.3 \times 10^{-4})) \quad (30)$$

where \mathcal{M} is the molarity of the KCl solution. The quantitative accuracy of this curve-fit is obviously limited to systems similar to the one considered in [16]. However, equation (30) qualitatively gives the correct behavior of $\zeta(\text{pH}, \mathcal{M})$ for various other systems [14, 15].

Species Concentrations

A variety of species are considered in this work, ranging from model proteins and dyes in samples, to the ions of aqueous buffer solutions. The transport of these species is governed by [13]:

$$\frac{\partial c_i}{\partial t} + \nabla \cdot [c_i(\mathbf{u} + \mathbf{u}_i^e)] = \nabla \cdot (D_i \nabla c_i) + \hat{w}_i \quad (31)$$

where c_i is the concentration of species i , and D_i is the corresponding diffusivity. The electromigration velocity \mathbf{u}_i^e accounts for the electrophoretic movement of electrically charged species relative to the bulk flow. This velocity is given by [13]

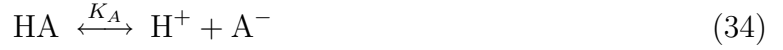
$$\mathbf{u}_i^e = -\beta_i z_i F \nabla \phi \quad (32)$$

where β_i is the electrophoretic mobility for species i , z_i is the charge number, F is the Faraday constant (9.648×10^4 C/mol), and ϕ is the electrostatic field potential. The term \hat{w}_i is a source term from the chemical and electrochemical reactions in which species i is involved. Note that for each species, the diffusivity D_i and the mobility β_i are coupled through the Nernst-Einstein equation [13]

$$D_i = RT\beta_i \quad (33)$$

where R is the universal gas constant and T the temperature.

The integration of equation (31) is performed differently depending on the chemical time scales involved. In general, electrolyte association and dissociation reaction rates are several orders of magnitude faster than electrophoretic phenomena [17] and typical sample-processing reactions. Thus, direct integration of fast reactions would impose severe time step restrictions. In order to avoid these difficulties, an equilibrium approach for the electrolyte reactions is implemented. For example, consider a weak acid HA, which dissociates according to



where

$$K_A \equiv \frac{[\text{H}^+][\text{A}^-]}{[\text{HA}]} \quad (35)$$

is the corresponding dissociation constant. Instead of integrating equation (31) for the concentrations of species HA and A^- individually, consider the combined concentration of both of these quantities $\theta_a = [\text{HA}] + [\text{A}^-]$. The source terms for $[\text{HA}]$ and $[\text{A}^-]$ from the electrolyte reaction (34) cancel out in the θ_a transport equation, which is the sum of the transport equations for the two individual quantities.

$$\begin{aligned} \frac{\partial \theta_a}{\partial t} + \nabla \cdot [c_{\text{HA}}(\mathbf{u} + \mathbf{u}_{\text{HA}}^e) + c_{\text{A}^-}(\mathbf{u} + \mathbf{u}_{\text{A}^-}^e)] = \\ \nabla \cdot [D_{\text{HA}} \nabla c_{\text{HA}} + D_{\text{A}^-} \nabla c_{\text{A}^-}] \end{aligned} \quad (36)$$

Therefore, barring any other chemical reactions involving these species, θ_a is a conserved quantity and can be integrated with equation (36) without a chemical source term [18–20]. Note that if the chemical source terms for HA or A^- in equation (31) do include participation by reactions other than the HA buffer chemistry, e.g. by (typically slow) sample chemistry, then the utilization of θ_a is still advantageous in that it eliminates the fast electrolyte reactions, but in this case θ_a is no longer a conserved scalar. In either case, one arrives at a governing equation for θ_a , which does not include the fast reaction terms. Once

θ_a is known, the concentrations of the individual components of the weak acid are obtained from:

$$[\text{HA}] = \frac{[\text{H}^+]}{[\text{H}^+] + K_A} \theta_a \equiv \alpha_{\text{HA}} \times \theta_a \quad (37)$$

$$[\text{A}^-] = \frac{K_A}{[\text{H}^+] + K_A} \theta_a \equiv \alpha_{\text{A}^-} \times \theta_a \quad (38)$$

Note that this construction is equally useful for buffers with multiple dissociation states, where θ_a is the sum of concentrations of the weak acid and all of its dissociated states. Since the mobilities and diffusivities are generally different for the species that make up θ_a , the convection and diffusion terms in the transport equation for θ_a are calculated as the sum of the convection and diffusion for each species in θ_a . A similar approach holds for weak bases.

For strong acids and bases, which are fully dissociated in the solution, or for other species that do not take part in electrolyte dissociation and association reactions, equation (31) can be integrated directly.

In most of the cases studied in this work, the model proteins and fluorescent dyes were assumed to have a fixed charge, so their concentrations could be integrated using equation (31), with an appropriate finite-rate chemical source term.

In reality though, proteins typically have a large number of dissociation states. Therefore, depending on the pH, their overall net charge can be either positive or negative, as indicated by their titration curve. While it is conceptually possible to model each of the dissociation reactions with its own dissociation constant, as described above for the weak acids and bases, this is not practical for proteins due to the large number of dissociation reactions that would have to be included. Instead, an ampholyte formulation was implemented in this work, based on [19, 21–23]. In this formulation, all individual dissociation states of a protein are lumped into one ampholyte species, with a net charge equal to the charge averaged over all dissociation states of the protein. This net charge is determined as a function of pH from an experimentally obtained titration curve for the protein. Given the large size of a protein compared to the ions that dissociate from it, the protein diffusion coefficient D is considered to be independent of its dissociation state. The electrophoretic mobility β , however, depends strongly on the ionic strength of the solution as modeled by the Debye-Hückel-Henry description [21, 22]:

$$\beta = \frac{eg(\kappa r)}{F6\pi\mu r(1 + \kappa r)} \quad (39)$$

where e is the unit charge (C) and r is the particle radius (m). The parameter κ (1/m) is the inverse of the Debye length, defined as

$$\kappa = \frac{1}{\lambda_D} = \sqrt{\frac{4 \times 10^3 F^2 I}{\epsilon RT}} \quad (40)$$

In this equation I is the ionic strength (mol/l) of the solution defined as

$$I = 1/2 \sum_{i=1}^{ns} z_i^2 c_i \quad (41)$$

with all concentrations c_i in mol/l. Note that the summation for the ionic strength goes over all ns species in the solution. However, since the charges in proteins are generally far apart compared to the Debye length, the Linderstrøm-Lang approximation is used for proteins in the solution. Under this approximation, a z -valent ion with concentration c is assumed to behave as a monovalent ion with concentration zc . Therefore, the contribution of each protein i to the ionic strength in the solution is $1/2z_i c_i$ instead of $1/2z_i^2 c_i$ [22]. Further, the factor $g(\kappa r)$ is a dimensionless function that varies sigmoidally from 1 to 1.5 and the radius of the protein is obtained from the Stokes equation [21]

$$r = \frac{kT}{6\pi\mu D} \quad (42)$$

where k is the Boltzmann constant.

Since a thin double layer is assumed, the system is also assumed to satisfy the electroneutrality condition

$$\sum_i z_i c_i = 0 \quad (43)$$

everywhere in the domain. The concentrations of H^+ and OH^- are obtained from this electroneutrality condition and the water dissociation constant

$$[H^+][OH^-] = K_w \quad (44)$$

Note that the composition, and therefore also the total charge, of weak acids and bases in the system depends on the H^+ concentration (see equations (37,38) above). The substitution of equations (38) and (44) into the electroneutrality condition (43), in order to account for the dependence of $[A^-]$ and $[OH^-]$ on $[H^+]$, introduces non-linear terms in this equation. For buffers with multiple dissociation states, even more non-linear terms are introduced. Therefore, an iterative solution of the electroneutrality condition for $[H^+]$ is usually required.

Electrostatic Field Strength

Allowing for concentration field gradients, the electrostatic field potential, ϕ is obtained from the current continuity constraint [13],

$$\nabla \cdot (\sigma \nabla \phi) = -F \sum_i z_i \nabla \cdot (D_i \nabla c_i) \quad (45)$$

This equation is coupled to the species concentrations through the right hand side (diffusion of charge) and the electrical conductivity σ of the solution

$$\sigma = F^2 \sum_i z_i^2 \beta_i c_i \quad (46)$$

The electrostatic field strength is then obtained as $\mathbf{E} = -\nabla \phi$.

Stochastic Formulation

The discussion above provided a detailed description of the key elements of the deterministic model. When random inputs are present, a stochastic variant of the deterministic model is used which is obtained in similar fashion as that outlined in section 2. Specifically, PC decompositions of random parameters and solution variables are substituted into the governing equations, and Galerkin projections are then used to derive evolution equations for the PC coefficients. This results in the following system of coupled differential-algebraic equations:

$$\frac{\partial \mathbf{u}_k}{\partial t} = - \sum_{i=0}^P \sum_{j=0}^P \mathcal{M}_{ijk} (\mathbf{u}_i \cdot \nabla) \mathbf{u}_j - \nabla p_k + \sum_{i=0}^P \sum_{j=0}^P \mathcal{M}_{ijk} \nu_i \nabla^2 \mathbf{u}_j \quad (47)$$

$$\nabla \cdot \mathbf{u}_k = 0 \quad (48)$$

$$\begin{aligned} \frac{\partial c_{m,k}}{\partial t} = & - \sum_{i=0}^P \sum_{j=0}^P \mathcal{M}_{ijk} \nabla \cdot (c_{m,i} (\mathbf{u}_j + \mathbf{u}_{m,j}^e)) \\ & + \sum_{i=0}^P \sum_{j=0}^P \mathcal{M}_{ijk} \nabla \cdot (D_{m,i} \nabla c_{m,j}) + \hat{w}_{m,k} \end{aligned} \quad (49)$$

$$\sum_{i=0}^P \sum_{j=0}^P \mathcal{M}_{ijk} \nabla \cdot (\sigma_i \nabla \phi_j) = -F \sum_m z_m \sum_{i=0}^P \sum_{j=0}^P \mathcal{M}_{ijk} \nabla \cdot (D_{m,i} \nabla c_{m,j}) \quad (50)$$

where

$$\mathbf{u}_{m,j}^e = \frac{\langle \Psi_j \mathbf{u}^e \rangle}{\langle \Psi_j^2 \rangle} = \sum_{k=0}^P \sum_{i=0}^P \mathcal{M}_{kij} \beta_k z F \nabla \phi_i \quad (51)$$

$$\hat{w}_{m,k} = \frac{\langle \Psi_k \hat{w} \rangle}{\langle \Psi_k^2 \rangle} \quad (52)$$

$$\sigma_i = F^2 \sum_m z_m^2 \sum_{j=0}^P \sum_{k=0}^P \mathcal{M}_{jki} \beta_{m,j} c_{m,k} \quad (53)$$

Equations (47), (49), and (50) each represent a set of $P + 1$ coupled equations to be solved for the mode strengths u_k , $c_{m,k}$, and ϕ_k , $k = 0, \dots, P$.

3.2 Stochastic Electrochemical Microchannel Flow Code

The stochastic formulation outlined in section 3.1 above has been implemented in a flexible computational code. As illustrated in Fig. 3, the code has a modular construction that accommodates mixtures with different reacting species and buffer solution. A brief discussion of the function of each of the modules is provided below.

Spatial discretization

The governing equations are discretized on a rectangular domain with a Cartesian mesh of uniform cell size Δx and Δy in the x and y directions respectively. Field variables are

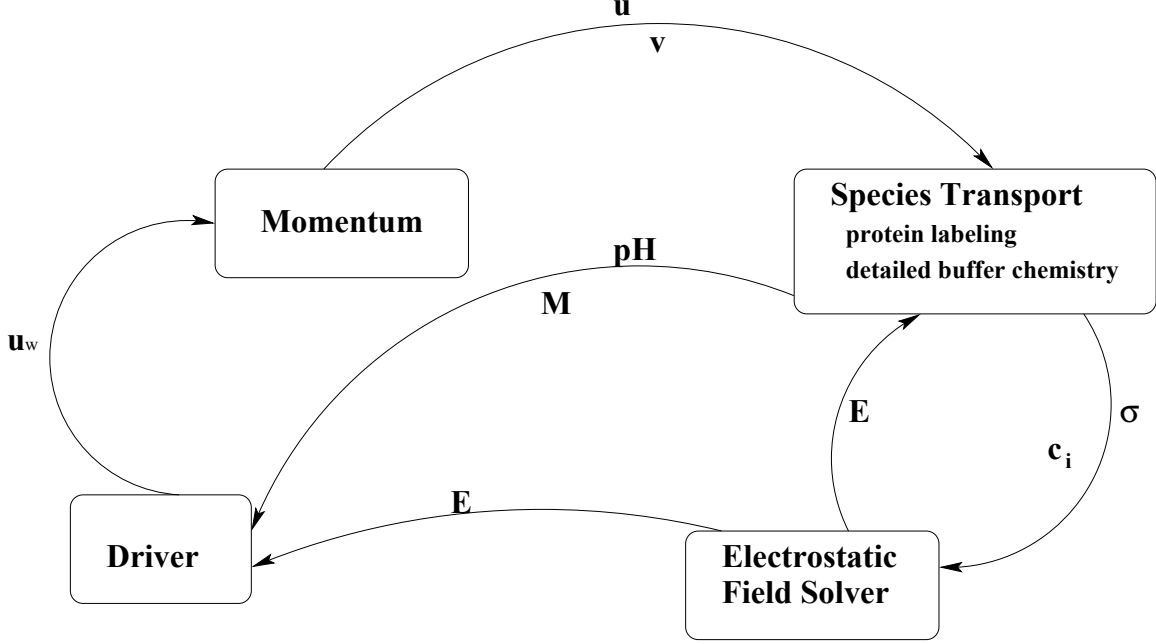


Figure 3: Schematic illustration of the modular nature of the stochastic electrochemical microchannel flow code.

defined following a staggered grid where vector quantities are defined at the cell faces while the scalar quantities are discretized on the cell centers (Fig. 4). Unless otherwise noted, second-order centered differences are used to approximate derivatives in the interior of the domain.

Momentum

Numerical integration of the momentum equations is performed using a modified version of the SPM outlined in section 2. In order to overcome the diffusive stability restrictions associated with low-Reynolds-number flow, an operator split formulation is introduced. The latter involves a mixed scheme where the convective term is treated using a third order Adams-Bashforth scheme over the global time step Δt , while the diffusion term is several smaller substeps using a second-order Runge Kutta method. We symbolically express the integration as:

$$\frac{\mathbf{u}_k^* - \mathbf{u}_k^n}{\Delta t} = \mathcal{F} \left\{ \mathcal{C}m_k^{(n,n-1,n-2)}, \mathcal{D}m_k^{(s),s=1,\dots,M} \right\} \quad (54)$$

$$\frac{\mathbf{u}_k^{(n+1)} - \mathbf{u}_k^*}{\Delta t} = -\nabla p_k^{(n+1)} \quad (55)$$

where \mathcal{F} symbolically represents the operator split action which depends on the convective term $\mathcal{C}m_k$ evaluated at three time steps t_n, t_{n-1} and t_{n-2} , and the diffusive term $\mathcal{D}m_k$ computed at M substages between times t_n and t_{n+1} .

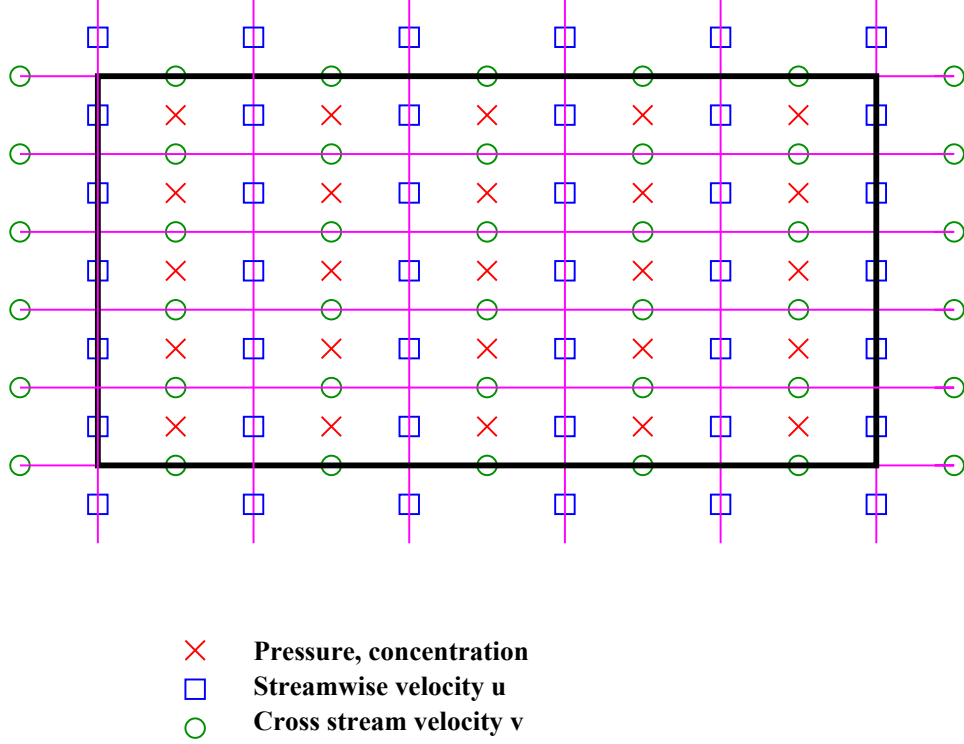


Figure 4: Schematic illustration of the computational grid, showing the discretization scheme for primary variables.

The pressure term needed in the second step is obtained by combining Eq. 55 with the weak formulation of the continuity constraint

$$\nabla \cdot \mathbf{u}_k^{(n+1)} = 0 \quad k = 0, \dots, P \quad (56)$$

resulting in a system of decoupled Poisson equations expressed as:

$$\nabla^2 p_k^{(n+1)} = -\frac{1}{\Delta t} \nabla \cdot \mathbf{u}_k^{(*)} \quad k = 0, \dots, P \quad (57)$$

A direct fast Fourier solver is used to invert Eq. (57) and thus determine the pressure modes p_k .

Concentration

Some of the species involved in electrochemical microchannel are characterized by very low molecular diffusivities, which may be as low as $10^{-11} \text{ m}^2/\text{s}$ or smaller. Proteins are prominent examples of such slowly-diffusing species. This situation leads to microchannel flows with high Peclet numbers, which provides significant challenge to the computations. Well-known difficulties include susceptibility of the discretization to develop spurious high-frequency

wiggles, which in some situations may lead to breakdown of the computations. In order to overcome these difficulties, a Godunov upwind scheme was developed for the spectral formulation. Details of this upwind discretization are provided in [24].

In conjunction with upwind discretization of the convection terms, an explicit AB3 scheme is used to update the concentration fields. We have:

$$\frac{c_i^{n+1} - c_i^n}{\Delta t} = \frac{23}{12}H^n - \frac{16}{12}H^{n-1} + \frac{5}{12}H^{n-2} \quad (58)$$

where

$$H \equiv -\mathbf{u} \nabla c_i + \nabla \cdot (D_i \nabla c_i) + \hat{w}_i(\mathbf{c}) \quad (59)$$

and Δt is the time step.

Electrostatic Field

Finite difference discretization of the electrostatic field equation results in the following linear system of $N_x \times N_y \times (P + 1)$ equations:

$$\begin{aligned} \sum_{l=0}^P \sum_{m=0}^P \mathcal{M}_{klm} [(W_l)_{i,j}(\phi_m)_{i+1,j} + (E_l)_{i,j}(\phi_m)_{i-1,j} + \\ (N_l)_{i,j}(\phi_m)_{i,j+1} + (S_l)_{i,j}(\phi_m)_{i,j-1} + (C_l)_{i,j}(\phi_m)_{i,j}] \\ = (f_k)_{i,j} \quad k = 0, \dots, P. \end{aligned} \quad (60)$$

where

$$\begin{aligned} (E_l)_{i,j} &= -\frac{(\sigma_l)_{i+1,j} + (\sigma_l)_{i,j}}{2\Delta x^2} \\ (W_l)_{i,j} &= -\frac{(\sigma_l)_{i,j} + (\sigma_l)_{i-1,j}}{2\Delta x^2} \\ (N_l)_{i,j} &= -\frac{(\sigma_l)_{i,j+1} + (\sigma_l)_{i,j}}{2\Delta y^2} \\ (S_l)_{i,j} &= -\frac{(\sigma_l)_{i,j} + (\sigma_l)_{i,j-1}}{2\Delta y^2} \\ (C_l)_{i,j} &= \frac{(\sigma_l)_{i+1,j} + 2(\sigma_l)_{i,j} + (\sigma_l)_{i-1,j}}{2\Delta x^2} + \frac{(\sigma_l)_{i,j+1} + 2(\sigma_l)_{i,j} + (\sigma_l)_{i,j-1}}{2\Delta y^2} \\ (f_k)_{i,j} &= -F \sum_s z_s \sum_{l=0}^P \sum_{m=0}^P \mathcal{M}_{lmk} \nabla \cdot (D_{s,l} \nabla c_{s,m}) \end{aligned} \quad (61)$$

with indices i and j denoting the cell location.

In order to efficiently invert the system above, a specially tailored multigrid solver was developed in [25]. The algorithm globally iterates over the spatial domain cells using a Gauss-Seidel scheme:

- Loop on ou (Gauss-Seidel index)
 - For $i = 1$ to N_x , do
 - * For $j = 1$ to N_y , do
 - Find $(\phi_k)_{i,j}^{ou+1}$ such that:

$$\begin{aligned}
 \sum_{l=0}^P \sum_{m=0}^P \mathcal{M}_{klm} (C_l)_{i,j} (\phi_m)_{i,j}^{ou+1} &= (f_k^n)_{i,j} - \\
 \sum_{l=0}^P \sum_{m=0}^P \mathcal{M}_{klm} [(W_l)_{i,j} (\phi_m)_{i+1,j}^{ou} &+ (E_l)_{i,j} (\phi_m)_{i-1,j}^{ou+1} + \\
 (N_l)_{i,j} (\phi_m)_{i,j+1}^{ou} &+ (S_l)_{i,j} (\phi_m)_{i,j-1}^{ou+1}] \\
 &\equiv (Q_k)_{i,j}^{ou} \\
 k = 0, \dots, P &
 \end{aligned} \tag{62}$$

- * End of loop on j
 - End of loop on i
- End of loop on ou

At each spatial location, Eq. (62) are inverted using successive over-relaxation (SOR) scheme, which yields estimates of the stochastic modes $(\phi_{k=0,\dots,P})_{i,j}^{(ou+1)}$.

In its simplest form, known as V-cycle, the multigrid scheme consists of first solving the original problem on the computational (finest) grid by running few iterations. This is followed by iterating on the projected residuals on consecutively coarser grids. Once the final (coarsest) grid level is attained, the solution is transferred to the previous grid level via a prolongation step. Iterations are then performed on finer grid levels until the finest grid is reached. The V-cycle is repeated until sufficiently small residuals are achieved on the finest grid.

For slender domains, the convergence rate of the above multigrid solver is further enhanced using a line relaxation method, which essentially amounts to extending spatial coarsening to the larger spatial dimension. Convergence is accelerated due to the faster damping of the long-wave error modes on the coarse quasi-1D grid, as well as the lower CPU cost when relaxing the residual over a fewer number of cells [26]. For additional details on the stochastic multigrid solver, see [25] (Appendix C).

Electroneutrality

As explained in section 3.1, the individual concentrations of the buffer ions and $[H^+]$ are obtained from the electroneutrality condition. In the stochastic case, this condition results in a set of non-linear algebraic relations between $P + 1$ stochastic modes. This coupled non-linear system of equations is iteratively solved at each point in the domain, using a Newton solver from the NITSOL package [27]. The solver uses an inexact Newton method

with backtracking. Using the solution from the previous time step as initial guess, the convergence is generally very fast.

UQ Toolkit

As mentioned earlier, the governing equations for the spectral mode strengths of the field variables are obtained by substituting the PC expansions for those field variables in their original, deterministic governing equations. Instead of explicitly writing out these equations for the spectral mode strengths, it is also possible to retain the governing equations in their original form, but take into account during the implementation that all arithmetic needs to be performed on stochastic instead of deterministic variables.

To facilitate this approach, we developed an uncertainty quantification (UQ) toolkit[†] which contains subroutines to perform most of the common operations on stochastic variables that are represented by PC expansions. Using this toolkit, many algorithms that were originally designed for deterministic problems can easily be converted for stochastic computations by merely replacing mathematical operators with calls to their stochastic equivalent. The details of some of these operations are explained below.

Aside from additions, one of the most common operations is the multiplication of two stochastic variables. Consider two stochastic variables, u and v , with the following PC representations:

$$u = \sum_{i=0}^P u_i \Psi_i \quad (63)$$

$$v = \sum_{j=0}^P v_j \Psi_j \quad (64)$$

We need to find the modes w_k in the PC representation of $w = uv$:

$$w = \sum_{k=0}^P w_k \Psi_k \quad (65)$$

As mentioned before, these coefficients are obtained by using the orthogonality property of the PC basis functions:

$$w_k = \sum_{i=0}^P \sum_{j=0}^P \mathcal{M}_{ijk} u_i v_j \quad k = 0, \dots, P \quad (66)$$

Since the tensor \mathcal{M}_{ijk} is a function of the PC basis functions only, it only needs to be calculated once during a preprocessing step and can then be stored for use throughout the computations. The implementation of equation (66) also takes advantage of the fact that this tensor is sparse, reducing the amount of storage and CPU time needed.

[†]To obtain a copy of the UQ toolkit users are directed to send a request to the PI at knio@jhu.edu.

A similar procedure could also be used to determine the PC expansion for the product of three stochastic variables $g = uvw$. This would give the spectral coefficients g_k as

$$g_l = \sum_{i=0}^P \sum_{j=0}^P \sum_{k=0}^P D_{ijkl} u_i v_j w_k \quad l = 0, \dots, P \quad (67)$$

where

$$D_{ijkl} \equiv \frac{\langle \Psi_i \Psi_j \Psi_k \Psi_l \rangle}{\langle \Psi_l^2 \rangle} \quad (68)$$

Instead of this pure spectral approach, however, a pseudo-spectral approach has been developed in order to calculate products such as $g = uvw$ by repeated use of the regular product function. First the product uv is calculated with equation (66), and the result of this multiplication is multiplied in the same way with w to give the PC expansion for g . The advantage of this pseudo-spectral approach is that it does not require the evaluation and storage of the fourth-rank tensor D_{ijkl} , is more efficient, and is easy to generalize to products of any number of variables. Some aliasing errors are introduced though in this approach, but they were found to be negligible as long as the order of the PC expansions is chosen sufficiently high.

Another frequent operation is the calculation of the inverse of a stochastic quantity. To explain how this operation is implemented, consider again three stochastic variables, u , v , and w , with their respective PC expansions given by equations (63–65). If we wish to calculate $u = w/v$, then this implies $w = uv$, which is given by equation (66). This equation, assuming the modes w_k and v_j are known, represents a system of $P + 1$ linear equations in the unknown modes u_i . Since it is a sparse system of equations, it is solved efficiently in this work with a GMRES iterative solver, taken from the SLATEC library [28].

More challenging is the evaluation of non-polynomial functions of stochastic variables such as exponentials and logarithms, which typically show up in chemical rate expressions. These operations can be performed by expanding them in Taylor series around the mean of the argument. For example, the exponential of a stochastic quantity u , with a PC expansion given by equation (63), is computed as

$$e^u = e^{u_0} \left(1 + \sum_{n=1}^N \frac{d^n}{n!} \right) \quad (69)$$

where

$$d = u - u_0 = \sum_{i=1}^P u_i \Psi_i \quad (70)$$

is the stochastic part of u . The powers d^n are again calculated in a pseudo-spectral way with the product formula (66), as $d^n = d d^{n-1}$, with d^{n-1} known from the previous term in the Taylor series. The number of terms N in this truncated series is chosen adaptively to satisfy a given tolerance level.

The Taylor series approach works reasonably well as long as the uncertainties in the field variables are moderate and the probability density functions (PDFs) of those variables are

not too skewed. For highly skewed PDFs, however, high order PC expansions are required to capture this stochastic information, and the evaluation of high power terms d^n in the Taylor series can become inaccurate. In these situations, an alternative approach based on integrations [7], can be used in order to provide more accurate estimates.

All the operations described above, among many others, have been implemented in the UQ toolkit library. The UQ toolkit greatly facilitates the development of stochastic solvers from scratch, as well as the conversion of existing deterministic routines into stochastic ones.

3.3 Applications and Demonstrations

Demonstration efforts conducted during this project fell within three main areas of application. These include: (1) Development and application of a quasi-1D design model for band-crossing reactions; (2) Application of the UQ toolkit to simplified CAD models; and (3) Demonstration of combined detailed physical modeling and uncertainty quantification capabilities for the case of protein labeling reactions in a microchannel. Applications in the first two areas are discussed in detail [29] and in [24], respectively; for brevity, results of these applications are omitted from this report. Instead, this section focuses on providing highlights of detailed computations of bio-reactions in electrochemical microchannel flow.

Protein Labeling in a Homogeneous Buffer

To illustrate the stochastic uncertainty quantification methodology, this section describes protein labeling in a simple homogeneous system. Figure 5 shows the time evolution of the concentrations of the unlabeled and labeled protein in a homogeneous potassium phosphate buffer at a pH of 8.25. In this problem, the dye D was assumed to be present in abundance so that the source term for the labeled protein in equation 31 can be written as

$$\hat{w}_L = k_L[U] \quad (71)$$

The rate constant k_L in this reaction is pH dependent, given by the following equation:

$$k_L = k_L^0 + d_L e^{-(\text{pH} - \text{pH}_0)^2 / \delta_{\text{pH}}^2} \quad (72)$$

The Gaussian dependence of this relationship on pH is based on the shape of the measured pH-dependence of the rate of production of the high-fluorescence-efficiency species from the reaction of Naphthalene-2,3-dicarboxaldehyde (NDA) with amino acids in the presence of CN^- [30]. The following parameters were used in this expression: $k_L^0 = 0.25 \times 10^{-3} \text{ s}^{-1}$, $d_L = 2.15 \text{ s}^{-1}$, $\text{pH}_0 = 9.25$, and $\delta_{\text{pH}} = 0.85$. Both proteins U and L, as well as the dye D were assumed to have no charge, and therefore the buffer equilibrium and pH did not change with time. For this simulation, a standard deviation of 1% was assumed for all parameters in the rate expression (72), as well as for the electrolyte dissociation constants. Third order PC expansions were used.

The resulting uncertainty in the protein concentrations is indicated in Fig. 5 with “error bars” that span the $\pm 3\sigma$ range, where σ indicates the standard deviation. Clearly, uncertainty in the input parameters causes large uncertainties in the simulated concentrations.

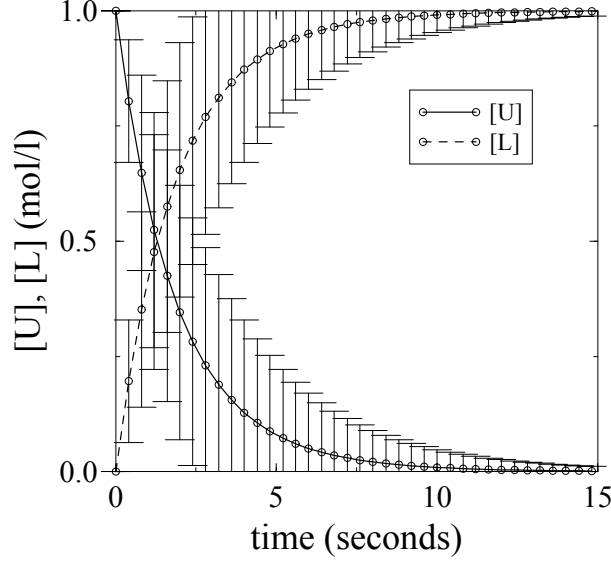


Figure 5: Time evolution of U and L concentrations in a homogeneous protein labeling reaction. The uncertainty in these concentrations, due to a 1 % uncertainty in the labeling reaction rate parameters, is indicated by $\pm 3\sigma$ “error bars”.

At the point where $[U] = 0.5$, a standard deviation of 1% in the parameter pH_0 is magnified about 16 times in the standard deviation of $[U]$.

Note that after about 3 seconds, the range of the $\pm 3\sigma$ “error bars” becomes so large that it seems to include concentrations for U that are negative, which is clearly not physically possible. However, the interval $\pm 3\sigma$ around the mean value properly represents the full range of possibilities for a certain variable only when its probability density function is Gaussian, and therefore symmetric. Figure 6 shows the probability density function of $[U]$, generated from its PC expansion at various points in time. When the mean value of $[U]$ is sufficiently far away from zero, this PDF has a Gaussian shape. However, for mean values of $[U]$ closer to zero, the PDF becomes narrower and more skewed. This predicted uncertainty properly reflects the physical system behavior where all unlabeled protein reacts away, but its concentration can not be negative.

Parametric Uncertainty in 2D Electro-osmotic Microchannel Flow

This section presents some results of a study of parametric uncertainty in electro-osmotic microchannel flow [31]. Figure 7 shows the geometry considered for these test problems, consisting of a rectangular microchannel in which a protein U and dye D react to form a labeled protein L. An external electrostatic potential is applied across the system to generate an electroosmotic flow in the x -direction. The unlabeled protein U has a charge of +1 versus a charge of -1 for the dye D, so electrophoresis will move U forward and D backward, relative

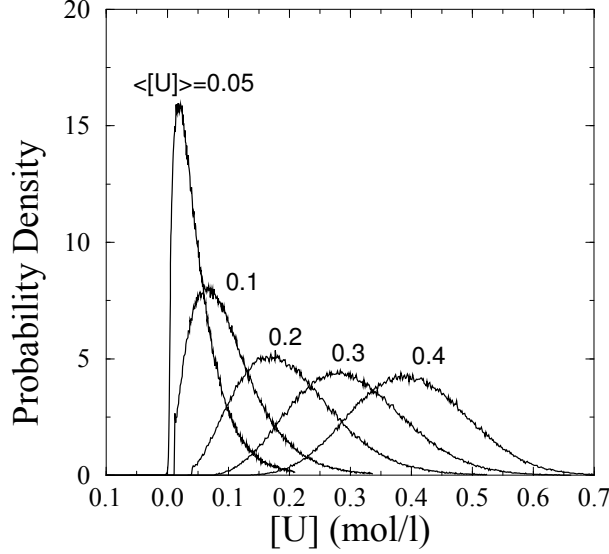


Figure 6: PDF of the unlabeled protein concentration at different mean values. As the unlabeled protein reacts away, its PDF becomes narrower and more skewed.

to the bulk flow. An aqueous potassium phosphate (KH_2PO_4) buffer solution is considered. Therefore, the species in the solution are the proteins U and L, the dye D, the electrolytes H^+ , OH^- , K^+ as well as the components of phosphoric acid H_3PO_4 , H_2PO_4^- , HPO_4^{2-} , and PO_4^{3-} .

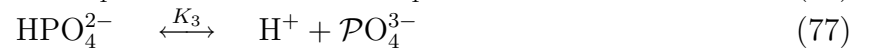
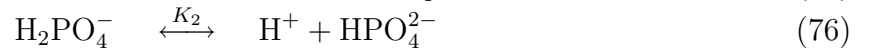
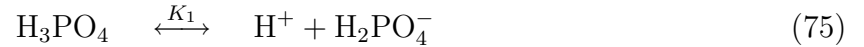
The proteins in this solution are assumed to have a fixed charge and can therefore be integrated with equation (31) with a chemical reaction source term \hat{w}_i according to a model irreversible labeling reaction



As before, the rate constant was modeled by equation (72), but with the following parameters: $k_L^0 = 0.25 \times 10^6 \text{ mol}^{-1}.\text{l.s}^{-1}$, $d_L = 2.15 \times 10^6 \text{ mol}^{-1}.\text{l.s}^{-1}$, $\text{pH}_0 = 7.40$, and $\delta_{\text{pH}} = 0.85$. The chemical source terms used in equation (31) are correspondingly

$$\hat{w}_U = \hat{w}_D = -\hat{w}_L = -k_L[\text{U}][\text{D}] \quad (74)$$

The concentration of the K^+ ion, which is fully dissociated and is a conserved quantity can also be integrated by equation (31) directly (without a source term). Phosphoric acid, however, is a weak acid and will dissociate according to the following electrolyte reactions



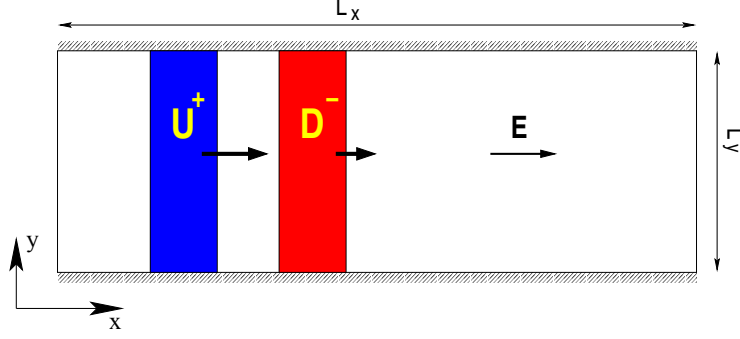


Figure 7: A plug of protein U and dye D are introduced in a rectangular microchannel and react to form a labeled protein L.

where the K_i are the corresponding dissociation constants. An equilibrium formulation is used for these fast electrolyte reactions. Therefore, we consider the total concentration of this weak acid

$$\theta_a = [\text{H}_3\text{PO}_4] + [\text{H}_2\text{PO}_4^-] + [\text{HPO}_4^{2-}] + [\text{PO}_4^{3-}] \quad (78)$$

whose transport equation is obtained similarly to equation (36) by adding up the transport equations for all the components in θ_a so the dissociation reaction source terms disappear. The concentrations of the individual components of θ_a are then calculated as $c_i = \alpha_i \theta_a$, where the α_i are calculated from the equilibrium expressions for the dissociation reactions (75-77) and can be written as a function of $[\text{H}^+]$ and the dissociation constants only:

$$\alpha_{\text{H}_3\text{PO}_4} = \frac{[\text{H}^+]^3}{[\text{H}^+]^3 + K_1[\text{H}^+]^2 + K_1K_2[\text{H}^+] + K_1K_2K_3} \quad (79)$$

$$\alpha_{\text{H}_2\text{PO}_4^-} = \frac{K_1[\text{H}^+]^2}{[\text{H}^+]^3 + K_1[\text{H}^+]^2 + K_1K_2[\text{H}^+] + K_1K_2K_3} \quad (80)$$

$$\alpha_{\text{HPO}_4^{2-}} = \frac{K_1K_2[\text{H}^+]}{[\text{H}^+]^3 + K_1[\text{H}^+]^2 + K_1K_2[\text{H}^+] + K_1K_2K_3} \quad (81)$$

$$\alpha_{\text{PO}_4^{3-}} = \frac{K_1K_2K_3}{[\text{H}^+]^3 + K_1[\text{H}^+]^2 + K_1K_2[\text{H}^+] + K_1K_2K_3} \quad (82)$$

Equation (30) is used to model the dependence of the zeta potential on pH and buffer molarity. The concentration of the fully dissociated potassium ion, $[\text{K}^+]$, is used for the local buffer molarity \mathcal{M} along the walls. The temperature is assumed constant in this work, with all species properties and reaction rate constants evaluated at 298 K.

All parameters and field variables, were represented with third order polynomial chaos expansions. The highest order stochastic modes in the expansions of the predicted field variables were significantly lower than the lower order modes, indicating that the third order expansions were sufficiently accurate.

Referring to Fig. 7, a microchannel was considered with a length $L_x = 1$ cm and a height $L_y = 1$ mm. The potassium phosphate buffer solution was initialized with a uniform concentration of 10^{-3} mol/l and a pH of 7.25. The Gaussian profiles for the initial U and D concentrations had peak concentrations of 10^{-4} mol/l, located at $x = 2.5$ mm and $x = 4$ mm respectively, and a width in x of 0.75 mm. A fixed charge of +1 was assumed for the unlabeled protein U and a charge of -1 for the dye D, resulting in a neutral labeled protein L. The electrostatic potential difference ΔV across the domain was set to 1000 V, giving an average field strength of 1 kV/cm. An uncertainty of 1 % was assumed in the mobility of U, in the labeling rate parameter pH_0 , the dissociation constant K_2 , and the potential difference ΔV . Third order polynomial chaos expansions were used in the computations with a total of 35 stochastic modes. The time step was set to 2×10^{-4} s and the domain was discretized with 512×32 cells in x and y .

Figure 8 shows a contour plot of the mean concentrations of the proteins and dye at $t = 0.12$ s. At this point in time, the plugs of U and D have just met at $x \approx 4$ mm, and labeled protein is generated at the interface. Note that the labeling reaction is fast compared

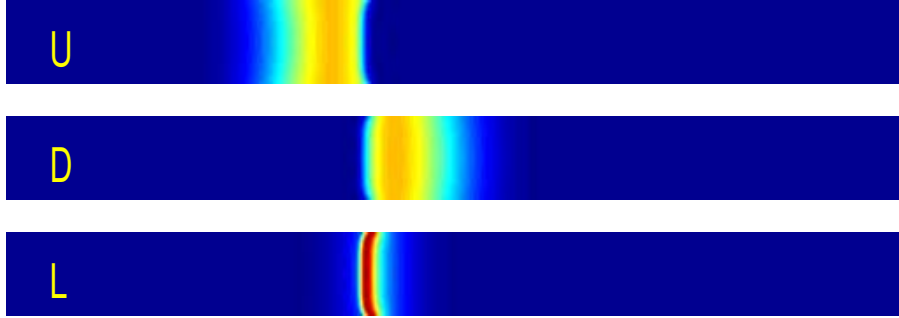


Figure 8: Mean concentrations of proteins U, L, and dye D at $t = 0.12$ s. U and D just met and L is produced at their interface. The values of the contour levels go linearly from 0 (blue) to 1.3×10^{-4} mol/l (red). In this figure, as well as in all subsequent contour plots, the full physical domain is shown, from 0 to 1 cm in x and from 0 to 1 mm in y .

to the electroosmotic and electrophoretic transport. Consequently, U and D react as soon as they meet, resulting in almost no overlap between the U and D profiles, and a sharp profile for L. Since L is neutral, it travels with the bulk convective velocity, which is the average of the total convective velocities of U and D. Therefore the peak value of L is always located at the interface of U and D, and since L is generated in that same area, its peak concentration will keep increasing. At $t = 0.12$ s, the peak concentration for L is 1.3×10^{-4} mol/l, which is already higher than the peak concentrations of 9.4×10^{-5} mol/l for U and D.

The standard deviations in the concentrations of Fig. 8 are given in Fig. 9. The highest uncertainties appear in the reaction zone at the interface between U and D, with a maximum coefficient of variation of about 20 % in the L concentration. Even though Fig. 9 only shows the overall uncertainty in the concentrations, a strong feature of the PC formalism is that

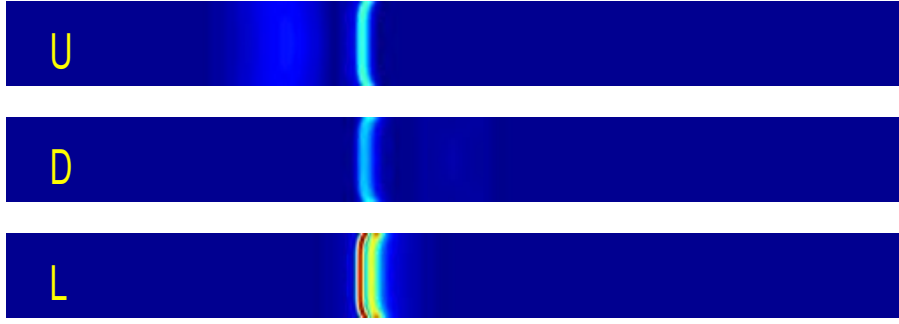


Figure 9: Standard deviation of the protein and dye concentrations at $t = 0.12$ s. The values of the contour levels go linearly from 0 (blue) to 1.1×10^{-5} mol/l (red). The largest uncertainties are found in the reaction zone.

the contributions of the uncertainty in individual parameters to this overall uncertainty can easily be retrieved, as explained in [31]. Figure 10, for example, shows the contributions from each of the 4 uncertain input parameters to the standard deviation of the L concentration, in the area around the reaction zone, at $y = 0.5$ mm. The total standard deviation of [L] is given by the curve labeled “all” in this figure. This overall standard deviation has a profile with a double peak, which for a single peak mean species profile, is characteristic of uncertainty caused by the convection velocity. When a single peak species profile is transported by an uncertain convection velocity, the uncertainty in the position of the peak at a given point in time will cause the most variability at the sides of the peak, where the profile has a steep slope in the x -direction. At the top of the profile, there is no concentration gradient and uncertainties in peak position cause little uncertainty in the observed concentrations at that location.

As indicated by the curve labeled “ ΔV ”, the uncertainty in the applied electrostatic field potential has the most dominant contribution to the overall standard deviation. Since both the electroosmotic and electrophoretic velocities are directly proportional to ΔV , the uncertainty caused by this parameter naturally shows a double peak, characteristic of convection velocity uncertainty. Similarly, the parameter β_U affects the electrophoretic transport of the reactant U and its resulting contribution to the standard deviation of [L] also has a double peak, albeit smaller than the ΔV contribution.

The contribution of parameter pH_0 also shows a double peak, but with its center located on the left side of the [L] profile, where the gradient of [L] in x is very steep. The steepness of the [L] profile in that area is largely determined by the speed of the labeling reaction compared to the convection speed, with a faster reaction rate leading to a sharper increase in [L]. With the pH in this area between 7.0 and 7.1 (not shown), equation (72) predicts significant variability in k_L for changes in pH_0 . So the uncertainty in pH_0 mainly affects the slope of the [L] profile on the left side, consistent with the observed contribution of parameter pH_0 in Fig. 10.

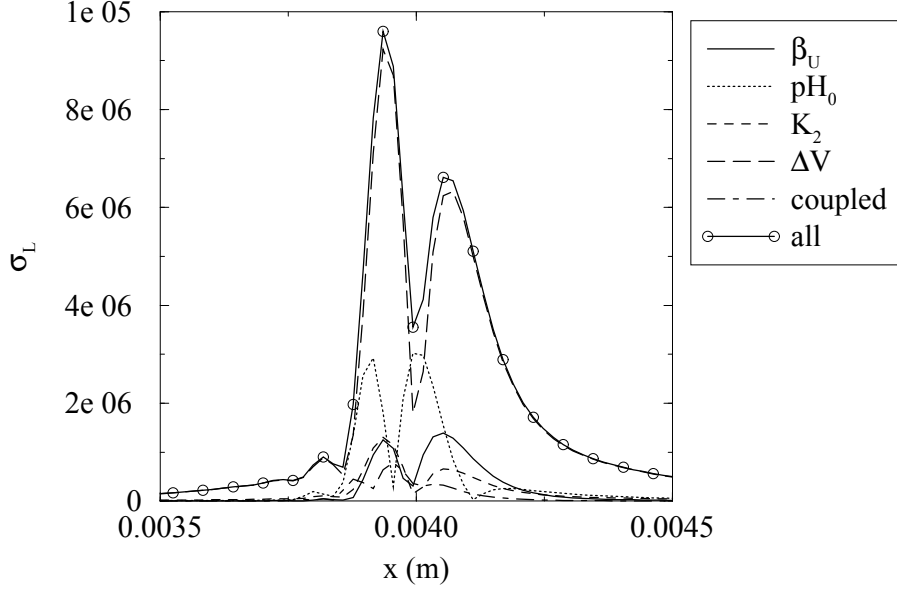


Figure 10: Major contributions of individual input parameters to the overall standard deviation in $[L]$ in the area around the reaction zone at $t = 0.12$ s, $y = 0.5$ mm. The uncertainty in the applied voltage potential “ ΔV ” has the most dominant contribution to the overall standard deviation in $[L]$.

Figure 10 further shows more minor contributions, from the dissociation parameter K_2 and from the coupled terms. Even though their contribution is small in this case, those coupled terms are interesting from a theoretical point of view, as they represent coupled effects of independent parameters. In the current figure, those terms represent the sum of three different coupled effects: the coupled effect of ΔV and β_U , of ΔV and pH_0 , and of ΔV and K_2 .

As time goes on and the U and D plugs cross each other, nearly all U and D are consumed in the labeling reaction. At $t = 0.50$ s, only labeled protein L remains, with its mean concentration and standard deviation as shown in Fig. 11. The maximum mean concentration of L at this point in time is 2.4×10^{-4} mol/l in the center of the channel, and about 3.2×10^{-4} mol/l near the walls. So the L concentration is up to three times as large as the initial U and D concentrations. The standard deviation in L, as shown in the bottom plot of Fig. 11, is very large near the wall, with maximum values up to 10^{-4} mol/l and coefficients of variation up to 100 %. Again, the standard deviation in $[L]$ exhibits the double peak near the centerline, which is characteristic of uncertainty caused by the convection velocity.

What is particularly significant though, is the major distortion of the L plug, as opposed to the straight profile observed at early times. This distortion is caused by the disturbance of the buffer electrolyte, in response to the movement and annihilation of the charged protein U and the dye D. To explain why this is physically happening, consider Fig. 12, which shows



Figure 11: Mean (top) and standard deviation (bottom) of the labeled protein concentration L at $t = 0.50$ s. The initially flat profiles are now severely distorted. The values of the contour levels go linearly from 0 (blue) to 3.2×10^{-4} mol/l (red) in the top plot and from 0 (blue) to 10^{-4} mol/l (red) in the bottom plot.

the mean and standard deviation of the electrical conductivity σ of the electrolyte solution at $t = 0.50$ s. Because two charged molecules are used up for every new labeled protein,

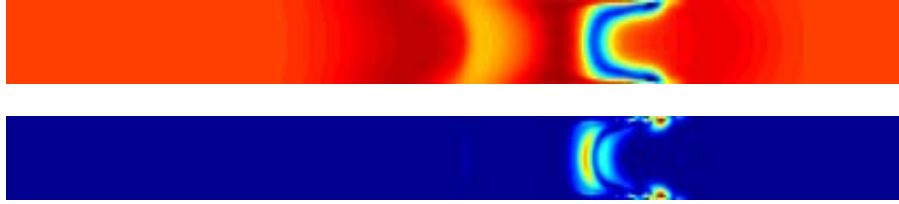


Figure 12: Mean (top) and standard deviation (bottom) of the electrical conductivity of the electrolyte solution at $t = 0.50$ s. Annihilation of ions in the labeling reaction results in a significantly lower mean electrical conductivity near the L plug. The values of the contour levels go linearly from 7.1×10^{-3} S/m (blue) to 1.3×10^{-2} S/m (red) in the top plot and from 0 (blue) to 1.5×10^{-3} S/m (red) in the bottom plot.

the area around the L plug has a reduced concentration of ions, with a mean electrical conductivity of almost a third lower than in the undisturbed buffer. Upstream of the L plug, the electrical conductivity shows some smaller fluctuations, which stem from shifts in the buffer equilibrium. Since the buffer ions are primarily negatively charged, those disturbances travel slower than the labeled protein plug. The bottom plot of Fig. 12 shows that the highest uncertainties in the electrical conductivity are found around the L plug, near the center and especially at the walls.

The large spatial variations in the electrical conductivity in turn cause non-uniformities in the electrical field strength, as shown in Figs. 13 and 14. Near the L plug, the mean electrostatic field strength in the x -direction reaches a value up to 40 % higher than in the undisturbed flow. This increase strongly affects the local electroosmotic and electrophoretic velocities, causing an increased wall velocity, leading to the observed distortion of the L plug. The largest uncertainties are again found near the L plug, with maxima up to 10 %.

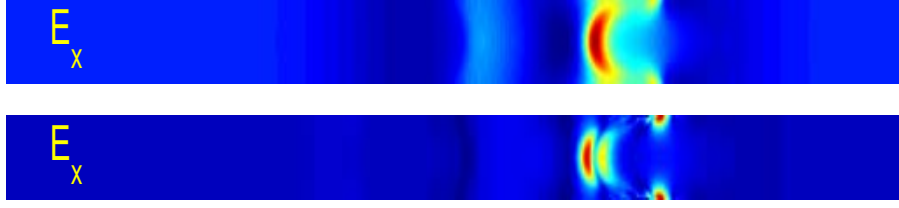


Figure 13: Mean (top) and standard deviation (bottom) of the electrical field strength in the x -direction at $t = 0.50$ s. Near the L plug, the mean streamwise electrical field strength is about 40 % higher than in the undisturbed flow. The values of the contour levels go linearly from 91.4 kV/m (blue) to 146 kV/m (red) in the top plot and from 0.20 kV/m (blue) to 13 kV/m (red) in the bottom plot.

Even though the initial field strength in the y -direction was zero, Fig. 14 shows that this



Figure 14: Mean (top) and standard deviation (bottom) of the electrical field strength in the y -direction at $t = 0.50$ s. The magnitude of the mean of this field strength is up to 15 % of the initial field strength in the x -direction. The values of the contour levels go linearly from -16.3 kV/m (blue) to 16.3 kV/m (red) in the top plot and from 0 (blue) to 5.8 kV/m (red) in the bottom plot.

y -component is quite significant at $t = 0.50$ s. The magnitude of this field strength is up to 15 % of the initial, streamwise electrostatic field strength for the mean value. Even though this y -component does not affect the electroosmotic flow velocity directly, it does provide electrophoretic ion transport in the wall-normal direction, which can further distort sample profiles.

As indicated by equation (29), the electroosmotic wall velocity depends on both the local electrostatic field strength and ζ potential, which in turn depends on the pH and the buffer molarity, as modeled by equation (30). Since all these variables are disturbed by the charged protein movement and annihilation, the electroosmotic wall velocity varies in the streamwise direction. These wall velocity changes in turn cause pressure gradients and local recirculation zones, as indicated by the velocity fields in Figs. 15 and 16. Figure 15 shows the streamwise velocity field, which has a mean wall velocity that is up to 20 % higher near the L plug.

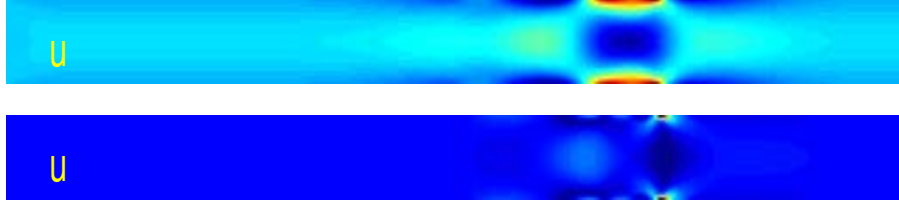


Figure 15: Mean (top) and standard deviation (bottom) of the streamwise velocity at $t = 0.50$ s. The local increase in the electroosmotic wall velocity leads to recirculation zones near the L plug. The largest uncertainties are found near the wall. The values of the contour levels go linearly from 6.8 mm/s (blue) to 9.1 mm/s (red) in the top plot and from 5.6×10^{-3} mm/s (blue) to 0.59 mm/s (red) in the bottom plot.

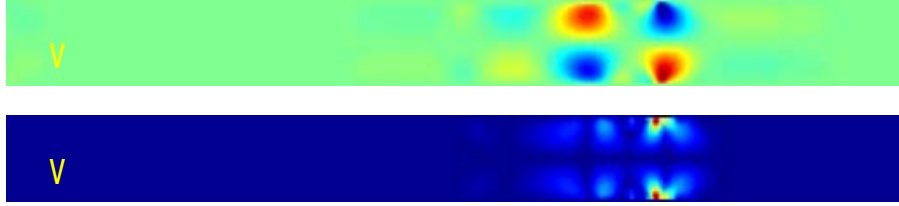


Figure 16: Mean (top) and standard deviation (bottom) of the wall-normal velocity at $t = 0.50$ s. The mean of this velocity has a magnitude of up to 6 % of the initial streamwise velocity. The values of the contour levels go linearly from -0.56 mm/s (blue) to 0.56 mm/s (red) in the top plot and from 0 (blue) to 0.26 mm/s (red) in the bottom plot.

The wall-normal velocity field shows positive and negative velocities near the L plug, with magnitudes up to 6 % of the initial streamwise velocity.

Clearly, the recirculation zones in the flow field will distort initially flat sample profiles. This increases the hydrodynamic dispersion, on top of the electrokinetic dispersion caused by non-uniformities in the electrophoretic transport.

Sample Dispersion in Electro-osmotic Microchannel Flow with Random Zeta Potential Variability

The previous section showed an example of parametric uncertainty in model input parameters, and the subsequent uncertainty in the model results. In this section, an example is given where the uncertainty does not stem from a few input parameters but from inherent variability in the boundary conditions along the walls of the microchannel. For example, non-uniformities in the wall material, wall roughness from the channel etching process, or wall fouling by protein deposition can all lead to variabilities in the wall ζ -potential. This variability can be modeled as a random process and represented with a Karhunen-Loève

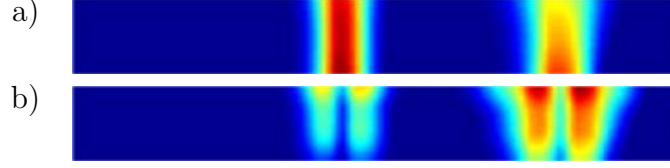


Figure 17: Overlay of the mean a) and Standard Deviation b) of the labeled protein concentration $[L]$ at times $t = 0.24$ s and $t = 0.72$ s. The profiles spread out as they move downstream (to the right), especially along the top wall, which has the non-uniform ζ -potential. The maximum value for the mean of $[L]$ is 1.5×10^{-6} mol/l and the maximum standard deviation is 5.4×10^{-7} mol/l.

expansion [29, 32, 33].

Referring to Fig. 7, a two-dimensional flow is assumed in a channel with length $L_x = 1$ cm and depth $L_y = 100$ μ m. The channel was initialized with an aqueous potassium phosphate buffer solution at a concentration of 10^{-3} mol/l and a pH of 7.25. At time zero, a plug of unlabeled protein U^{2+} was introduced as well as a plug of dye D^{2-} , at $x = 0.2$ cm and $x = 0.4$ cm respectively. Both plugs were Gaussian with a maximum concentration of 10^{-5} mol/l. An external electrostatic potential of 1 kV is applied across the system to generate electroosmotic flow in the x -direction. Given the charge number difference, electrophoresis will cause the U^{2+} plug to cross with the D^{2-} plug. As the protein and dye mix, they react according to a model irreversible labeling reaction



to form a neutral labeled protein L .

Along the bottom wall of the channel, the ζ -potential exhibits no random variability, i.e. it is solely given by Eq.(30). However, along the top wall, a random variability was assumed in the ζ -potential, with a coefficient of variation of 10 % and a correlation length of $50 L_y$. A PC representation for this random variability was obtained using a Karhunen-Loève expansion with 4 stochastic modes (see Eq. (1)). All parameters and field variables, were represented with third order polynomial chaos expansions.

Figure 17 shows both the mean value and the standard deviation in the concentration of the labeled protein L , at two points in time. At time $t = 0.24$ s, the U and D bands have just crossed and the labeling reaction is finished. At this point in time, the L band in Fig. 17a has a maximum concentration of 1.5×10^{-6} mol/l. As the labeled protein moves downstream, molecular diffusion and dispersion spread the L profile, as is clearly visible at $t = 0.72$ s. The standard deviation in the labeled protein concentration, shown in Fig. 17b, reflects the uncertainty in L due to the random variability in the ζ -potential. Analyte dispersion in this case is due to both electrokinetic and hydrodynamic dispersion, as can be explained with the help of Fig. 18. Figure 18a shows the electrical conductivity, which varies in the channel due to the disturbance of the potassium phosphate buffer equilibrium as ions move through the channel and are depleted through the protein labeling reaction (the

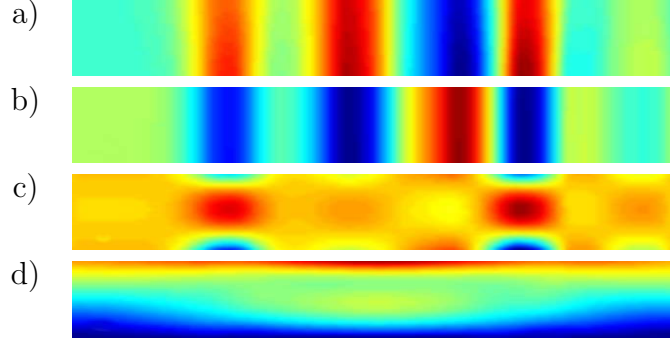


Figure 18: Filled contour plots of several fields at time $t = 0.72$ s. a) Mean electrical conductivity, ranging from 0.0121 to 0.0124 S/m; b) Mean electrostatic field strength in x , ranging from 991 to 1011 V/cm; c) Mean streamwise velocity field, ranging from 7.4 to 7.6 mm/s; d) Standard deviation in streamwise velocity field, ranging from 0 to 0.7 mm/s

generation of one L molecule removes two ions from the solution). The electrostatic field strength, as shown in Fig. 18b, varies accordingly, which causes non-uniform electrophoretic forces on charged analyte profiles. The resulting differences in the propagation speeds of the leading and trailing edges of a charged analyte plug can lead to electrokinetic dispersion. However, while this mechanism affects the unlabeled protein and dye bands in the solution (not shown), it does not affect the labeled protein in this specific case, as L is neutral. The non-uniformities in the electrostatic field strength do affect the electroosmotic wall velocity, given by Eqn. (29), and therefore disturb the bulk velocity field, as shown in Figs. 18c and d. The mean value of the electroosmotic wall velocity is affected primarily by the electrostatic field strength, but also by the buffer pH, buffer molarity, and wall effects through the ζ -potential. Variations in this wall velocity create local accelerations and decelerations with associated pressure gradients in the flow to maintain conservation of mass, as illustrated schematically in Fig. 19. This figure shows an analyte plug traveling through a channel with a non-uniform electrostatic field strength. Pressure gradients upstream of the high field strength area have given the plug a parabolic profile. As the plug travels through the high field strength area, the edges near the wall are accelerated, resulting in a distorted analyte plug. Molecular diffusion in the cross-stream direction smoothens out this distortion, but generates a wider analyte plug, which is the well-known mechanism behind hydrodynamic dispersion. The uncertainty in the streamwise velocity field is primarily caused by the variability in the ζ -potential due to wall effects. The maximum standard deviation of 10 % near the top wall, as shown in Fig. 18d, is consistent with the magnitude of this random ζ -potential variability.

The variability in the ζ -potential clearly is a significant contributor to hydrodynamic dispersion. To study this in more details, a set of cases was ran to investigate the sensitivity of the hydrodynamic dispersion with respect to the statistics of the ζ -potential variability for a system with only neutral, non-reacting analytes. As neutral analytes do not perturb

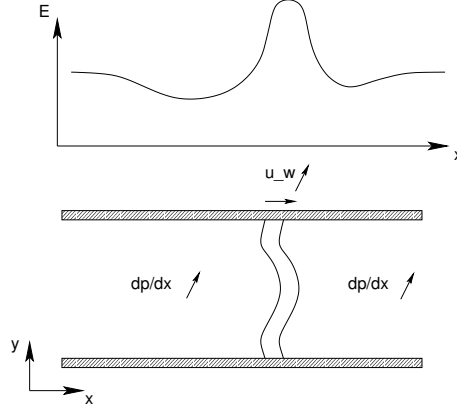


Figure 19: Effect of non-uniform electrostatic field strength on hydrodynamic dispersion of an analyte plug. A local increase of the electroosmotic wall velocity creates local accelerations in the flow that induce pressure gradients elsewhere in the channel. The resulting non-uniform velocity profile distorts the analyte plugs and increases dispersion.

the buffer, those cases had a uniform buffer and electric field strength, so that electrokinetic dispersion was absent. Each time, a random ζ -potential variability was identically imposed on both fully correlated walls, with various choices for the coefficient of variation (COV) and the correlation length L_C . Unless otherwise noted, eight modes were used in the Karhunen-Loève expansion with a 2nd order PC expansion for the parameter and field variables. As suggested by the convergence analysis, eight modes can be sufficiently accurate provided the ζ -potential variability has a relatively long correlation length. The channel size for these cases was 1 cm long by 100 μm deep.

Figure 20 depicts the behavior of the sample dispersion and the corresponding effective diffusive coefficients for various COV's ranging from 10 to 30%. The correlation length for these cases was set to $50 L_y$. As the COV increases, the sample dispersion drastically increases. In fact, Fig. 21 suggests that the mean square width increases almost quadratically with the COV. Although the proteins of interest are characterized by a low diffusion coefficient ($D_{\text{molecular}} = 6.19 \times 10^{-10} \text{m}^2/\text{sec}$) leading to minimal dispersion under ideal situations, the effective diffusion coefficient due to random ζ -potential variability can be up to 2 orders of magnitude higher than the corresponding molecular diffusion.

The role of the ζ -potential scale of fluctuation is illustrated in Figure 22. The COV in these cases was held constant at 10 % and only the correlation length was varied. For the present conditions, the analyte dispersion is more significant in the case of high frequency fluctuations.

A clear interpretation of this trend can be drawn by observing the standard deviation profile of the streamwise velocity u shown in Fig. 23. The results indicate that the velocity gradient across the channel is more pronounced in the case of low correlation length. Zones of the sample plug at different locations across the channel will move with higher differential

bulk velocity leading to a higher dispersion. This has been further quantified in terms of the L^2 norm of the velocity gradient:

$$L_{\frac{\partial \mathbf{u}}{\partial y}}^2(L_C) = \left[\int_0^{L_x} \int_0^{L_y} \left\langle \left(\frac{\partial \mathbf{u}}{\partial y} \right)^2 \right\rangle dy dx \right]^{\frac{1}{2}} \quad (84)$$

$$= \left[\int_0^{L_x} \int_0^{L_y} \sum_{i=0}^P \left(\frac{\partial \mathbf{u}_i}{\partial y} \right)^2 \langle \psi_i \psi_i \rangle dy dx \right]^{\frac{1}{2}} \quad (85)$$

The monotonic increase of the effective dispersion coefficient with the above term is plotted in Fig. 24.

Note that Figs. 20 and 22 both show $\langle \delta^2 \rangle$, which is the mean of the width squared of the U profile, over all possible ζ -potential realizations. Beyond this mean behavior of the U profile, the stochastic methodology also gives full statistical information about this concentration profile. Figure 25 for example show the probability density functions for the location and the width (squared) respectively of the U profile at $t = 0.45$ s for the case with $L_C = 25L_y$ and $\text{COV} = 0.10$. The rather sharp lower bound in the PDF for δ^2 corresponds to the situation of uniform ζ -potential, in which all band spreading is due to molecular diffusion only. Knowing the expected range for the dispersion allows for reliability assessments of electrophoretic separation devices that have non-uniform wall surface properties due to, for example, the microchannel fabrication process, impurities in the wall material or nanoscale events such as protein deposition at the walls.

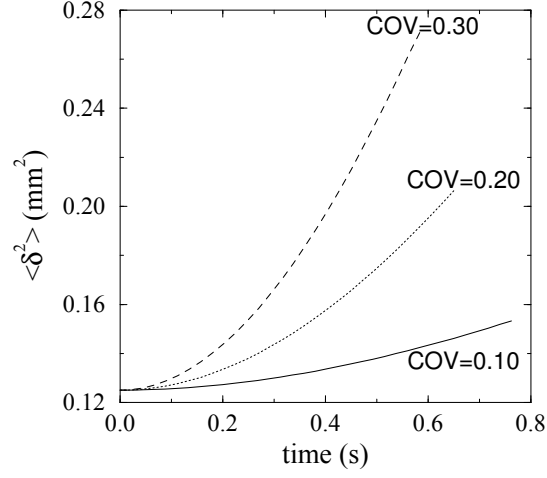


Figure 20: Time evolution of $\langle \delta^2 \rangle$ for a random ζ -potential variability with $L_C = 50$ channel depths. Effective diffusion coefficient (scaled by the molecular diffusivity D_{mol}) for COV= 0.10: 47, COV=0.20: 181, COV=0.30: 397.

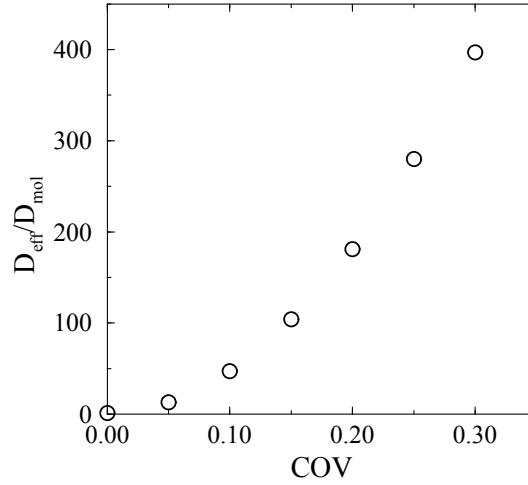


Figure 21: Ratio of effective over molecular diffusion coefficient as a function of COV.

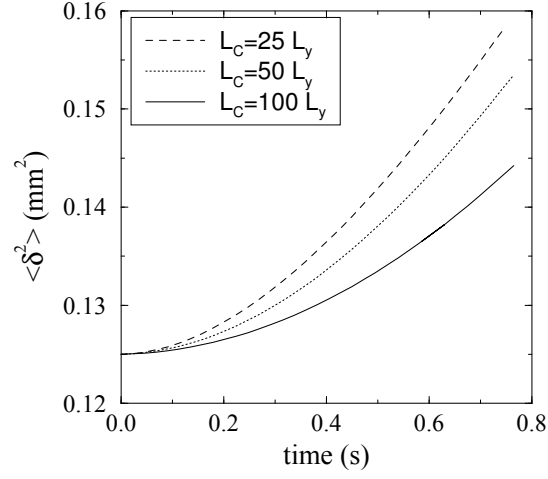


Figure 22: Time evolution of $\langle \delta^2 \rangle$ for a random ζ -potential variability with $COV = 0.10$. Effective diffusion coefficient (scaled by the molecular diffusivity D_{mol}) for $L_C = 25$: 54, $L_C = 50$: 47, $L_C = 100$: 32.

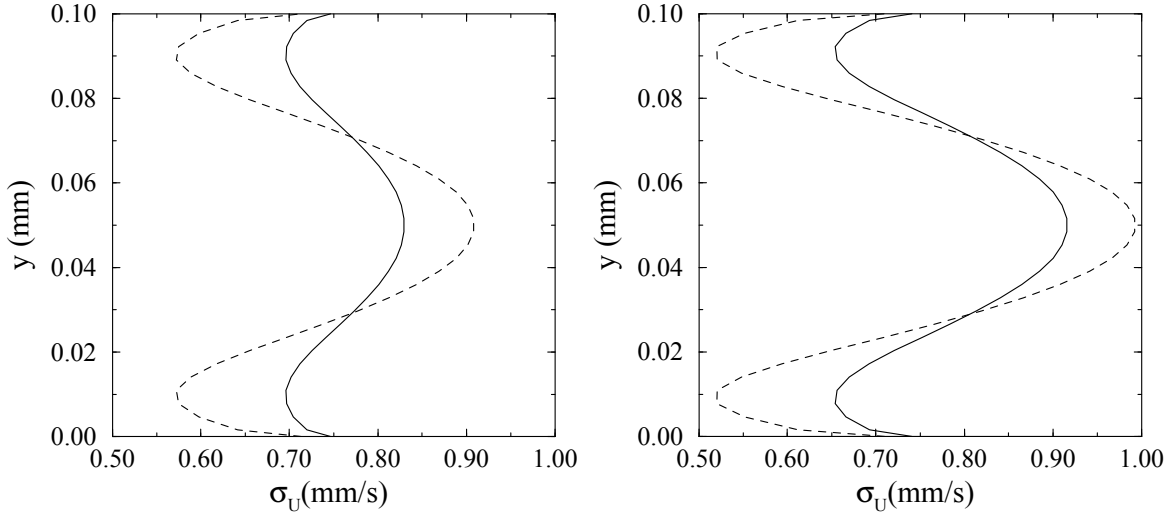


Figure 23: Standard deviation profile of the streamwise standard deviation velocity σ_u in cases with $L_C = 25L_y$ (dashed) and $L_C = 100L_y$ (solid) at $x = 3$ mm on the left and $x = 6$ mm on the right.

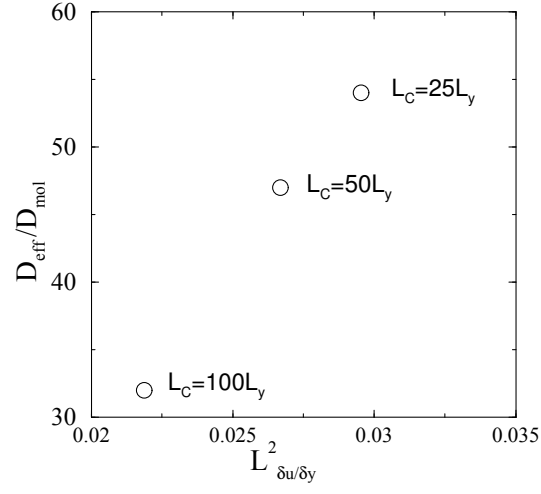


Figure 24: Variation of the effective diffusivity D_{eff} with respect to the velocity gradient.

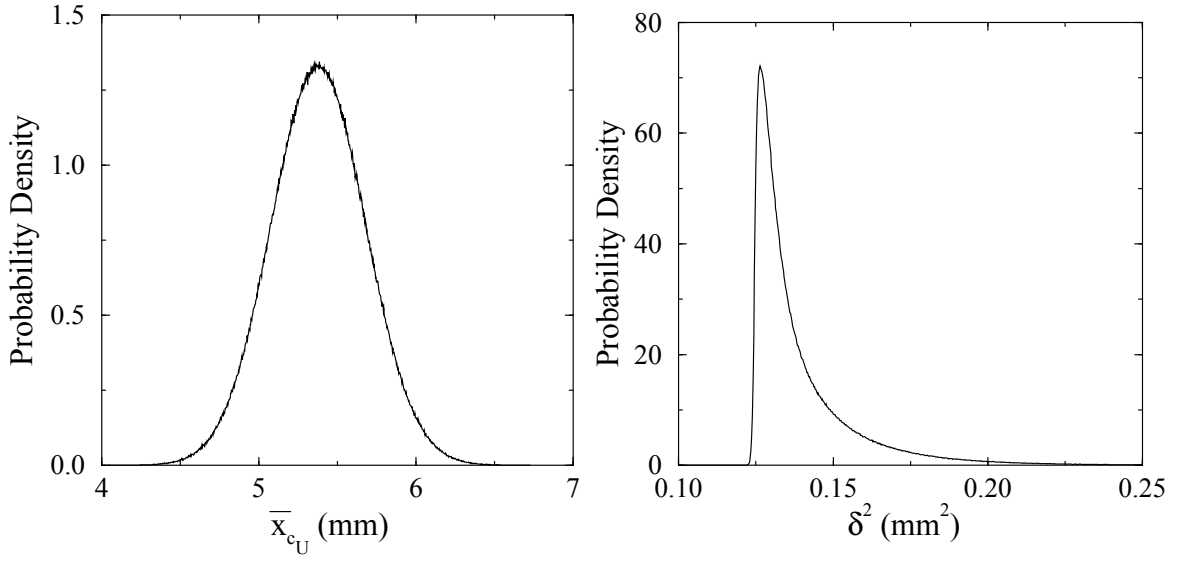


Figure 25: Probability density function for the location (left) and spatial variance δ^2 (right) of the U profile at $t = 0.45$ in a case with $L_C = 25L_y$ and $COV = 0.1$.

4 Conclusions

This project has achieved its key objectives. We developed (1) a theoretical formulation for UQ in an electrochemical microchannel flow, (2) associated numerical algorithms for solution of the resulting governing equation system, and (3) a C++/F77 code for solving this system (the initial parallel code target was replaced with more advanced physical model development involving realistic protein behavior). The construction relies on a specialized implementation of the chemical species conservation equations that allows handling of both fast electrolyte buffer chemistry and slow sample chemistry.

The overall construction was demonstrated on relevant model problems involving electrochemical microchannel flow, and was used to study band-pass protein-labeling and sample dispersion in a microchannel. These studies elucidated the amplification of parametric uncertainties in these flows, and highlighted specific parameters with dominant role in the uncertainty in model predictions. They also allowed a critical evaluation of the present global expansions used for UQ, and lead to a significant focus on theoretical developments of a UQ strategy based on local stochastic expansions.

The work lead to valuable couplings to other DARPA-funded projects on band-crossing reactions and CAD of microfluid systems. The results of the work were published in technical journals, and presented in professional meetings.

References

- [1] S. Wiener. The Homogeneous Chaos. *Amer. J. Math.*, 60:897–936, 1938.
- [2] R.H. Cameron and W.T. Martin. The orthogonal development of nonlinear functionals in series of Fourier-Hermite functionals. *Ann. Math.*, 48:385–392, 1947.
- [3] R.G. Ghanem and O.M. Knio. A probabilistic framework for the validation and certification of computer simulations. In *Proceedings of 1st JANNAF Modeling and Simulation Subcommittee Meeting*, 2000.
- [4] M. Loève. *Probability Theory*. Springer, 1977.
- [5] G. Kallianpur. *Stochastic Filtering Theory*. Springer-Verlag, 1980.
- [6] R.G. Ghanem and P.D. Spanos. *Stochastic Finite Elements: A Spectral Approach*. Springer Verlag, 1991.
- [7] B.J. Debuschere, H.N. Najm, P.P. Pébray, O.M. Knio, R.G. Ghanem, and O.P. Le Maître. Numerical challenges in the use of Polynomial Chaos representations for stochastic processes. *SIAM J. Sci. Comp.*, 2003. in press.
- [8] R. Ghanem. Ingredients for a general purpose stochastic finite element formulation. *Computer Methods in Applied Mechanics and Engineering*, 168:19–34, 1999.
- [9] O.P. Le Maître, O.M. Knio, H.N. Najm, and R.G. Ghanem. A stochastic projection method for fluid flow. i. basic formulation. *Journal of Computational Physics*, 173:481–511, 2001.
- [10] A.J. Chorin. A numerical method for solving incompressible viscous flow problems. *J. Comput. Phys.*, 2:12–26, 1967.
- [11] J. Kim and P. Moin. Application of a fractional-step method to incompressible navier-stokes equations. *J. Comput. Phys.*, 59:308–323, 1985.
- [12] O.P. Le Maître, M.T. Reagan, H.N. Najm, R.G. Ghanem, and O.M. Knio. A stochastic projection method for fluid flow. ii. random process. *Journal of Computational Physics*, 181:9–44, 2002.
- [13] R.F. Probstein. *Physicochemical Hydrodynamics*. Wiley-Interscience Publication, New-York, 2nd edition, 1995.
- [14] V.L. McGuffin and M.F.M. Tavares. Computer assisted optimization of separations in capillary zone electrophoresis. *Anal. Chem.*, 69:152–164, 1997.
- [15] Q.-H. Wan. Effect of electroosmotic flow on the electrical conductivity of packed capillary columns. *J. Phys. Chem. B*, 101(24):4860–4862, 1997.

- [16] P.J. Scales, F. Grieser, T.W. Healy, L.R. White, and D.Y.C. Chan. Electrokinetics of the Silica-Solution Interface: A Flat Plate Streaming Potential Study. *Langmuir*, 8:965–974, 1992.
- [17] W. Thormann and R.A. Mosher. *Theory of Electrophoretic Transport and Separations: The Study of Electrophoretic Boundaries and Fundamental Separation Principles by Computer Simulation*, volume 2 of *Advances in Electrophoresis*, pages 45–108. VCH Publishing, Weinheim, Germany, 1988.
- [18] O.A. Palusinski, A. Graham, R.A. Mosher, M. Bier, and D.A. Saville. Theory of Electrophoretic Separations. Part II: Construction of a Numerical Simulation Scheme and Its Applications. *AIChE Journal*, 32(2):215–223, 1986.
- [19] G.O. Roberts, P.H. Rhodes, and R.S. Snyder. Dispersion effects in capillary zone electrophoresis. *J. Chromatogr.*, 480:35–67, 1989.
- [20] S.V. Ermakov, S.C. Jacobson, and J.M. Ramsey. Computer simulations of electrokinetic transport in microfabricated channel structures. *Anal. Chem.*, 70:4494–4504, 1998.
- [21] R.A. Mosher, D. Dewey, W. Thormann, D.A. Saville, and M. Bier. Computer simulation and experimental validation of the electrophoretic behavior of proteins. *Anal. Chem.*, 61:362–366, 1989.
- [22] R.A. Mosher, P. Gebauer, J. Caslavská, and W. Thormann. Computer simulation and experimental validation of the electrophoretic behavior of proteins. 2. model improvement and application to isotachophoresis. *Anal. Chem.*, 64:2991–2997, 1992.
- [23] R.A. Mosher, P. Gebauer, and W. Thormann. Computer simulation and experimental validation of the electrophoretic behavior of proteins. III. use of titration data predicted by the protein’s amino acid composition. *J. Chromatogr.*, 638:155–164, 1993.
- [24] A. Matta. Numerical simulation and uncertainty quantification in microfluidic systems. Technical report, Department of Civil Engineering, Johns Hopkins University, 2003. Ph.D. Thesis.
- [25] O.P. Le Maître and O.M. Knio and B.D. Debuschere and H.N. Najm and R.G. Ghanem. A multigrid solver for two-dimensional stochastic diffusion equations. *Computer Methods in Applied Mechanics and Engineering*, 192:4723–4744, 2003.
- [26] U. Trottenberg, C. Oosterlee, and A. Schüller. *Multigrid*. Academic Press, San Francisco, 2001.
- [27] M. Pernice and H.F. Walker. NITSOL: A Newton Iterative Solver for Nonlinear Systems. *SIAM J. Sci. Comput.*, 19(1):302–318, 1998.
- [28] Slatec common mathematical library, version 4.1. <http://www.netlib.org/slatec/>, 1993.

- [29] A. Matta, B.J. Debusschere, H.N. Najm, O.M. Knio, and R.G. Ghanem. Sample dispersion due to buffer disturbances and random zeta potential variability in electroosmotic microchannel flows. 2004. in preparation.
- [30] P. de Montigny, J.F. Stobaugh, R.S. Givens, R.G. Carlson, K.S. Srinivasachar, L.A. Sternson, and T. Higuchi. Naphtalene-2,3-dicarboxaldehyde/cyanide ion: A rationally designed fluorogenic reagent for primary amines. *Analytical Chemistry*, 59:1096–1101, 1987.
- [31] B. Debusschere, H.N. Najm, A. Matta, O.M. Knio, R.G. Ghanem, and O.P. Le Maître. Protein labeling reactions in electrochemical microchannel flow: Numerical prediction and uncertainty propagation. *Physics of Fluids*, 15(8):2238–2250, 2003.
- [32] B.J. Debusschere, H.N. Najm, A. Matta, O.M. Knio, R.G. Ghanem, and O.P. Le Maître. Sample dispersion due to buffer disturbances and zeta potential variability in electroosmotic microchannel flows. In *Proc. IMECE'03*, number IMECE2003-43091, Washington, DC, Nov. 2003. 2003 ASME Int. Mech. Eng. Congress.
- [33] B. Debusschere, H. Najm, A. Matta, O. Knio, R. Ghanem, and O. Le Maître. Study of sample dispersion mechanisms in an electroosmotically pumped microchannel. In *Proc. MicroTAS 2003*, Squaw Valley, CA, Oct. 2003. The 7th International Conference on Micro Total Analysis Systems.

A Personnel

Following is a list of personnel involved in this research project:

- Dr. Omar M. Knio (PI), Department of Mechanical Engineering, The Johns Hopkins University.
- Dr. Roger G. Ghanem (Co-PI), Department of Civil Engineering, The Johns Hopkins University.
- Dr. Habib N. Najm (Co-PI), Combustion Research Facility, Sandia National Laboratories.
- Dr. Bert Debusschere, Post-doctoral Associate, Combustion Research Facility, Sandia National Laboratories.
- Dr. Mohamed Jardak, Post-doctoral Associate, Department of Civil Engineering, The Johns Hopkins University.
- Dr. Olivier P. Le Maître, Visiting Scientist, Department of Mechanical Engineering, The Johns Hopkins University. Dr. Le Maître is a faculty member at the Centre d'Etude de Mécanique d'Ile de France, Université d'Evry Val d'Essonne, France. He was directly involved in this project during his visit to the ME Department at Hopkins in Summer of 2000, 2001, 2002, 2003. While at his home institution, he continues his collaboration with us at no additional cost to the project.
- Ms. Tao Shu, graduate student, Department of Mechanical Engineering, JHU. September 2000–August 2001. Ms. Shu received her M.S. Degree in Summer 2001.
- Mr. Alain Matta, graduate student, Department of Civil Engineering, JHU. Mr. Matta received his Ph.D. Degree in Fall 2003.
- Dr. Etienne Besnoin, Post-doctoral Associate, Department of Mechanical Engineering, JHU.

B List of Publications and Presentations

B.1 Journal Papers

1. O.P. Le Maître, O.M. Knio, R.G. Ghanem & H.N. Najm (2001) “A Stochastic Projection Method for Fluid Flow. I. Basic Formulation,” *Journal of Computational Physics*, **173**, 481–511.
2. S. Sakamoto & R. Ghanem (2002) “Simulation of multi-dimensional non-Gaussian non-stationary random fields,” *Probabilistic Engineering Mechanics* **17**, 167–176.
3. O.P. Le Maître, M.T. Reagan, H.N. Najm, R.G. Ghanem & O.M. Knio, (2002) “A Stochastic Projection Method for Fluid Flow. II. Random Process,” *Journal of Computational Physics* **181**, 9–44.
4. O.P. Le Maître, O.M. Knio, B.D. Debusschere, H.N. Najm & R.G. Ghanem (2003) “A Multigrid Solver for Two-Dimensional Stochastic Diffusion Equations,” *Computer Methods in Applied Mechanics and Engineering* **192**, 4723–4744.
5. B. Debusschere, H.N. Najm, A. Matta, O.M. Knio, R.G. Ghanem & O.P. Le Maître (2003) “Protein Labeling Reactions in Electrochemical Microchannel Flow: Numerical Prediction and Uncertainty Propagation,” *Phys. Fluids* **15**(8), 2238–2250.
6. O. Le Maître, M.T. Reagan, B. Debusschere, H.N. Najm, R.G. Ghanem & O.M. Knio (2003) “Natural Convection in a Closed Cavity under Stochastic, Non-Boussinesq Conditions,” submitted to *SIAM J. Sci. Comput.*
7. B.J. Debusschere, H.N. Najm, P.P. Pebay, O.M. Knio, R.G. Ghanem and O.P. Le Maître (2004), “Numerical Challenges in the Use of Polynomial Chaos Representations for Stochastic Processes,” *SIAM J. Sci. Comput.*, in press
8. A. Matta, O.M. Knio, R.G. Ghanem, C.-H. Chen, J. Santiago, B. Debusschere & H.N. Najm (2004) “Computational Study of Band Crossing Reactions,” *Journal of Microelectromechanical Systems* **13**, 310–322.
9. O. Le Maître, O.M. Knio, R.G. Ghanem, H.N. Najm (2004) “Uncertainty Propagation Using Wiener-Haar Expansions,” *J. Comput. Phys.*, in press.
10. O. Le Maître, R.G. Ghanem, H.N. Najm, O.M. Knio (2004) “Multi-Resolution Analysis of Wiener-Type Uncertainty Propagation Schemes,” *J. Comput. Phys.*, in press.

B.2 Proceedings

1. O.P. Le Maître, O.M. Knio, R.G. Ghanem & H.N. Najm (2000) “A Stochastic Projection Method for Microchannel Flow,” in *Technical Proceedings of the Fourth International Conference on Modeling and Simulation of Microsystems*, (Computational Publications; Cambridge, MA), pp. 246–249.

2. R.G. Ghanem & O.M. Knio (2000) "A Probabilistic Framework for the Validation and Certification of Computer Simulations," in *Proceedings of 1st JANNAF Modeling and Simulation Subcommittee Meeting*, Monterey, CA, November 13–17, 2000.
3. O. Knio, O. Le Maître, H. Najm & R. Ghanem (2001) "Stochastic projection method in microfluidic simulations," presented at 6th US National Congress on Computational Mechanics, Dearborn, MI August 1-4, 2001.
4. R. Ghanem, (2001) "The Characterization and Management of Uncertainty in Model-Based Predictions," to appear in *Modeling and Simulation-Based Life Cycle Engineering*, Edited by Ken Chong and Sunil Saigal, Taylor and Francis.
5. B. Debusschere, H. Najm, A. Matta, T. Shu, O. Knio, R. Ghanem & O. Le Maître (2002) "Uncertainty Quantification in a Reacting Electrochemical Microchannel Flow," *Technical Proceedings of the Fifth International Conference on Modeling and Simulation of Microsystems*, (Computational Publications; Cambridge, MA), pp. 384–387.
6. B. Debusschere, H. Najm, A. Matta, O. Knio, R. Ghanem & O. Le Maître (2002) "Study of Sample Dispersion Mechanisms in an Electroosmotically Pumped Microchannel," in *Proceedings of Sixth International Conference on Modeling and Simulation of Microsystems*, San Francisco, CA, February 23-27, 2003.
7. B.J. Debusschere, H.N. Najm, A. Matta, O.M. Knio, R.G. Ghanem, O.P. Le Maître (2003) "Sample dispersion due to buffer disturbances and zeta potential variability in electroosmotic microchannel flows," to appear in the *Proceedings of IMECE'03*, 2003 ASME International Mechanical Engineering Congress & Exposition, Nov. 16-21, 2003, Washington DC.
8. H. Najm, B. Debusschere, O. Knio, R. Ghanem, A. Matta, O. Le Maître (2003) "Uncertainty Quantification in Models of Microfluid Systems", to appear in the *Proceedings of IMECE'03*, 2003 ASME International Mechanical Engineering Congress & Exposition, Nov. 16-21, 2003, Washington DC.
9. B.J. Debusschere, H.N. Najm, A. Matta, O.M. Knio, R.G. Ghanem, O.P. Le Maître (2003) "Study of Sample Dispersion Mechanisms in an Electrically Pumped Microchannel," in *Proceedings of MicroTAS 2003*, Oct. 5-9, 2003, Squaw Valley CA.

B.3 Theses

1. T. Shu (2001) "Stochastic Simulation of Reacting Microchannel Flow," M.S. Thesis, Department of Mechanical Engineering, The Johns Hopkins University.
2. A. Matta (2003) "Numerical Simulation and Uncertainty Quantification in Microfluidic Systems," Ph.D. Thesis, Department of Civil Engineering, The Johns Hopkins University.

B.4 Conference Presentations

1. O.M. Knio, R.G. Ghanem & H.N. Najm (2000) “Quantitative Uncertainty Assessment and Numerical Simulation of Micro-Fluid Systems,” presented at the Composite CAD/Bio-Flips Meeting, Park-City, Utah, August 1–4, 2000.
2. O.M. Knio, R.G. Ghanem & H.N. Najm (2001) “Quantitative Uncertainty Assessment and Numerical Simulation of Micro-Fluid Systems,” presented at the BioFlips PI Meeting, Isle of Palms, SC, February 21–23, 2001.
3. O.P. Le Maître, O.M. Knio, R.G. Ghanem & H.N. Najm (2001) “Propagation of uncertainty in viscous flow using stochastic spectral method,” presented at ICFD Conference on Numerical Methods in Fluid Dynamics, Oxford UK, March 26–29, 2001.
4. O.M. Knio, R.G. Ghanem, H.N. Najm, O. Le Maître, T. Shu, A. Matta & B. Debusschere (2001) “Quantitative Uncertainty Assessment and Numerical Simulation of Micro-Fluid Systems,” presented at the BioFlips/Symbiosys PI Meeting, Honolulu, Hawaii, August 8–10, 2001.
5. B. Debusschere, H. Najm, O. Knio, R. Ghanem (2001) “Uncertainty Quantification of Protein Labeling in a Microchannel,” presented at *54th Annual Meeting of the APS Division of Fluid Dynamics*, San Diego, CA, November 2001.
6. O.M. Knio, A. Matta, R.G. Ghanem, H.N. Najm & B. Debusschere, “Quantitative Uncertainty Assessment and Numerical Simulation of Micro-Fluid Systems,” presented at the BioFlips/Symbiosys PI Meeting, Miami, FL, February 20–22, 2002.
7. R.G. Ghanem, A. Matta, O.M. Knio, H.N. Najm, B.J. Debusschere (2001) “Probabilistic modeling and prediction of flows in micro-channels,” presented at 15th Engineering Mechanics Division Conference of the American Society of Civil Engineers, Columbia Univ., NY, NY, June 2–5, 2002.
8. O.M. Knio, A. Matta, R.G. Ghanem, H.N. Najm & B. Debusschere, “Quantitative Uncertainty Assessment and Numerical Simulation of Micro-Fluid Systems,” presented at the BioFlips/Symbiosys PI Meeting, Portland, OR, August 21–23, 2002.
9. B. Debusschere, H. Najm, O. Knio, A. Matta, R. Ghanem & O. Le Maitre (2002) “Numerical Simulation and Quantitative Uncertainty Assessment of Microchannel Flow,” presented at the DFD02 Meeting of the American Physical Society.
10. H.N. Najm, M.T. Reagan, B.J. Debusschere, O.M. Knio, A. Matta, R.G. Ghanem, O.P. Le Maitre (2002) “Uncertainty Quantification in Models of Reacting Thermofluid Systems,” DOE-MICS / NSF-DMS Workshop on predictability of complex phenomena. Dec. 16–18, 2002, Santa Fe, New Mexico.

11. B. Debuschere, H. Najm, A. Matta, O. Knio, R. Ghanem & O. Le Maître (2002) “Study of Sample Dispersion Mechanisms in an Electroosmotically Pumped Microchannel,” Presented at the Sixth International Conference on Modeling and Simulation of Microsystems, San Francisco, CA, February 23-27, 2003.
12. B. Debuschere, H. Najm, O. Knio, R. Ghanem A. Matta, & O. Le Maître, “Uncertainty Quantification in Electrochemical Microchannel Flow,” presented at the SIAM Conference on Computational Science and Engineering, San Diego, CA, February 10–13, 2003.
13. B.J. Debuschere, H.N. Najm, A. Matta, O.M. Knio, R.G. Ghanem, O.P. Le Maitre (2003) “Numerical simulation and quantitative uncertainty assessment of electrochemical microchannel flow,” presented at *7th US National Congress on Computational Mechanics*, Jul. 28-30, 2003, Albuquerque NM.
14. B.J. Debuschere, H.N. Najm, A. Matta, O.M. Knio, R.G. Ghanem, O.P. Le Maître (2003) “Study of Sample Dispersion Mechanisms in an Electrically Pumped Microchannel,” *MicroTAS 2003*, Oct. 5-9, 2003, Squaw Valley CA.
15. O.M. Knio, A. Matta, R.G. Ghanem, H.N. Najm & B. Debuschere, “Quantitative Uncertainty Assessment and Numerical Simulation of Micro-Fluid Systems,” presented at the BioFlips/Symbiosys PI Meeting, Monterey, CA, Sep. 10-12, 2003.

B.5 Invited Lectures

1. R. Ghanem, “Characterization and Computation of the State of Stochastic Systems,” Colorado University in Denver, Department of Mathematics, February 26, 2001.
2. R. Ghanem, ‘Uncertainty in Model Prediction,’ Workshop on Uncertainty In Model-based Predictions, Albuquerque, NM, March 20-21 2001.
3. O.M. Knio, “Quantitative Uncertainty Assessment and Numerical Simulation of Thermo-Fluid Systems,” FU-Berlin, 5/8/2001.
4. R. Ghanem, “Towards a rational integration of uncertainty into model-based predictions,” Keynote lecture, *5ème Colloque National en Calcul des Structures*, Giens, France, 15-18 May 2001.
5. H.N. Najm, “Uncertainty Quantification in Fluids Modeling”, University of Rome, 7/18/2001.
6. R. Ghanem, “Quantifying and Managing Uncertainty in Model-Based Predictions,” Invited talk at the DARPA Uncertainty Workshop for the Accelerated Insertion of Materials Initiative, Annapolis, MD, August 27-28, 2001.

7. O. Knio, “A Stochastic Projection Method for Fluid Flow,” Lawrence Berkeley National Laboratory, 3/20/2002.
8. O. Knio, “A Stochastic Projection Method for Fluid Flow,” Carnegie Mellon University, 6/24/2002.

C Copies of Selected Publications

This appendix provides a copy of the following publications:

- O.P. Le Maître, O.M. Knio, R.G. Ghanem & H.N. Najm (2001) “A Stochastic Projection Method for Fluid Flow. I. Basic Formulation,” *Journal of Computational Physics*, **173**, 481–511.
- O.P. Le Maître, M.T. Reagan, H.N. Najm, R.G. Ghanem & O.M. Knio, (2002) “A Stochastic Projection Method for Fluid Flow. II. Random Process,” *Journal of Computational Physics* **181**, 9-44.
- O.P. Le Maître, O.M. Knio, B.D. Debusschere, H.N. Najm & R.G. Ghanem (2003) “A Multigrid Solver for Two-Dimensional Stochastic Diffusion Equations,” *Computer Methods in Applied Mechanics and Engineering* **192**, 4723-4744.
- B. Debusschere, H.N. Najm, A. Matta, O.M. Knio, R.G. Ghanem & O.P. Le Maître (2003) “Protein Labeling Reactions in Electrochemical Microchannel Flow: Numerical Prediction and Uncertainty Propagation,” *Phys. Fluids* **15**(8), 2238–2250.
- A. Matta, O.M. Knio, R.G. Ghanem, C.-H. Chen, J. Santiago, B. Debusschere & H.N. Najm (2004) “Computational Study of Band Crossing Reactions,” *Journal of Microelectromechanical Systems*, in press.

A Stochastic Projection Method for Fluid Flow

I. Basic Formulation

Olivier P. Le Maître,^{*} Omar M. Knio,^{†,1} Habib N. Najm,[‡] and Roger G. Ghanem[§]

^{*}Centre d'Etudes de Mécanique d'Ile de France, Université d'Evry Val d'Essonne, 40, rue du Pelvoux, 91020 Evry Cedex, France; [†]Department of Mechanical Engineering, The Johns Hopkins University, Baltimore, Maryland 21218-2686; [‡]Combustion Research Facility, Sandia National Laboratories, Livermore, California 94550; and [§]Department of Civil Engineering, The Johns Hopkins University, Baltimore, Maryland 21218-2686
E-mail: olm@iup.univ-evry.fr; knio@jhu.edu; hnnajm@ca.sandia.gov; ghanem@jhu.edu

Received November 7, 2000; revised July 10, 2001

We describe the construction and implementation of a stochastic Navier–Stokes solver. The solver combines a spectral stochastic uncertainty representation scheme with a finite difference projection method for flow simulation. The uncertainty quantification scheme is adapted from the spectral stochastic finite element method (SSFEM), which is based on regarding uncertainty as generating a new dimension and the solution as being dependent on this dimension. In the SSFEM formalism, the stochastic dependence is represented in terms of the polynomial chaos system, and the coefficients in the corresponding spectral representation are obtained using a Galerkin approach. It is shown that incorporation of the spectral uncertainty representation scheme into the projection method results in a coupled system of advection–diffusion equations for the various uncertainty fields, and in a *decoupled* system of pressure projection steps. This leads to a very efficient stochastic solver, whose advantages are illustrated using steady and transient simulations of transport and mixing in a microchannel. © 2001 Academic Press

Key Words: stochastic; Navier–Stokes; polynomial chaos; uncertainty.

1. INTRODUCTION

Simulation of complex physical systems is in many instances made more difficult by various uncertainties, which may include inexact knowledge of system forcing, initial and boundary conditions, and parametric uncertainties in the physical model and in physical properties of the medium. The latter may exhibit a random component with significant spatial

¹Corresponding author.

or temporal fluctuations, or may be inaccurately known. An example concerns chemical or biological microfluid systems, whose modeling involves complex kinetic mechanisms which may include dozens of species—each characterized by thermodynamic and transport properties—and hundreds of elementary reactions specified in terms of rate parameters. Thus, simulation and design of these microdevices, which is the primary motivation behind the present effort, involve complex physical models having a large number of parameters that may be known in an approximate fashion only. Consequently, in order to become effective tools, it is essential for simulation-based design approaches to include a rational assessment of uncertainty.

Uncertainty quantification is typically based on Monte Carlo (MC) techniques [1, 2] that essentially amount to performing deterministic simulations for randomly selected conditions, and then conducting a statistical analysis on the resulting set of realizations in order to extract the relevant statistical properties of the process. The Monte Carlo approach is known to be robust and to be able to deal with very complex situations. However, because of CPU costs and storage limitations, this approach is often restricted to problems involving a small number of uncertain parameters and/or degrees of freedom.

In this work an alternative approach is adopted which is adapted from the spectral stochastic finite element method (SSFEM) [3]. The essential concept in SSFEM is to regard uncertainty as generating a new dimension and the solution as being dependent on this dimension. A convergent expansion along the new dimension is then sought in terms of the polynomial chaos system [4, 5], and the coefficients in this representation are determined through a Galerkin approach. SSFEM offers several advantages over MC approaches; in particular, it generally results in efficient uncertainty propagation schemes and yields quantitative estimates of the sensitivity of the solution with respect to uncertainties in model data. In addition, this quantitative information is expressed in a format that permits it to be readily used to probe the dependence of specific observables on particular components of the input data, to design experiments in order to better calibrate and test the validity of postulated models, or to assess “off-design” performance. SSFEM has been used in various applications, including structural mechanics problems (e.g., [3, 6]) and flow in random porous media (e.g., [7, 8]). A modified SSFEM approach has been recently applied to complex kinetic mechanisms [9], but this method has not yet been used in more general fluid problems.

Note, however, that the polynomial chaos expansions on which SSFEM is based have been used in various contexts, for instance in the development of variance reduction or convergence acceleration techniques [10–12], and also in the analysis of turbulent velocity fields [13–15]. In particular, the analysis of Chorin [15] indicates that in complex problems involving shock formation or an energy cascade, polynomial chaos expansions may lose their advantages or cease to be useful. Such difficulties do not arise in the present work, which aims at adapting the stochastic representation formalism to microfluid applications at a low Reynolds number.

As summarized in Section 2, we restrict our attention in this paper to the case of advection and mixing in two-dimensional, incompressible flow. Specifically, we focus on a class of simplified problems in which the uncertainty in the solution process arises as a result of either random viscosity or the dependence of the viscosity on a random temperature. We first start with a simplified setting in which the temperature is treated as a Gaussian random variable that is spatially uniform. Thus, the fluid viscosity is also uniform, but both linear and nonlinear viscosity laws are considered in the analysis. A more complicated setting is then

considered, which consists of a double-inlet channel where the inlet temperature of one of the streams has a random Gaussian component. In this case, the uncertain boundary condition leads to stochastic velocity and temperature fields that are coupled by the temperature dependence of viscosity.

In Section 3, a spectral uncertainty representation scheme is introduced based on the decomposition of the solution process in terms of the polynomial chaos system. This representation is then introduced into the original system of equations, and a Galerkin procedure is used to determine the coefficients in the spectral expansion. It is shown that this approach results in a coupled system of advection–diffusion equations for the stochastic velocity (and temperature) fields, with a decoupled set of stochastic divergence constraints. This feature is then exploited in Section 4 by constructing an efficient stochastic projection method (SPM) which provides a stochastic characterization of the solution process at a cost that is essentially proportional to the number of terms in the spectral expansion. The advantages of the stochastic projection method (SPM) are illustrated in Section 5 in light of computational experiments conducted for the model problems introduced in Section 3. Major conclusions are given in Section 6.

2. GOVERNING EQUATIONS

We consider the two-dimensional flow, in (x, y) plane, of an incompressible, uniform-density Newtonian fluid inside a narrow channel of height H and width B . As shown in Fig. 1, the boundaries of the computational domain Ω consist of inflow (Γ_i) and outflow (Γ_o) boundaries, respectively located at $y = 0$ and $y = H$, and solid boundaries (Γ_{ns}) located at $x = 0$ and $x = B$.

The evolution of the flow within the channel is governed by the Navier–Stokes equations

$$\begin{aligned} \frac{\partial \mathbf{u}}{\partial t} + (\mathbf{u} \cdot \nabla) \mathbf{u} &= -\nabla p + \nabla \cdot \bar{\sigma} \quad (a) \\ \nabla \cdot \mathbf{u} &= 0 \quad (b), \end{aligned} \tag{1}$$

where \mathbf{u} is the velocity field, \tilde{p} is the pressure, ρ is the density, $p \equiv \tilde{p}/\rho$, τ is the viscous stress, and $\bar{\sigma} \equiv \tau/\rho$. When the dynamic viscosity is uniform, the viscous force can be

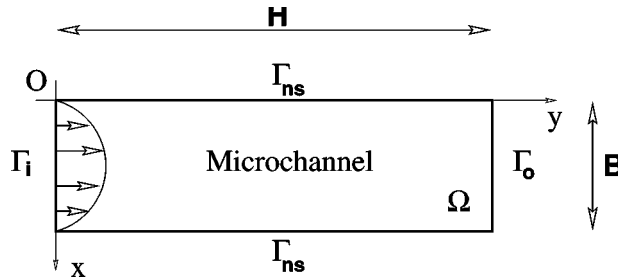


FIG. 1. Schematic representation of the computational domain. The inflow and outflow boundaries, respectively Γ_i and Γ_o , are located at $y = 0$ and $y = H$. Γ_{ns} refers to the channel walls, which are located at $x = 0$ and $x = B$. The computational domain consists of the region $\Omega \equiv [0, B] \times [0, H]$.

expressed as

$$\nabla \cdot \bar{\sigma} \equiv \nabla \cdot [\nu \bar{S}] = \nu \nabla^2 \mathbf{u}, \quad (2)$$

where ν is the kinematic viscosity and \bar{S} is the symmetric part of the velocity gradient tensor. The governing equations are supplemented with velocity boundary conditions, which consist of imposed velocity at the inflow, outflow conditions on Γ_o , and no-slip conditions on the solid walls.

In addition to the Navier–Stokes equations (1), we also consider the temperature distribution within the microchannel. The evolution of the temperature field, T , is governed by the energy equation

$$\frac{\partial T}{\partial t} + \nabla \cdot (\mathbf{u}T) = \nabla \cdot (\lambda \nabla T), \quad (3)$$

where λ is the thermal diffusivity. We use adiabatic conditions at the solid walls, outflow conditions at Γ_o , and Dirichlet conditions at inflow. Note that when the viscosity is independent of temperature, the evolution of the flow field can be determined independently of Eq. (3). On the other hand, when ν depends on T , a nontrivial coupling exists between the Navier–Stokes and the energy equations.

3. STOCHASTIC FORMULATION

3.1. Problems and Methodology

As mentioned in the introduction, we focus on the case of uncertain transport properties and boundary conditions, and restrict our attention to stochastic processes generated by Gaussian random variables. Within this restricted scope, three different problems of increasing complexity are considered:

1. In the first problem (P1), we consider the case of an uncertain viscosity, which is treated as a Gaussian random variable. The viscosity is assumed to be spatially uniform, and solution of the energy equation is not required.
2. In the second problem (P2), we also consider uncertainty in viscosity, which is taken to be generated by a Gaussian stochastic temperature. The temperature is assumed to be uncertain, but spatially uniform, and the uncertainty in viscosity is reflected through a nonlinear viscosity law.
3. In the third problem (P3), we consider a coupled problem which involves a temperature-dependent viscosity and an evolving temperature field. In this case, the uncertainty is generated by a random boundary condition on the inlet temperature.

As mentioned in the introduction, we develop a spectral representation of the stochastic processes, following the approach outlined in [3]. The methodology is based on a two-step procedure; first, the uncertain data is expressed in terms of a “normalized” Gaussian random variable ξ . The dependence of the solution process on ξ is then expanded in terms of the polynomial chaos system. In the present case, a single random variable is considered so the polynomial chaos basis functions are orthogonal Hermite polynomials in the random variable ξ . This spectral expansion is introduced into the governing equations and the coefficients are determined using a weighted residual procedure.

3.2. Statement of P1

As mentioned earlier, for this problem the uncertain viscosity coefficient is spatially uniform and is modeled as a Gaussian random variable. The governing equations consist of the momentum and continuity equations

$$\frac{\partial \mathbf{u}}{\partial t} + (\mathbf{u} \cdot \nabla) \mathbf{u} = -\nabla p + \nu \nabla^2 \mathbf{u} \quad (4)$$

$$\nabla \cdot \mathbf{u} = 0, \quad (5)$$

with deterministic boundary conditions on the velocity. The viscosity is expressed as

$$\nu = \nu_0 + \xi_1 \nu_1, \quad (6)$$

where ν_0 is the mean viscosity, ξ_1 is a “normalized” Gaussian variable (having with zero mean and unit variance), while ν_1 is a deterministic coefficient which corresponds to the standard deviation of the viscosity.

Remark. The index on ξ is introduced in order to emphasize the fact that the present approach can be extended to the situation where ν is a random process with spatial variation. In this case, we rely on the Karhunen–Loève expansion to decompose ν as [16],

$$\nu(\mathbf{x}) = \nu_0(\mathbf{x}) + \sum_{i=1}^L \lambda_i \nu_i(\mathbf{x}) \xi_i,$$

where the λ_i ’s are deterministic coefficients, the ξ_i ’s are orthogonal (uncorrelated) Gaussian random variables, the functions $\nu_i(\mathbf{x})$ are the eigenvalues of the viscosity autocorrelation function, and L is the order of the expansion. While we do not address this situation in the present work, we still retain the notation of the more general case. Also note that with the use of Gaussian noise in the viscosity, negative values are, in principle, possible. Below, this situation avoided by ensuring that the standard deviation in viscosity is substantially smaller than the mean. In more general situations, a non-Gaussian distribution may be needed to ensure that negative viscosities have negligible likelihood.

The dependence of the solution on the stochastic viscosity is expressed by expanding the velocity and pressure fields as

$$\mathbf{u}(\mathbf{x}) = \sum_{i=0}^P \mathbf{u}_i(\mathbf{x}) \Psi_i(\xi_1) \quad (7)$$

$$p(\mathbf{x}) = \sum_{i=0}^P p_i(\mathbf{x}) \Psi_i(\xi_1), \quad (8)$$

where the Ψ_i denote the polynomials chaoses in the random variable ξ_1 , \mathbf{u}_i and p_i are (yet undetermined) deterministic coefficients, and P is the order of the polynomial chaos expansion. Expressions for Ψ_i (in the case of a single Gaussian random variable) are provided in the Appendix. The effect of the expansion order, P , is analyzed in Section 5.2.

Next, we introduce the polynomial chaos expansions (7 and 8) into the governing equations (4 and 5), which results in

$$\sum_{i=0}^P \Psi_i \frac{\partial \mathbf{u}_i}{\partial t} + \sum_{i=0}^P \sum_{j=0}^P (\mathbf{u}_i \cdot \nabla) \mathbf{u}_j \Psi_i \Psi_j = - \sum_{i=0}^P \Psi_i \nabla p_i + (\nu_0 + \nu_1 \xi_1) \nabla^2 \sum_{i=0}^P \Psi_i \mathbf{u}_i \quad (9)$$

$$\sum_{i=0}^P \Psi_i \nabla \cdot \mathbf{u}_i = 0. \quad (10)$$

Multiplying Eq. (9) by Ψ_k and taking the expected value (denoted using the double bracket $\langle \cdot \rangle$) we obtain

$$\begin{aligned} \sum_{i=0}^P \frac{\partial \mathbf{u}_i}{\partial t} \langle \Psi_i \Psi_k \rangle + \sum_{i=0}^P \sum_{j=0}^P (\mathbf{u}_i \cdot \nabla) \mathbf{u}_j \langle \Psi_i \Psi_j \Psi_k \rangle \\ = - \sum_{i=0}^P \nabla p_i \langle \Psi_i \Psi_k \rangle + \sum_{i=0}^P \nabla^2 \mathbf{u}_i \langle (\nu_0 + \nu_1 \xi_1) \Psi_i \Psi_k \rangle \quad k = 0, \dots, P. \end{aligned} \quad (11)$$

By virtue of the orthogonality of the polynomial chaos, (11) reduces to

$$\begin{aligned} \frac{\partial \mathbf{u}_k}{\partial t} \langle \Psi_k \Psi_k \rangle + \sum_{i=0}^P \sum_{j=0}^P (\mathbf{u}_i \cdot \nabla) \mathbf{u}_j \langle \Psi_i \Psi_j \Psi_k \rangle \\ = - \nabla p_k \langle \Psi_k \Psi_k \rangle + \sum_{i=0}^P \nabla^2 \mathbf{u}_i \langle (\nu_0 + \nu_1 \xi_1) \Psi_i \Psi_k \rangle \quad k = 0, \dots, P. \end{aligned} \quad (12)$$

Dividing by $\langle \Psi_k \Psi_k \rangle$, using the fact that $\Psi_1 = \xi_1$ (see Appendix), and expanding the last term finally leads to the following coupled system of evolution equations for the velocity “modes”:

$$\frac{\partial \mathbf{u}_k}{\partial t} + \sum_{i=0}^P \sum_{j=0}^P (\mathbf{u}_i \cdot \nabla) \mathbf{u}_j \frac{\langle \Psi_i \Psi_j \Psi_k \rangle}{\langle \Psi_k \Psi_k \rangle} = - \nabla p_k + \nu_0 \nabla^2 \mathbf{u}_k + \nu_1 \sum_{i=0}^P \nabla^2 \mathbf{u}_i \frac{\langle \Psi_1 \Psi_i \Psi_k \rangle}{\langle \Psi_k \Psi_k \rangle}. \quad (13)$$

We follow a similar treatment for the velocity divergence constraint. Specifically, we multiply Eq. (10) with Ψ_k and then take the expectation to obtain

$$\nabla \cdot \mathbf{u}_k = 0, \quad (14)$$

which in fact corresponds to a weak formulation of the original continuity equation. Boundary conditions and numerical solution schemes will be discussed later.

3.3. Statement of P2

Here, we consider that the viscosity is temperature-dependent and that the temperature T is uncertain and can be modeled as a Gaussian distribution. We let T_0 denote the mean temperature, T_1 the standard deviation, and represent T as

$$T = T_0 + \xi_1 T_1, \quad (15)$$

where ξ_1 is a normalized Gaussian random variable with zero mean. We assume a polynomial representation of the viscosity in the neighborhood of T_0 and restrict our attention to the second-order case

$$\frac{\nu(T)}{\nu_0} = 1 + a_1(T - T_0) + a_2(T - T_0)^2, \quad (16)$$

where a_1 and a_2 are given constants and $\nu_0 \equiv \nu(T_0)$. Substituting Eq. (15) into Eq. (16) we obtain the following stochastic representation for ν :

$$\frac{\nu(T_0 + \xi_1 T_1)}{\nu_0} = 1 + \beta_1 \xi_1 + \beta_2 \xi_1^2, \quad (17)$$

where $\beta_1 \equiv a_1 T_1$ and $\beta_2 \equiv a_2 T_1^2$. It follows that the viscous force in the momentum equation (4) can be written as

$$\nabla \cdot [\nu \tilde{\mathbf{S}}] = \nu_0 \nabla \cdot \left[\sum_{i=0}^P (1 + \beta_1 \xi_1 + \beta_2 \xi_1^2) \tilde{\mathbf{S}}_i \Psi_i \right], \quad (18)$$

where $\mathbf{u}(\mathbf{x})$ is expanded as in Eq. (7). Multiplying by Ψ_k and taking the expectation we find

$$\langle \nabla \cdot [\nu \tilde{\mathbf{S}}] \Psi_k \rangle = \nu_0 \sum_{i=0}^P \nabla^2 \mathbf{u}_i \langle \Psi_i \Psi_k \rangle + \nu_0 \beta_1 \sum_{i=0}^P \nabla^2 \mathbf{u}_i \langle \xi_1 \Psi_i \Psi_k \rangle + \nu_0 \beta_2 \sum_{i=0}^P \nabla^2 \mathbf{u}_i \langle \xi_1^2 \Psi_i \Psi_k \rangle. \quad (19)$$

Using the definitions $\Psi_1 = \xi_1$ and $\Psi_2 = \xi_1^2 - 1$ in Eq. (19) we get

$$\begin{aligned} \langle \nabla \cdot [\nu \tilde{\mathbf{S}}] \Psi_k \rangle &= \nu_0 (1 + \beta_2) \nabla^2 \mathbf{u}_k \langle \Psi_k \Psi_k \rangle + \nu_0 \beta_1 \sum_{i=0}^P \nabla^2 \mathbf{u}_i \langle \Psi_1 \Psi_i \Psi_k \rangle \\ &\quad + \nu_0 \beta_2 \sum_{i=0}^P \nabla^2 \mathbf{u}_i \langle \Psi_2 \Psi_i \Psi_k \rangle. \end{aligned} \quad (20)$$

Substituting into the Navier–Stokes equation, we obtain the following coupled system for the velocity and pressure modes:

$$\begin{aligned} \frac{\partial \mathbf{u}_k}{\partial t} + \sum_{i=0}^P \sum_{j=0}^P (\mathbf{u}_i \cdot \nabla) \mathbf{u}_j \frac{\langle \Psi_i \Psi_j \Psi_k \rangle}{\langle \Psi_k \Psi_k \rangle} \\ = -\nabla p_k + \nu_0 (1 + \beta_2) \nabla^2 \mathbf{u}_k + \nu_0 \beta_1 \sum_{i=0}^P \nabla^2 \mathbf{u}_i \frac{\langle \Psi_1 \Psi_i \Psi_k \rangle}{\langle \Psi_k \Psi_k \rangle} \\ + \nu_0 \beta_2 \sum_{i=0}^P \nabla^2 \mathbf{u}_i \frac{\langle \Psi_2 \Psi_i \Psi_k \rangle}{\langle \Psi_k \Psi_k \rangle} \quad k = 0, \dots, P. \end{aligned} \quad (21)$$

As before, the continuity equation results in the divergence constraints $\nabla \cdot \mathbf{u}_k = 0$, $k = 0, \dots, P$.

Note that if $a_2 = 0$, then the viscosity evolves linearly with T , and problem P1 is recovered with the choice $\nu_1 = a_1 T_1$. On the other hand, where $a_2 \neq 0$, it is clear that ν is no longer Gaussian. In the computations, we analyze the effect of non-Gaussian statistics by contrasting linear and nonlinear viscosity laws.

3.4. Statement of P3

In the third problem, the temperature is no longer assumed spatially uniform and its evolution is governed by the energy equation (3). The kinematic viscosity is assumed to vary linearly with temperature, according to

$$\frac{\nu(\mathbf{x})}{\nu_0} = 1 + K'(T(\mathbf{x}) - T_{ref}), \quad (22)$$

where T_{ref} is a reference temperature, $\nu_0 \equiv \nu(T_{ref})$, and K' is a constant. Note that the temperature-dependence of the viscosity provides a nontrivial coupling between the energy and Navier–Stokes equations. The uncertainty in the process is considered to arise as a result of a stochastic temperature profile, T_{in} , at the inlet of the microchannel.

As before, we rely on the polynomial chaos expansion of the stochastic fields

$$T(\mathbf{x}) = \sum_{i=0}^P T_i(\mathbf{x})\Psi_i \quad (23)$$

$$\mathbf{u}(\mathbf{x}) = \sum_{i=0}^P \mathbf{u}_i(\mathbf{x})\Psi_i \quad (24)$$

$$p(\mathbf{x}) = \sum_{i=0}^P p_i(\mathbf{x})\Psi_i \quad (25)$$

$$\nu(\mathbf{x}) = \nu_0(1 - K'T_{ref}) + \nu_0 K' \sum_{i=0}^P T_i(\mathbf{x})\Psi_i. \quad (26)$$

Introducing (23) into the energy equation, multiplying by Ψ_k , and evaluating the expectation, we get

$$\frac{\partial T_k}{\partial t} + \sum_{i=0}^P \sum_{j=0}^P \mathbf{u}_i \cdot \nabla T_j \frac{\langle \Psi_i \Psi_j \Psi_k \rangle}{\langle \Psi_k \Psi_k \rangle} = \lambda \nabla^2 T_k \quad k = 0, \dots, P. \quad (27)$$

Analogously, we introduce Eqs. (24)–(26) into Eq. (1) and perform a similar decomposition to obtain

$$\begin{aligned} \frac{\partial \mathbf{u}_k}{\partial t} + \sum_{i=0}^P \sum_{j=0}^P (\mathbf{u}_i \cdot \nabla) \mathbf{u}_j \frac{\langle \Psi_i \Psi_j \Psi_k \rangle}{\langle \Psi_k \Psi_k \rangle} \\ = -\nabla p_k + \nu_0(1 - K'T_{ref})\nabla^2 \mathbf{u}_k \\ + \nu_0 K' \sum_{i=0}^P \sum_{j=0}^P \nabla \cdot (T_j \mathbf{S}(\mathbf{u}_i)) \frac{\langle \Psi_i \Psi_j \Psi_k \rangle}{\langle \Psi_k \Psi_k \rangle} \quad k = 0, \dots, P, \end{aligned} \quad (28)$$

with the same velocity divergence constraints as in Eq. (14).

3.5. Treatment of Boundary Conditions

Similar to the treatment of field variables, a “weak formulation” approach is adopted for the boundary conditions. For brevity, we only illustrate this approach for the inflow

condition. As mentioned earlier, the velocity profile is imposed at the channel inlet; we have

$$\mathbf{u}(\mathbf{x} \in \Gamma_i) = \mathbf{u}_{in}, \quad (29)$$

where \mathbf{u}_{in} denotes the deterministic velocity at Γ_i . Expanding the above equation in terms of the polynomial chaos system, we have

$$\mathbf{u}_0(\mathbf{x} \in \Gamma_i) = \mathbf{u}_{in} \quad (30)$$

$$\mathbf{u}_k(\mathbf{x} \in \Gamma_i) = 0 \quad k = 1, \dots, P. \quad (31)$$

Similarly, for the inflow temperature conditions we have

$$T_k(\mathbf{x} \in \Gamma_i) = \langle T_{in} \Psi_k \rangle \quad k = 0, \dots, P. \quad (32)$$

Thus, unlike the inlet velocity profile, the inflow temperature may admit stochastic components whose amplitudes are specified by the right-hand side of Eq. (32). As mentioned in Section 3.4, a random temperature component at inflow results in strong coupling between the momentum and energy equations.

4. SOLUTION METHOD

It can be observed from the previous section that the equation system governing the evolution of the uncertainty modes \mathbf{u}_k , p_k , $k = 0, \dots, P$, has a similar form to the original Navier–Stokes equation. Because of the appearance of coupling terms, however, the system size is by a factor of P larger than the corresponding deterministic system. If not addressed properly, the enlargement of the system size in the stochastic formulation can constitute a major drawback, especially when the implementation of a fast $O(N)$ solver is not possible. Another consideration that has guided the present development is a desire to base the proposed development on existing deterministic solvers and computer codes.

Our approach to the formulation of the stochastic solver is based on the observation that the velocity divergence constraints are *decoupled*, and this suggests the implementation of a projection scheme [17] in which the advection and diffusion terms are integrated in a first fractional step, and the divergence constraints are then enforced in a second fractional step. Because the divergence constraints are decoupled, this approach results in a set of $P + 1$ decoupled pressure projection steps. Since these steps typically account for the bulk of the computational effort in incompressible flow simulations, the solution of the stochastic system can be obtained at essentially a cost of $P + 1$ deterministic solutions. Coupled with the spectral nature of the stochastic representation, this leads to a highly efficient stochastic solver, as illustrated in the examples of the following section. Note that in the case of multiple random variables, the stochastic solution can be determined at a cost essentially of L deterministic solutions, where L is the order of the Karhunen–Loève expansion (Eq. (3.2)). Generally, P and L are generally much smaller than the number of independent MC realizations that are needed for adequate representation of the uncertainty. This feature, together with the decoupled structure of the pressure projection steps, is behind the efficiency of SPM.

The formulation of the stochastic solver adapts elements of previously developed low-Mach-number solvers in [18, 19]. We rely on discretization of all fields variables using a

uniform Cartesian mesh with cell size Δx and Δy in the x - and y -directions, respectively. The velocity modes \mathbf{u}_k are defined on cell edges, while the scalar fields p_k , T_k , and v_k are defined on cell centers. Spatial derivatives are approximated using second-order centered differences.

As mentioned earlier, the governing equations are integrated using a fractional step projection scheme, and the implementation of the scheme is illustrated for the stochastic formulation developed in Section 3.4. In the first fractional step, we integrate the coupled advection–diffusion equations,

$$\begin{aligned} \frac{\partial \mathbf{u}_k}{\partial t} + \sum_{i=0}^P \sum_{j=0}^P (\mathbf{u}_i \cdot \nabla) \mathbf{u}_j \frac{\langle \Psi_i \Psi_j \Psi_k \rangle}{\langle \Psi_k \Psi_k \rangle} \\ = v_0(1 - K'T_{ref})\nabla^2 \mathbf{u}_k + v_0 K' \sum_{i=0}^P \sum_{j=0}^P \nabla \cdot (T_j \bar{\mathbf{S}}(\mathbf{u}_i)) \frac{\langle \Psi_i \Psi_j \Psi_k \rangle}{\langle \Psi_k \Psi_k \rangle} \end{aligned} \quad (33)$$

for $k = 0, \dots, P$. The explicit, second-order Adams–Bashforth scheme is used for this purpose; we thus have

$$\frac{\mathbf{u}_k^* - \mathbf{u}_k^n}{\Delta t} = \frac{3}{2} \mathbf{H}_k^n - \frac{1}{2} \mathbf{H}_k^{n-1} \quad k = 0, \dots, P, \quad (34)$$

where \mathbf{u}_k^* are the predicted velocity modes, Δt is the time step,

$$\mathbf{H}_k \equiv v_0(1 - K'T_{ref})\nabla^2 \mathbf{u}_k + \sum_{i=0}^P \sum_{j=0}^P C_{ijk} [v_0 K' \nabla \cdot (T_j \bar{\mathbf{S}}(\mathbf{u}_i)) - (\mathbf{u}_i \cdot \nabla) \mathbf{u}_j], \quad (35)$$

$$C_{ijk} \equiv \frac{\langle \Psi_i \Psi_j \Psi_k \rangle}{\langle \Psi_k \Psi_k \rangle}, \quad (36)$$

and the superscripts refer to the time level. A similar treatment is used for the energy equation, which is integrated using

$$\frac{T_k^{n+1} - T_k^n}{\Delta t} = \frac{3}{2} J_k^n - \frac{1}{2} J_k^{n-1} \quad k = 0, \dots, P, \quad (37)$$

where

$$J_k \equiv \lambda \nabla^2 T_k - \sum_{i=0}^P \sum_{j=0}^P C_{ijk} \mathbf{u}_i \cdot \nabla T_j. \quad (38)$$

In the second fractional step, we perform a pressure correction to the predicted velocity in order to satisfy the divergence constraints. Specifically, we have

$$\frac{\mathbf{u}_k^{n+1} - \mathbf{u}_k^*}{\Delta t} = -\nabla p_k \quad k = 0, \dots, P, \quad (39)$$

where the pressure fields p_k are determined so that the fields \mathbf{u}_k^{n+1} satisfy the divergence constraints in (14), i.e.,

$$\nabla \cdot \mathbf{u}_k^{n+1} = 0 \quad (40)$$

Combining Eqs. (39) and (40) results in the following system of *decoupled* Poisson equations:

$$\nabla^2 p_k = -\frac{1}{\Delta t} \nabla \cdot \mathbf{u}_k^* \quad k = 0, \dots, P. \quad (41)$$

Similar to the original projection method, the above Poisson equations are solved, independently, subject to Neumann conditions that are obtained by projecting Eq. (39) in the direction normal to the domain boundary [17, 20]. The weak formulation approach outlined in Section 3.5 is used for this purpose. Fast Fourier-based solvers are employed for the inversion of the discrete operators.

5. RESULTS

5.1. Results for P1

Parabolic Inlet Profile

We start by examining a simplified case where a deterministic parabolic velocity profile is imposed at the channel inlet. We use

$$u_{in} = 0, \quad v_{in} = V_{ref} \left[1 - 4 \left(\frac{x}{B} - 0.5 \right)^2 \right], \quad (42)$$

where (u_{in}, v_{in}) are the x - and y -components of the inlet velocity, V_{ref} is the reference velocity, and B is the channel width. The flow is characterized by the Reynolds number based on B , v_0 , and V_{ref} :

$$Re \equiv \frac{B V_{ref}}{v_0}. \quad (43)$$

As mentioned earlier, we are interested in applications with moderate to low Reynolds numbers, so that the flow is stable and laminar.

The (deterministic) solution for steady flow in the channel is the well-known Poiseuille solution [21]

$$u(x, y) = 0, \quad v(x, y) = v_{in}(x), \quad \frac{\partial p}{\partial x} = 0, \quad \frac{\partial p}{\partial y} = -\frac{4\mu V_{ref}}{B^2}, \quad (44)$$

where $\mu = \rho\nu$ is the dynamic viscosity. Thus, when the inlet profile is parabolic, the velocity field is independent of the axial coordinate, y , and, as long as this solution is stable, the velocity is independent of the viscosity as well.

It follows from the above remarks that for the present inlet velocity conditions, an uncertainty in the viscosity would only affect the rate of pressure drop. We have

$$\frac{\partial p}{\partial y} = \frac{-4\rho V_{ref}}{B^2} \nu = \frac{-4\rho V_{ref}}{B^2} (v_0 + v_1 \xi_1) \equiv \frac{\partial p_0}{\partial y} \Psi_0 + \frac{\partial p_1}{\partial y} \Psi_1. \quad (45)$$

Using the definitions $\Psi_0 = 1$ and $\Psi_1 = \xi_1$, and exploiting the orthogonality of the Hermite polynomials we get

$$\frac{\partial p_0}{\partial y} = \frac{-4\rho V_{ref} \nu_0}{B^2} \quad (46)$$

and

$$\frac{\partial p_1}{\partial y} = \frac{-4\rho V_{ref} \nu_1}{B^2} = \frac{\nu_1}{\nu_0} \frac{\partial p_0}{\partial y}. \quad (47)$$

Furthermore, the variance $\sigma_{\partial p}^2$ of the pressure gradient is given by

$$\sigma_{\partial p}^2 \equiv \left\langle \left(\frac{\partial p}{\partial y} - \frac{\partial p_0}{\partial y} \right)^2 \right\rangle = \left\langle \left(\frac{\partial p_1}{\partial y} \Psi_1 \right)^2 \right\rangle = \left(\frac{\partial p_1}{\partial y} \right)^2. \quad (48)$$

Thus, for Poiseuille flow, the effect of uncertainty in viscosity can be characterized analytically.

The analytical expressions derived above are used to verify the predictions of the stochastic projection scheme. Results are obtained for a channel flow with $Re = 40.62$ and $\nu_1/\nu_0 = 0.2$. The simulations are performed in a domain with aspect ratio $H/B = 6$, using a 64×256 computational grid, a time step $\Delta t = 10^{-3} B/V_{ref}$, and a polynomial chaos expansion with $P = 2$. Figure 2 shows the ratio of the computed pressure gradients $\partial p_1/\partial y$ and $\partial p_0/\partial y$, at steady-state, along the centerline of the channel. The results are in excellent agreement with the theoretical prediction in (47). For $y/B > 2$, the analytical and computed results are practically identical, but tiny differences occur near the domain inlet. The maximum relative error between the exact and computed pressure gradient ratios is, however, quite small and falls below 0.05%.

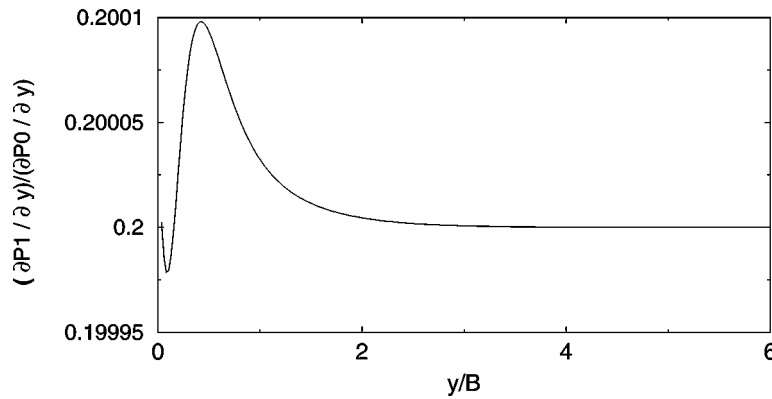


FIG. 2 Pressure gradient ratio $(\partial p_1/\partial y)/(\partial p_0/\partial y)$ along the channel centerline versus the normalized stream-wise coordinate y/B . Results are obtained for a channel with $H/B = 6$, $Re = 40.62$, and $\nu_1/\nu_0 = 0.2$. The simulation is performed using a grid with 64×256 cells, $\Delta t V_{ref}/B = 10^{-3}$, and a polynomial chaos expansion with $P = 2$.

Uniform Inflow

Here, we consider the case of a uniform inlet velocity profile:

$$u_{in} = 0, \quad v_{in} = V_{ref}. \quad (49)$$

With this inflow condition, the steady (deterministic) flow gradually evolves toward a parabolic Poiseuille profile. The transition reflects the growth of a laminar boundary layer which eventually fills the channel; this delimits the entrance length, whose value depends on the Reynolds number [22]. Within the transition region, the flow field is no longer uniform so that, in the stochastic case, all of the velocity and pressure modes exhibit a nontrivial behavior.

In order to illustrate this behavior, a simulation is performed for a channel with $Re = 81.24$ and $\nu_1/\nu_0 = 0.3$. The simulation is performed using a uniform grid with 64×256 , a time step $\Delta t V_{ref}/B = 2 \times 10^{-3}$, and a polynomial chaos expansion with $P = 3$. The unsteady equations are integrated in time until steady conditions are reached. Results are shown in Figs. 3–5, which depict contours of the streamfunction, the streamwise velocity, and the cross-stream velocity, respectively. The streamfunction is reconstructed from the steady velocity field. In each figure, plots are generated for the mean ($k = 0$) as well as modes 1 and 2. The results illustrate the growth of the boundary layer in the entrance region. For the mean flow modes ($k = 0$), entrance effects extend up to $y/B \simeq 4$, and the the corresponding distribution becomes uniform at larger streamwise locations. The streamwise velocity modes

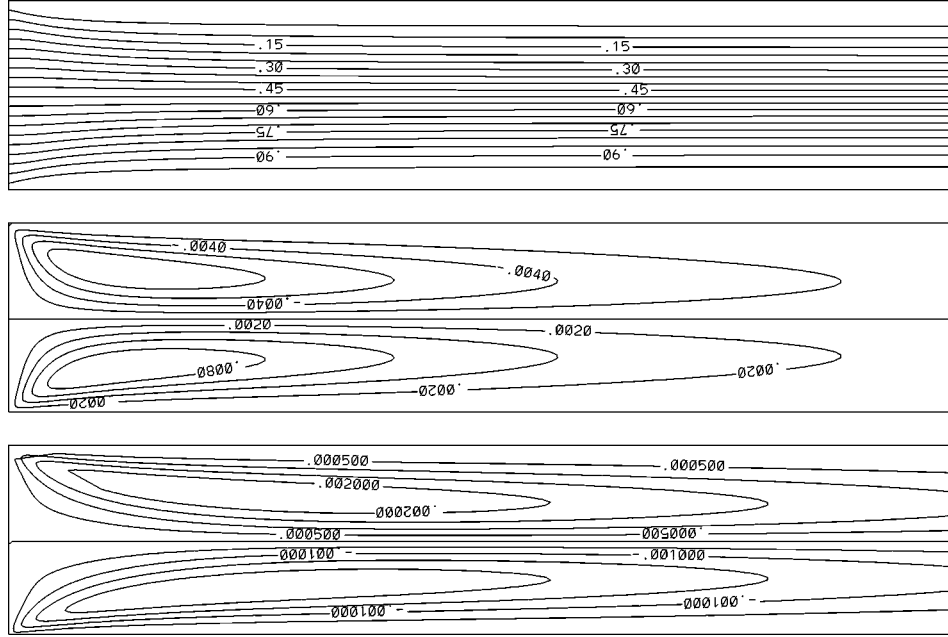


FIG. 3. Contour plots of the streamfunction distribution corresponding to u_0 (top), u_1 (center), and u_2 (bottom). Results are obtained for a channel with $H/B = 6$, $Re = 81.24$, and $\nu_1/\nu_0 = 0.2$. The flow is from left to right along the $+y$ -direction; the entire domain ($0 \leq y/B \leq 6$, $0 \leq x/B \leq 1$) is shown. The simulation is performed using a grid with 64×256 cells, $\Delta t V_{ref}/B = 2 \times 10^{-3}$, and a polynomial chaos expansion with $P = 3$.

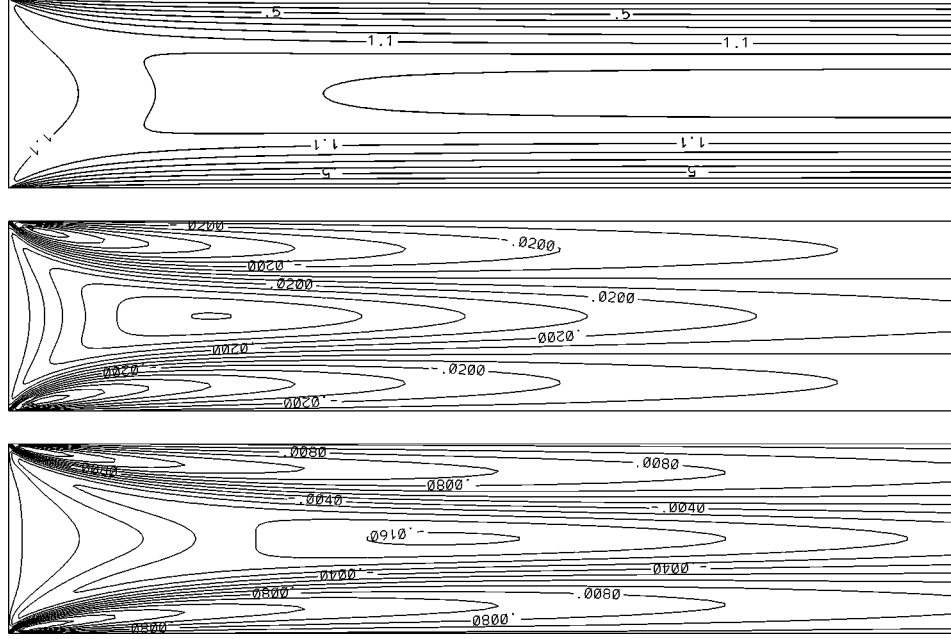


FIG. 4. Contour plots of the streamwise velocity components v_0 (top), v_1 (center), and v_2 (bottom). Same parameters as in Fig. 3.

v_1 and v_2 exhibit appreciable variation up to 4 to 5 channel widths, but the cross-stream velocity modes u_0 , u_1 , and u_2 have negligible values outside the region $0 \leq y/B \leq 3$.

Note that the magnitudes of the fields decrease as k increases, which reflects the fast convergence of the spectral stochastic representation. The stochastic velocity field resulting from the uncertainty in viscosity is dominated by the first mode, which exhibits recirculation regions near the channel entrance that are symmetric with respect to the centerline. Below, we contrast the present solution with results obtained using a nonlinear viscosity law.

5.2. Solution for P2

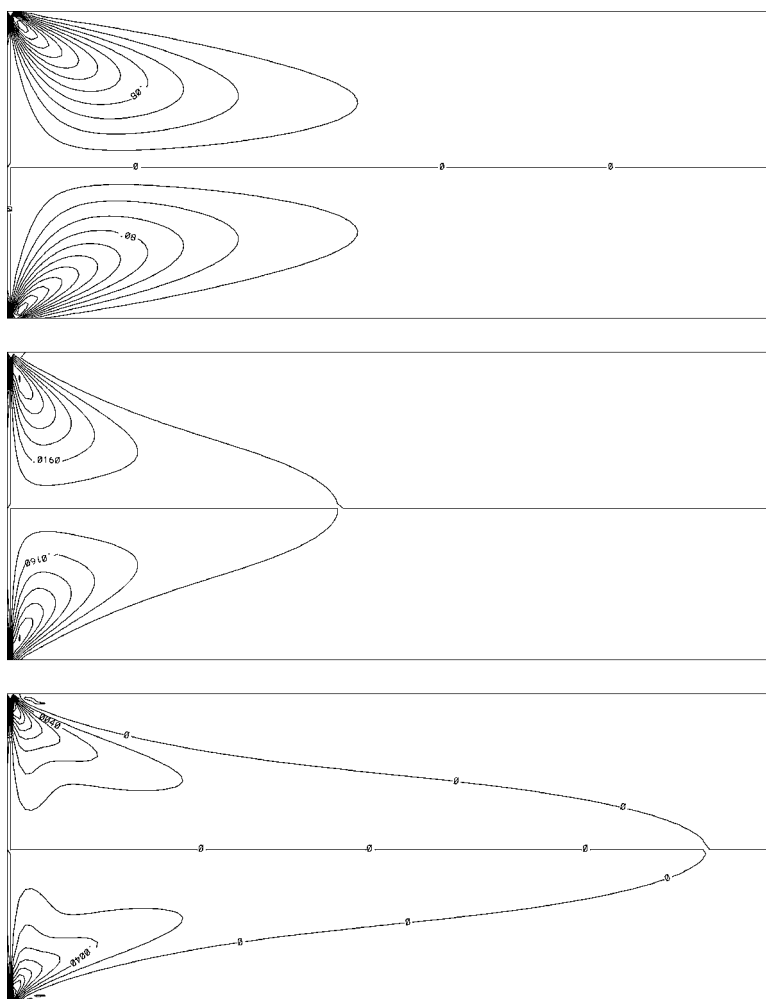
In this section, we focus once more on a straight channel with uniform inflow but consider that the viscosity is temperature-dependent. The nonlinear viscosity law

$$\frac{\nu(T)}{\nu(T_0)} = 1 + a_1(T - T_0) + a_2(T - T_0)^2 = 1 + a_1 T_0 \left(\frac{T}{T_0} - 1 \right) + a_2 T_0^2 \left(\frac{T}{T_0} - 1 \right)^2 \quad (50)$$

is assumed, together with a Gaussian, spatially uniform temperature field given by

$$T = T_0 + T_1 \xi_1, \quad (51)$$

where T_0 is the mean (reference) temperature and T_1 is the standard deviation. Computations are performed for a channel at $Re = V_{ref}B/\nu_0 = 81.24$, where $\nu_0 \equiv \nu(T_0)$. The coefficients in the nonlinear viscosity law are $a_1 T_0 = 9$ and $a_2 T_0^2 = 45$. Meanwhile, the



standard deviation in the temperature is fixed as $T_1/T_0 = 1/30$. The nonlinear viscosity law is plotted in Fig. 6 together with the scaled probability density function of the temperature. Note for this choice of parameters, linearization of the viscosity law (i.e., setting $a_2 = 0$) would result in the same problem last considered. Thus, the effect of the nonlinearity in the viscosity law can be examined by comparing the results with those given in Section 3.2.

67

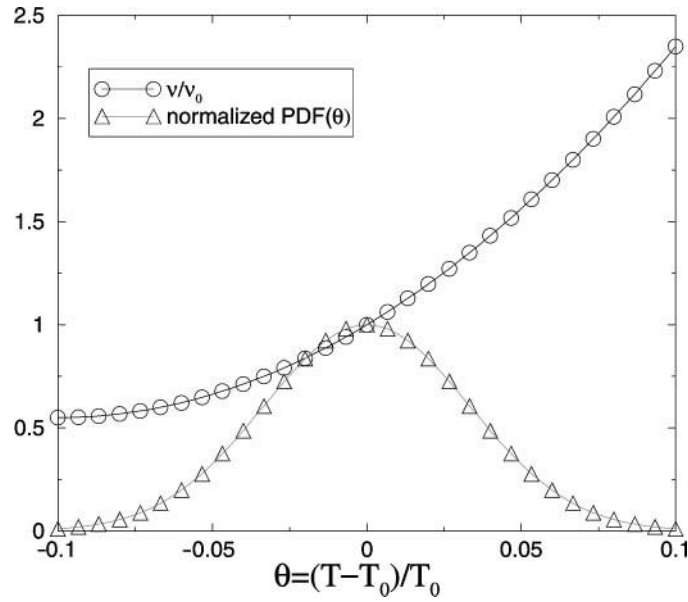


FIG. 6. Dependence of viscosity on the temperature given in Eq. (50) and the scaled probability density function of T .

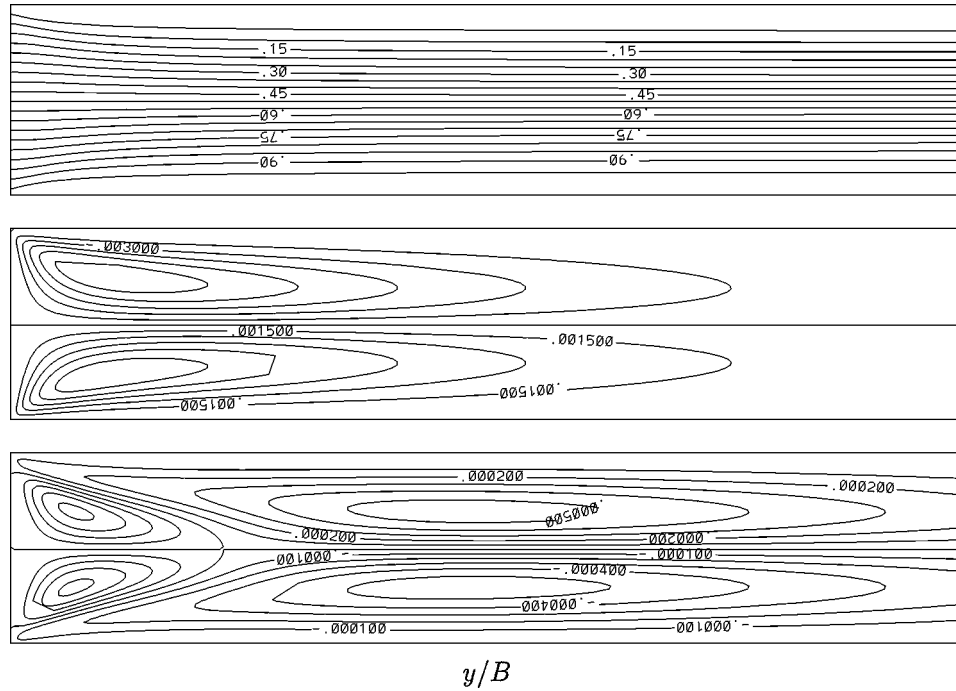
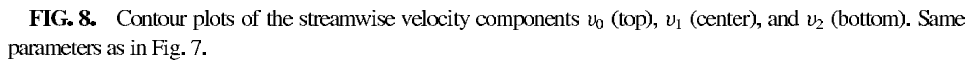


FIG. 7. Contour plots of the streamfunction distribution corresponding to u_0 (top), u_1 (center), and u_2 (bottom). Results are obtained for a channel with $H/B = 6$, $Re = 81.24$, the nonlinear viscosity law and stochastic temperature shown in Fig. 6. The simulation is performed using a grid with 64×256 cells, $\Delta t V_{ref}/B = 10^{-3}$, and a polynomial chaos expansion with $P = 3$.



On the other hand, the “stochastic modes” \mathbf{u}_1 and \mathbf{u}_2 exhibit noticeable differences from the corresponding fields obtained with a linear viscosity law. The distributions reveal a more complex structure in the nonlinear case, especially for the second mode where one can notice the presence of multiples lobes that are symmetrically distributed on both sides of the channel centerline. Thus, the nonlinear term in the viscosity law can have a dramatic impact on the variance fields.

In order to further examine the effects of the viscosity law on the predictions, we linearize the governing equations and thus consider the unsteady Stokes problem. In this formulation, the nonlinear inertial terms are omitted and the evolution of the flow field follows a gradual decay toward the steady at a rate that is governed by the viscous time scale. This simple flow evolution enables us to perform straightforward comparison of different solutions during the transient. In addition, by contrasting the results of the Stokes and Navier–Stokes computations, one can gain additional insight into the role of inertial effects on the structure of the variance fields. Unsteady Stokes solutions are performed for a viscosity law with $a_2 T_0^2 = 45$ (the nonlinear case) and the predictions are contrasted with results obtained with $a_2 = 0$ (the linear case). For both cases, instantaneous distributions of the standard deviation in the u and v velocity components and in the streamfunction are shown in Fig. 10. The simulations are initialized with the fluid at rest and the fields are generated at a fixed time instant $t_a = V_{ref} t / B = 1$, before the decay of the flow transient. The variance σ_f^2 of a generic field variable $f(\mathbf{x}, \xi_1)$ is obtained from the corresponding polynomial chaos

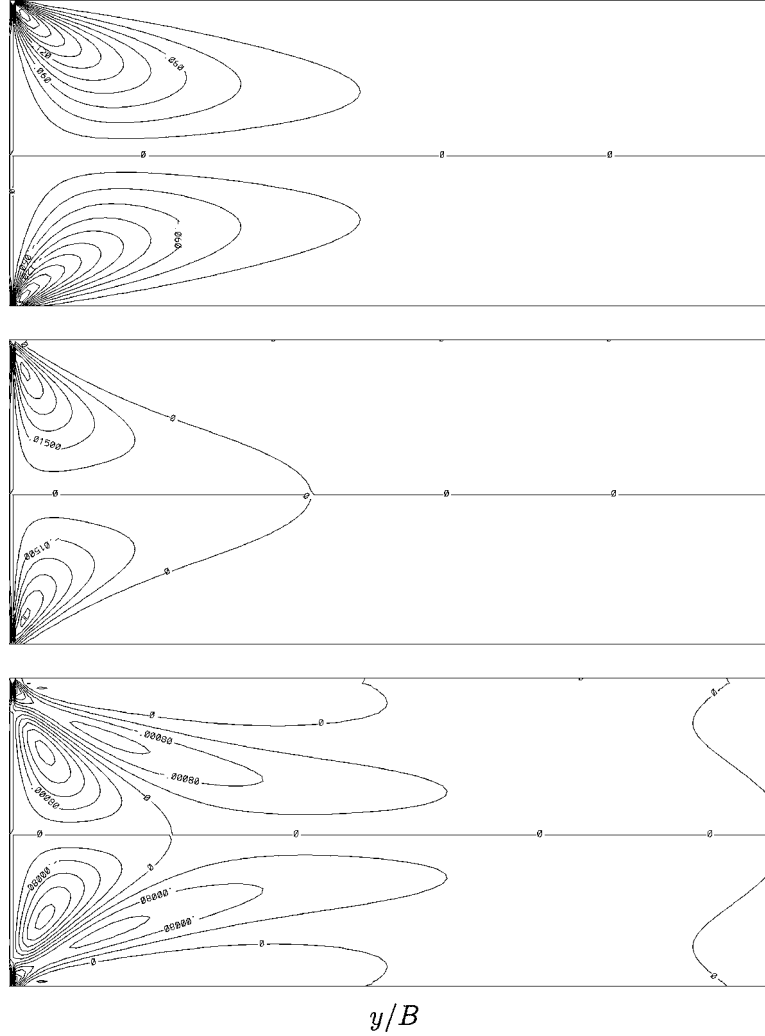


FIG. 9. Contour plots of the cross-stream velocity components u_0 (top), u_1 (center), and u_2 (bottom). Only the first half of the domain ($y/B \leq 3$) is shown. Same parameters as in Fig. 7.

expansion using

$$\sigma_f^2(\mathbf{x}) \equiv \langle (f(\mathbf{x}) - f_0(\mathbf{x}))^2 \rangle = \left\langle \left(\sum_{i=1}^P f_i(\mathbf{x}) \Psi_i \right)^2 \right\rangle = \sum_{i=1}^P f_i^2(\mathbf{x}) \langle \Psi_i^2 \rangle. \quad (52)$$

The results in Fig. 10 show that significant magnitude differences exist between the predictions obtained using linear and nonlinear viscosity laws. In particular, the difference between the two standard deviation fields exhibits peak values that are comparable to those of the corresponding fields. However, unlike our experiences above using the Navier–Stokes solver, the distributions for the two viscosity laws in the Stokes case have a very similar structure. This indicates that nonlinear advective effects can have a substantial impact on the structure of the variance field.

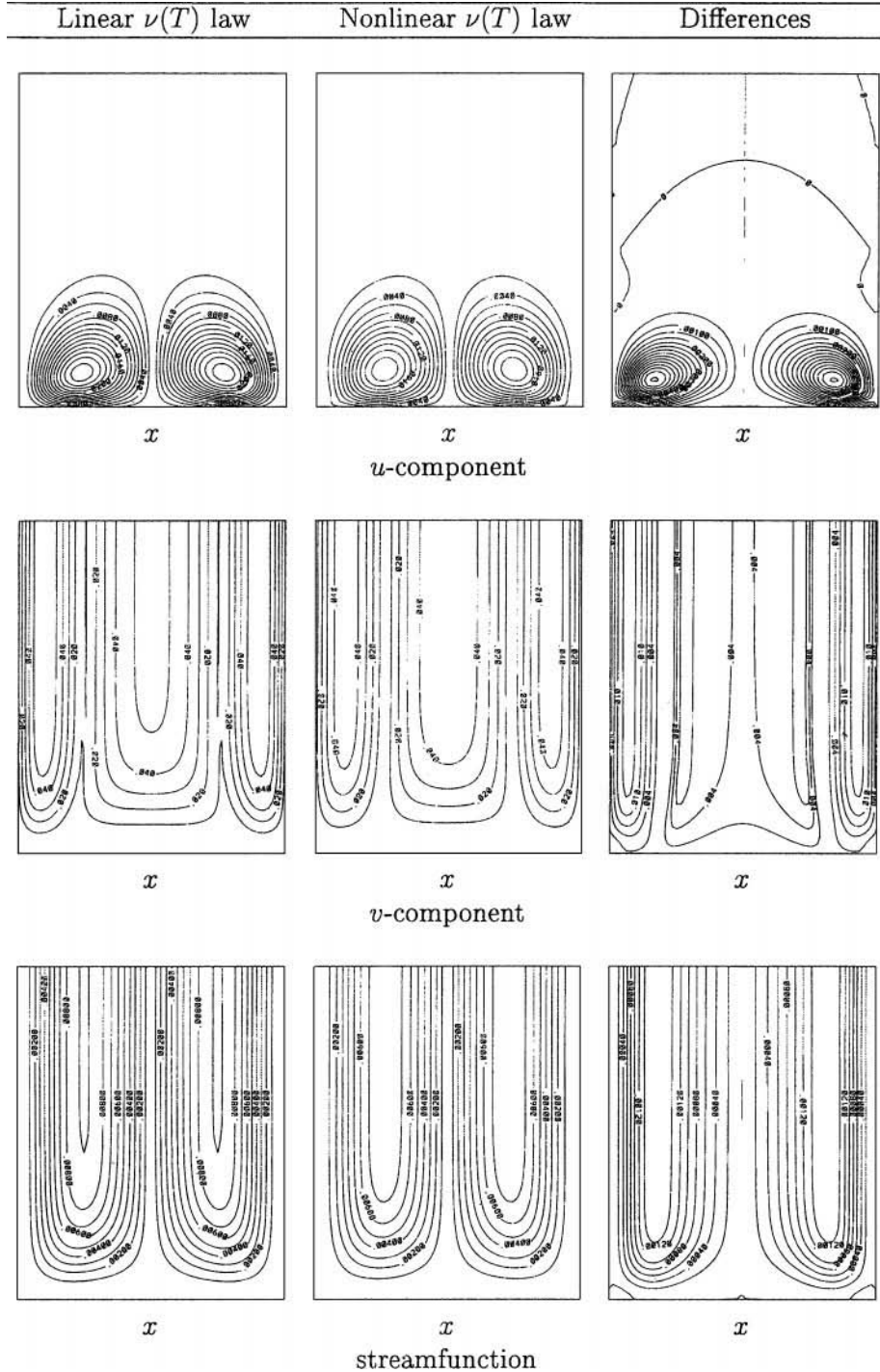


FIG. 10. Contour plots of the standard deviation in the u -component (top), the v -component (center), and streamfunction (bottom). Only the first quarter of the domain ($y \leq 1.5B$) is represented. The results are based on the computed Stokes solution at $t_a = V_{ref}t/B = 1$, using a linear viscosity law with $a_1T_0 = 9$ (left) and a nonlinear viscosity law with $a_1T_0 = 9$ and $a_2T_0^2 = 45$ (middle). The difference between the two standard deviation fields is plotted on the right. In both cases, the solutions are obtained on a grid with 64×256 cells, a time step $\Delta t V_{ref}/B = 10^{-3}$, and a polynomial chaos expansion with $P = 3$.

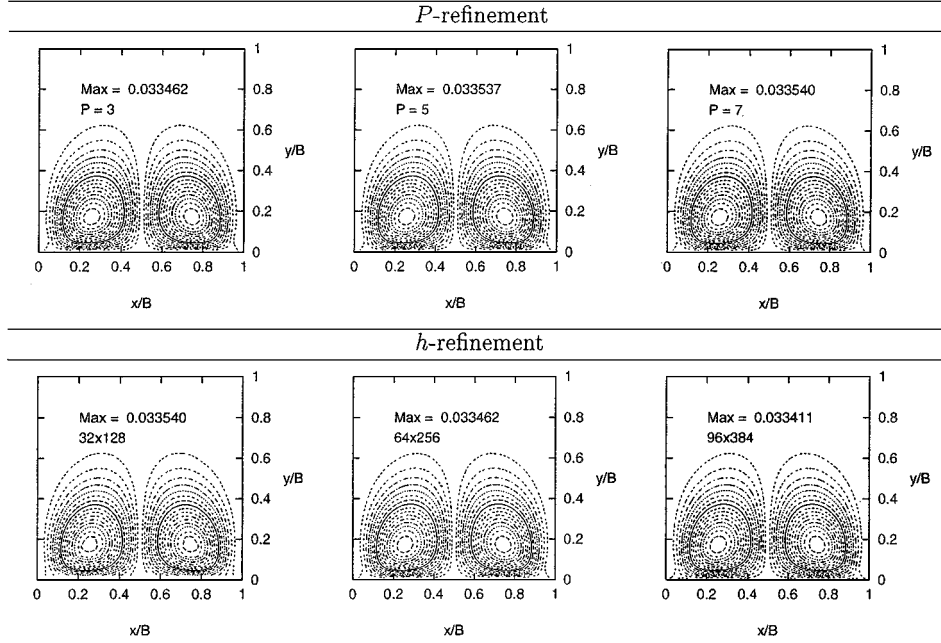


FIG. 11. Effect of the order P and cell size h on the standard deviation of the u -velocity.

We also use the Stokes problem to investigate the sensitivity of the computed solution with respect to refinement of the computational grid (h refinement) and the order of the polynomial chaos expansion (P refinement). Results of this study are given in Fig. 11, which depicts distributions of standard deviation in the cross-stream velocity u . The P -refinement tests are based on results obtained with $P = 3, 5$, and 7 , using a 64×256 grid and a time step $\Delta t V_{ref}/B = 10^{-3}$. The h -refinement tests are based on three grids having 32×128 , 64×256 , and 96×384 cells in the x - and y -directions, respectively; in these tests, $P = 3$ and the time steps are $\Delta t V_{ref}/B = 10^{-3}$ for the two coarsest grids and 5×10^{-4} for the finest. The results show that, for the Stokes problem, the standard deviation distribution and peak values are essentially unaffected by the value of P , which demonstrates the fast convergence of the spectral expansion. Figure 11 also shows that the predictions at two finest grid levels are nearly identical, while a slightly higher peak in the standard deviation can be observed for the coarsest grid level. Further examination of the results (not shown) reveals that differences between the coarse level predictions and the more refined computations are restricted to a small region near the channel inlet, and that at larger downstream distances, the coarse grid provides accurate prediction of the solution.

5.3. Solution for P3

Implementation of the stochastic scheme for P3 is illustrated based on simulations of the flow and temperature fields in the double-inlet microchannel schematically shown in Fig. 12. The channel inlet consists of two streams having identical parabolic velocity profiles with peak velocity V_{ref} . The two inlet streams are separated by a plate of thickness D . Thus, the problem can be treated as the wake of a slender bluff body of width D that is located at the center of the channel. The flow is characterized by the Reynolds number

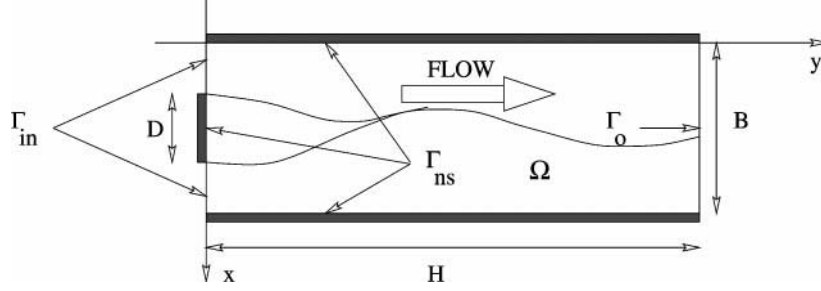


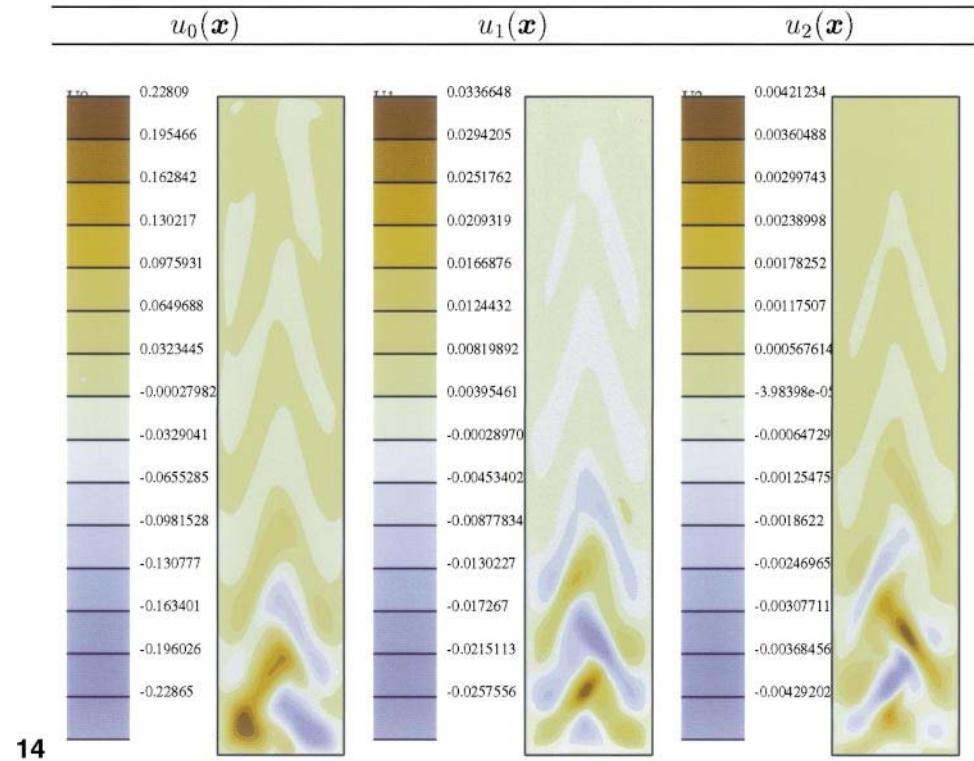
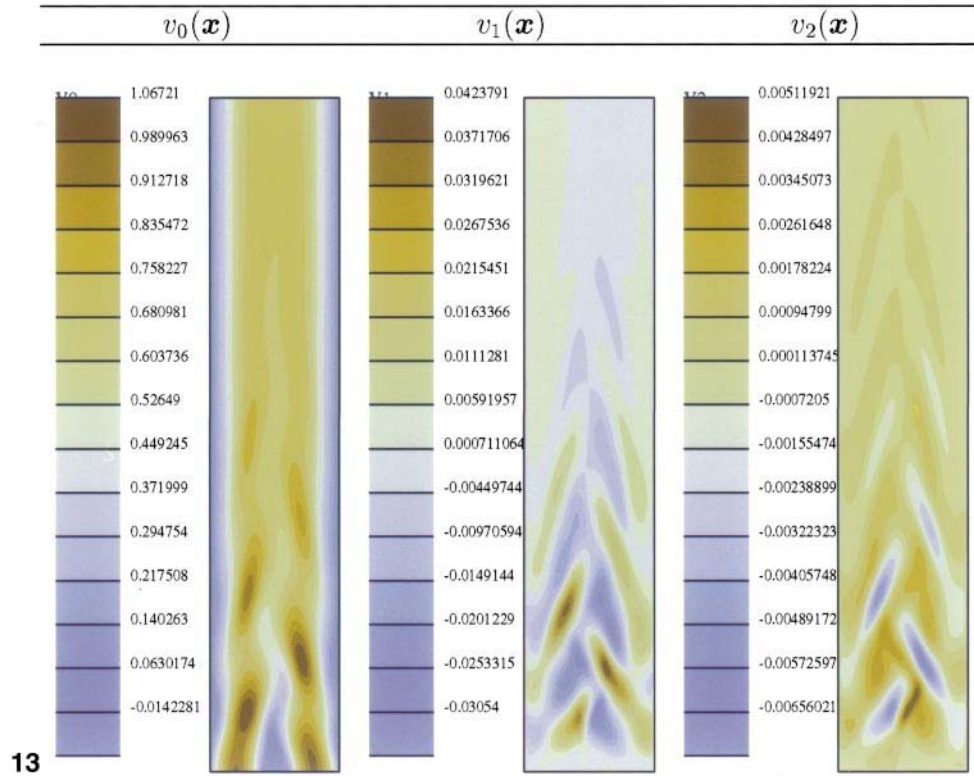
FIG. 12. Schematic illustration of the double-inlet microchannel.

$Re \equiv V_{ref}B/\nu_0$, the blockage ratio D/B , and the Prandtl number λ/ν_0 . As indicated in Section 3.4, $\nu_0 \equiv \nu(T_{ref})$ is the reference viscosity. Note that the blockage ratio and Re can be combined to define a Reynolds number based on the plate thickness, $Re_D \equiv V_{ref}B/\nu_0 = Re D/B$. If Re_D is large enough, the wake of the plate is unstable and periodic vortex shedding is observed, at least for small downstream distances. This situation is considered in the example below. Specifically, we consider a doublet inlet microchannel with blockage ratio $D/B = 0.2$ and Reynolds number $Re = 826$. The Reynolds number based on the plate thickness is $Re_D = 165.2$.

As mentioned in Section 3.4, the uncertainty in this problem is taken to arise as a result of a stochastic temperature boundary condition. Specifically, the temperature of the first inlet is taken to be deterministic and equal to T_{ref} . Meanwhile, the temperature of the second inlet is treated as a random Gaussian variable, with a mean value of T_{ref} and standard deviation of $0.1T_{ref}$. The fluid viscosity is assumed to depend on the temperature according to Eq. (22). This provides a strong coupling between the momentum and energy equations, which is examined in the computations by varying the coupling parameter K' . Specifically, results are obtained using $K = 0.1, 0.2$, and 0.4 , where $K \equiv K'T_{ref}$. In all cases, the Prandtl number $\lambda/\nu_0 = 6$. The computations are performed in a domain with $H/B = 5$, using a 100×352 grid, a time step $\Delta t V_{ref}/B = 2 \times 10^{-3}$, and a polynomial chaos expansion with $P = 3$.

Figures 13 and 14 depict instantaneous contours of streamwise and cross-stream velocity, respectively, at a dimensionless time $t V_{ref}/B = 100$. Plotted in each figure are distributions of the mean instantaneous prediction together with those of modes 1 and 2; results obtained using $K = 0.4$ are used. The distributions of the mean field exhibit the presence of well-defined patches that are arranged in a wavy pattern, which reflects the development of an unstable wake. The results also reveal that the strengths of the vortices shed into the wake gradually decrease with downstream distance. This effect can be clearly observed in Fig. 14, which shows that the magnitude of the cross-stream velocity component decreases with increasing distance from the channel entrance. Thus, the strengths of the vortices decay with y and, for the selected value of the Reynolds number, one would in fact expect a steady parabolic profile at large downstream distances.

Near the channel entrance, the distributions of u_1 and u_2 (Figs. 13 and 14) also reveal the presence of well-defined structures that are spatially well correlated with those of the mean field. The velocity magnitudes of the first mode are roughly an order of magnitude higher than those of the second mode. With increasing downstream distance, the magnitudes of u_1 and u_2 gradually decrease. This trend is also expected because, at large downstream distances, one would recover a parabolic velocity profile whose strength is solely determined



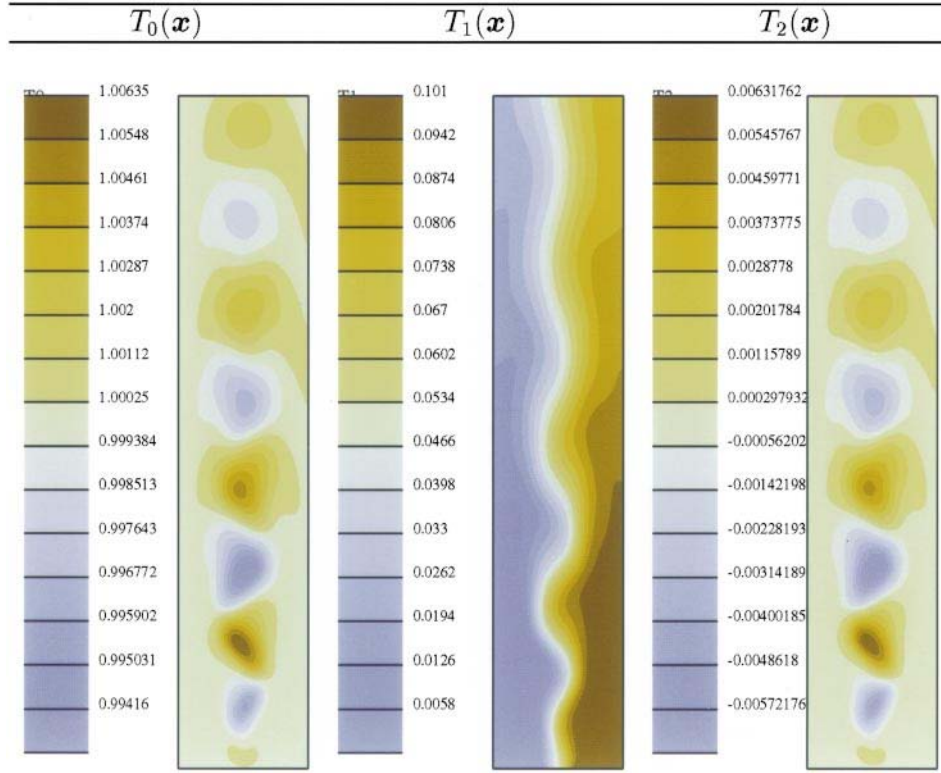


FIG. 15. Instantaneous distribution of T_0 , T_1 , and T_2 at $tV_{ref}/B = 100$. Temperature is normalized using T_{ref} , and results obtained using $K = 0.4$ are used. The flow is from bottom to top, along the $+y$ -direction.

by the volume flux in the channel. In this problem, the volume flux is deterministic, which indicates that all velocity modes with $k \geq 1$ vanish as y increases.

Figure 15 shows instantaneous temperature contours for $K = 0.4$, generated at the same time as in Figs. 13 and 14. The distributions of T_0 and T_2 show the presence of well-defined patches of alternating signs which are consequently arranged at the center of the domain. The strength of the temperature fluctuations within these patches first increases with y , reaches a maximum value around $y/B \sim 2$, and then decreases as we move further downstream. Near the channel entrance, the distribution of T_1 reflects the inlet temperature conditions, which are deterministic for the first inlet and stochastic in the second; thus, T_1 vanishes near the first inlet, peaks near the second, with a gradual transition region at the face of the solid plate. As one moves downstream, the width of this transition region increases leading to the formation of an asymmetric wavy pattern around the wake centerline, with small positive values near the left wall and high values near the right wall. Note that the peak value decreases as one moves downstream while the minimum increases, which

FIG. 13. Instantaneous distribution of v_0 , v_1 , and v_2 at $tV_{ref}/B = 100$. Velocity is normalized using V_{ref} , and results obtained using $K = 0.4$ are used. The flow is from bottom to top, along the $+y$ -direction.

FIG. 14. Instantaneous distribution of u_0 , u_1 , and u_2 at $tV_{ref}/B = 100$. Velocity is normalized using V_{ref} , and results obtained using $K = 0.4$ are used. The flow is from bottom to top, along the $+y$ -direction.

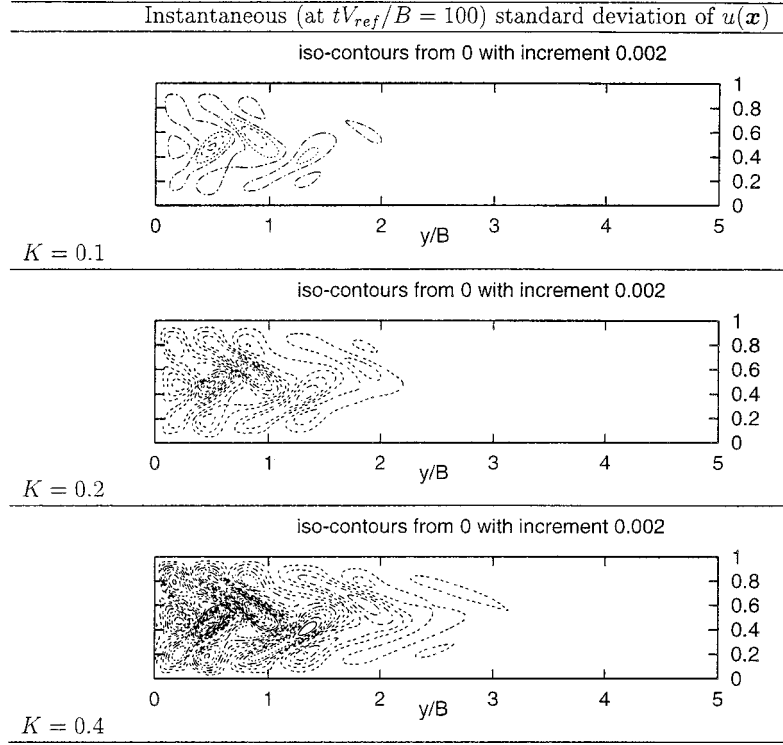


FIG. 16. Instantaneous distribution of the standard deviation of the normalized u -velocity field at time $tV_{ref}/B = 100$; top: $K = 0.1$, middle: $K = 0.2$, bottom: $K = 0.4$.

illustrates how the uncertainty in the boundary condition diffuses as it advected by the flow.

The close correspondence between the temperature fluctuations in the distributions of T_0 and T_2 in Fig. 15 is remarkable, and it is instructive to use the uncertainty representation scheme to interpret the results. The polynomial chaos expansion of the temperature field can be written as

$$\begin{aligned} T(\mathbf{x}, \xi_1) &= T_0(\mathbf{x})\Psi_0(\xi_1) + T_1(\mathbf{x})\Psi_1(\xi_1) + T_2(\mathbf{x})\Psi_2(\xi_1) + \dots \\ &= T_0(\mathbf{x}) + T_1(\mathbf{x})\xi_1 + T_2(\mathbf{x})(\xi_1^2 - 1) + \dots \end{aligned} \quad (53)$$

For $\xi_1 = 0$ the two inlet streams have an identical temperature, T_{ref} . This implies that in this case the temperature field is uniform and everywhere equal to T_{ref} . Using $\xi_1 = 0$ and truncation at $P = 2$, Eq. (53) gives

$$T(\mathbf{x}, \xi_1 = 0) \simeq T_0(\mathbf{x}) - T_2(\mathbf{x}), \quad (54)$$

i.e., the temperature prediction corresponding to $\xi_1 = 0$ is the difference between the mean and second mode. Since, as indicated above, $T(\mathbf{x}, \xi_1 = 0) = T_{ref}$, the fluctuations in T_0 and T_2 should cancel out, so long as the spectral truncation used is valid. This constraint is in fact reflected in the distributions shown in Fig. 15, which also indicates that the (truncated)

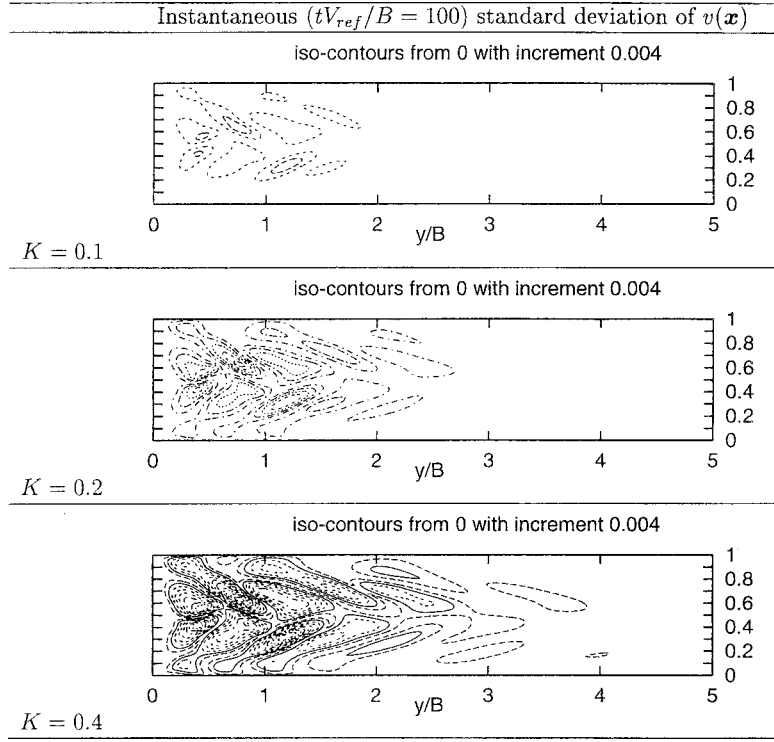


FIG. 17. Instantaneous distribution of the standard deviation of the normalized v -velocity field at time $tV_{ref}/B = 100$; top: $K = 0.1$, middle: $K = 0.2$, bottom: $K = 0.4$.

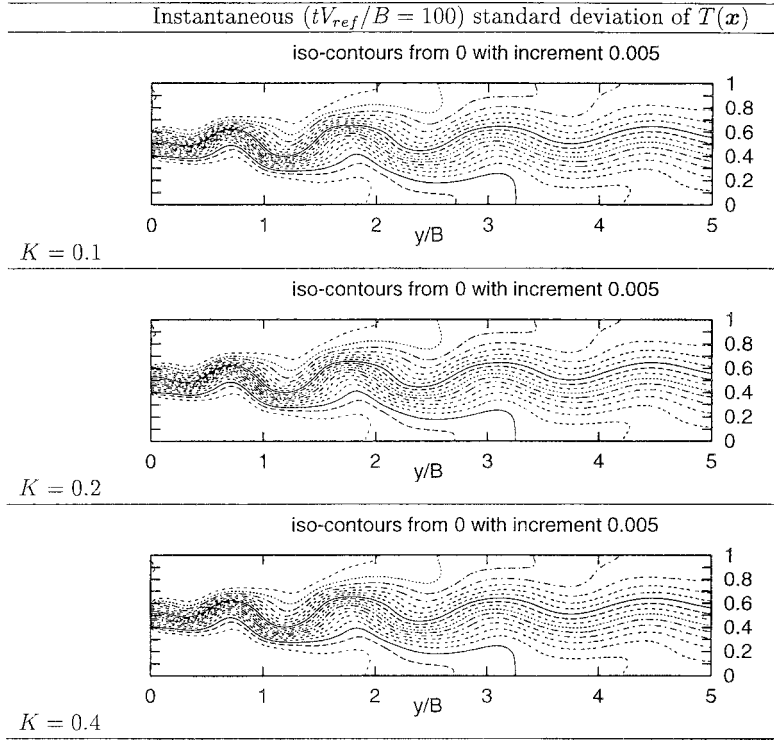


FIG. 18. Instantaneous distribution of the standard deviation of the normalized temperature field at time $tV_{ref}/B = 100$; top: $K = 0.1$, middle: $K = 0.2$, bottom: $K = 0.4$.

higher modes have little impact on the present predictions. One should also note that

$$\langle T(\mathbf{x}) \rangle = T_0(\mathbf{x}) \neq T(\mathbf{x}, \xi_1 = 0), \quad (55)$$

which indicates that the expected temperature field does not coincide with the “deterministic” prediction for $\xi_1 = 0$.

Instantaneous distributions of the standard deviation of u , v , and T are shown in Figs. 16–18, respectively. Plotted are results obtained at $tV_{ref}/B = 100$ using $K = 0.1$, 0.2, and 0.4. The results indicate that the normalized standard deviation for the streamwise (v) and cross-stream (u) velocity components increase with increasing K . As expected, the largest standard deviation values occur in the near wake, where strong vortical structures are present. On the other hand, the contours of the temperature standard deviation exhibit a wavy, asymmetric spreading band near the center of the domain. Unlike the standard deviation of the velocity field, the standard deviation of the temperature is essentially insensitive to the coupling parameter K . Thus, for the present conditions, the propagation of the uncertainty in the temperature field appears to be dominated by the deterministic thermal diffusion coefficient and advection with the (stochastic) mean velocity field.

Profiles of time-averaged values of the streamwise velocity, cross-stream velocity, and temperature are given in Fig. 19. The figure depicts profiles of the first three modes, generated at the streamwise plane $y/B = 1.25$ using simulations with $K = 0.1, 0.2$, and 0.4. The time-averaged profiles reveal trends similar to those observed in the instantaneous distributions.

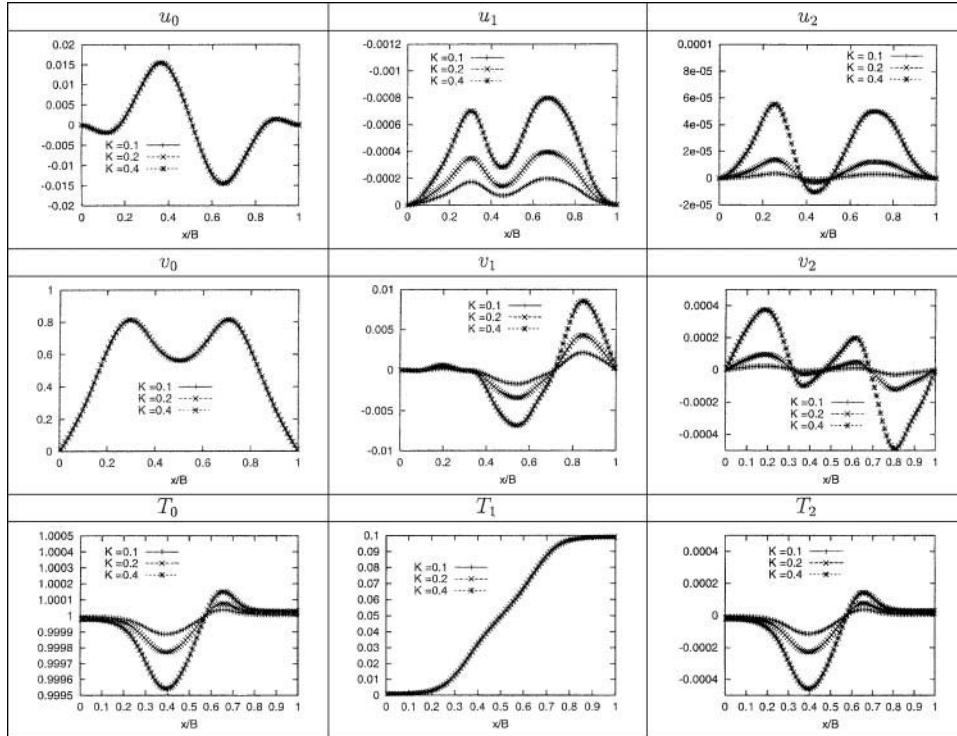


FIG. 19. Time-averaged profiles of U (top), v (center) and T (bottom), at the plane $y/B = 1.25$. The modes correspond to $k = 0$ (left), $k = 1$ (center) and $k = 2$ (right). The curves depict results obtained for $K = 0.1, 0.2$ and 0.4.

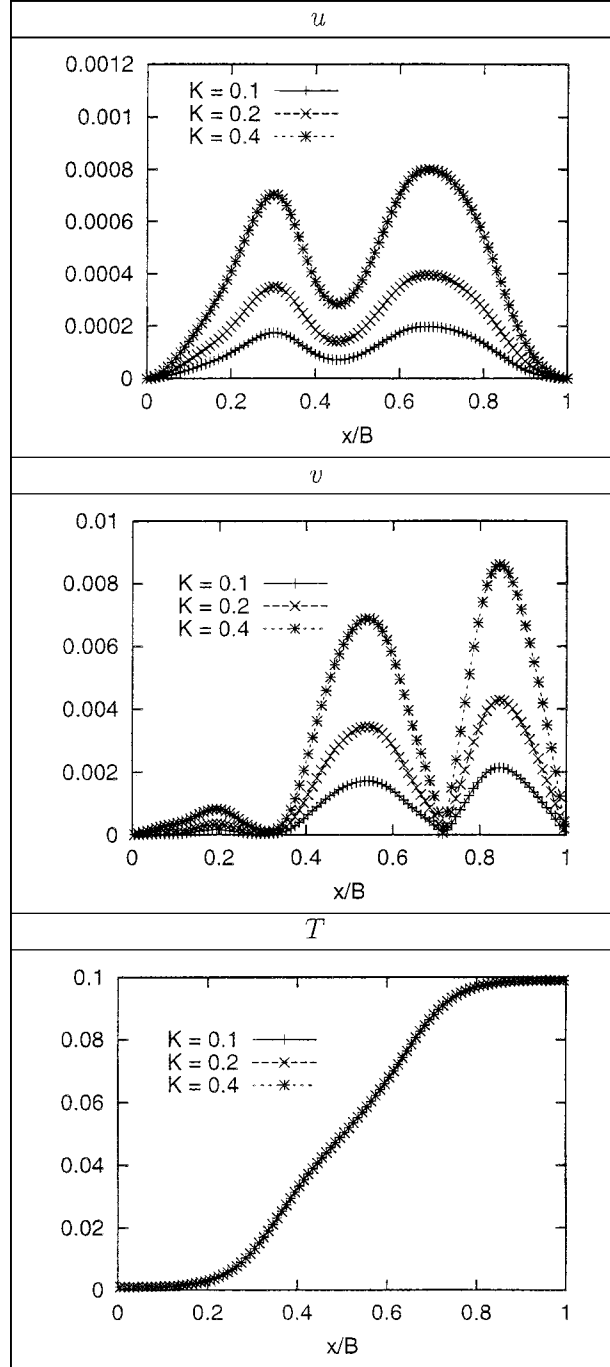


FIG. 20. Time-averaged standard deviation profiles at the plane $y = 1.25B$ for the normalized u -velocity (top), the normalized v -velocity (middle), and the normalized temperature (bottom). The curves depict results obtained for $K = 0.1, 0.2$, and 0.4 .

The mean velocity profiles clearly reflect the development of the unstable wake. Meanwhile, the uncertainty in the velocity field is dominated by the contribution of the first mode, whose peak values are significantly larger than those of the second mode. The results also indicate that as K increases, the uncertainty in the velocity field also increases. This behavior is in sharp contrast with that observed for the temperature profile. The mean temperature prediction exhibits a pronounced dependence on K while the first mode appears to be insensitive to K . As discussed earlier, the fluctuations in the profiles of T_0 and T_2 are quite similar, but are dominated by T_1 which is forced at the inlet boundary. The above trends are also reflected in Fig. 20, which depicts profiles of the normalized standard deviation of the mean velocity components and of temperature. Combined with the results in Fig. 19, it is evident that the contribution of the first mode to the standard deviation is dominant. One can also observe the insensitivity of the temperature standard deviation to the selected value of K , and the strong dependence of the velocity uncertainty on the coupling parameter.

We conclude the discussion with a brief remark on the possible use of the quantitative uncertainty propagation scheme. For instance, in the case of the streamwise profile, the standard deviation is vanishingly small at cross-stream locations ($x/B \sim 0.3$ and $x/B \sim 0.7$) where the mean signal approaches its peak value (compare Figs. 19 and 20). The ratio of the standard deviation to the mean value is clearly minimized at the corresponding locations. Consequently, these positions provide ideal sites for probing the streamwise velocity, in a fashion that minimizes the effect of the uncertainty in stochastic inlet temperature. This illustrates how the stochastic simulation results may be applied to experiment design.

6. CONCLUSION

In this paper, a stochastic scheme is developed which allows the propagation of uncertainty in incompressible Navier–Stokes simulations. The uncertainty representation scheme is based on the polynomial chaos expansion of the solution in terms of the random input data, and on determining the coefficients of this spectral using a Galerkin procedure. The computational uncertainty propagation scheme is constructed by combining the uncertainty representation scheme with a projection method for an incompressible Newtonian fluid. It is shown that this construction results in a coupled system of advection–diffusion equations for the stochastic velocity coefficients, and in a decoupled system of projection steps for the corresponding pressure fields.

Implementation of the stochastic solver is illustrated based on simulations of steady and transient flow in a microchannel at low to moderate Reynolds numbers. Attention is focused on the simplified situation where the uncertain data can be represented as a random variable, and the resulting stochastic scheme is applied to analyze uncertainty in transport properties and boundary conditions. The simulations highlight the efficiency of the stochastic solver, which benefits from the fast convergence of the spectral representation. In particular, for all cases analyzed, it is found that only a small number of terms in the spectral expansion are needed to ensure an accurate representation. The efficiency of the computational scheme also stems from the decoupled structure of the discrete projection steps, which enables us to determine the stochastic solution at the cost of a few deterministic calculations.

As mentioned earlier, the present analysis has been restricted to the case of a single random variable and to incompressible flow of a nonreacting fluid. It should be noted that the first restriction can be immediately relaxed within the present uncertainty representation

framework which has been applied in a variety of more elaborate situations involving random processes, correlated random inputs, and stochastic data with non-Gaussian statistics [23, 24]. It is also appears that the incompressible and nonreacting flow assumptions can also be relaxed, in particular by relying on low-Mach-number reacting flow models (e.g., [18, 19]). Extension of the current scheme along these directions is the focus of ongoing efforts.

APPENDIX

The first five polynomials Ψ_j and their corresponding variance $\langle \Psi_j^2 \rangle$ are provided in the following table:

Order j	Polynomial $\Psi_j(\xi)$	$\langle \Psi_j^2 \rangle$
$j = 0$	$\Psi_0(\xi) = 1$	$\langle \Psi_0^2 \rangle = 1$
$j = 1$	$\Psi_1(\xi) = \xi$	$\langle \Psi_1^2 \rangle = 1$
$j = 2$	$\Psi_2(\xi) = \xi^2 - 1$	$\langle \Psi_2^2 \rangle = 2$
$j = 3$	$\Psi_3(\xi) = \xi^3 - 3\xi$	$\langle \Psi_3^2 \rangle = 6$
$j = 4$	$\Psi_4(\xi) = \xi^4 - 6\xi^2 + 3$	$\langle \Psi_4^2 \rangle = 24$

The expectation is defined with respect to the Gaussian measure:

$$\langle f \rangle = \frac{1}{\sqrt{2\pi}} \int_{-\infty}^{\infty} f(\xi) \exp\left(-\frac{\xi^2}{2}\right) d\xi.$$

The polynomials satisfy the orthogonality condition $\langle \Psi_i \Psi_j \rangle = 0$ for $i \neq j$. Expectations of the form $\langle \Psi_i \Psi_j \Psi_k \rangle$ arise in the governing equations. Numerical values for $i, j, k \leq 4$ are given in the following table:

Expectation of $\Psi_i \Psi_j \Psi_k$	value
$\langle \Psi_0 \Psi_0 \Psi_0 \rangle$	1
$\langle \Psi_0 \Psi_1 \Psi_1 \rangle$	1
$\langle \Psi_0 \Psi_2 \Psi_2 \rangle$	2
$\langle \Psi_0 \Psi_3 \Psi_3 \rangle$	6
$\langle \Psi_0 \Psi_4 \Psi_4 \rangle$	24
$\langle \Psi_1 \Psi_1 \Psi_2 \rangle$	2
$\langle \Psi_1 \Psi_2 \Psi_3 \rangle$	6
$\langle \Psi_1 \Psi_3 \Psi_4 \rangle$	24
$\langle \Psi_2 \Psi_2 \Psi_2 \rangle$	8
$\langle \Psi_2 \Psi_2 \Psi_4 \rangle$	24
$\langle \Psi_2 \Psi_3 \Psi_3 \rangle$	36
$\langle \Psi_2 \Psi_4 \Psi_4 \rangle$	192
$\langle \Psi_3 \Psi_3 \Psi_4 \rangle$	216
$\langle \Psi_4 \Psi_4 \Psi_4 \rangle$	1728

Other expectations can be deduced from permutation of indices,

$$\langle \Psi_i \Psi_j \Psi_k \rangle = \langle \Psi_i \Psi_k \Psi_j \rangle = \langle \Psi_j \Psi_i \Psi_k \rangle = \langle \Psi_j \Psi_k \Psi_i \rangle = \langle \Psi_k \Psi_i \Psi_j \rangle = \langle \Psi_k \Psi_j \Psi_i \rangle,$$

and values that are not reported in the table are null.

For a viscosity law of the form

$$\frac{\nu(\xi)}{\nu_0} = 1 + \beta_1 \xi + \beta_2 \xi^2,$$

the first three terms of the polynomial chaos expansion of the incompressible momentum and continuity equations are given by:

$$\begin{aligned} \text{Mode 0:} & \begin{cases} \frac{\partial \mathbf{u}_0}{\partial r} + (\mathbf{u}_0 \cdot \nabla) \mathbf{u}_0 + \nabla p_0 - \nu_0(1 + \beta_2) \nabla^2 \mathbf{u}_0 \\ = -(\mathbf{u}_1 \cdot \nabla) \mathbf{u}_1 - 2(\mathbf{u}_2 \cdot \nabla) \mathbf{u}_2 + \nu_0 \beta_1 \nabla^2 \mathbf{u}_1 + 2\nu_0 \beta_2 \nabla^2 \mathbf{u}_2 \quad \nabla \cdot \mathbf{u}_0 = 0 \end{cases} \\ \text{Mode 1:} & \begin{cases} \frac{\partial \mathbf{u}_1}{\partial r} + (\mathbf{u}_1 \cdot \nabla) \mathbf{u}_0 + (\mathbf{u}_0 \cdot \nabla) \mathbf{u}_1 + 2[(\mathbf{u}_1 \cdot \nabla) \mathbf{u}_2 + (\mathbf{u}_2 \cdot \nabla) \mathbf{u}_1] \\ = -\nabla p_1 + \nu_0(1 + 3\beta_2) \nabla^2 \mathbf{u}_1 + \nu_0 \beta_1 \nabla^2 \mathbf{u}_0 + 2\nu_0 \beta_1 \nabla^2 \mathbf{u}_2 \quad \nabla \cdot \mathbf{u}_1 = 0 \end{cases} \\ \text{Mode 2:} & \begin{cases} \frac{\partial \mathbf{u}_2}{\partial r} + (\mathbf{u}_2 \cdot \nabla) \mathbf{u}_0 + (\mathbf{u}_0 \cdot \nabla) \mathbf{u}_2 + (\mathbf{u}_1 \cdot \nabla) \mathbf{u}_1 + \nabla p_2 \\ = \nu_0(1 + \beta_2) \nabla^2 \mathbf{u}_2 + \nu_0 \beta_1 \nabla^2 \mathbf{u}_1 + \nu_0 \beta_2 \nabla^2 \mathbf{u}_0 \quad \nabla \cdot \mathbf{u}_2 = 0. \end{cases} \end{aligned}$$

The above expansion is truncated at $P = 2$.

ACKNOWLEDGMENTS

This effort was sponsored by the Defense Advanced Research Projects Agency (DARPA) and Air Force Research Laboratory, Air Force Materiel Command, USAF, under Agreement F30602-00-2-0612. The U.S. government is authorized to reproduce and distribute reprints for governmental purposes notwithstanding any copyright annotation thereon. Computations were performed at the National Center for Supercomputer Applications.

REFERENCES

1. J. M. Hammersley and D. C. Handscomb, *Monte Carlo Methods* (Methuen, London, 1964).
2. S. Ross, *Simulation* (Academic Press, San Diego, 1997).
3. R. G. Ghanem and P. D. Spanos, *Stochastic Finite Elements: A Spectral Approach* (Springer-Verlag, Berlin/New York, 1991).
4. S. Wiener, The homogeneous chaos, *Am. J. Math.* **60**, 897 (1938).
5. R. H. Cameron and W. T. Martin, The orthogonal development of nonlinear functionals in series of Fourier-Hermite functionals, *Ann. Math.* **48**, 385 (1947).
6. R. G. Ghanem and P. D. Spanos, A spectral stochastic finite element formulation for reliability analysis, *J. Eng. Mech. ASCE* **117**, 2351 (1991).
7. R. Ghanem, Probabilistic characterization of transport in heterogeneous porous media, *Comp. Meth. Appl. Mech. Eng.* **158**, 199 (1998).
8. R. Ghanem and S. Dham, Stochastic finite element analysis for multiphase flow in heterogeneous porous media, *Transp. Porous Media* **32**, 239 (1998).

9. B. D. Phenix, J. L. Dinaro, M. A. Tatang, J. W. Tester, J. B. Howard, and G. J. McRae, Incorporation of parametric uncertainty into complex kinetic mechanisms: Application to hydrogen oxidation in supercritical water, *Combust Flame* **112**, 132 (1998).
10. A. J. Chorin, Hermite expansions in Monte-Carlo computation, *J. Comput. Phys.* **8**, 472 (1971).
11. F. H. Maltz and D. L. Hitzl, Variance reduction in Monte Carlo computations using multi-dimensional Hermite polynomials, *J. Comput. Phys.* **32**, 345 (1979).
12. D. L. Hitzl and F. H. Maltz, Adaptive estimation procedures for multi-parameter Monte Carlo computations, *J. Comput. Phys.* **37**, 218 (1980).
13. W. C. Meecham and D. T. Jeng, Use of the Wiener-Hermite expansion for nearly normal turbulence, *J. Fluid Mech.* **32**, 225 (1968).
14. S. C. Crow and G. H. Canavan, Relationship between a Wiener-Hermite expansion and an energy cascade, *J. Fluid Mech.* **41**, 387 (1970).
15. A. J. Chorin, Gaussian fields and random flow, *J. Fluid Mech.* **63**, 21 (1974).
16. M. Loève, *Probability Theory* (Springer-Verlag, Berlin/New York, 1977).
17. A. J. Chorin, A numerical method for solving incompressible viscous flow problems, *J. Comput. Phys.* **2**, 12 (1967).
18. H. N. Najm, P. S. Wyckoff, and O. M. Knio, A semi-implicit numerical scheme for reacting flow. I. Stiff chemistry, *J. Comput. Phys.* **143**, 381 (1998).
19. O. M. Knio, H. N. Najm, and P. S. Wyckoff, A semi-implicit numerical scheme for reacting flow. II. Stiff, operator-split formulation, *J. Comput. Phys.* **154**, 428 (1999).
20. J. Kim and P. Moin, Application of a fractional-step method to incompressible Navier-Stokes equations, *J. Comput. Phys.* **59**, 308 (1985).
21. G. K. Batchelor, *An Introduction to Fluid Dynamics* (Cambridge Univ. Press, Cambridge, UK, 1985).
22. R. L. Panton, *Incompressible Flow* (Wiley, New York, 1984).
23. R. Ghanem, The nonlinear gaussian spectrum of lognormal stochastic processes and variables, *ASME J. Appl. Mech.* **66**, 964 (1999).
24. R. Ghanem, Ingredients for a general purpose stochastic finite elements formulation, *Comput. Meth. Appl. Mech. Eng.* **168**, 19 (1999).

A Stochastic Projection Method for Fluid Flow

II. Random Process

Olivier P. Le Maître,^{*} Matthew T. Reagan,[†] Habib N. Najm,[‡]
Roger G. Ghanem,[‡] and Omar M. Knio^{§,1}

^{*}*Centre d'Etudes de Mécanique d'Ile de France, Université d'Evry Val d'Essone, 40 rue du Pelvoux, 91020 Evry cedex, France;* [†]*Combustion Research Facility, Sandia National Laboratories, Livermore, California 94550;* [‡]*Department of Civil Engineering, The Johns Hopkins University, Baltimore, Maryland 21218-2686; and* [§]*Department of Mechanical Engineering, The Johns Hopkins University, Baltimore, Maryland 21218-2686*
E-mail: olm@iup.univ-evry.fr, mtreaga@ca.sandia.gov, hnnajm@ca.sandia.gov, ghanem@jhu.edu, and knio@jhu.edu

Received October 1, 2001; revised May 1, 2002

An uncertainty quantification scheme is developed for the simulation of stochastic thermofluid processes. The scheme relies on spectral representation of uncertainty using the polynomial chaos (PC) system. The solver combines a Galerkin procedure for the determination of PC coefficients with a projection method for efficiently simulating the resulting system of coupled transport equations. Implementation of the numerical scheme is illustrated through simulations of natural convection in a 2D square cavity with stochastic temperature distribution at the cold wall. The properties of the uncertainty representation scheme are analyzed, and the predictions are contrasted with results obtained using a Monte Carlo approach. © 2002 Elsevier Science (USA)

Key Words: stochastic; natural convection; Navier-Stokes; polynomial chaos; Karhunen–Loève; uncertainty.

1. INTRODUCTION

Uncertainty propagation and quantification can be an essential step in the development of complex models, in particular when these models involve inexact knowledge of system forcing or system parameters. This article is part of an effort that aims at developing uncertainty quantification schemes for fluid systems involving transport and chemistry.

As an initial step toward these objectives, a stochastic projection method (SPM) was developed in a previous work [1]. In [1] attention was focused on an incompressible flow model,

¹ Corresponding author.

where uncertain model data are generated by a single random variable. SPM combines a projection method for fluid flow with a spectral representation of the effect of uncertainty in terms of the polynomial chaos (PC) system [2–9]. The objectives of the present effort are twofold: (1) to extend the capabilities of SPM to situations involving random processes, and (2) to generalize the underlying formulation so as to account for weak compressibility effects. To illustrate the development, we focus on natural convection in an enclosed cavity. This topic has received considerable attention in the recent literature and various approaches have been proposed, including models based on the well-known Boussinesq approximation (e.g., [10–12]) as well as low-Mach-number models (e.g., [13, 14]). In addition, simulations of internal natural convection have been used as benchmark tests for different flow regimes [10, 15–27].

In one of its simplest forms, the problem consists of a square or rectangular cavity with adiabatic horizontal boundaries and differentially but uniformly heated vertical walls. In practice, however, this idealized situation may be difficult to achieve, for instance due to imperfections in insulation and/or nonuniform heating and cooling. Computed solutions are often very sensitive to applied boundary conditions, which can complicate comparison with experimental measurements [28].

The present effort aims at generalizing the previous construction [1] along two directions, namely, by considering flows with (small) temperature and density gradients and by considering uncertain model data associated with a random process. Motivated in part by the aforementioned observations, we focus on the idealized case of natural convection in a square cavity under stochastic boundary conditions. As outlined in Section 2, we restrict the study to natural convection in the Boussinesq limit. A stochastic formulation is then introduced in Section 3 which consists of treating the hot wall as having a uniform temperature and imposing a stochastic temperature distribution on the cold vertical boundary. The latter is treated as a Gaussian process characterized by its variance and correlation length. The Karhunen–Loève expansion [29] is then applied to construct an efficient representation of this process and to generalize the PC representation used in the previous version of SPM [1]. A brief validation study of the deterministic prediction is first performed in Section 5 and is used to select an appropriate grid resolution level. The convergence properties of the spectral stochastic scheme are then analyzed in Section 6, and the properties of the computed velocity and temperature modes are examined in Section 7. To verify the spectral computations, a nonintrusive spectral projection (NISP) approach is introduced and applied in Section 8. The essential idea in NISP is to use deterministic predictions to determine the stochastic response of the system. Two variants are considered, one based on high-order Gauss–Hermite (GH) quadrature [30, 31] and the other on Latin hypercube sampling (LHS) strategy [32]. The predictions of both sampling schemes are contrasted with the spectral computations and are used to further examine its properties. In Section 9, a quantitative analysis of the effects of the imposed stochastic temperature profile is provided. Major conclusions are summarized in Section 10.

2. DETERMINISTIC FORMULATION

We consider a square 2D cavity, of side L_e , filled with a Newtonian fluid of density ρ , molecular viscosity μ , and thermal conductivity κ . The coordinate system is chosen so that y is the vertical direction, pointing upward, and the x axis is horizontal. The two horizontal walls are assumed to be adiabatic. The left vertical wall is maintained at uniform

temperature T_h , and the right vertical wall is maintained at T_c . We assume that $T_h > T_c$, so that the left vertical wall (located at $x = 0$) is referred to as the hot wall, while the right vertical wall is the cold wall.

In the Boussinesq limit, $2(T_h - T_c)/(T_h + T_c) \ll 1$, the normalized governing equations are expressed as [12]

$$\frac{\partial \mathbf{u}}{\partial t} + \mathbf{u} \cdot \nabla \mathbf{u} = -\nabla p + \frac{Pr}{\sqrt{Ra}} \nabla^2 \mathbf{u} + Pr \theta \mathbf{e}_y, \quad (1)$$

$$\nabla \cdot \mathbf{u} = 0, \quad (2)$$

$$\frac{\partial \theta}{\partial t} + \nabla \cdot (\mathbf{u} \theta) = \frac{1}{\sqrt{Ra}} \nabla^2 \theta, \quad (3)$$

where \mathbf{u} is the velocity, t is time, p is pressure, \mathbf{e}_y is the unit vector in the vertical y direction, and $\theta \equiv (T - T_{\text{ref}})/\Delta T_{\text{ref}}$ is the normalized temperature. The reference temperature $T_{\text{ref}} \equiv (T_h + T_c)/2$ and the reference temperature difference $\Delta T_{\text{ref}} \equiv T_h - T_c$. Unless otherwise noted, variables are normalized with respect to the appropriate combination of reference length L_e , velocity V , time $\tau \equiv L_e/V$, and pressure $P = \rho V^2$. The normalization leads to the usual definitions of Prandtl and Rayleigh numbers, respectively $Pr = \mu c_p/\kappa$ and $Ra = \rho g \beta \Delta T_{\text{ref}} L_e^3/(\mu \kappa)$, where β is the coefficient of thermal expansion and g is gravitational acceleration. In all cases, the deterministic system is integrated from an initial state of rest using $Pr = 0.71$ and $Ra = 10^6$. For this choice of physical parameters, a steady, laminar recirculating flow regime occurs [12].

3. STOCHASTIC FORMULATION

We consider the effect of “random” fluctuations on the cold wall. The normalized mean wall temperature at $x = 1$ is expressed as

$$\theta_1(y) \equiv \theta(x = 1, y) = \theta_c + \theta'(y) = -\frac{1}{2} + \theta'(y). \quad (4)$$

Using angle brackets to denote expectations, we have $\langle \theta_1 \rangle = \theta_c$; i.e., θ' has vanishing expectation and the mean (dimensional) temperature along the cold wall is independent of y and equals T_c .

The random component is assumed to be given by a Gaussian process which is characterized by its variance σ_θ^2 and an autocorrelation function \mathcal{K} given by

$$\mathcal{K}(y_1, y_2) \equiv \mathcal{K}(|y_1 - y_2|) \equiv \langle \theta'(y_1) \theta'(y_2) \rangle = \sigma_\theta^2 \exp[-|y_1 - y_2|/L_c], \quad (5)$$

where L_c is the normalized correlation length. \mathcal{K} can be expanded in terms of its eigenvalues, λ_i , and eigenfunctions, $f_i(y)$, using [9, 33, 34]

$$\mathcal{K}(y_1, y_2) = \sum_{i=0}^{\infty} \lambda_i f_i(y_1) f_i(y_2), \quad (6)$$

and θ' can be accordingly expressed in the usual Karhunen–Loève (KL) expansion as [29]

$$\theta'(y) = \sum_{i=0}^{\infty} \sqrt{\lambda_i} f_i(y) \xi_i, \quad (7)$$

where the ξ_i 's are uncorrelated Gaussian variables having vanishing expectation and unit variance.

The eigenvalues and eigenfunctions of \mathcal{K} are solutions of the corresponding integral operator [9, 33, 34],

$$\int_0^1 \mathcal{K}(y_1, y_2) f(y_2) dy_2 = \lambda f(y_1). \quad (8)$$

This Fredholm equation can be solved numerically, but an analytical solution for the kernel in Eq. (5) is available [9] and is given by

$$f_n(y) = \begin{cases} \frac{\cos[\omega_n(y - 1/2)]}{\sqrt{\frac{1}{2} + \frac{\sin(\omega_n)}{2\omega_n}}} & \text{if } n \text{ is even,} \\ \frac{\sin[\omega_n(y - 1/2)]}{\sqrt{\frac{1}{2} - \frac{\sin(\omega_n)}{2\omega_n}}} & \text{if } n \text{ is odd,} \end{cases} \quad (9)$$

where

$$\lambda_n = \sigma_\theta^2 \frac{2L_c}{1 + (\omega_n L_c)^2}, \quad (10)$$

and ω_n are the positive (ordered) roots of the characteristic equation

$$[1 - L_c \omega \tan(\omega/2)][L_c \omega + \tan(\omega/2)] = 0. \quad (11)$$

Since the first positive root of Eq. (11) is $\omega_0 = 0$, corresponding to $f_0 = 0$, Eq. (7) may be rewritten as

$$\theta'(y) = \sum_{i=1}^{\infty} \xi_i \sqrt{\lambda_i} f_i(y). \quad (12)$$

Figure 1 depicts the first 10 eigenvalues and eigenfunctions for a process with $L_c = 1$. Note that as the index increases, the eigenfunctions exhibit higher frequencies while the corresponding eigenvalues decrease. As discussed in [9] the decay rate of the spectrum increases with decreasing L_c .

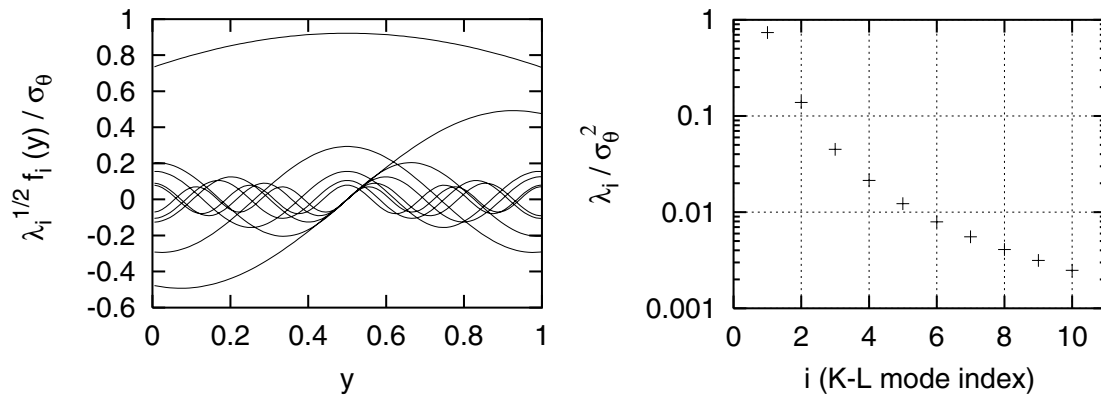


FIG. 1. Karhunen-Loève expansion for the temperature fluctuation $\theta'(y)$ corresponding to an exponential correlation function with characteristic length $L_c = 1$. In the left plot, the first ten mode shapes ($\sqrt{\lambda_i} f_i(y)$) are reported. The right plot shows the eigenvalues λ_i . The quantities have been respectively normalized using σ_θ and σ_θ^2 .

TABLE I
 E_σ^2 and E_σ^∞ for Various Values of N_{KL} for $L_c = 1/2, 1$, and 2

	N_{KL}				
	4	6	10	20	40
$E_\sigma^2(N_{\text{KL}}) - L_c = 1/2$	0.5882E-1	0.3751E-1	0.2161E-1	0.1045E-1	0.5129E-2
$E_\sigma^2(N_{\text{KL}}) - L_c = 1$	0.2947E-1	0.1871E-1	0.1077E-1	0.5213E-2	0.2562E-2
$E_\sigma^2(N_{\text{KL}}) - L_c = 2$	0.1473E-1	0.9337E-2	0.5376E-2	0.2604E-2	0.1280E-2
$E_\sigma^\infty(N_{\text{KL}}) - L_c = 1/2$	0.1076E-0	0.6592E-1	0.3453E-1	0.1300E-1	0.5590E-2
$E_\sigma^\infty(N_{\text{KL}}) - L_c = 1$	0.5346E-1	0.3255E-1	0.1704E-1	0.6429E-2	0.2792E-2
$E_\sigma^\infty(N_{\text{KL}}) - L_c = 2$	0.2657E-1	0.1615E-1	0.8456E-2	0.3197E-2	0.1395E-2

In numerical implementations, the KL expansion [Eq. (12)] is truncated, and the temperature “fluctuation” is approximated as

$$\theta' = \sum_{i=1}^{N_{\text{KL}}} \xi_i \sqrt{\lambda_i} f_i(y), \quad (13)$$

where N_{KL} is the number of modes retained in the computations. The error introduced by this truncation is quantified in terms of the L_p norms:

$$E_{\mathcal{K}}^p(N_{\text{KL}}) = \left[\int_0^1 \int_0^1 \left| \mathcal{K}(y_1, y_2) - \sum_{i=1}^{N_{\text{KL}}} \lambda_i f_i(y_1) f_i(y_2) \right|^p dy_1 dy_2 \right]^{1/p}, \quad (14)$$

$$E_\sigma^p(N_{\text{KL}}) = \left[\int_0^1 \left| \sigma_\theta - \sqrt{\sum_{i=1}^{N_{\text{KL}}} \lambda_i f_i^2(y)} \right|^p dy \right]^{1/p}. \quad (15)$$

Table I reports E_σ^2 and E_σ^∞ for different values of N_{KL} and for $L_c = 1/2, 1$, and 2 ; Table II provides the corresponding values of $E_{\mathcal{K}}^2$ and $E_{\mathcal{K}}^\infty$. The results indicate that at fixed N_{KL} the “truncation” errors scale approximately as $1/L_c$. At fixed correlation length, E_σ^2 and $E_{\mathcal{K}}^2$ decrease as N_{KL}^1 , while E_σ^∞ and $E_{\mathcal{K}}^2$ exhibit faster decay rates. The effect of truncation of \mathcal{K} is further illustrated in Fig. 2, which depicts the truncated correlation function and its deviation from the exact solution for $L_c = 1$. The results indicate that the truncation error is mainly concentrated in a thin band around the axis $y_1 = y_2$ and that it exhibits rapid

TABLE II
 $E_{\mathcal{K}}^2$ and $E_{\mathcal{K}}^\infty$ for Various Values of N_{KL} for $L_c = 1/2, 1$, and 2

	N_{KL}				
	4	6	10	20	40
$E_{\mathcal{K}}^2(N_{\text{KL}}) - L_c = 1/2$	0.3366E-1	0.1791E-1	0.8176E-2	0.2988E-2	0.1249E-2
$E_{\mathcal{K}}^2(N_{\text{KL}}) - L_c = 1$	0.1736E-1	0.9076E-2	0.4107E-2	0.1496E-2	0.6247E-3
$E_{\mathcal{K}}^2(N_{\text{KL}}) - L_c = 2$	0.8789E-2	0.4562E-2	0.2057E-2	0.7882E-3	0.3124E-3
$E_{\mathcal{K}}^\infty(N_{\text{KL}}) - L_c = 1/2$	0.2188E-0	0.1439E-0	0.8462E-1	0.4149E-1	0.2051E-1
$E_{\mathcal{K}}^\infty(N_{\text{KL}}) - L_c = 1$	0.1127E-0	0.7285E-1	0.4250E-1	0.2076E-1	0.1026E-1
$E_{\mathcal{K}}^\infty(N_{\text{KL}}) - L_c = 2$	0.5699E-1	0.3660E-1	0.2128E-1	0.1039E-1	0.5130E-2

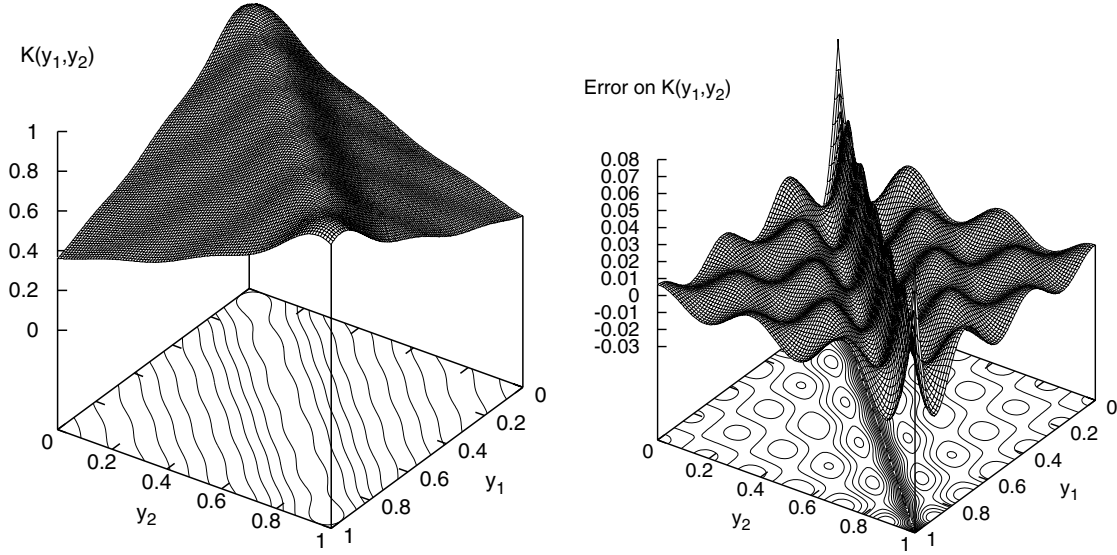


FIG. 2. Truncated correlation function $\mathcal{K}(y_1, y_2)$ (left) and its deviation from the exact value (right). An exponential autocorrelation function is used with $L_c = 1$. The truncation is at $N_{\text{KL}} = 6$.

oscillatory decay as one moves away from the axis. It thus appears that the truncation, which removes the highest frequency modes, primarily affects the short-scale correlations. The truncated modes are expected to have a weak influence on the solution and this is in fact reflected in the analysis that follows, which indicates that a modest number of KL modes is generally sufficient.

4. SPECTRAL STOCHASTIC REPRESENTATION

As in [1], the dependence of the solution on the uncertain model data is represented in terms of the PC system. We illustrate this representation for generic field variable, $\Phi(\mathbf{x}, t, \boldsymbol{\xi})$, where $\boldsymbol{\xi} = \xi_1, \dots, \xi_{N_{\text{KL}}}$. Φ is decomposed according to

$$\Phi(\mathbf{x}, t, \boldsymbol{\xi}) = \sum_{i=0}^P \Phi_i(\mathbf{x}, t) \Psi_i(\boldsymbol{\xi}), \quad (16)$$

where Φ_i are (yet to be determined) deterministic “coefficients,” Ψ_i denote the polynomial chaos [2, 3, 29], while $P + 1$ is the total number of modes used in the spectral expansion. Note that the Ψ_i are multidimensional orthogonal polynomials of the uncorrelated Gaussians, and that for $i = 1, \dots, N_{\text{KL}}$, $\Psi_i(\boldsymbol{\xi}) = \xi_i$; i.e., these N_{KL} polynomials are linear in the ξ_i . General expressions for Ψ_i , including higher order terms, can be found in [9].

We rely on Eq. (16) to form representations of the stochastic velocity, pressure, and temperature distributions. Governing equations for the unknown expansion coefficients are obtained by inserting the expansion into the governing equations and using a Galerkin approach that takes advantage of the orthogonality of the polynomial chaoses [1, 9]. This results in the coupled system

$$\frac{\partial \mathbf{u}_k}{\partial t} + (\mathbf{u} \cdot \nabla \mathbf{u})_k = -\nabla p_k + \frac{Pr}{\sqrt{Ra}} \nabla^2 \mathbf{u}_k + Pr \theta_k \mathbf{e}_y, \quad (17)$$

$$\nabla \cdot \mathbf{u}_k = 0, \quad (18)$$

$$\frac{\partial \theta_k}{\partial t} + \nabla \cdot (\mathbf{u} \theta)_k = \frac{1}{\sqrt{Ra}} \nabla^2 \theta_k, \quad (19)$$

for $k = 0, \dots, P$. Here, $\mathbf{u}_k(\mathbf{x}, t)$, $p_k(\mathbf{x}, t)$, and $\theta_k(\mathbf{x}, t)$ are the coefficients in the PC expansion of the normalized velocity, pressure, and temperature fields, respectively. The quadratic velocity–velocity and velocity–temperature products are given by

$$(\mathbf{u} \cdot \nabla \mathbf{u})_k = \sum_{i=0}^P \sum_{j=0}^P C_{ijk} \mathbf{u}_i \nabla \mathbf{u}_j \quad (20)$$

and

$$(\mathbf{u}\theta)_k = \sum_{i=0}^P \sum_{j=0}^P C_{ijk} \mathbf{u}_i \theta_j, \quad (21)$$

where

$$C_{ijk} \equiv \frac{\langle \Psi_i \Psi_j \Psi_k \rangle}{\langle \Psi_k^2 \rangle}. \quad (22)$$

Note that although $C_{ijk} = 0$ for $1 \leq i, j, k \leq N_{\text{KL}}$, it is generally nonvanishing, so that the Galerkin procedure results in a coupled system for the velocity and temperature modes. Note, however, that the velocity divergence constraints are decoupled, which enables us to adapt the SPM developed in [1]. This approach is outlined in the following sections.

4.1. Boundary Conditions

Following [1], boundary conditions are treated in a “weak sense”; i.e., the Galerkin approach is also applied at the boundaries. In particular, the PC decomposition is also introduced into the corresponding expressions, and orthogonal projections are used to derive boundary conditions for the velocity and temperature modes. For the setup outlined in Section 3, we obtain

$$\mathbf{u}_k = 0, \quad k = 0, \dots, P \quad \forall \mathbf{x} \in \partial\Omega, \quad (23)$$

$$\frac{\partial \theta_k}{\partial y} = 0, \quad k = 0, \dots, P \quad \text{for } y = 0 \text{ and } y = 1, \quad (24)$$

$$\theta_0(x = 0, y) = \frac{1}{2}, \quad \theta_0(x = 1, y) = -\frac{1}{2}, \quad (25)$$

$$\theta_k(x = 0, y) = 0, \quad \theta_k(x = 1, y) = \sqrt{\lambda_k} f_k(y) \quad \text{for } k = 1, \dots, N_{\text{KL}}, \quad (26)$$

$$\theta_k(x = 0, y) = \theta_k(x = 1, y) = 0 \quad \text{for } k > N_{\text{KL}}. \quad (27)$$

Here $\Omega = [0, 1] \times [0, 1]$ denotes the computational domain, and $\partial\Omega$ is its boundary.

4.2. Solution Method

As mentioned earlier, the solution scheme is an adapted version of the SPM introduced in [1]. Numerical integration of the governing equations of the stochastic mode follows an explicit fractional step procedure that is based on first advancing the velocity and temperature modes using

$$\tilde{\mathbf{u}}_k = \frac{4\mathbf{u}_k^n - \mathbf{u}_k^{n-1}}{3} + \frac{2\Delta t}{3} \left[-2(\mathbf{u} \cdot \nabla \mathbf{u})_k^n + (\mathbf{u} \cdot \nabla \mathbf{u})_k^{n-1} + \frac{Pr}{\sqrt{Ra}} \nabla^2 \mathbf{u}_k^n + Pr \theta_k^n \mathbf{e}_y \right], \quad (28)$$

$$\theta_k^{n+1} = \frac{4\theta_k^n - \theta_k^{n-1}}{3} + \frac{2\Delta t}{3} \left[\nabla \cdot (-2(\mathbf{u}\theta)_k^n + (\mathbf{u}\theta)_k^{n-1}) + \frac{1}{\sqrt{Ra}} \nabla^2 \theta_k^n \right], \quad (29)$$

where superscripts refer to the time level and Δt is the time step. Note that since we are primarily interested in the steady-state solution of this system, we have combined explicit second-order time discretization of the convective terms and with first-order discretization of the buoyancy and viscous terms. As in [1], spatial derivatives are approximated using second-order centered differences. In the second fractional step, the “intermediate” velocity modes $\tilde{\mathbf{u}}_k$ are updated so as to satisfy the divergence constraints [35, 36]; we use

$$\mathbf{u}_k^{n+1} = \tilde{\mathbf{u}}_k - \frac{2\Delta t}{3} \nabla p_k^{n+1}, \quad (30)$$

where p_k are solutions to the Poisson equations

$$\nabla^2 p_k^{n+1} = \frac{3}{2\Delta t} \nabla \cdot \tilde{\mathbf{u}}_k \quad (31)$$

with homogeneous Neumann conditions [35, 36]. Note that these elliptic systems for the various modes are *decoupled*, a key feature in the efficiency of SPM [1].

In the implementations presented in the following, we relied on a conservative second-order finite-difference discretization on a uniform Cartesian mesh with (N_x, N_y) cells in the x and y directions respectively. A direct, Fourier-based, fast Poisson solver is used to invert Eqs. (31). Since these inversions account for the bulk of the CPU times, and since systems for individual modes are decoupled, the computational cost scales essentially as $O(N \log N)$, where $N \equiv N_x \times N_y \times (P + 1)$. This estimate is in fact reflected in the tests that follow.

5. DETERMINISTIC PREDICTION

We start with a brief discussion of deterministic predictions, obtained by setting the order (N_O) of the PC expansion to zero. In this case, the stochastic boundary conditions reduce to those of the classical problem with uniform hot and cold wall temperatures, $\theta_h = 1/2$ and $\theta_c = -1/2$. The resulting predictions are used to validate the computations and to select a

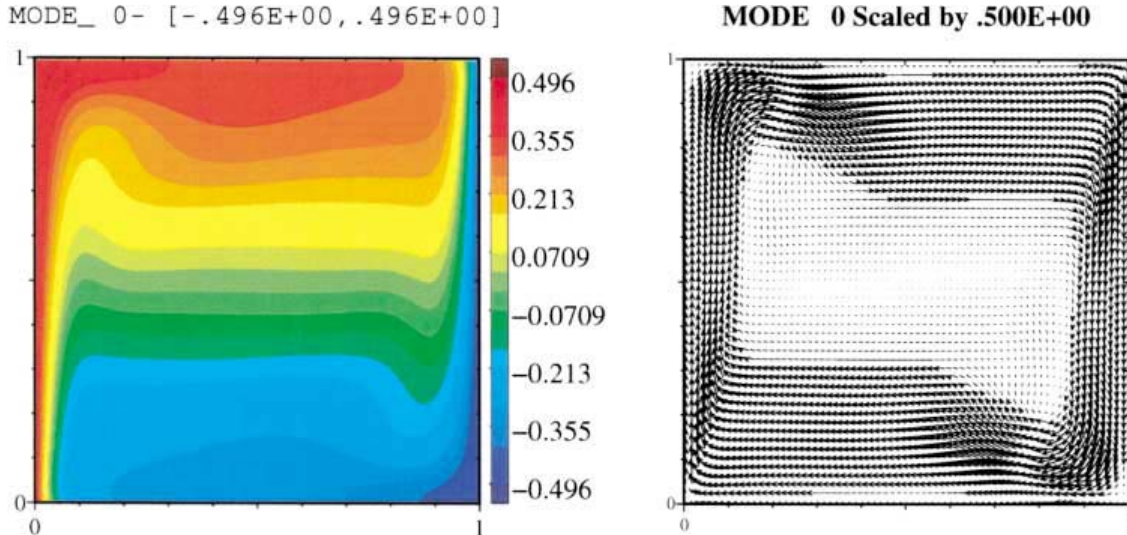


FIG. 3. Scaled temperature field (left) and velocity vectors (right) for the deterministic temperature boundary conditions ($\theta_h = -\theta_c = 1/2$) computed using zero-order spectral expansion ($N_O = 0$).

suitable grid size. To this end, the results are compared with the spectral computations of Le Quéré [12]. For $Ra = 10^6$, Le Quéré found a steady Nusselt number $Nu = 8.8252$, with the Nusselt number defined by

$$Nu \equiv - \int_0^1 \frac{\partial \theta}{\partial x} dy. \quad (32)$$

Following a systematic grid refinement study, we find that a computational grid with $N_x = 140$ and $N_y = 100$ is sufficient for accurate predictions. Starting from an initial state of rest, the computations are carried out until steady conditions are reached. Specifically, the computations are stopped when the maximum change in any field quantity falls below a tolerance $\epsilon = 10^{-10}$. (Double precision arithmetic is used.) For the current grid resolution, the steady Nusselt number is found to be $Nu = 8.8810$, which is within 0.63% of the prediction of Le Quéré. The structure of the steady field, depicted in Fig. 3, reveals thermal boundary layers on the hot and cold walls and a clockwise circulation of the fluid; these predictions are also in good agreement with the results reported in [12].

6. CONVERGENCE ANALYSIS

An analysis of the convergence of the spectral representation scheme is performed in this section. Following the previous discussion, we are presently dealing with a two-parameter discretization that involves the number N_{KL} of Karhunen–Loève modes, as well as the order N_O of the PC expansion. As discussed in [9], the total number P of orthogonal polynomials increases monotonically with N_{KL} and N_O [9].

6.1. Convergence of KL Expansion

In Section 3, we observed that the KL expansion converged rapidly and consequently speculated that truncation of this expansion would have little effect on the predictions. We now examine this expected trend by computing the mean Nusselt number,

$$\overline{Nu} = - \int_0^1 \frac{\partial \theta_0}{\partial x} dy, \quad (33)$$

and its standard deviation,

$$\sigma(Nu) = \left(\sum_{i=1}^P \left\{ \left[- \int_0^1 \frac{\partial \theta_i}{\partial x} dy \right]^2 \langle \Psi_i \Psi_i \rangle \right\} \right)^{1/2}, \quad (34)$$

for N_{KL} ranging from 2 to 10. For brevity, we restrict our attention to a first-order PC expansion, and results are obtained with fixed $L_c = 1$ and $\sigma_\theta = 0.25$.

The average of the local heat flux variance along the wall is given by

$$\overline{\sigma^2(\partial \theta / \partial x)} = \int_0^1 \sum_{i=1}^P \left[\frac{\partial \theta_i}{\partial x} \right]^2 \langle \Psi_i \Psi_i \rangle dy. \quad (35)$$

and should be carefully distinguished from $\sigma^2(Nu)$. At steady state, the net heat flux on the hot wall equals that on the cold wall; since this relationship holds for arbitrary realization,

TABLE III
**Effect of N_{KL} on \overline{Nu} and $\sigma(Nu)$ for $N_O = 1$,
 $L_c = 1$, and $\sigma_\theta = 0.25$**

N_{KL}	\overline{Nu}	$\sigma(Nu)$	P
2	8.96344	2.47009	2
4	8.97114	2.46979	4
6	8.97179	2.46980	6
8	8.97190	2.46980	8
10	8.97192	2.46980	10

$\sigma^2(Nu)$ has the same value on the hot wall as on the cold wall. On the other hand, $\overline{\sigma^2}(\partial\theta/\partial x)$ is expected to assume a higher value on the cold wall, where random fluctuations are imposed, than on the hot wall, since these fluctuations are expected to be smoothed out by diffusion.

Computed values of \overline{Nu} and $\sigma(Nu)$ are reported in Table III. As expected, the results show that for the present conditions \overline{Nu} and $\sigma(Nu)$ converge rapidly with N_{KL} . To further examine the predictions, we plot in Fig. 4 the distribution of the normalized heat flux $-\partial\theta/\partial x$ along the hot and cold walls as a function of P . (Note that for $N_O = 1$, $P = N_{KL}$.) Clearly, on the hot wall, only modes 0 and 1 contribute significantly to the local heat flux; for the higher modes, $\partial\theta_i/\partial x$ is close to zero for all y . This situation contrasts with the distribution of the heat fluxes on the cold wall, where significant heat flux fluctuations are observed for all the PC modes. However, as noted earlier, the net heat fluxes across the hot and cold walls are equal at steady state. Thus, when integrated along the boundary, the significant fluctuations of the higher modes on the cold wall tend to cancel out. This explains the rapid convergence of integral quantities in Table III.

The standard deviation of the local heat flux, shown in Fig. 5, closely reflects these trends. In particular, by comparing points symmetrically across the midplane, the results clearly show that the values on the cold wall are generally larger than those on the hot wall. Also note that the curve for the cold wall exhibits a noticeable waviness that

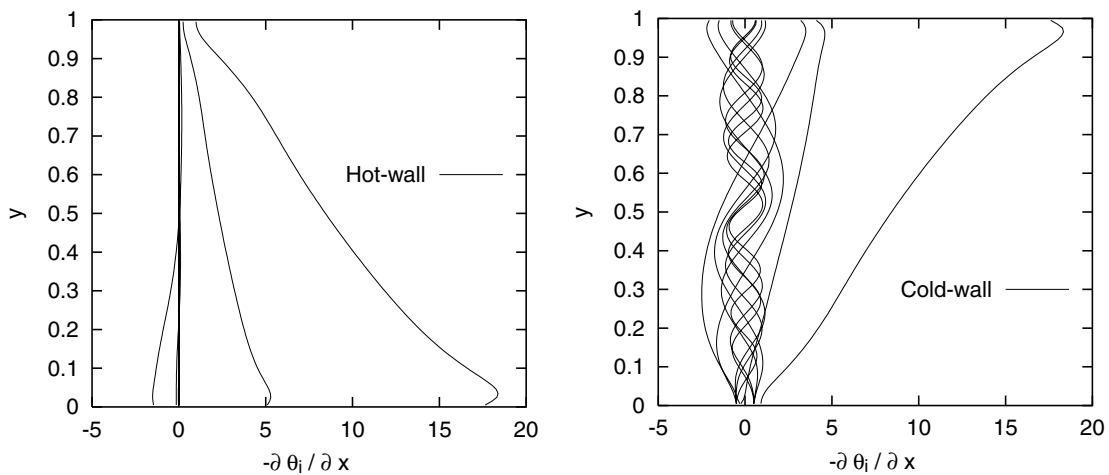


FIG. 4. Local heat fluxes versus y on the hot (left) and cold (right) walls, for modes 0–10. A first-order expansion is used with $N_{KL} = 10$, $L_c = 1$, and $\sigma_\theta = 0.25$.

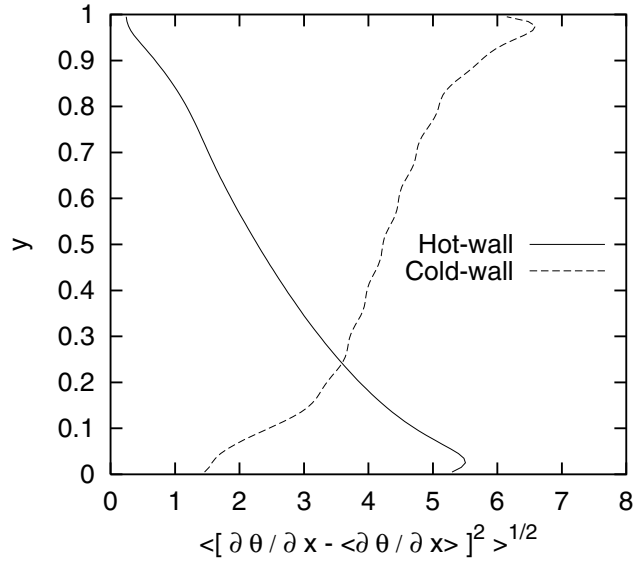


FIG. 5. Standard deviation of the local heat fluxes versus y on the hot and cold walls. A first-order expansion is used with $N_{\text{KL}} = 10$, $L_c = 1$, and $\sigma_\theta = 0.25$.

corresponds to the imposed conditions, whereas the curve for the hot-wall distribution is smooth.

6.2. Convergence of PC Expansion

In this section, we analyze the convergence of the PC expansion by contrasting results obtained with $N_O = 1, 2$, and 3 . Results are obtained with $L_c = 1$ and $\sigma_\theta = 0.25$, using both four and six KL modes.

Wall heat transfer. The computed values of \overline{Nu} and $\sigma(Nu)$ are reported in Table IV, together with the number P of polynomials used. The results exhibit a fast convergence as the order of the PC expansion, N_O , increases. The differences in \overline{Nu} and $\sigma(Nu)$ between second- and third-order solutions are less than 0.01% and 0.05%, respectively. The close quantitative agreement between the results for $N_O = 2$ and 3 indicates that, at least as far as integral quantities are concerned, a second-order expansion is sufficiently accurate. This fast convergence rate is also indicative of the smooth dependence of the solution with respect to the imposed random temperature fluctuations.

Plotted in Fig. 6 are the heat flux distributions along the cold (top row) and hot (bottom row) walls for $N_O = 1, 2$, and 3 . Results are obtained with $N_{\text{KL}} = 4$ and curves are plotted

TABLE IV
Mean Nusselt Number and Its Standard Deviation for First-, Second-, and Third-Order PC Expansion with $N_{\text{KL}} = 4$ and 6 for $L_c = 1$ and $\sigma_\theta = 0.25$

N_O	\overline{Nu}		$\sigma(Nu)$		P	
	$N_{\text{KL}} = 4$	$N_{\text{KL}} = 6$	$N_{\text{KL}} = 4$	$N_{\text{KL}} = 6$	$N_{\text{KL}} = 4$	$N_{\text{KL}} = 6$
1	8.97114	8.97179	2.46979	2.46980	5	7
2	8.97289	8.97352	2.46323	2.46327	15	27
3	8.97337	8.97340	2.46239	2.46245	34	83

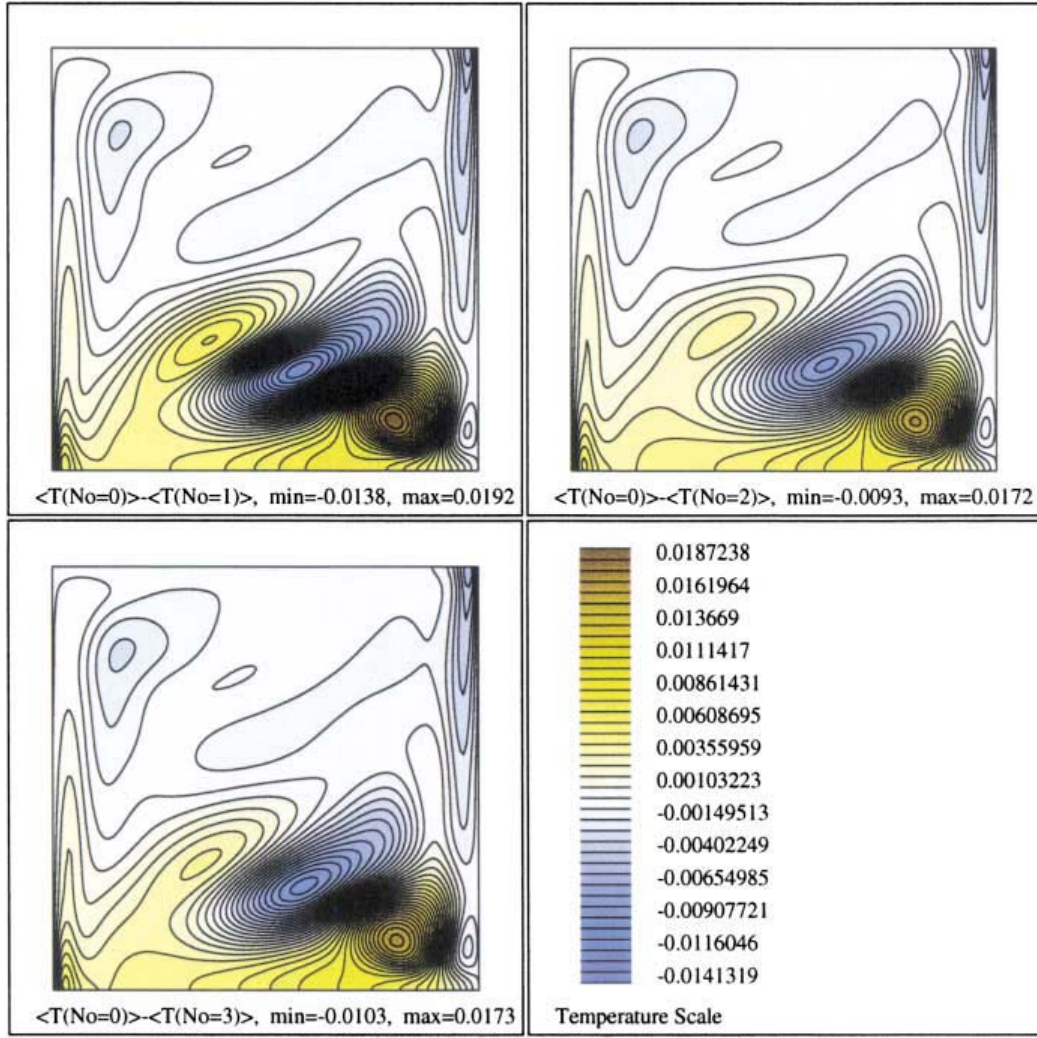


FIG. 8. Contours of $\theta^0 - \langle \theta^{N_O} \rangle$. Plots are generated for $N_O = 1, 2$, and 3 . Results are obtained with $N_{KL} = 4$, $L_c = 1$, and $\sigma_\theta = 0.25$.

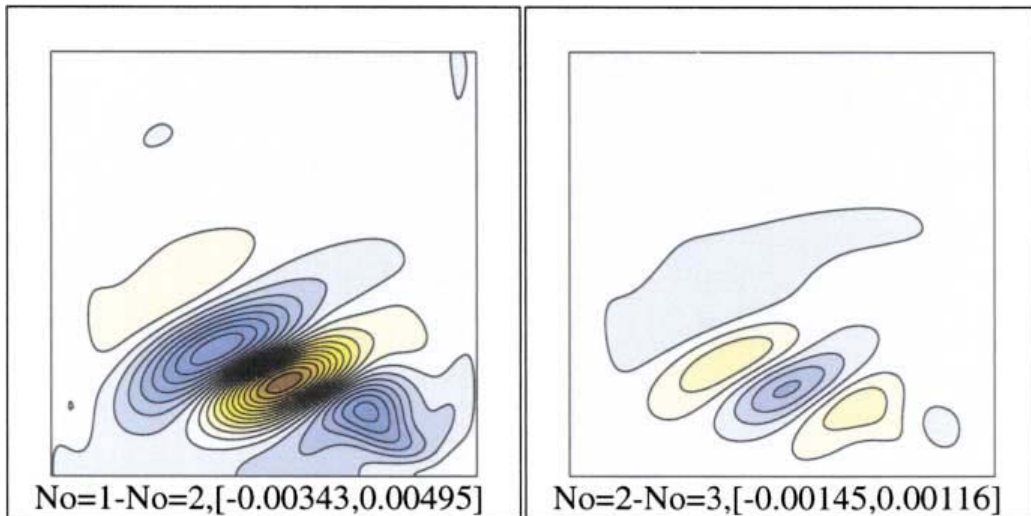


FIG. 9. Contour plots of $\langle \theta^1 \rangle - \langle \theta^2 \rangle$ (left) and $\langle \theta^2 \rangle - \langle \theta^3 \rangle$ (right). Results are obtained with $N_{KL} = 4$, $L_c = 1$, and $\sigma_\theta = 0.25$.

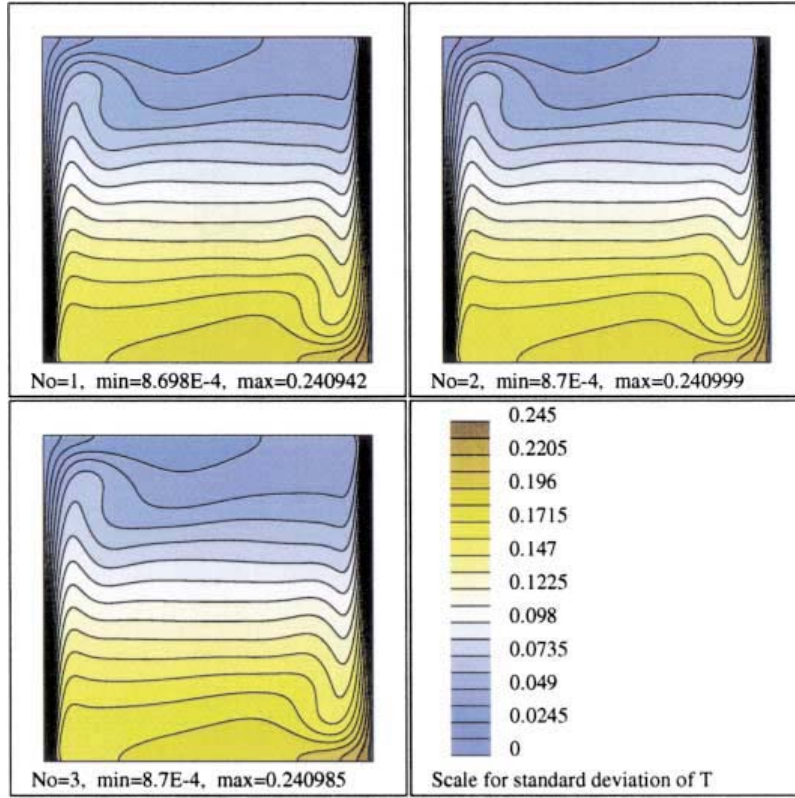


FIG. 10. Contours of standard deviation in temperature for $N_O = 1, 2$, and 3 . Results are obtained with $N_{KL} = 4$, $L_c = 1$, and $\sigma_\theta = 0.25$.

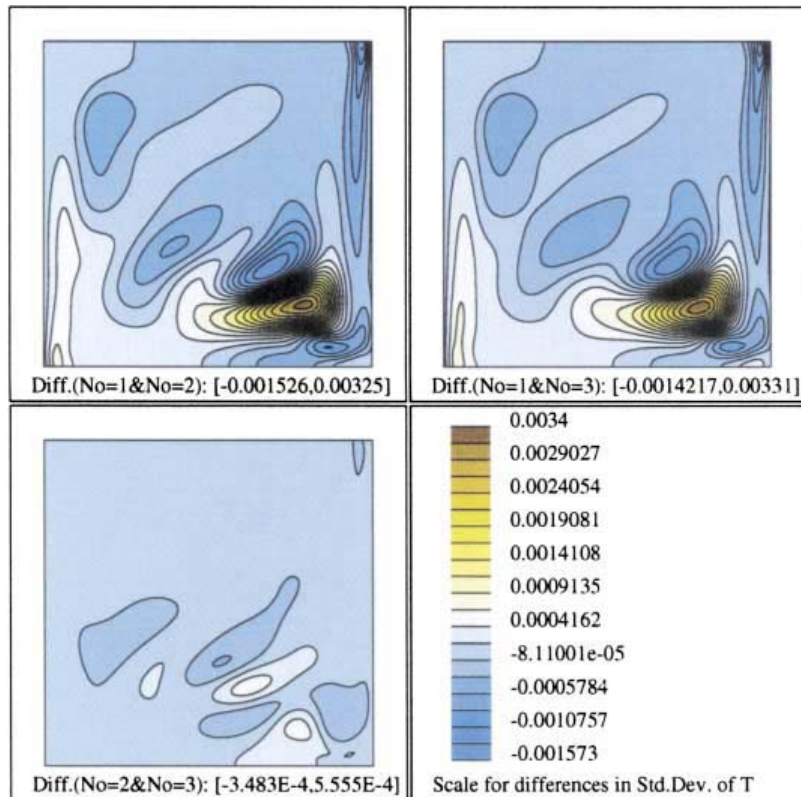


FIG. 11. Differences in the temperature standard deviation computed using $N_O = 1, 2$, and 3 . In all cases, $N_{KL} = 6$, $L_c = 1$, and $\sigma_\theta = 0.25$.

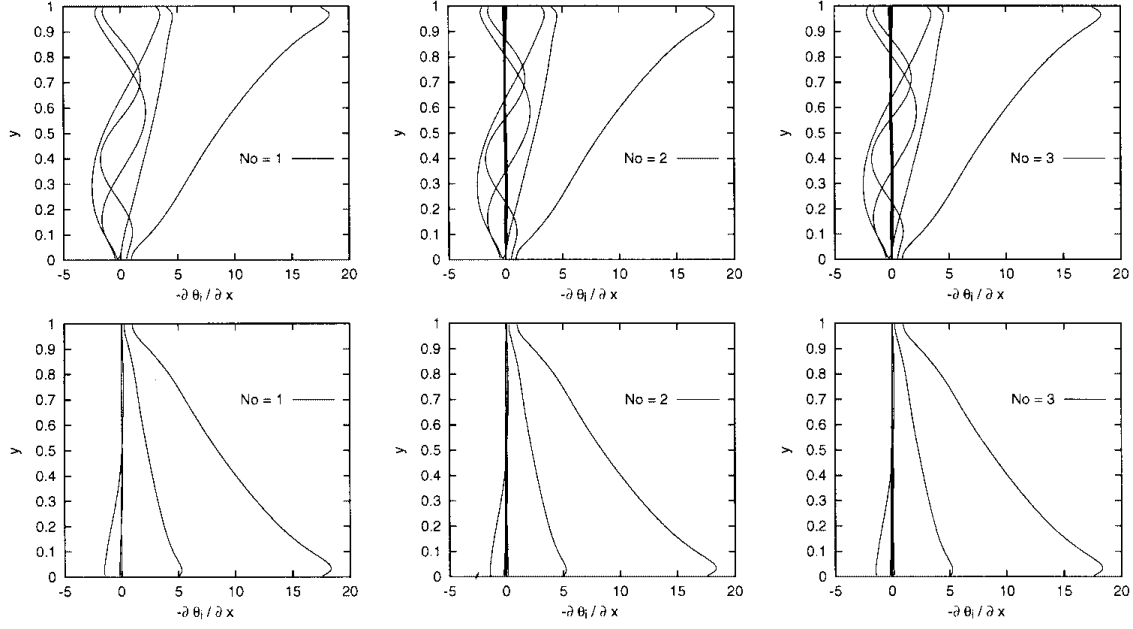


FIG. 6. Local heat flux versus y on the cold (top row) and hot (bottom row) walls. Results are obtained with $N_{KL} = 4$, $L_c = 1$, and $\sigma_\theta = 0.25$. Curves are plotted for every mode in the PC expansion. $P = 4$ for $N_O = 1$, $P = 14$ for $N_O = 2$, and $P = 34$ for $N_O = 3$.

for every mode in the PC expansion. The local heat flux profiles for the “first-order modes” (index $i \leq 4$) have shapes similar to those reported in Fig. 4: these modes have significant amplitude on the cold wall, whereas modes higher than 2 are much less pronounced on the hot wall. On both walls, the first-order modes are slightly influenced by the order of the PC expansion. Whereas increasing N_O introduces more modes in the expansion ($P = 14$ for $N_O = 2$ and $P = 33$ for $N_O = 3$), the heat fluxes associated with these higher order modes are very low. Consequently, the “correction” of the local heat fluxes, arising when N_O is increased, is weak whenever $N_O > 1$. This fact is also shown in Fig. 7, where the local heat-flux standard deviations are plotted for $N_O = 1, 2$, and 3.

The present analysis of wall heat fluxes only shows how the solution converges, globally or locally, on the vertical boundaries. To further investigate the behavior of the spectral

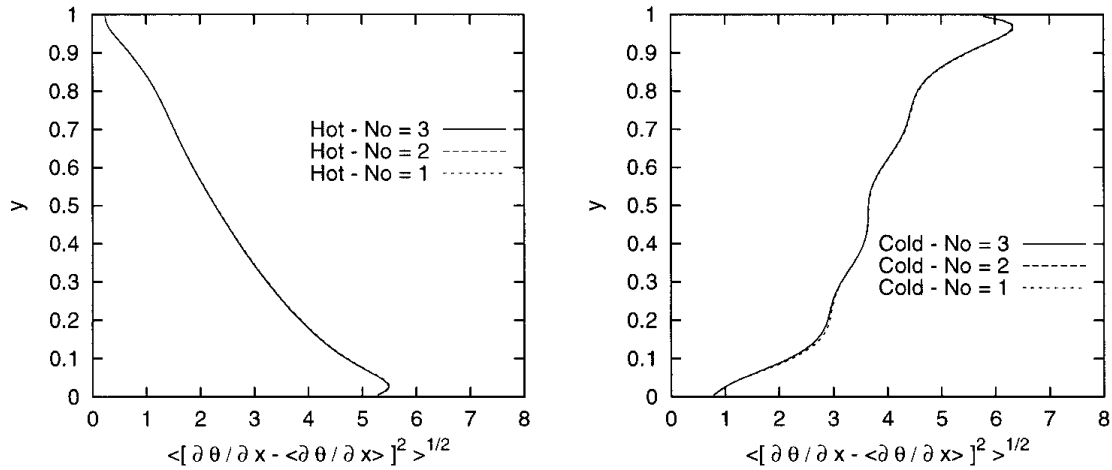


FIG. 7. Local standard deviation of the heat fluxes on the hot (left) and cold (right) walls, for $N_O = 1, 2$, and 3. Results are obtained with $N_{KL} = 4$, $L_c = 1$, and $\sigma_\theta = 0.25$.

representation, we analyze the temperature and velocity fields within the cavity. We focus our attention on the distributions of mean quantities and their standard deviations and postpone to Section 7 the examination of individual mode structure.

Temperature field. We start by noting that, since the natural convection in the cavity is not a linear process, the mean temperature distribution differs from the deterministic prediction corresponding to the mean temperature boundary condition, $\theta_c = -1/2$. This deterministic prediction, corresponding to $\xi_i = 0, i = 1, \dots, N_{KL}$, shall be denoted by θ^0 . Meanwhile, we shall denote by $\langle \theta^{N_O=1,2,3} \rangle \equiv \theta_0(N_O)$ the mean predictions obtained using first-, second-, and third-order PC expansions, respectively.

Examination of the mean temperature fields obtained with $N_O = 1, 2$, and 3 (not shown) reveals that these fields have features like those of θ^0 (shown earlier in Fig. 3). Thus, we have found it more convenient to analyze the difference fields $\theta^0 - \langle \theta^{N_O \geq 1} \rangle$. These difference fields are plotted in Fig. 8 for $N_{KL} = 4$. A close agreement is observed between the plots corresponding to the different expansion orders. Only a very weak dependence of the local magnitudes on N_O can be detected. Thus, increasing N_O has only a weak effect on the expected temperature field. To further demonstrate the convergence of the spectral representation, the differences $\langle \theta^{N_O=1} \rangle - \langle \theta^{N_O=2} \rangle$ and $\langle \theta^{N_O=2} \rangle - \langle \theta^{N_O=3} \rangle$ are displayed in Fig. 9. The results show that, at least as far as the mean field is concerned, the first-order expansion captures most of the effects of uncertainty. The difference $\langle \theta^{N_O=2} \rangle - \langle \theta^{N_O=3} \rangle$ is very small, indicating that the truncated terms have a weak impact on the mean temperature.

Figure 8 also shows that the mean temperature along the cold wall is higher than that of θ^0 . The opposite situation is reported along the hot wall, where the mean temperature is lowered by the uncertainty. These changes are responsible for the improvement of the global heat-transfer coefficient \overline{Nu} . In addition, the mean temperature on the bottom of the cavity is significantly lower than that of θ^0 ; in the upper part of the cavity, the mean and deterministic predictions are nearly equal. To explain these trends, one notes that the mean clockwise flow circulation is not altered by the stochastic boundary conditions (as will be shown later). So, on average, the fluid is traveling downward along the cold wall, where it is affected by random temperature conditions. The random fluctuations are transported across the cavity to the hot wall. As the fluid travels upward along the hot wall, uncertainty is reduced due to diffusion, so that when reaching the upper part of the cavity, the fluid temperature has lost most of its uncertainty, and its mean value is close to that of θ^0 . We also observe that the deviation of the mean temperature field from θ^0 exhibits a complex structure, with alternating signs, in the lower right quadrant, where the deviation from θ^0 peaks. This pattern is closely correlated with the uncertainties in the velocity fields, as will be further discussed.

Additional insight into the role of stochastic boundary conditions can be gained from Fig. 10, which depicts the temperature standard deviation fields for $N_O = 1, 2$, and 3. The results show that the standard deviation distribution has a structure similar to that of the mean, with two layers parallel to the vertical walls and a horizontal stratified arrangement from the bottom to the top of the cavity. The standard deviation vanishes on the hot wall, where deterministic conditions are imposed, and reaches its maximum on the cold wall, with values close to σ_θ . This spatial distribution is consistent with the arguments just presented regarding the role of circulation in driving the uncertainty.

Finally, in Fig. 11, it is shown that the expansions for $N_O = 1, 2$, and 3 provide essentially the same estimate of the temperature standard deviation, with differences in the fourth

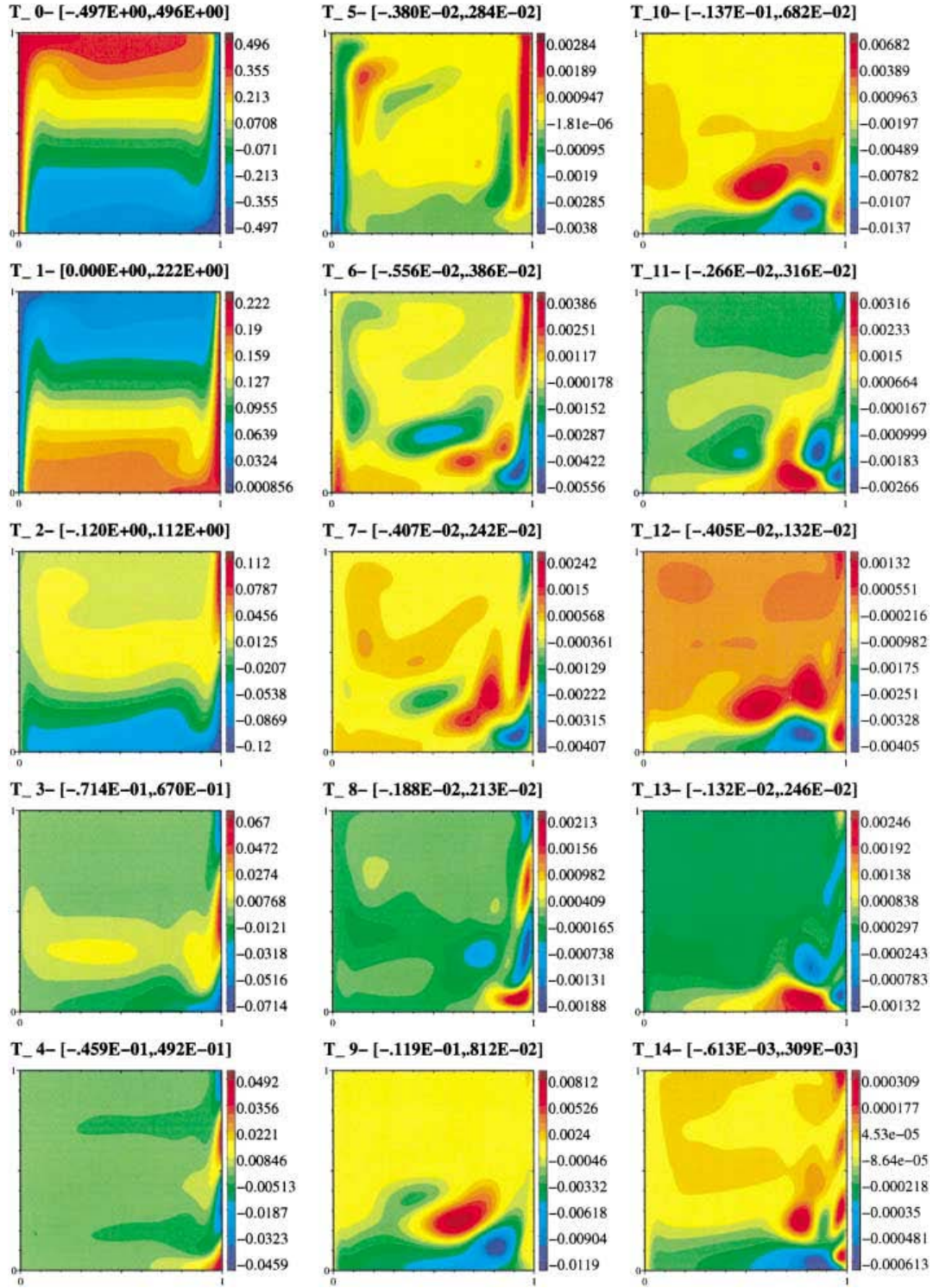


FIG. 17. Scaled temperature fields θ_k for $k = 0, \dots, 14$. Results are obtained with $N_{KL} = 4$, $N_O = 2$, $L_c = 1$, and $\sigma_\theta = 0.25$.

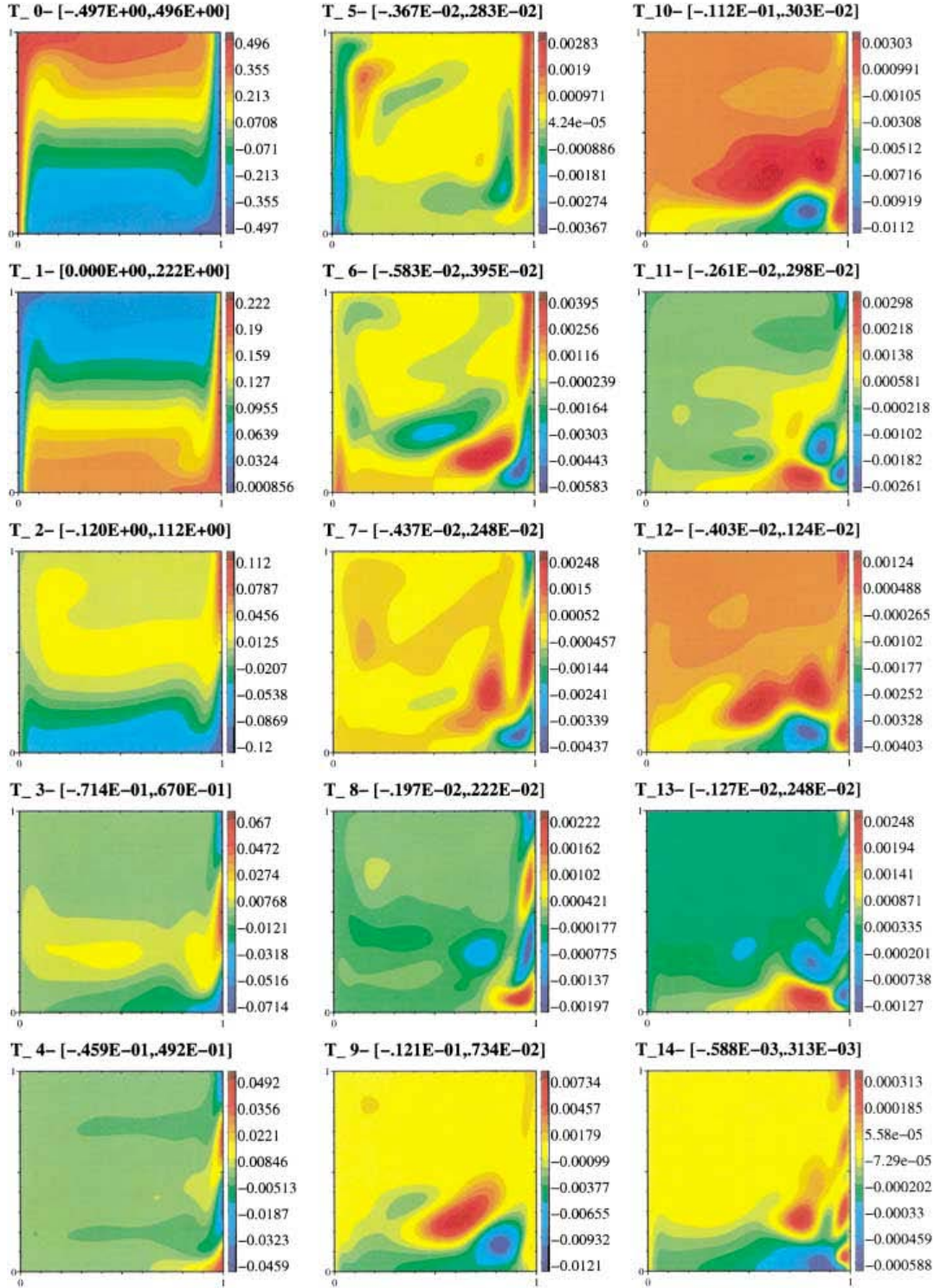


FIG. 19. Scaled temperature fields θ_k for $N_{KL} = 4$, obtained using NISP/GH predictions with $N_d = 81$, $L_c = 1$, and $\sigma_\theta = 0.25$.

(No=3)–(No=0)–Scale=5

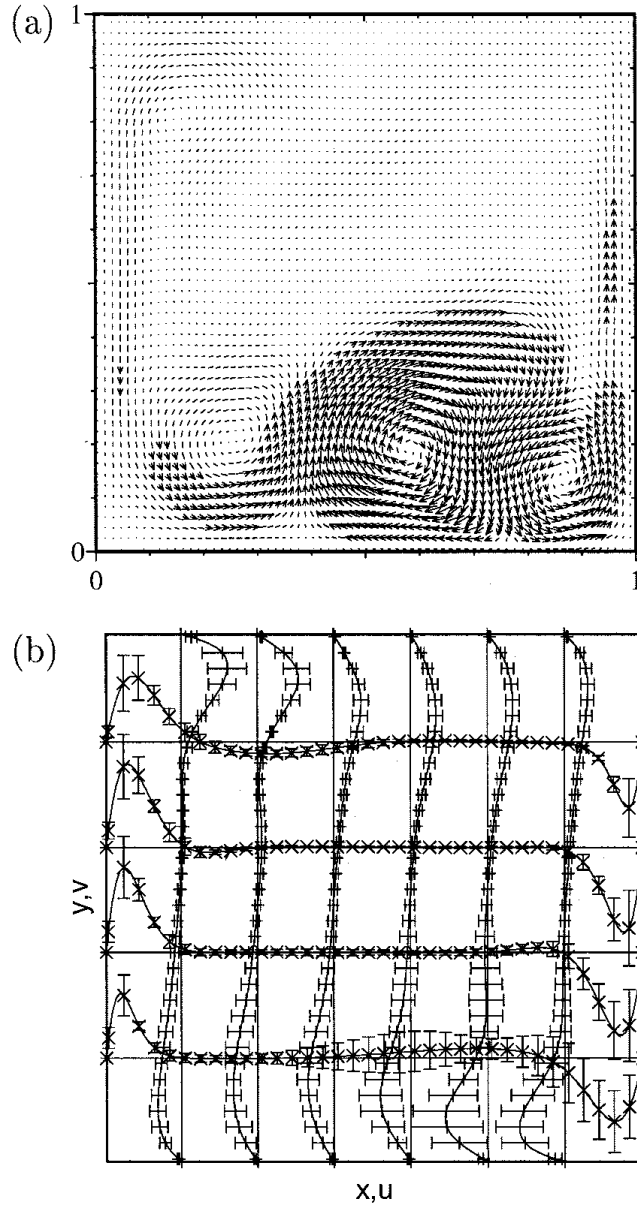


FIG. 12. (a) Velocity map of the difference $\langle \mathbf{u}^{No=3} \rangle - \mathbf{u}^0$. (b) Profiles of mean horizontal velocity ($\langle \langle \mathbf{u}^{No=3} \rangle \rangle$) and mean vertical velocity ($\langle \langle v^{No=3} \rangle \rangle$). The profiles are independently scaled for clarity. The scaled length of the bars corresponds to 6 times the local standard deviation. Results are obtained with $N_{KL} = 6$, $L_c = 1$, and $\sigma_\theta = 0.25$.

significant digit. These results also demonstrate the fast convergence rate of the spectral expansion and the fact that in the present case a first-order expansion captures most of the standard deviation.

Velocity field. As was done for the temperature distribution, we start by examining the deviation of the mean velocity field from \mathbf{u}^0 , which denotes the deterministic solution corresponding to the mean temperature condition ($\theta_c = -1/2$). The mean velocity fields corresponding to first-, second-, and third-order PC expansions will be denoted by $\langle \mathbf{u}^{No=1,2,3} \rangle$, respectively. For each case, we find that the deviation of the mean solution from \mathbf{u}^0 is small, and we consequently focus on the differences $\langle \mathbf{u}^{No \geq 1} \rangle - \mathbf{u}^0$.

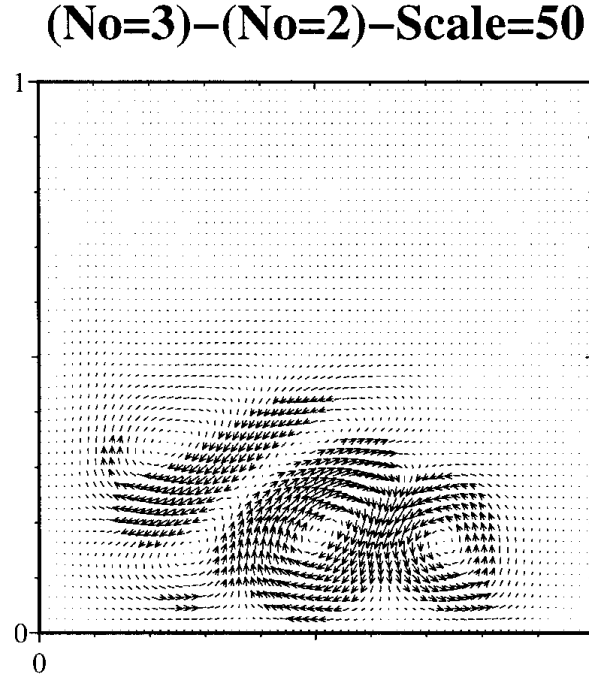


FIG. 13. Velocity map of the difference $\langle \mathbf{u}^{No=3} \rangle - \langle \mathbf{u}^{No=2} \rangle$. Results are obtained with $N_{KL} = 6$, $L_c = 1$, and $\sigma_\theta = 0.25$.

Figure 12a shows the distribution of $\langle \mathbf{u}^{No=3} \rangle - \mathbf{u}^0$ for a simulation with $N_{KL} = 6$, $L_c = 1$, and $\sigma_\theta = 0.25$. The difference field exhibits three complex structures that lie in the lower part of the cavity. While these structures resemble the recirculating eddies of the mean flow, it should be emphasized that the velocity magnitudes have been scaled by a factor of 10 compared to those in Fig. 3. Thus, with respect to \mathbf{u}^0 , the mean field is significantly perturbed in the regions occupied by these structures, but it is not actually recirculating. This can be verified by inspecting the mean solution itself, depicted in Fig. 12b, using the profiles of mean horizontal and mean vertical velocity. The profiles show that the mean flow is not recirculating but that flow “reversal,” hence recirculation, in the lower right corner is likely to occur. In this region, one observes large standard deviations and low mean velocities, especially outside the boundary layers; this is indicative of large sensitivity to the stochastic boundary conditions. This trend is consistent with earlier observations regarding the deviations $\theta^0 - \langle \theta^{No \geq 1} \rangle$, which exhibited maxima at these same locations.

To verify that the behavior of the stochastic solution is well represented, and consequently that the previously mentioned trends are not an artifact of the method, we inspect in Fig. 13 the distribution of $\langle \mathbf{u}^{No=3} \rangle - \langle \mathbf{u}^{No=2} \rangle$. The velocity map is generated with a scaling factor that is 10 times larger than that used in Fig. 12a. The results clearly demonstrate that there are very small differences between the second- and third-order solutions and that both provide accurate representations of the stochastic process.

Remarks. We close this section with two remarks regarding the ability of the spectral representation to accurately reproduce individual events and regarding the CPU costs of the spectral solution scheme.

Recall that the spectral representation relies on a weighted residual procedure to determine the mode coefficients. This representation is the closest polynomial to the exact

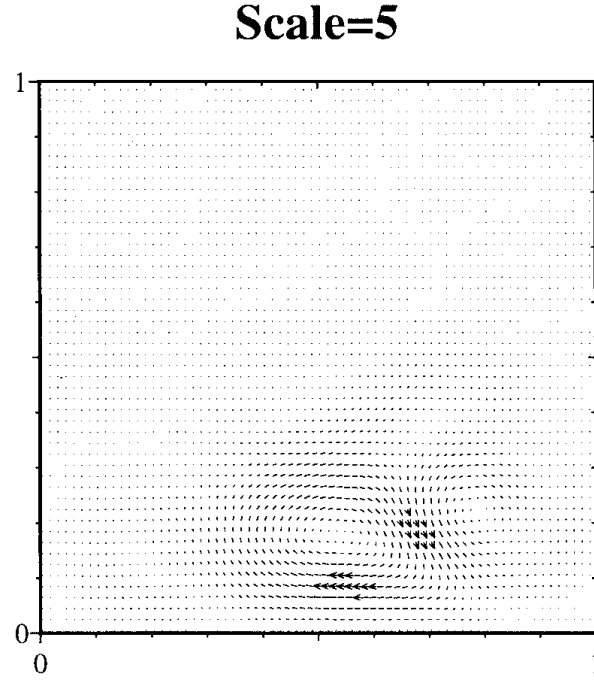


FIG. 14. Velocity map of the difference $\mathbf{u}^{No=2}(\xi=0) - \mathbf{u}^0$. Results are obtained with $N_{KL} = 6$, $L_c = 1$, and $\sigma_\theta = 0.25$.

response “surface” in the corresponding L_2 norm. Although optimal in this sense, the PC representation does not guarantee that individual “realizations” are exactly interpolated. However, our experiences indicate that when the PC representation is of sufficiently high order, it can also be used to obtain highly accurate estimates of individual realizations. This quality is illustrated in Fig. 14, where we plot the difference between \mathbf{u}^0 and the second-order solution evaluated at $\xi = 0$, i.e., $\mathbf{u}^{No=2}(\xi=0)$. The figure is generated with a scaling factor 10 times larger than that used for the deterministic solution of Fig. 3, demonstrating that the agreement between \mathbf{u}^0 and $\mathbf{u}^{No=2}(\xi=0)$ is indeed very good.

Regarding the performance of the spectral computations, we had anticipated earlier that the CPU cost would scale linearly with P , with near unity coefficient. As shown in Fig. 15, this behavior is in fact observed, and, together the spectral behavior of the errors in the spectral approximation, can be used to guide the selection of a suitable stochastic discretization level that properly balances accuracy and CPU cost.

7. MODE BEHAVIOR

In this section, we examine individual velocity and temperature modes in PC expansion. For brevity, we restrict our attention to spectral predictions obtained with $N_{KL} = 4$, $N_O = 2$, $L_c = 1$, and $\sigma_\theta = 0.25$. For this spectral resolution $P = 14$, giving a total of 15 modes. Thus, we end up with a moderate number of velocity and temperature distributions, which are analyzed in the following.

7.1. Velocity

Figure 16 provides vector maps for all the modes in the computations. Different scaling factors are used to represent the various fields, as indicated in the labels. Note that the zeroth

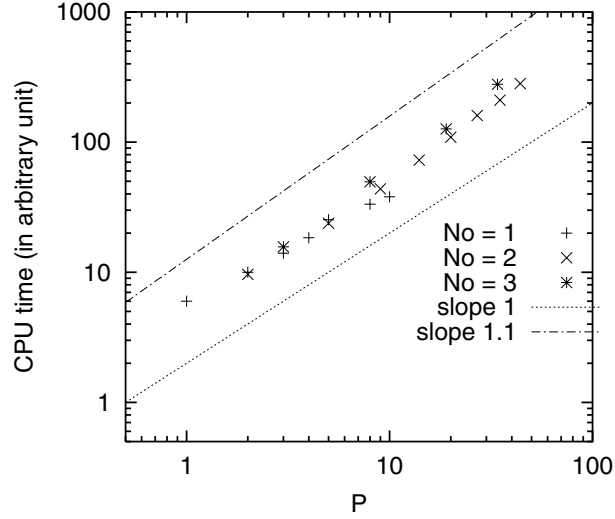


FIG. 15. CPU time needed to perform 100 time steps for PC expansions with different N_O and N_{KL} . A fixed mesh size of 140×100 cells is used. Scaled CPU times are reported as a function of the largest polynomial index P .

mode corresponds to the mean velocity field, which has been already studied in Section 6.2. Thus, we shall focus on the higher modes.

The first-order velocity modes $v_k, k = 1, \dots, 4$, follow mode 0 in the first column of Fig. 16. They correspond to the polynomial $\Psi_k = \xi_k$ for $k = 1, \dots, N_{KL} = 4$. Thus, these modes reflect the linear response of the stochastic velocity field to the corresponding Karhunen–Loève eigenfunctions appearing in Eq. (13) and plotted in Fig. 1. Note that the first KL mode has a nearly uniform, positive value and that it exhibits a positive velocity along the cold wall and a negative velocity along the hot wall. This is not surprising since, for $\xi_1 > 0$, the first Karhunen–Loève mode tends to decrease the temperature difference between the two walls. However, the structure of \mathbf{u}_1 is not similar to that of \mathbf{u}_0 . The two fields are governed by different dynamics, as shown in the Appendix, where the governing equations are given for a first-order PC expansion. One observes that the first mode is advected (and “stretched”) by the mean velocity (\mathbf{u}_0) and not by \mathbf{u}_1 . This observation, which also applies for $\mathbf{u}_2, \mathbf{u}_3$, and \mathbf{u}_4 , remains true for a second-order expansion.

In the neighborhood of the cold wall, all the first-order velocity modes clearly reflect the shape of the corresponding Karhunen–Loève mode. For instance, for \mathbf{u}_2 , the velocity points upward on the highest part of the cold wall and downward in its lowest part, as the associated temperature perturbation is respectively positive and negative (Fig. 1). For \mathbf{u}_1 and \mathbf{u}_2 , the velocity magnitudes are significant near all solid boundaries; on the other hand, for \mathbf{u}_3 and \mathbf{u}_4 , the velocity magnitudes are negligible on the hot wall. For the first-order modes, the velocity magnitudes decrease with increasing mode index; note in particular that the scale factor for \mathbf{u}_4 is twice that of \mathbf{u}_3 . If a larger value for N_{KL} is used, the additional first-order velocity fields are weaker than those retained, being localized near the cold boundary (not shown). This trend is consistent with our earlier discussion of the weakening effects of the higher frequency, random fluctuations.

The second-order velocity fields $\mathbf{u}_k, k = 5, \dots, 14$, are plotted in the center and right columns of Fig. 16; the same scaling factor is used for these modes, allowing straightforward comparison. Note that this scaling factor is 80 times larger than that of \mathbf{u}_0 and 10 times

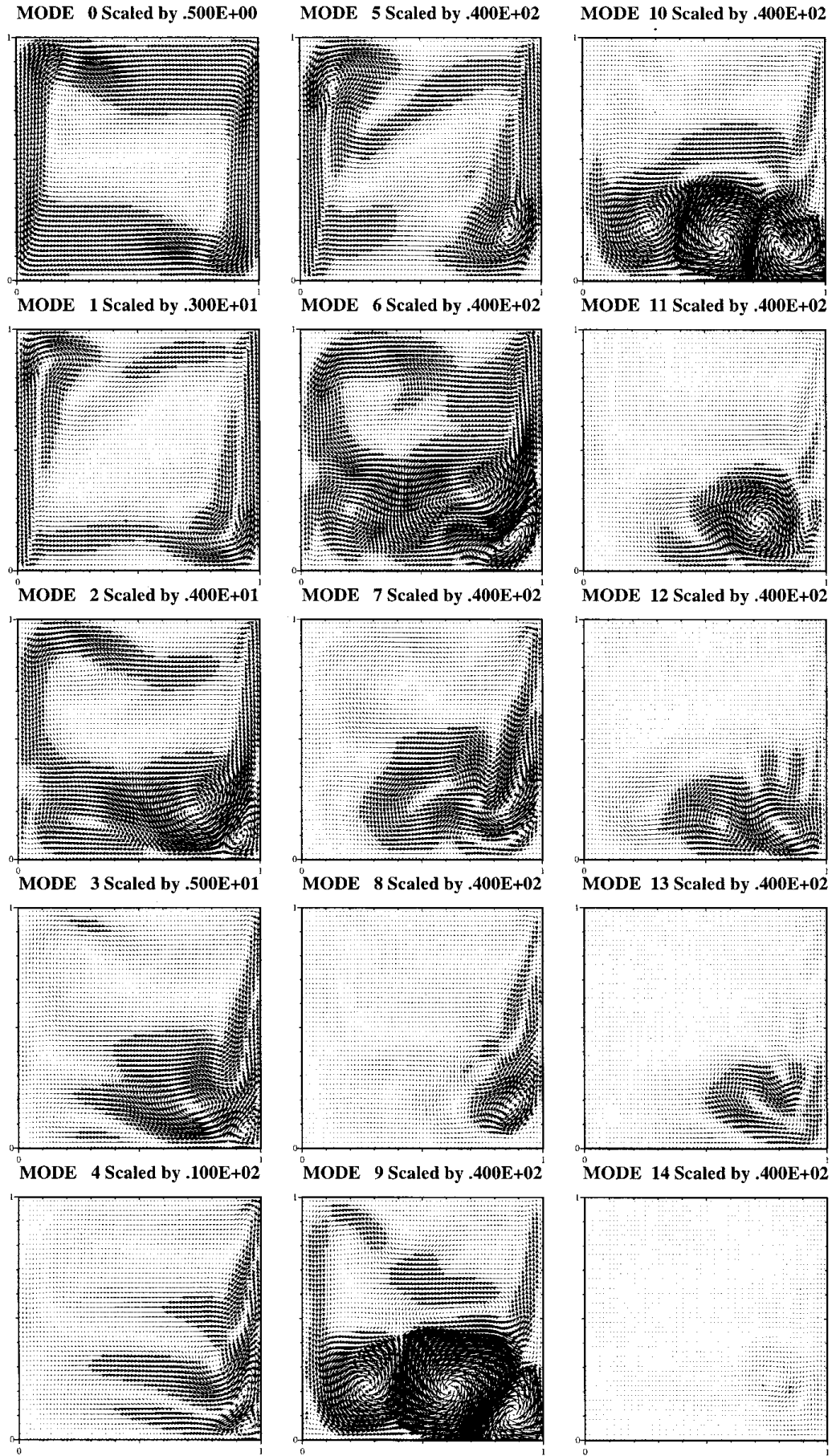


FIG. 16. Velocity fields u_k for $k = 0, \dots, 14$. Results are obtained with $N_{\text{KL}} = 4$, $N_O = 2$, $L_c = 1$, and $\sigma_\theta = 0.25$. Note that different velocity scales are used, as indicated in the labels.

larger than that of \mathbf{u}_4 . Thus, the magnitudes of the second-order velocity fields are much smaller than those of zeroth- and first-order modes. This rapid decay also reflects the rapid convergence of the PC expansion.

The second-order velocity modes have very different patterns, some being only significant along the cold wall and others affecting the entire cavity. Some of these structures can be easily interpreted. For example, \mathbf{u}_5 , which corresponds to $\Psi_5 = \xi_1^2 - 1$, has a structure similar to that of \mathbf{u}_1 . For other modes, the structure of the corresponding velocity fields are quite complex and difficult to interpret. It is interesting to note, however, that the velocity fields involving the second KL mode ($\mathbf{u}_6, \mathbf{u}_9, \mathbf{u}_{10}$, and \mathbf{u}_{11}) seem to have the most significant magnitudes, suggesting that this mode has greater impact on the stochastic process than the others. On the other hand, second-order polynomials associated with the fourth KL mode appear to be very weak.

7.2. Temperature

Figure 17 shows contour plots of the temperature modes $\theta_k, k = 0, \dots, 14$. Since the mean temperature field θ_0 has been analyzed earlier, we will focus on first- and second-order modes.

The contours of the first mode, θ_1 , are similar to those of θ_0 , even though the corresponding values differ. This is not surprising since these two modes obey similar boundary conditions, with θ_0 being subjected to a uniform Dirichlet condition on the cold wall, while θ_1 is nearly uniform there. However, some differences between the distributions of θ_1 and θ_0 can be observed at the lower right corner of the cavity. These differences appear to be governed by the circulation of the mean flow in the cavity. To appreciate this effect, we note that it is the mean field \mathbf{u}_0 which contributes to the transport of θ_1 ; the heat flux associated with \mathbf{u}_1 , which points upward near the cold wall, is dependent on the mean temperature field θ_0 (see the Appendix). The role of the mean field in the transport of θ_2, θ_3 , and θ_4 can also be appreciated from the corresponding contour plots. Note that θ_2, θ_3 , and θ_4 are very small in the upper half of the cavity but have significant values in the lower part of the cavity and/or in the vicinity of the cold wall. In particular, for θ_3 and θ_4 one observes fluctuations of alternating sign that are localized near the cold boundary and that coincide with the shape of the corresponding KL mode.

As for velocity, the second-order temperature modes are more difficult to interpret than the first-order modes. The only structures that can be easily identified are the imposed cold-wall distributions. The results indicate that significant mode coupling occurs, which can be detected by inspecting the modes involving mixed products of the ξ_i 's. For instance, for θ_7 a second-order coupling between ξ_1 and ξ_3 is involved; this mode exhibits three distinct zones along the cold wall, which reflect the shape of the third mode in the KL expansion. Apart from such identifiable features, the second-order modes can have complex distributions, some of which are localized in the lower part of the cavity, while others extend throughout the domain.

Regarding the amplitude of the second-order modes, we note those modes involving ξ_2 and ξ_3 , i.e., the second and third KL eigenfunctions, are dominant. Thus, not all second-order modes contribute equally to the stochastic process. In general, however, the second-order temperature modes are at least one order of magnitude lower than the first-order modes. This is consistent with earlier observations regarding the convergence of the expansion.

8. NONINTRUSIVE SPECTRAL PROJECTION

To verify the spectral computations of the previous section, a NISP approach is developed. The starting point in NISP is the observation that the modes \mathbf{u}_i and T_i can be obtained by projecting deterministic computations onto the PC basis. If $\mathbf{u}^d(\boldsymbol{\xi})$ and $T^d(\boldsymbol{\xi})$ denote the deterministic solution corresponding to a particular realization $\boldsymbol{\xi} = (\xi_1, \dots, \xi_{N_{\text{KL}}})$, then the polynomial coefficients are, by definition, given by

$$(\mathbf{u}_i, T_i) = \frac{\langle (\mathbf{u}, T)^d \Psi_i \rangle}{\langle \Psi_i \Psi_i \rangle} \equiv \int_{-\infty}^{\infty} d\xi_1 \cdots \int_{-\infty}^{\infty} d\xi_{N_{\text{KL}}} \left[(\mathbf{u}, T)^d(\boldsymbol{\xi}) \frac{\Psi_i(\boldsymbol{\xi})}{\langle \Psi_i^2 \rangle} \prod_{k=1}^{N_{\text{KL}}} \frac{\exp(-\xi_k^2/2)}{\sqrt{2\pi}} \right]. \quad (36)$$

8.1. Gauss–Hermite Quadrature

For moderate values of N_{KL} , our multidimensional integration can be efficiently performed using Gauss–Hermite quadrature [30, 31]. Using n collocation points along each “stochastic direction,” Eq. (36) can be approximated as

$$(\mathbf{u}_i, T_i) = \sum_{n_1=1}^n \cdots \sum_{n_{N_{\text{KL}}}=1}^n (\mathbf{u}, T)^d(x_{n_1}, \dots, x_{n_{N_{\text{KL}}}}) \frac{\Psi_i(x_{n_1}, \dots, x_{n_{N_{\text{KL}}}})}{\langle \Psi_i \Psi_i \rangle} \prod_{k=1}^{N_{\text{KL}}} w_{n_k}, \quad (37)$$

where (x_k, w_k) , $k = 1, \dots, n$, denote the one-dimensional GH integration points and weights. The quadrature in (37) is exact when the integrand is a polynomial of degree of $2n - 1$ or less. Thus, the coefficients can be exactly estimated if the process is spanned by polynomials of degree less than or equal to $(2n - 1)/2$. In this situation, the number of deterministic realizations N_d required in the NISP approach for given N_{KL} and N_O is $N_d = (2N_O - 1)^{N_{\text{KL}}}$. It should be emphasized that for arbitrary N_{KL} and N_O , N_d is always greater than P , the number of polynomials in the spectral approach used here. Since the CPU time in the spectral approach is approximately P times that of a deterministic solution, NISP is not as efficient as the spectral approach. Its main advantage, however, is that it makes use of a deterministic solver without the need for any modifications and so is “nonintrusive.”

NISP/GH computations are performed for a case with $N_{\text{KL}} = 4$ and $N_O = 2$. We use $n = 3$ and so obtain $N_d = 81$ deterministic realizations for the corresponding GH quadrature points. (In contrast, the intrusive spectral approach discussed previously has $P = 14$, for a total of 15 modes.) Velocity and temperature modes obtained using NISP are plotted in Figs. 18 and 19, respectively. The corresponding results obtained using the intrusive spectral approach were given in Figs. 16 and 17 and have extensively discussed in the previous section.

For the velocity fields, we find an excellent agreement between the intrusive spectral results (Fig. 16) and the NISP predictions (Fig. 18) for the zeroth- and first-order modes. For the second-order modes (\mathbf{u}_k , $k = 5, \dots, 14$), small deviations are observed between the two sets, but the primary structure of the modes is quite similar. These small deviations are pronounced for coupled modes involving ξ_2 and ξ_3 ; the deviations are substantially smaller for the nonmixed quadratic modes. Despite these small deviations, the agreement between the intrusive and NISP/GH predictions is very satisfactory.

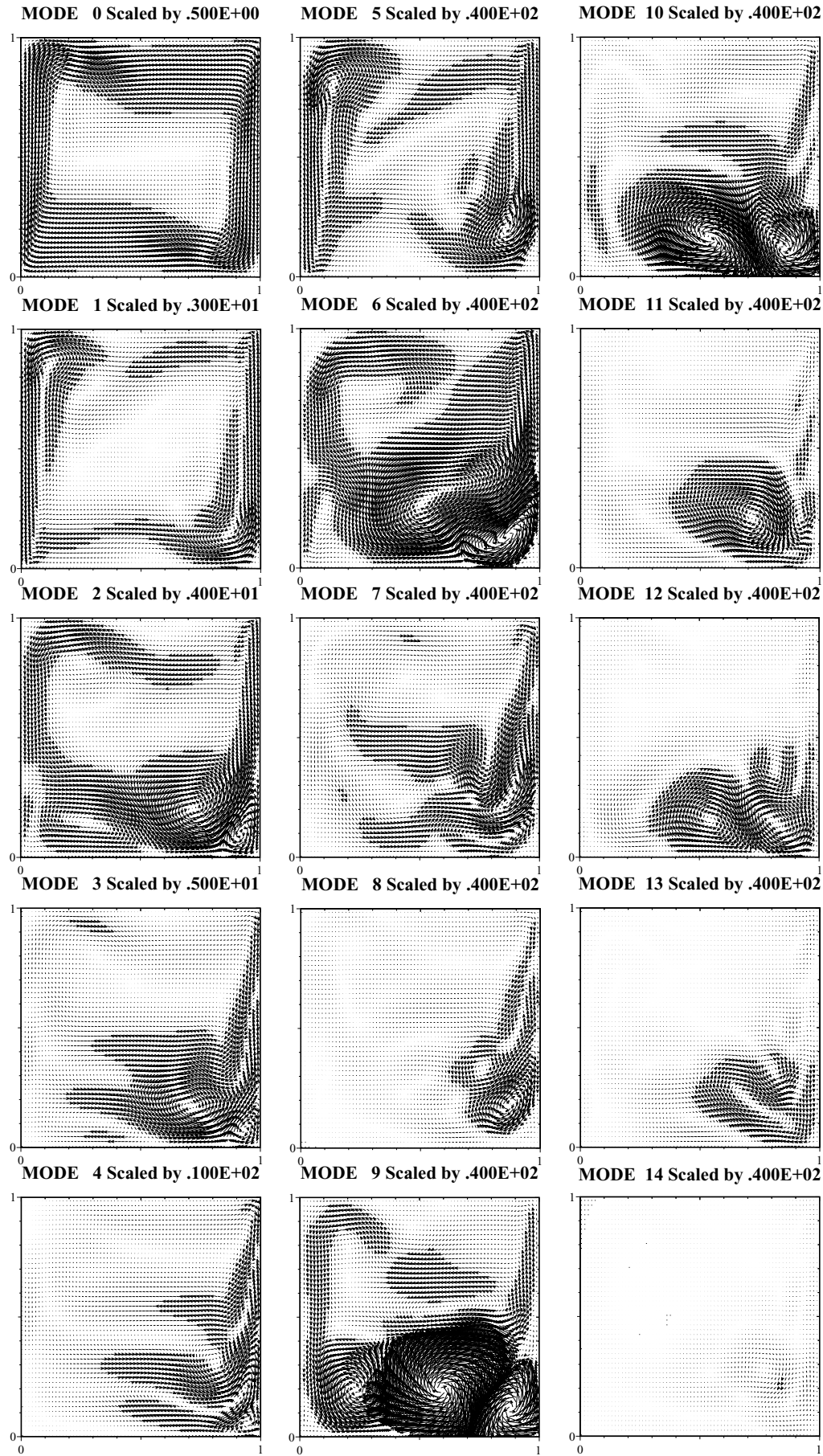


FIG. 18. Velocity fields u_k for $N_{KL} = 4$, obtained using NISP/GH predictions with $N_d = 81$. Note that different scale factors apply on vector magnitudes. $L_c = 1$ and $\sigma_\theta = 0.25$.

Comparison of the temperature modes in Figs. 19 and 17 reveal trends similar to those of the velocity modes. In particular, the zeroth- and first-order modes are in excellent quantitative agreement, as can be appreciated by inspecting the maxima and minima reported on individual frames. These values also provide a good illustration of the deviations observed in the second-order modes. Again the largest differences are observed for modes involving mixed products. The small magnitude of these differences, compared to the characteristic values of the first-order terms, is evident and should be emphasized.

The origin of deviations between intrusive and NISP/GH predictions can be traced to the errors inherent in both approaches. These primarily consist of spectral truncation errors in the intrusive approach and aliasing errors in the NISP predictions. Obviously, complete agreement between NISP and spectral computations can only be achieved in the case of a finite spectrum. Since we are presently dealing with second-order spectral representations, agreement would occur if the third- and higher order modes vanish identically, which is clearly not the case: the third-order terms are very small, but not identically vanishing.

To further examine these differences, we rely on the L_2 norms of the differences between the same temperature modes in two different solutions, $T^{(1)}$ and $T^{(2)}$, defined according to

$$\mathcal{E}_{ik}^2 \equiv \left[\int \int (T_i^{(1)} - T_k^{(2)})^2 dx dy \right]^{1/2}. \quad (38)$$

The indices i and k are selected so that Ψ_i in the PC expansion of $T^{(1)}$ refers to the same polynomial Ψ_k in the polynomial expansion for $T^{(2)}$. Obviously, $i = k$ when $T^{(1)}$ and $T^{(2)}$ have the same number of KL modes, N_{KL} .

We have first compared modal solutions obtained with intrusive spectral computations using the same order PC expansion but different number of KL modes. In this case, the error measure is only relevant for the modes that are shared in both representations, namely, those belonging to the expansion having lower N_{KL} value. A sample of this exercise is shown in Fig. 20, which shows the L_2 norm between temperature modes obtained using second-order expansions with $N_{\text{KL}} = 4$ and 6. As is evident in the figure, the L_2 errors between the

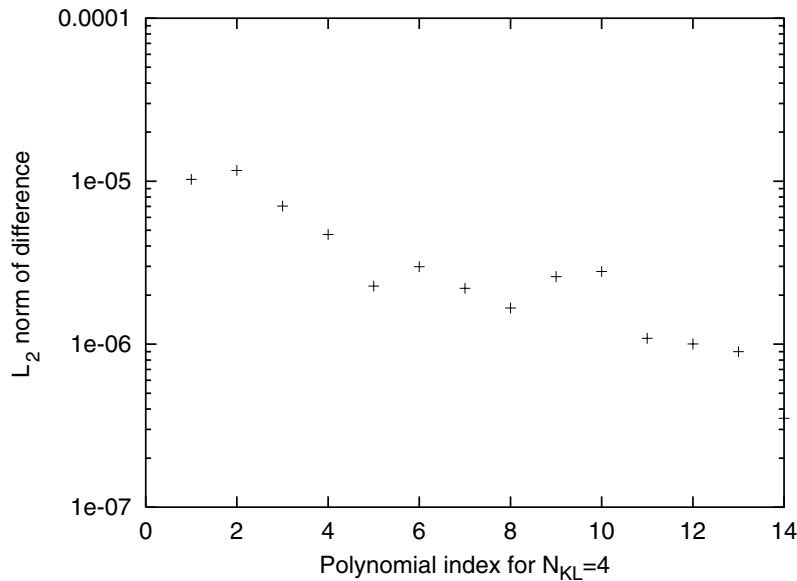


FIG. 20. L_2 norm of the difference in the common temperature modes obtained with intrusive spectral calculations using $N_{\text{KL}} = 4$ and $N_{\text{KL}} = 6$. In both cases, a second-order PC expansion is used.

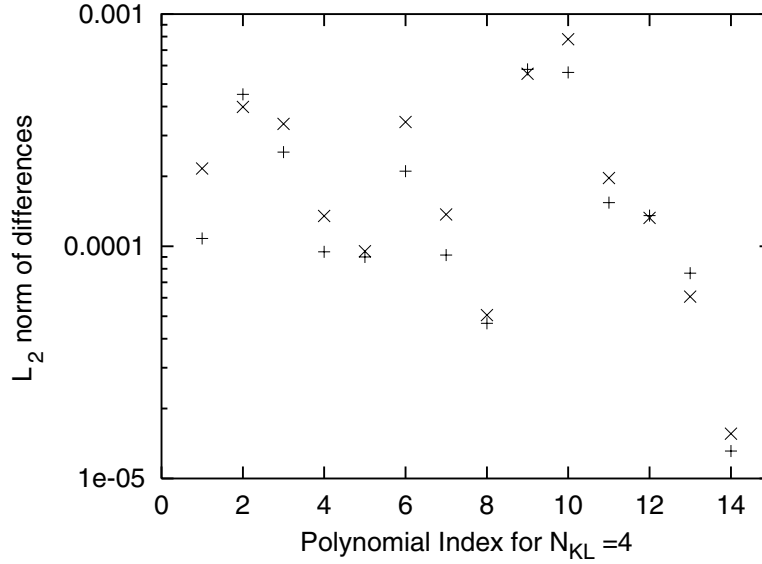


FIG. 21. L_2 norms of differences in temperature modes obtained with intrusive spectral predictions using second- and third-order PC expansions (+), and between predictions obtained using the second-order spectral and second-order NISP/GH predictions (x). In all cases, $N_{KL} = 4$.

modal solutions are very small, indicating a very good agreement between the predictions. The same analysis was repeated with third-order PC expansions (not shown) and revealed similar trends. This further supports earlier claims that for the present conditions $N_{KL} = 4$ is sufficient for adequate representation of the stochastic boundary conditions.

Figure 21 shows the L_2 norm of the differences between the second-order and third-order intrusive predictions and between second-order intrusive and second-order NISP/GH results. In all cases, we use $N_{KL} = 4$ and L_2 norms are shown for all 14 modes in the second-order PC expansion. The results indicate that for all modes the L_2 norms are small, with magnitudes falling below 10^{-3} . In addition, the differences between second-order NISP and intrusive predictions are comparable to corresponding deviations obtained using intrusive spectral computations with $N_O = 2$ and 3. Thus, the deviations between the NISP/GH and intrusive spectral predictions are of the same order as the spectral truncation errors in the latter approach.

8.2. Latin Hypercube Sampling

As mentioned earlier, a Latin hypercube sampling approach is also applied to determine PC mode distributions. LHS is a stratified sampling technique where the random variable distributions are divided into equal probability intervals, and events are formed by randomly selecting variables within each of these intervals [32]. LHS typically requires fewer samples than simple pseudo-random sampling to reach the same degree of convergence, and a uniform sampling of phase space is assured within the limits of the sample size. In the computations, the DAKOTA toolkit [37–39] is used to generate the necessary samples of the uncorrelated Gaussian variables appearing in the KL expansion. Individual realizations are then projected onto the PC basis to determine the mode distributions.

NISP/LHS computations are performed for a case with $N_{KL} = 6$, $L_c = 1$, and $\sigma_\theta = 0.25$. The sampling tools in DAKOTA were used to generate a six-dimensional array of uncorrelated normalized Gaussians. The convergence of the mode amplitudes and the mean

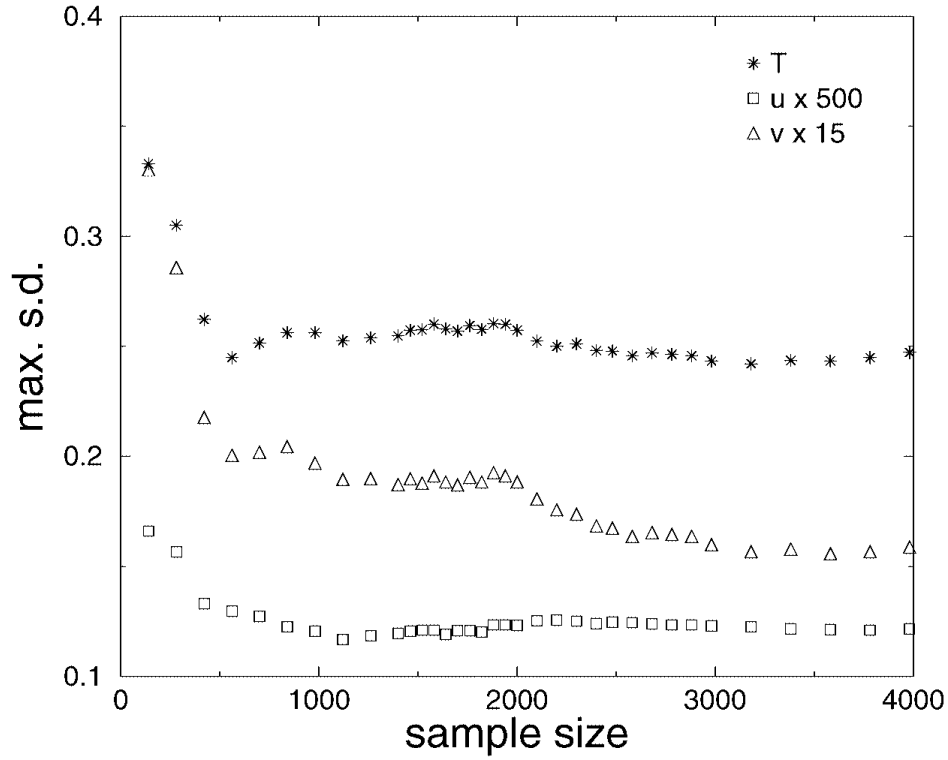


FIG. 22. Maximum standard deviation of temperature, u -velocity, and v -velocity over the computational domain plotted vs the sample size. Note that the velocity standard deviations are scaled, as indicated in the legend.

Nusselt number were monitored as the number of realizations increased. An example of the convergence diagnostics is given in Fig. 22, which shows the maximum standard deviation for temperature and velocity in the entire domain as a function of the sample size. For the present set of conditions, a sample of size of 4000 was deemed sufficient for the analysis, even though statistics are evidently not fully converged, as can be appreciated from the figure.

In the following, we discuss results obtained from NISP/LHS computations in light of the aforementioned NISP/GH results and the earlier “intrusive” spectral results. The spatial distributions of PC modes of order ≤ 2 obtained using NISP/LHS (not shown) were first compared with corresponding predictions obtained with second- and third-order intrusive computations. The comparison reveals an excellent agreement for the mean and first-order modes but noticeable quantitative and qualitative differences do occur in the second-order modes. We briefly illustrate these differences by plotting in Fig. 23 the L_2 norm of the differences between (i) the NISP/LHS results and the second-order intrusive predictions, and (ii) the NISP/LHS results and third-order intrusive predictions; the L_2 norm of differences between second- and third-order spectral predictions are also shown for comparison. As observed earlier, the second- and third-order predictions are in excellent agreement with each other, with L_2 norms falling below 10^{-3} . The differences between the NISP/LHS and spectral predictions are also small, but the corresponding L_2 norms are about an order of magnitude larger than those of differences between spectral predictions. It can also be observed that the L_2 norms of differences between the NISP/LHS and intrusive predictions are nearly the same for both second-order and third-order spectral expansions. This indicates that the differences between NISP/LHS and spectral results are strongly affected by the sampling errors in the NISP/LHS approach and that, although still small, these errors are substantially larger than spectral truncation errors.

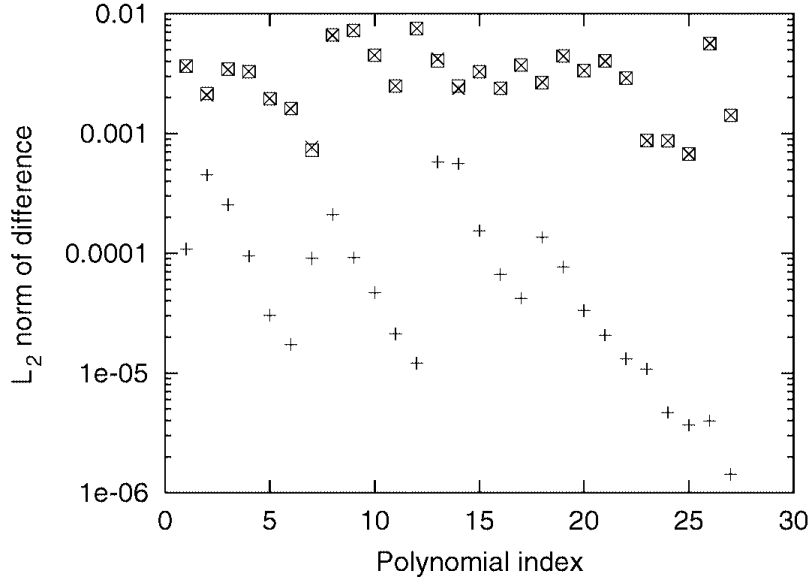


FIG. 23. L_2 norm of differences in temperature modes obtained with intrusive spectral predictions using second- and third-order PC expansions (+), intrusive second-order and NISP/LHS with 4000 realizations (\times), and intrusive third-order and NISP/LHS with 4000 realizations (\square). In all cases, $N_{KL} = 6$, and the comparison is restricted to second-order modes.

Additional insight into the convergence of the NISP/LHS computations can be gained from Fig. 24, which shows the L_2 norm of the differences in mode distributions between the NISP/LHS and second-order intrusive results, as a function of the sample size. Plotted in Fig. 24a are L_2 norms for the mean and first-order modes; results for modes 7–13 are shown in Fig. 24b. Generally, the difference between NISP/LHS and spectral predictions diminishes quickly, but a residual difference remains for all modes as the sample size increases. The difference decays quicker for the mean and the first-order modes (Fig. 24a), than for modes 7–13 (Fig. 24b). As can be observed in Fig. 23, the differences between NISP/LHS and intrusive spectral predictions are such that L_2 norms corresponding to the mean and first-order modes are comparable to or smaller than those corresponding to some of the second-order modes. Since the latter are significantly weaker than the former, this indicates that the NISP/LHS predictions of the higher order modes have large relative errors and are not well converged. This also shows that the sampling errors in NISP/LHS are behind the observed differences in the distributions of second-order modes.

9. UNCERTAINTY QUANTIFICATION

We conclude this study with a quantitative analysis of the effects of the stochastic boundary conditions on heat transfer statistics within the cavity. We rely on spectral computations using $N_{KL} = 6$, $N_O = 2$, and a 140×100 computational grid. Results are obtained for three different correlation lengths and standard deviations, namely, $L_c = 0.5, 1$, and 2 and $\sigma_\theta = 0.125, 0.25$, and 0.5 .

Computed values of \overline{Nu} and $\sigma(Nu)$ are reported in Tables V and VI, respectively. Table V provides the mean Nusselt number along with the difference $\overline{Nu} - Nu^0$, where Nu^0 denotes the Nusselt number corresponding to the deterministic prediction with $\theta_c = -1/2$. The results show that \overline{Nu} is larger than Nu^0 . For fixed correlation length, $\overline{Nu} - Nu^0$ increases

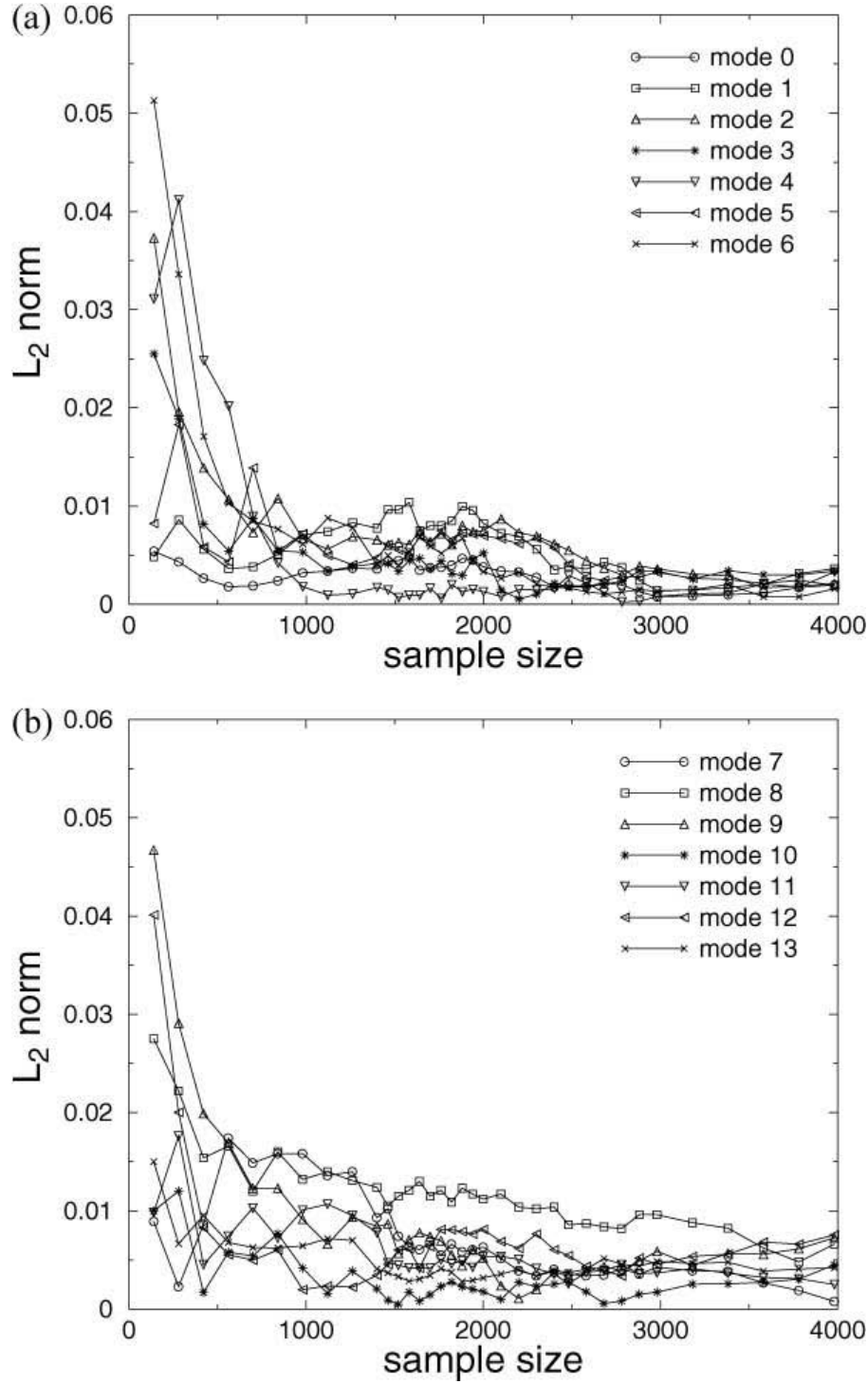


FIG. 24. L_2 norm of differences in temperature modes obtained with second-order intrusive and NISP/LHS predictions for different sample size: (a) modes 0–6, (b) modes 7–13. In both approaches, $N_{KL} = 6$, $L_c = 1$, and $\sigma_\theta = 0.25$.

approximately as σ_θ^2 . In contrast, \overline{Nu} exhibits a weaker dependence on L_c . This is not surprising since, in the range considered, the eigenvalues λ_i of KL modes vary slowly with the correlation length.

Unlike \overline{Nu} , for fixed L_c the standard deviation $\sigma(Nu)$ exhibits an approximately linear dependence on σ_θ , as shown in Table VI. Furthermore, compared with the mean, $\sigma(Nu)$ exhibits a more pronounced dependence on L_c . This trend is consistent with variations of

TABLE V
Mean Nusselt Number for Different Values of L_c
and σ_θ with $N_{KL} = 6$ and $N_O = 2$

L_c	σ_θ		
	0.125	0.25	0.5
\overline{Nu}			
0.5	8.902	8.967	9.228
1	8.904	8.974	9.268
2	8.905	8.977	9.293
$\overline{Nu} - Nu^0$			
0.5	0.021	0.086	0.347
1	0.023	0.093	0.387
2	0.024	0.096	0.412

the KL mode amplitudes with the correlation length. As L_c increases, the magnitude of the first KL modes increases, and since these modes have a dominant impact on the uncertainty, so does $\sigma(Nu)$.

Figure 25 depicts probability density functions (PDFs) of the Nusselt number computed from the spectral solution. Figure 25a shows that the most likely value of Nu is not significantly affected by σ_θ , showing a slight decrease as σ_θ increases. On the other hand, the skewness of the PDF increases with σ_θ . In particular, for $\sigma_\theta = 0.5$, one observes a flatter tail at high Nu values than for the lower values. These trends are consistent with earlier results in Table V, which show that $\overline{Nu} - Nu_0$ increases substantially as σ_θ increases.

The effect of L_c on the PDF of the Nusselt number is depicted in Fig. 25b for fixed $\sigma_\theta = 0.5$. Consistent with the results of Table VI the PDF becomes wider as L_c increases. Besides this trend, L_c appears to have a weak direct influence on the shape of the PDF.

Finally, we note that at $\sigma_\theta = 0.5$ the PDF can extend into the negative Nu range. This indicates that in extreme situations, the “mean” temperature on the right vertical wall may exceed the constant value on the left vertical wall, leading to a reversal of the circulation within the cavity and in the wall heat transfer. While such extremes have low probability and consequently make a small contribution to low-order statistics, they demonstrate the capability of the present method of treating situations with large uncertainty. To illustrate these large changes, we plot in Fig. 26 the velocity profiles across the cavity for fixed $L_c = 1$ and three different standard deviations, $\sigma_\theta = 0.125, 0.25$, and 0.5 . The length of the “uncertainty” bars is proportional to 6 times the local standard deviation. Clearly, the

TABLE VI
Standard Deviation of the Nusselt Number for Different
Values of L_c and σ_θ with $N_{KL} = 6$ and $N_O = 2$

L_c	$\sigma(Nu)$		
	$\sigma_\theta = 0.125$	$\sigma_\theta = 0.25$	$\sigma_\theta = 0.5$
0.5	1.097	2.186	4.334
1	1.236	2.463	4.859
2	1.322	2.634	5.178

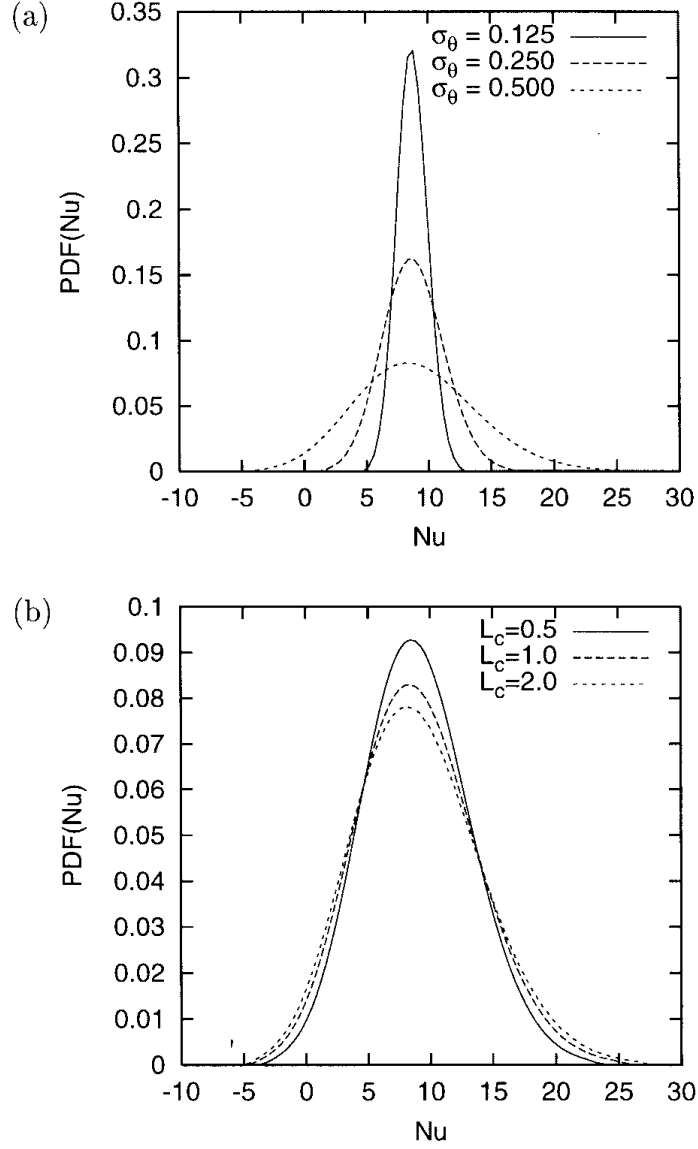


FIG. 25. PDFs of the Nusselt number computed from the spectral simulations using $N_{KL} = 6$ and $N_O = 2$: (a) $L_c = 1$ and $\sigma_\theta = 0.125, 0.25$, and 0.5 ; (b) $\sigma_\theta = 0.5$ and $L_c = 0.5, 1$, and 2 .

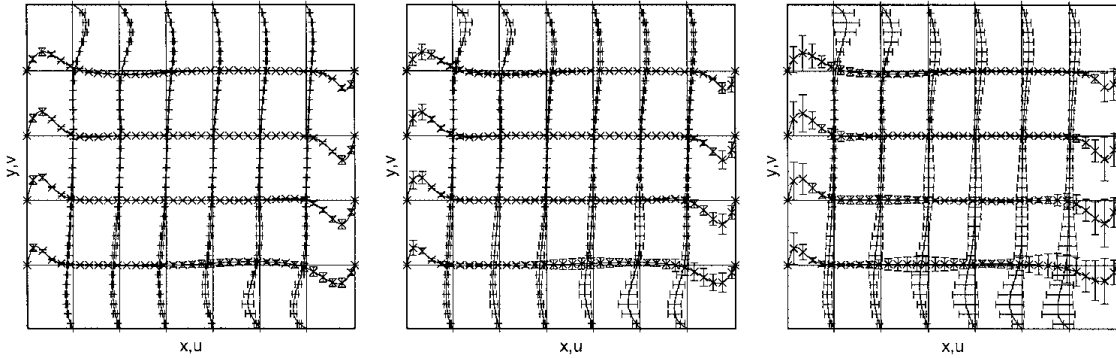


FIG. 26. Mean velocity profiles across the cavity for $\sigma_\theta = 0.125$ (left), 0.25 (center), and 0.5 (right). The error bars correspond to 6 times the local standard deviation. The same scaling is used for all three plots. Spectral results with $L_c = 1$, $N_{KL} = 6$, and $N_O = 2$ are used.

uncertainty bars increase as σ_θ increases. In particular, for $\sigma_\theta = 0.5$ the uncertainty bars suggest that events with upward velocity near the cold wall become probable. In contrast, one observes that the mean flow field is not strongly affected by σ_θ .

10. CONCLUSIONS

In this paper, the SPM [1] has been generalized to account for stochastic input data generated by a stochastic process. The Karhunen–Loève expansion is used to represent the stochastic input data. The dependence of the solution process on the random data is expressed in terms of the polynomial chaos system and the coefficients of the solution are determined using a weighted residual approach. The resulting stochastic formulation is incorporated into a finite-difference projection method, which results in an efficient stochastic solver.

The properties of the stochastic solver are analyzed in light of computed results for natural convection within a closed square cavity under stochastic temperature boundary conditions. In particular, the setup is used to examine the convergence properties of the spectral uncertainty representation scheme in terms of the number of KL modes and the order of the PC expansion. Computations are performed for a steady flow regime with Rayleigh number of 10^6 . For the selected conditions, the results indicate that the spectral representation converges rapidly, providing accurate results for a second-order expansion using as few as four KL modes. Numerical tests indicate that the CPU cost of the stochastic computations is essentially proportional to the number of modes used in the spectral representation, thus highlighting the efficiency of the stochastic model.

To verify the spectral predictions, stand-alone deterministic computations are performed and are used in conjunction with “nonintrusive” spectral projection approaches. Two variants of the NISP approach are implemented, one based on high-order Gauss–Hermite integration and the other on a Latin hypercube sampling strategy. Results obtained using Gauss quadrature are in excellent agreement with the spectral predictions, showing very small differences that are of the order of the spectral truncation errors. Predictions obtained using the Latin hypercube sampling scheme are also in agreement with the spectral predictions but exhibit differences that are an order of magnitude higher than those obtained using Gauss–Hermite quadrature. The verification study underscores the efficiency of the spectral computations, as the number of independent realizations needed to adequately represent the stochastic process is substantially higher than the corresponding number of PC modes. The analysis also shows that the nonintrusive approach based on Gauss–Hermite quadrature can be significantly more attractive than that using Latin hypercube sampling, at least for problems with a moderate number of stochastic dimensions.

The computations are used to quantify the effects of stochastic temperature conditions on the global heat transfer characteristics within the cavity. The results indicate that the mean Nusselt number, \overline{Nu} , is generally larger than Nu^0 , the Nusselt number corresponding to the mean (uniform) temperature profile. In particular, the difference $\overline{Nu} - Nu^0$ is found to increase quadratically with σ_θ , the standard deviation of the stochastic temperature profile, but shows a weak dependence on the correlation length L_c . Meanwhile, the standard deviation of the Nusselt number exhibits an approximately linear dependence on σ_θ and a more pronounced dependence on L_c than the mean Nusselt number.

So far, implementations of SPM have been restricted to flow conditions having relatively simple physical models, involving quadratic nonlinearities only. In other situations, more

complex physical models may arise that involve higher order nonlinearities. These result in additional computational challenges for the present approach, particularly regarding the implementation of the Galerkin scheme. Extensions that address these challenges in the context of chemically reacting flows are currently being developed.

APPENDIX

A first-order expansion gives a spectral basis involving a set of $P + 1 = N_{\text{KL}} + 1$ orthogonal polynomials:

$$\Psi_0 = 1, \quad \Psi_i = \xi_i \quad \text{for } i = 1, \dots, N_{\text{KL}} = P. \quad (39)$$

The governing equations for the zeroth-order velocity and temperature modes are

$$\frac{\partial \mathbf{u}_0}{\partial t} + \sum_{i=0}^{N_{\text{KL}}} \mathbf{u}_i \cdot \nabla \mathbf{u}_i = -\nabla p_0 + \frac{Pr}{\sqrt{Ra}} \nabla^2 \mathbf{u}_0, \quad (40)$$

$$\frac{\partial \theta_0}{\partial t} + \sum_{i=0}^{N_{\text{KL}}} \nabla \cdot (\mathbf{u}_i \theta_i) = \frac{1}{\sqrt{Ra}} \nabla^2 \theta_0. \quad (41)$$

For $k = 1, \dots, N_{\text{KL}}$ the governing equations can be expressed as

$$\frac{\partial \mathbf{u}_k}{\partial t} + \mathbf{u}_0 \nabla \mathbf{u}_k + \mathbf{u}_k \nabla \mathbf{u}_0 = -\nabla p_k + \frac{Pr}{\sqrt{Ra}} \nabla^2 \mathbf{u}_k, \quad (42)$$

$$\frac{\partial \theta_k}{\partial t} + \nabla \cdot (\mathbf{u}_0 \theta_k + \mathbf{u}_k \theta_0) = \frac{1}{\sqrt{Ra}} \nabla^2 \theta_k. \quad (43)$$

Meanwhile, continuity gives

$$\nabla \cdot \mathbf{u}_k = 0, \quad k = 0, \dots, N_{\text{KL}}. \quad (44)$$

The velocity boundary conditions are given by

$$\mathbf{u}_k(\mathbf{x}, t) = 0 \quad \forall \mathbf{x} \in \partial\Omega, \quad \forall t \quad \text{and} \quad k = 0, \dots, N_{\text{KL}}, \quad (45)$$

while the scaled temperature boundary conditions are

$$\theta_0(x = 0, y) = 1/2, \quad \theta_0(x = 1, y) = -1/2, \quad (46)$$

$$\theta_k(x = 0, y) = 0, \quad \theta_k(x = 1, y) = \sqrt{\lambda_k} f_k(y) \quad \text{for } k = 1, \dots, N_{\text{KL}}, \quad (47)$$

and

$$\frac{\partial \theta_k}{\partial y} = 0 \quad \text{for } y = 0, 1 \quad \text{and} \quad k = 0, \dots, N_{\text{KL}}. \quad (48)$$

The first-order PC expansion thus leads to a set of $N_{\text{KL}} + 1$ coupled momentum and heat equations and a set of $N_{\text{KL}} + 1$ decoupled divergence constraints.

ACKNOWLEDGMENTS

This work was supported by the Laboratory Directed Research and Development Program at Sandia National Laboratories, funded by the U.S. Department of Energy. Support was also provided by the Defense Advanced Research Projects Agency (DARPA) and Air Force Research Laboratory, Air Force Materiel Command, USAF, under agreement F30602-00-2-0612. The U.S. government is authorized to reproduce and distribute reprints for Governmental purposes notwithstanding any copyright annotation thereon. Computations were performed at the National Center for Supercomputer Applications.

REFERENCES

1. O. P. Le Maître, O. M. Knio, H. N. Najm, and R. G. Ghanem, A stochastic projection method for fluid flow. I. Basic formulation, *J. Comput. Phys.* **173**, 480 (2001).
2. S. Wiener, The homogeneous chaos, *Am. J. Math.* **60**, 897 (1938).
3. R. H. Cameron and W. T. Martin, The orthogonal development of nonlinear functionals in series of Fourier–Hermite functionals, *Ann. Math.* **48**, 385 (1947).
4. A. J. Chorin, Hermite expansions in Monte-Carlo computation, *J. Comput. Phys.* **8**, 472 (1971).
5. F. H. Maltz and D. L. Hitzl, Variance reduction in Monte Carlo computations using multi-dimensional Hermite polynomials, *J. Comput. Phys.* **32**, 345 (1979).
6. W. C. Meecham and D. T. Jeng, Use of the Wiener–Hermite expansion for nearly normal turbulence, *J. Fluid Mech.* **32**, 225 (1968).
7. S. C. Crow and G. H. Canavan, Relationship between a Wiener–Hermite expansion and an energy cascade, *J. Fluid Mech.* **41**, 387 (1970).
8. A. J. Chorin, Gaussian fields and random flow, *J. Fluid Mech.* **63**, 21 (1974).
9. R. G. Ghanem and P. D. Spanos, *Stochastic Finite Elements: A Spectral Approach* (Springer-Verlag, Berlin/New York, 1991).
10. G. De Vahl Davis and I. P. Jones, Natural convection in a square cavity: A comparison exercise, *Int. J. Numer. Methods Fluids* **3**, 227 (1983).
11. P. Le Quéré and T. Alziary de Roquefort, Computation of natural-convection in two-dimensional cavities with Tschebyscheff polynomials, *J. Comput. Phys.* **57**, 210 (1985).
12. P. Le Quéré, Accurate solution to the square thermally driven cavity at high Rayleigh number, *Comput. Fluids* **20**(1), 29 (1991).
13. D. R. Chenoweth and S. Paolucci, Natural convection in an enclosed vertical layer with large horizontal temperature differences, *J. Fluid Mech.* **169**, 173 (1986).
14. P. Le Quéré, R. Masson, and P. Perrot, A Chebyshev collocation algorithm for 2D non-Boussinesq convection, *J. Comput. Phys.* **103**, 320 (1992).
15. H. Paillere and P. Le Quéré, Modelling and simulation of natural convection flows with large temperature differences: A benchmark problem for low Mach number solvers, presented at 12th Seminar “Computational Fluid Dynamics” CEA/Nuclear Reactor Division, Saclay, France 2000.
16. M. Christon, P. Gresho, and S. Sutton, Computational predictability of natural convection flows in enclosure, in *Computational Fluid and Solid Mechanics*, edited by K. Bathe, Proceedings of First MIT Conference on Computational Fluid and Solid Mechanics (Elsevier, Amsterdam, 2001), pp. 1465–1468.
17. D. M. Christopher, Numerical prediction of natural convection flows in a tall enclosure, in *Computational Fluid and Solid Mechanics*, edited by K. Bathe, Proceedings of First MIT Conference on Computational Fluid and Solid Mechanics (Elsevier, Amsterdam, 2001), pp. 1469–1471.
18. G. Comini, M. Manzan, C. Nonino, and O. Saro, Finite element solutions for natural convection in a tall rectangular cavity, in *Computational Fluid and Solid Mechanics*, edited by K. Bathe, Proceedings of First MIT Conference on Computational Fluid and Solid Mechanics (Elsevier, Amsterdam, 2001), pp. 1472–1476.
19. G. Groce and M. Favero, Simulation of natural convection flow in enclosures by an unstaggered grid Finite volume algorithm, in *Computational Fluid and Solid Mechanics*, edited by K. Bathe, Proceedings of First MIT Conference on Computational Fluid and Solid Mechanics (Elsevier, Amsterdam, 2001), pp. 1477–1481.

20. P. M. Gresho and S. Sutton, 8:1 thermal cavity problem, in *Computational Fluid and Solid Mechanics*, edited by K. Bathe, Proceedings of First MIT Conference on Computational Fluid and Solid Mechanics (Elsevier, Amsterdam, 2001), pp. 1482–1485.
21. H. Johnston and R. Krasny, Computational predictability of natural convection flows in enclosures: A benchmark problem, in *Computational Fluid and Solid Mechanics*, edited by K. Bathe, Proceedings of First MIT Conference on Computational Fluid and Solid Mechanics (Elsevier, Amsterdam, 2001), pp. 1486–1489.
22. S.-E. Kim and D. Choudhury, Numerical investigation of laminar natural convection flow inside a tall cavity using a finite volume based Navier–Stokes solver, in *Computational Fluid and Solid Mechanics*, edited by K. Bathe, Proceedings of First MIT Conference on Computational Fluid and Solid Mechanics (Elsevier, Amsterdam, 2001), pp. 1490–1492.
23. T.-W. Pan and R. Glowinski, A projection/wave-like equation method for natural convection flows in enclosures, in *Computational Fluid and Solid Mechanics*, edited by K. Bathe, Proceedings of First MIT Conference on Computational Fluid and Solid Mechanics (Elsevier, Amsterdam, 2001), pp. 1493–1496.
24. A. G. Salinger, R. B. Lehoucq, R. P. Pawlowski, and J. N. Shadid, Understanding the 8:1 cavity problem via scalable stability analysis algorithms, in *Computational Fluid and Solid Mechanics*, edited by K. Bathe, Proceedings of First MIT Conference on Computational Fluid and Solid Mechanics (Elsevier, Amsterdam, 2001), pp. 1497–1500.
25. S. A. Suslov and S. Paolucci, A Petrov–Galerkin method for flows in cavities, in *Computational Fluid and Solid Mechanics*, edited by K. Bathe, Proceedings of First MIT Conference on Computational Fluid and Solid Mechanics (Elsevier, Amsterdam, 2001), pp. 1501–1504.
26. K. W. Westerberg, Thermally driven flow in a cavity using the Galerkin finite element method, in *Computational Fluid and Solid Mechanics*, edited by K. Bathe, Proceedings of First MIT Conference on Computational Fluid and Solid Mechanics (Elsevier, Amsterdam, 2001), pp. 1505–1508.
27. S. Xin and P. Le Quéré, An extended Chebyshev pseudo-spectral contribution to CPNCFE benchmark, in *Computational Fluid and Solid Mechanics*, edited by K. Bathe, Proceedings of First MIT Conference on Computational Fluid and Solid Mechanics (Elsevier, Amsterdam, 2001), pp. 1509–1513.
28. A. M. Lankhorst, *Laminar and Turbulent Natural Convection in Cavities; Numerical Modeling and Experimental Validation*, Ph.D. thesis (Delft University of Technology, 1991).
29. M. Loève, *Probability Theory* (Springer-Verlag, Berlin/New York, 1997).
30. M. Abramowitz and I. A. Stegun, *Handbook of Mathematical Functions* (Dover, New York, 1970).
31. O. M. Knio and R. G. Ghanem, *Polynomial Chaos Product and Moment Formulas: A User Utility*, Technical report (The Johns Hopkins University, Baltimore), to appear.
32. M. D. McKay, W. J. Conover, and R. J. Beckman, A comparison of three methods for selecting values of input variables in the analysis of output from a computer code, *Technometrics* **21**, 239 (1979).
33. R. Ghanem and S. Dham, Stochastic finite element analysis for multiphase flow in heterogeneous porous media, *Trans. Porous Media* **32**, 239 (1998).
34. R. Ghanem, Probabilistic characterization of transport in heterogeneous porous media, *Comput. Methods Appl. Mech. Eng.* **158**, 199 (1998).
35. A. J. Chorin, A numerical method for solving incompressible viscous flow problems, *J. Comput. Phys.* **2**, 12 (1967).
36. J. Kim and P. Moin, Application of a fractional-step method to the incompressible Navier–Stokes equations, *J. Comput. Phys.* **59**, 308 (1985).
37. M. S. Eldred, A. A. Giunta, S. F. Wojtkiewicz, B. G. van Bloemen Waanders, W. E. Hart, and M. P. Alleva, *DAKOTA, A Multilevel Parallel Object-Oriented Framework for Design Optimization, Parameter Estimation, Sensitivity Analysis, and Uncertainty Quantification, Version 3.0 Reference Manual*, Sandia Technical Report SAND02-XXXX, in preparation (Sandia National Laboratories, 2002); http://endo.sandia.gov/DAKOTA/papers/Dakota_hardcopy.pdf.
38. S. F. Wojtkiewicz, M. S. Eldred, R. V. Field, A. Urbina, and J. R. Red-Horse, *A Toolkit for Uncertainty Quantification in Large Computational Engineering Models, Meeting Paper 2001-1455* (AIAA Press, Washington, DC, 2001).
39. M. S. Eldred, *Optimization Strategies for Complex Engineering Applications*, Sandia Technical Report SAND98-0340 (Sandia National Laboratories, 1998).



ELSEVIER

Available online at www.sciencedirect.com

SCIENCE @ DIRECT®

Comput. Methods Appl. Mech. Engrg. 192 (2003) 4723–4744

**Computer methods
in applied
mechanics and
engineering**

www.elsevier.com/locate/cma

A multigrid solver for two-dimensional stochastic diffusion equations

O.P. Le Maître ^{a,*}, O.M. Knio ^b, B.J. Debuschere ^c, H.N. Najm ^c,
R.G. Ghanem ^d

^a *Université d'Evry Val d'Essonne, Centre d'Etudes de Mécanique d'Ile de France, 40 Rue du Pelvoux CE 1455,
91 020 Evry cedex, France*

^b *Department of Mechanical Engineering, Johns Hopkins University, Baltimore, MD 21218-2686, USA*

^c *Sandia National Laboratories, Combustion Research Facility, Livermore, CA 94550, USA*

^d *Department of Civil Engineering, Johns Hopkins University, Baltimore, MD 21218-2686, USA*

Received 4 October 2002; received in revised form 9 June 2003; accepted 11 July 2003

Abstract

Steady and unsteady diffusion equations, with stochastic diffusivity coefficient and forcing term, are modeled in two dimensions by means of stochastic spectral representations. Problem data and solution variables are expanded using the Polynomial Chaos system. The approach leads to a set of coupled problems for the stochastic modes. Spatial finite-difference discretization of these coupled problems results in a large system of equations, whose dimension necessitates the use of iterative approaches in order to obtain the solution within a reasonable computational time. To accelerate the convergence of the iterative technique, a multigrid method, based on spatial coarsening, is implemented. Numerical experiments show good scaling properties of the method, both with respect to the number of spatial grid points and the stochastic resolution level.

© 2003 Elsevier B.V. All rights reserved.

Keywords: Stochastic problem; Diffusion equation; Multigrid; Polynomial Chaos; Karhunen–Loève expansion; Random media

1. Introduction

Developments in the field of computational mechanics and physics are enabling the solution of increasingly more realistic engineering problems. These advances take advantage of (i) enhanced computational capabilities—including parallel platforms and parallel techniques; (ii) elaborate models to handle more physical effects with less approximation of the system dynamics; and (iii) the development of numerical methods to reduce computational time and/or improve accuracy. As with many other fields, the

* Corresponding author.

E-mail addresses: olm@cemif.univ-evry.fr (O.P. Le Maître), knio@jhu.edu (O.M. Knio), bjdebus@ca.sandia.gov (B.J. Debuschere), hnnajm@ca.sandia.gov (H.N. Najm), ghanem@jhu.edu (R.G. Ghanem).

field of computational stochastic mechanics has benefited from such recent developments, and reached a level of maturity that allows for simulations that provide meaningful predictions to problems involving uncertain data [36]. Computational stochastic mechanics is particularly attractive in engineering sciences and physics, where the system to be analyzed can rarely be characterized exactly, while numerical methods usually require deterministic inputs. The present work takes place in this context.

Uncertainties in simulations of mechanical systems can be related to an inexact knowledge of the system geometry (e.g. [4,32]), boundary and initial conditions (e.g. [23,24,43]), external forcing (e.g. [18]), physical properties, or model parameters. Uncertainties can sometimes be due to measurement difficulties or to the intrinsic randomness of the processes, as in the case of heterogeneous media [14,15,29]. In order to deal with these uncertainties, distinct computational strategies have emerged, including Monte Carlo simulations (MCS) [25] and the integration of stochastic differential equations (SDE) [17,20], or a blend of the two. In MCS, the response surface of the random process is estimated by computing the deterministic responses of the system for a (large) set of distinct conditions that appropriately sample the uncertainty domain. In contrast, integration of the SDE governing the system is usually more difficult than the corresponding deterministic problem. Usually, integration of the SDE is achieved approximately, through statistical linearizations, asymptotic expansions, perturbation methods or truncated spectral representations. In the present study, uncertainty is taken into account by means of spectral expansions along the stochastic dimensions using Polynomial Chaos (PC) representations [5,42]. This representation is used to obtain a full statistical characterization of the response, in contrast with the other cited approaches which are usually limited to the very first statistical moments. Moreover, the spectral representation is now well established. Over the last few years, this technique has been successfully applied in various settings, including both solid and fluid mechanics [14,18,19,21,23,24,26,28,29,33,36–38].

In this work, we focus on a “generic” diffusion problem for a quantity u , with a random, spatially varying isotropic diffusion coefficient λ , inside a two-dimensional domain \mathbf{D} . The general form of the governing equation for this problem can be expressed as:

$$\alpha \frac{\partial u(\mathbf{x}, t, \theta)}{\partial t} = \nabla \cdot [\lambda(\mathbf{x}, t, \theta) \nabla u(\mathbf{x}, t, \theta)] + s(\mathbf{x}, t, \theta), \quad (1)$$

where $\alpha = 0, 1$ in the steady and unsteady cases, respectively, s is a given stochastic source term, and $\theta(\omega)$ denotes the stochastic character of the solution. The formulation is completed by specifying boundary conditions for u (generally Neumann or Dirichlet conditions), as well as an initial condition in the unsteady case. The elliptic form of Eq. (1) has been thoroughly analyzed from the mathematical point of view; see for instance [3,7,20,40].

Our current interest in an efficient solution method for Eq. (1) comes from the simulation of reacting electrochemical microchannel flow [9], where the steady form of the equation governs the electric field. There, u is the electrostatic field potential, λ is the electrical conductivity, and s is the charge accumulation due to diffusion of dissociated species (ions). λ and s are expressed as:

$$\lambda = F^2 \sum z_i^2 \mu_i c_i, \quad s = F \sum z_i \nabla \cdot (D_i \nabla c_i), \quad (2)$$

where F is the Faraday constant, z_i , μ_i , D_i and c_i are the charge number, electrophoretic mobility, molar diffusivity and molar concentration of the species i respectively [35]. Eq. (1) becomes stochastic whenever λ , s or the initial/boundary conditions on u are uncertain. In addition to this specific example, Eq. (1) appears, by itself or as part of a larger system, in the formulation of many problems involving gradient diffusion processes [9,19–21,23,26,33,37], as well as a variety of problems such as 1D-linear elasticity problems [10] and electromagnetism [38]. Therefore, an abstract study in a broader context than electrochemical flow is well justified.

A major difficulty in the solution of Eq. (1) concerns the representation of the stochastic diffusivity and source fields, and of the solution itself. As stated before, we will make use of spectral representations [17]

for this purpose. For brevity, but without loss of generality, the diffusivity field will be represented in terms of the Karhunen–Loève (KL) expansion, which is assumed to be known. Following the discussion above, this enables us to avoid describing the auxiliary problem of explicitly modeling the uncertainty in λ , and consequently focus our attention on the solution for u , which is sought in terms of its PC representation [17,20,36]. While the source term s may also be given in terms of a KL representation or more generally by a PC expansion, we will restrict our attention in the numerical tests to the case where $s \equiv 0$, i.e. to the homogeneous form of Eq. (1). For the purpose of the present construction, this enables us to avoid unnecessary details associated with setting up a stochastic source field. Both of these restrictions, however, can be easily relaxed within the framework of the construction.

One potential drawback of the spectral approach is that the size of the system of equations that needs to be solved grows rapidly as the number of stochastic dimensions increases. Specifically, the size of the stochastic system scales with the number of spectral-expansion modes retained in the computation, which increases rapidly with the number of dimensions and with the order of the expansion. Furthermore, since the equations governing the uncertainty modes are generally coupled, the CPU time needed to solve the stochastic system can increase rapidly with system size. This poses a serious computational challenge, which requires the development of efficient solvers [30,31,34]. The present study specifically aims at this objective, in the context of the generic formulation given in Eq. (1). Specifically, we describe the adaptation of a (deterministic) multigrid (MG) technique [41] for the solution of the system of equations arising from the finite-difference discretization of the spectral representation of the stochastic diffusion equation.

This paper is organized as follows. In Section 2, we recall the basic concepts and properties of the PC expansion of a stochastic process. Using these concepts, the stochastic spectral formulation of Eq. (1) is derived in Section 3 and the difficulties inherent to the solution of the spectral equations are discussed. Next, the finite-difference discretization of the stochastic system is introduced (Section 4), and an iterative technique is proposed to solve the resulting set of equations. In Section 5, a multigrid technique, based on spatial coarsening, is developed to improve the convergence rate of the previous iterative method. The multigrid algorithm is applied to selected test problems in Section 6, and the tests are used to examine its efficiency and scalability properties. Major findings are summarized in Section 7.

2. Polynomial Chaos representation

2.1. Spectral representation

In this section, the spectral representation of the stochastic process $u(\mathbf{x}, t, \theta)$ by means of the PC system is introduced. We consider the case where the uncertainty is due to a set of N independent (uncorrelated) stochastic parameters. The problem is then said to possess N stochastic dimensions, denoted by ξ_1, \dots, ξ_N , which are considered as generators of new dimensions (in addition to the space and time dimensions) in the solution process. Thus we have $\theta \equiv \{\xi_1, \dots, \xi_N\}$. Noting that u is a non-linear functional of its stochastic argument θ , it is natural to look for an orthogonal expansion of u in terms of the random variables ξ_i , $i = 1, \dots, N$. This idea has led to the concepts of homogeneous chaos and of PC expansions [5,17,42], in the case of Gaussian variables. The case of non-Gaussian measures is discussed in [12,13], but will not be considered here.

The dependence of $u(\mathbf{x}, t, \theta)$ on its stochastic arguments is approximated with the following truncated expansion:

$$u(\mathbf{x}, t, \theta) = \sum_{k=0}^P u_k(\mathbf{x}, t) \Psi_k(\theta), \quad (3)$$

where u_k are deterministic coefficients and $\{\Psi_0, \dots, \Psi_P\}$ is a (truncated) orthogonal basis consisting of multidimensional Hermite polynomials in ξ_i . The truncation is such that the degree of the polynomials is at most equal to N_0 , the order of the expansion. The total number of modes, $P + 1$, depends on N and N_0 , according to [8]:

$$P + 1 = \frac{(N + N_0)!}{N!N_0!}. \quad (4)$$

The orthogonality of the spectral basis $\{\Psi_k, k = 0, \dots, P\}$ on which u is expanded is defined with respect to the inner product:

$$\langle \Psi_i \Psi_j \rangle \equiv \int \dots \int \Psi_i(\theta) \Psi_j(\theta) g(\xi_1) \dots g(\xi_n) d\xi_1 \dots d\xi_n, \quad (5)$$

where

$$g(\xi) = \frac{e^{-\xi^2/2}}{\sqrt{2\pi}} \quad (6)$$

is the Gaussian measure. Since θ is a Gaussian vector, inner products (Eq. (5)) and higher moments can be efficiently computed using moment formulas [22], based on a straightforward generalization of Gauss quadrature in one spatial dimension [1].

2.2. PC expansions of field variables

In general, all field variables may exhibit a stochastic character and should therefore be represented with PC expansions. In particular, the diffusivity and source fields can be expressed as:

$$\lambda(\mathbf{x}, t, \theta) = \sum_{k=0}^P \lambda_k(\mathbf{x}, t) \Psi_k(\theta), \quad s(\mathbf{x}, t, \theta) = \sum_{k=0}^P s_k(\mathbf{x}, t) \Psi_k(\theta), \quad (7)$$

respectively. Clearly, if λ and s are deterministic, then all modes with index $k > 0$ vanish identically. When this is not the case, the solution process u immediately admits a stochastic character, even when the boundary and, if relevant, initial conditions are deterministic.

The formulation above is quite general, and enables us to accommodate situations where the initial and boundary conditions on u , the diffusivity field, λ , and source field, s , are all uncertain. While the general case may be of interest, its treatment would require a detailed analysis of the source of uncertainty, which would distract from the present objective. Thus, in order to limit the scope of the simulations, while at the same time provide a meaningful test to the solver below, we restrict our attention to the case of a random diffusivity, deterministic boundary conditions, and vanishing source field. The diffusivity λ is assumed to be given by a Gaussian process with an exponentially decaying covariance function:

$$C(\mathbf{x}, \mathbf{x}') = \sigma_\lambda^2 \exp - \frac{\|\mathbf{x} - \mathbf{x}'\|}{L_c}, \quad (8)$$

where L_c is the correlation length and σ_λ is the standard deviation. We then use KL expansion [16,27] to express $\lambda(\mathbf{x})$ as:

$$\lambda(\mathbf{x}) = \bar{\lambda} + \sum_{k=1}^{\infty} \sqrt{\beta_k} \lambda_k(\mathbf{x}) \xi_k, \quad (9)$$

where $\bar{\lambda}$ is the mean value, ξ_k are uncorrelated Gaussian variables with zero mean and unit variance, while β_k and λ_k are, respectively, the eigenvalues and eigenfunctions appearing in the spectral representation of C :

$$C(\mathbf{x}, \mathbf{x}') = \sum_{k=1}^{\infty} \beta_k \lambda_k(\mathbf{x}) \lambda_k(\mathbf{x}'). \quad (10)$$

Note that, in general, $\bar{\lambda}$ may vary in space, but we shall restrict our attention in the computations below to the case of a uniform mean value.

In the computations below, the eigenvalues and eigenfunctions are obtained with the Galerkin procedure described in [14–16]. The eigenvalues, all positive, are arranged in decreasing magnitude, and the KL expansion is truncated after the first N terms. Also note that the first N Polynomial Chaos coincide with the normalized Gaussian variables ξ_k , i.e. $\Psi_k(\theta) = \xi_k$ for $k = 1, \dots, N$. Thus, the KL representation of λ can be formally viewed as a special case of a PC representation (Eq. (7)) in which polynomials of degree larger than one have vanishing coefficient. Different cases are considered by varying σ_λ and L_c , and analyzing their effect on the performance of the solver.

3. Continuous formulation and time discretization

3.1. Stochastic spectral diffusion equation

Introducing the PC expansions of the diffusivity, source and solution fields into the diffusion equation (1), one gets:

$$\alpha \sum_{k=0}^P \frac{\partial u_k}{\partial t} \Psi_k = \sum_{l=0}^P \sum_{m=0}^P \Psi_l \Psi_m \nabla \cdot [\lambda_l(\mathbf{x}, t) \nabla u_m(\mathbf{x}, t)] + \sum_{k=0}^P s_k(\mathbf{x}, t) \Psi_k. \quad (11)$$

Then, multiplying this equation by Ψ_i , evaluating its expectation and taking into account the orthogonality of the PC basis, we obtain:

$$\alpha \frac{\partial u_i(\mathbf{x}, t)}{\partial t} = \sum_{l=0}^P \sum_{m=0}^P \mathcal{M}_{ilm} \nabla \cdot [\lambda_l(\mathbf{x}, t) \nabla u_m(\mathbf{x}, t)] + s_i(\mathbf{x}, t) \quad \text{for } i = 0, \dots, P. \quad (12)$$

The *multiplication* tensor

$$\mathcal{M}_{ilm} \equiv \frac{\langle \Psi_i \Psi_l \Psi_m \rangle}{\langle \Psi_i \Psi_i \rangle} \quad (13)$$

is independent of the solution, and is therefore computed and stored during a pre-processing stage. A multi-dimensional Gauss-quadrature approach [22] is used for this purpose. The tensor \mathcal{M} is sparse with a structure that depends on the order of the PC expansion and on the number of stochastic dimensions. The sparse nature of \mathcal{M} comes from the fact that many of the triple products $\Psi_i \Psi_j \Psi_k$, have vanishing expectation. For instance, due to orthogonality $\langle \Psi_0 \Psi_i \Psi_j \rangle = \delta_{ij} \langle \Psi_i^2 \rangle$. Also note that the triple product $\Psi_i \Psi_j \Psi_k$ can be written as the product of 1D polynomials, according to:

$$\Psi_i \Psi_j \Psi_k(\xi_1, \dots, \xi_N) = \prod_{q=1}^N p_{ijk}^q(\xi_q), \quad (14)$$

where $p_{ijk}^q(\xi_q)$ is a triple product of 1D Hermite polynomials. Thus, in order for $\langle \Psi_i \Psi_j \Psi_k \rangle$ to vanish, it is sufficient that only one p_{ijk}^q has vanishing expectation. On the other hand, \mathcal{M} is generally *not* diagonal (except for $N_0 = 0$), which leads to coupling between the u_i modes. An immediate consequence of this

coupling is an increase in the size of the resulting system of equations to be solved, compared to the deterministic case.

For unsteady problems, the use of an explicit time integration scheme for Eq. (12), as proposed in [23] in the context of the Navier–Stokes equations, leads to a simple algorithm that requires direct evaluation of the coupling terms. The use of explicit time-schemes has shown its efficiency for transient computations, but explicit stability restrictions on the time step can prove prohibitive on fine grids. For steady-state problems, a pseudo-transient approach may also be conceived, but in this case as well stability restrictions may lead to poor computational efficiency. Consequently, the development of an efficient numerical solver for the coupled system of equations is needed. This approach is adopted in the development below.

3.2. Boundary and initial conditions

Boundary conditions, and, when relevant, initial conditions, are needed to solve Eq. (12). These are also implemented in a “weak sense”, i.e. the boundary conditions are also projected onto the PC basis, leading to explicit conditions for each of the u_i 's. As noted in the introduction, the boundary conditions in the present study can be either of the Neumann or Dirichlet type. For brevity, we assume here that the boundary conditions are deterministic; an example of the use of uncertain boundary conditions is given in [24]. Denoting by $\partial\mathbf{D}_D$ and $\partial\mathbf{D}_N$ the part of the boundaries of \mathbf{D} where Dirichlet and Neumann conditions apply, respectively, the boundary conditions for all modes are given by:

$$u_0(\mathbf{x}, t) = u^D(\mathbf{x}, t), \quad u_{i \in [1, P]}(\mathbf{x}, t) = 0 \quad \forall \mathbf{x} \in \partial\mathbf{D}_D, \quad (15)$$

$$\frac{\partial u_0}{\partial n}(\mathbf{x}, t) = g_0^N(\mathbf{x}, t), \quad \frac{\partial u_k}{\partial n}(\mathbf{x}, t) = 0, \quad k = 1, \dots, P \quad \forall \mathbf{x} \in \partial\mathbf{D}_N, \quad (16)$$

where n denotes the direction normal to the boundary.

Note that for steady problems involving only Neumann conditions, the modes of the source field must satisfy the integral constraints

$$\int_D s_k(\mathbf{x}) d\mathbf{x} = \int_{\partial\mathbf{D}} \sum_{l=0}^P \mathcal{M}_{kl0} \lambda_l g_0^N ds \quad \text{for } k = 1, \dots, P. \quad (17)$$

Here, ds is the surface element along $\partial\mathbf{D}$. For unsteady problems, an initial condition for u is required. This initial condition may be deterministic or uncertain. In the former case, we have

$$u_0(\mathbf{x}, t = 0) = u_0^0(\mathbf{x}), \quad u_k(\mathbf{x}, t = 0) = 0, \quad \text{for } k = 1, \dots, P. \quad (18)$$

On the other hand, when the initial condition is uncertain, initial conditions for all the modes u_k need to be specified.

3.3. Implicit time discretization

A simple, generic, example of an implicit time integration method is the Euler backward scheme, whose application to Eq. (12) results in the following semi-discrete form:

$$\frac{\alpha}{\Delta t} u_i^{n+1} - \sum_{l=0}^P \sum_{m=0}^P \mathcal{M}_{ilm} \nabla \cdot [\lambda_l^{n+1}(\mathbf{x}) \nabla u_m^{n+1}] = s_i^{n+1}(\mathbf{x}) + \frac{\alpha}{\Delta t} u_i^n, \quad (19)$$

where Δt is the time step and the superscripts refer to the time level. In the following, the dependence of λ and s on time is dropped, since these fields are assumed to be given.

4. Finite-difference discretization

4.1. Spatial discretization

Let $\mathbf{D} \equiv [0, L] \times [0, H]$ be a rectangular domain discretized in a set of $N_x \times N_y$ non-overlapping cells with uniform size $\Delta x = L/N_x$ and $\Delta y = H/N_y$ in the x - and y -directions. We denote by $(\Phi)_{i,j}$, for $i = 1, \dots, N_x$ and $j = 1, \dots, N_y$ the cell-averaged value of Φ , so that

$$(\Phi)_{i,j} \equiv \frac{1}{\Delta x \Delta y} \int_{(i-1)\Delta x}^{i\Delta x} \int_{(j-1)\Delta y}^{j\Delta y} \Phi(\mathbf{x}) \, dx \, dy, \quad (20)$$

where Φ stands for any of the field variables u_k , λ_k and s_k . Using this convention, we rely on the following centered, second-order spatial discretization of Eq. (19):

$$\begin{aligned} \frac{\alpha}{\Delta t} (u_k^{n+1})_{i,j} - \sum_{l=0}^P \sum_{m=0}^P \mathcal{M}_{klm} \left[\frac{(\lambda_l)_{i+1,j} + (\lambda_l)_{i,j}}{2} \frac{(u_m^{n+1})_{i+1,j} - (u_m^{n+1})_{i,j}}{\Delta x^2} \right. \\ \left. - \frac{(\lambda_l)_{i,j} + (\lambda_l)_{i-1,j}}{2} \frac{(u_m^{n+1})_{i,j} - (u_m^{n+1})_{i-1,j}}{\Delta x^2} + \frac{(\lambda_l)_{i,j+1} + (\lambda_l)_{i,j}}{2} \frac{(u_m^{n+1})_{i,j+1} - (u_m^{n+1})_{i,j}}{\Delta y^2} \right. \\ \left. - \frac{(\lambda_l)_{i,j} + (\lambda_l)_{i,j-1}}{2} \frac{(u_m^{n+1})_{i,j} - (u_m^{n+1})_{i,j-1}}{\Delta y^2} \right] = (s_k^{n+1})_{i,j} + \frac{\alpha}{\Delta t} (u_k^n)_{i,j}, \quad k = 0, \dots, P. \end{aligned} \quad (21)$$

The above equation can be re-cast in the following generic form:

$$\begin{aligned} \sum_{l=0}^P \sum_{m=0}^P \mathcal{M}_{klm} \left[(W_l)_{i,j} (u_m^{n+1})_{i+1,j} + (E_l)_{i,j} (u_m^{n+1})_{i-1,j} + (N_l)_{i,j} (u_m^{n+1})_{i,j+1} \right. \\ \left. + (S_l)_{i,j} (u_m^{n+1})_{i,j-1} + (C_l^k)_{i,j} (u_m^{n+1})_{i,j} \right] = (f_k^{n+1})_{i,j}, \quad k = 0, \dots, P, \end{aligned} \quad (22)$$

which shows that a linear system of $N_x \times N_y \times (P+1)$ equations must be solved in order to advance the solution by one time step. Of course, in the steady case this system is solved only once, and the superscripts indicating the time level are no longer needed.

4.1.1. Treatment of boundary conditions

Both Dirichlet and Neumann conditions are implemented using ghost cell techniques. For the case of Dirichlet condition, a ghost cell is introduced at the mirror image with respect to the boundary point of the neighboring interior cell. The value of the solution at the ghost cell is then determined by linearly extrapolating the solution from the interior, leading to a linear combination of the known value at the boundary and the neighboring interior node. Using this relationship, the ghost variables are then eliminated from the equation system. A similar approach is used in the case of a Neumann condition, based on expressing the known value of the normal derivative in terms of a second-order centered difference formula involving the solution at the neighboring internal node and the corresponding ghost node. The resulting relationship is then substituted into the equation system in order to eliminate the ghost variable. This approach results in a modified system of the form

$$\begin{aligned} \sum_{l=0}^P \sum_{m=0}^P \mathcal{M}_{klm} \left[(\tilde{W}_l)_{i,j} (u_m^{n+1})_{i+1,j} + (\tilde{E}_l)_{i,j} (u_m^{n+1})_{i-1,j} + (\tilde{N}_l)_{i,j} (u_m^{n+1})_{i,j+1} \right. \\ \left. + (\tilde{S}_l)_{i,j} (u_m^{n+1})_{i,j-1} + (\tilde{C}_l^k)_{i,j} (u_m^{n+1})_{i,j} \right] = (\tilde{f}_k^{n+1})_{i,j}, \end{aligned} \quad (23)$$

where the tildes are used to indicate the modified values after implementation of the boundary conditions.

4.2. Iterative method

Since the size of system (23) is large for most applications, iterative solution methods are preferred over direct schemes. In this work, Gauss–Seidel iterations are used [39].

4.2.1. Outer iterations

Let us denote by $(\tilde{\mathbf{u}}_m)_{i,j}^{ou}$ the estimate of $(\mathbf{u}_m^{n+1})_{i,j}$ after the ou -th Gauss–Seidel iteration. This estimate can be computed by applying the following algorithm, called *outer iterations*, in contrast with the *inner iterations* described later:

- Loop on ou (Gauss–Seidel index)
 - For $i = 1$ to N_x , do
 - For $j = 1$ to N_y , do
 - Find $(\tilde{\mathbf{u}}_k)_{i,j}^{ou+1}$ such that:

$$\begin{aligned} \sum_{l=0}^P \sum_{m=0}^P \mathcal{M}_{klm}(\tilde{\mathbf{C}}_l)_{i,j} (\tilde{\mathbf{u}}_m)_{i,j}^{ou+1} &= (\tilde{\mathbf{f}}_k^n)_{i,j} - \sum_{l=0}^P \sum_{m=0}^P \mathcal{M}_{klm} \left[(\tilde{\mathbf{W}}_l)_{i,j} (\tilde{\mathbf{u}}_m)_{i+1,j}^{ou} + (\tilde{\mathbf{E}}_l)_{i,j} (\tilde{\mathbf{u}}_m)_{i-1,j}^{ou+1} \right. \\ &\quad \left. + (\tilde{\mathbf{N}}_l)_{i,j} (\tilde{\mathbf{u}}_m)_{i,j+1}^{ou} + (\tilde{\mathbf{S}}_l)_{i,j} (\tilde{\mathbf{u}}_m)_{i,j-1}^{ou+1} \right] \\ &\equiv (Q_k)_{i,j}^{ou}, \quad k = 0, \dots, P \end{aligned} \quad (24)$$

End of loop on j

- End of loop on i
- End of loop on ou

Thus,

$$(R_k)_{i,j}^{ou} = (Q_k)_{i,j}^{ou} - \sum_{l=0}^P \sum_{m=0}^P \mathcal{M}_{klm}(\tilde{\mathbf{C}}_l)_{i,j} (\tilde{\mathbf{u}}_m)_{i,j}^{ou}$$

is the local residual of Eq. (24), for the k th mode, at the ou -th Gauss–Seidel iteration.

4.2.2. Inner iterations

For each point in space, Eq. (24) can be rewritten in vector form as:

$$\begin{bmatrix} \sum_{l=0}^P \mathcal{M}_{00l}(\tilde{\mathbf{C}}_l) & \dots & \sum_{l=0}^P \mathcal{M}_{0Pl}(\tilde{\mathbf{C}}_l) \\ \vdots & \ddots & \vdots \\ \sum_{l=0}^P \mathcal{M}_{P0l}(\tilde{\mathbf{C}}_l) & \dots & \sum_{l=0}^P \mathcal{M}_{PPl}(\tilde{\mathbf{C}}_l) \end{bmatrix} \cdot \begin{pmatrix} (\tilde{\mathbf{u}}_0)^{ou+1} \\ \vdots \\ (\tilde{\mathbf{u}}_P)^{ou+1} \end{pmatrix} = \begin{pmatrix} (Q_0)^{ou} \\ \vdots \\ (Q_P)^{ou} \end{pmatrix}, \quad (25)$$

where the grid-point indices have been dropped for clarity. Thus, at this stage, one has to solve a system of $P + 1$ equations to compute $(\tilde{\mathbf{u}}_{k=0,\dots,P})_{i,j}^{ou+1}$ from Eq. (24). A standard relaxation method (SOR) [39] is employed for this purpose. Denoting by ω the over-relaxation parameter, and by $[A_{km}]$ the system matrix corresponding to (25), the iterations are performed according to:

- Loop over in (SOR index)
 - Do $k = 0, \dots, P$
 - Compute a new estimate of $(\tilde{\mathbf{u}}_k)$ solution of Eq. (25) using

$$(\tilde{\mathbf{u}}_k)_{in+1} = (1 - \omega)(\tilde{\mathbf{u}}_k)_{in} + \frac{\omega}{A_{kk}} \left((Q_k)_{in} - \sum_{m=0}^{k-1} A_{km}(\tilde{\mathbf{u}}_m)_{in+1} - \sum_{m=k+1}^P A_{km}(\tilde{\mathbf{u}}_m)_{in} \right) \quad (26)$$

- End of loop over k .
- End of loop over in .

Note that for convenience, the Gauss–Seidel index ou has been dropped in Eq. (26).

Remark. The above decomposition of the iterative scheme into outer and inner loops may appear artificial, since a global iteration on the three-dimensional system for $(u_k^{n+1})_{i,j}$ could be constructed. However, in view of the implementation of the multigrid scheme, which is based on spatial coarsening, it is found more convenient to clearly distinguish the inner iterations—which locally update the spectral coefficients of the solution, from the outer iterations—which account for the spatial coupling. In addition, computational tests (not shown) indicate that the convergence of the outer GS iteration is greatly improved when a more accurate estimate of the exact solution of Eq. (25) is used.

4.3. Convergence of the iterative scheme

The efficiency of the overall iterative method proposed above is estimated through the convergence rate of $(\tilde{u})^{ou}$ towards $(u)^{n+1}$, as the number of iterations ou increases. This convergence rate depends on the spectral radius of the system (23). Since \mathcal{M}_{klm} does not depend on the solution variables or parameters, the spectral radius is only a function of the stochastic diffusivity field $\lambda(x, \theta)$, of the time-step Δt (if relevant), and of Δx and Δy . For the deterministic problem ($P = 0$), it is known that $(\lambda)_{i,j} \geq 0$ for all i, j is necessary to ensure convergence, and that the convergence rate deteriorates when $\alpha/\Delta t$ decreases. In the stochastic case, the positivity of $\lambda_{i,j}$ is not ensured for all possible realizations. On the other hand, the numerical experiences in Section 6 indicate that the iterations converge when the coefficient of variation (COV), $\sigma_\lambda/\bar{\lambda}$, is sufficient small. As COV increases, the convergence rate of the present iterative scheme deteriorates; convergence fails above a critical value. These experiences appear to be consistent with the theoretical results in [2], where uniformly distributed random variables were used to ensure positivity. In the latter case, it is shown [2] that when COV is small, the solution exists and may be obtained by successive approximation.

The measure of convergence is obtained through the L^2 -norm of the residual for a given mode l which is expressed as:

$$\mathcal{N}_l \equiv \left\{ \sum_{i=1}^{N_x} \sum_{j=1}^{N_y} [(R_l)_{i,j}]^2 \Delta x \Delta y \right\}^{1/2}. \quad (27)$$

The convergence of the iterative method will be further analyzed in Section 6 by monitoring the evolution of the maximum (over all modes) normalized residual:

$$\mathcal{R}_p \equiv \frac{\max_l [\mathcal{N}_l(p)]}{\max_l [\mathcal{N}_l(p=0)]} \quad (28)$$

where the index p refers to the number of MG cycles.

5. Multigrid acceleration

It is known from the analysis of deterministic diffusion equations that the convergence rate is a function of spatial frequencies. Specifically, the longest wavelengths exhibit the lowest convergence rate, while short scales converge faster. To improve convergence, acceleration techniques based on spatial coarsening have been proposed in the literature [6,11,41]. In the present work, we develop a multigrid technique for the stochastic case.

The basic idea of the multigrid technique is to treat the modes with low spatial frequencies on coarser grids, since fine spatial resolution is not required for these modes. The gain of the method is due to the faster convergence of the long-wave modes on the coarser grids, as well as the lower CPU cost of the corresponding iterations. Since multigrid methods are widely used, we will just recall the main ingredients of the approach, namely (i) the definition of the grid levels, (ii) the projection step and (iii) the prolongation procedure.

5.1. Definition of grid levels

Thanks to the regular structure of the computational grid, the coarsening is made by merging a set of neighboring grid cells to give a single cell on the next (coarser) grid level. This leads to a hierarchical set of grids. In the current implementation, a coarsening step consists of merging four cells (two in each direction) with surface areas $\Delta x^k \times \Delta y^k$ each, to obtain a child cell with surface area $\Delta x^{k+1} \times \Delta y^{k+1} = 4\Delta x^k \times \Delta y^k$, the superscripts denoting the respective grid levels. Thus, starting from a grid level k , made of $N_x^k \times N_y^k$ cells, the next grid level contains $N_x^{k+1} \times N_y^{k+1} = (N_x^k \times N_y^k)/4$ cells. Clearly, this process can be repeated as long as N_x^k and N_y^k are even numbers. Whenever one of the number of cells in a direction is odd, the coarsening automatically switches to a one-dimensional coarsening procedure in which only two cells are merged to make a child cell. This procedure is illustrated in Fig. 1, where the successive grid levels are plotted. Clearly the procedure is optimal when N_x and N_y are powers of 2.

5.2. Projection and prolongation procedures

On the finest grid level, a small number N_{ou} of outer iterations is first performed. This provides approximate solutions $(\tilde{u}_m)_{i,j}^{N_{ou}}$ with residuals $(R_m)_{i,j}^{N_{ou}}$. These residuals are then projected onto the next coarser grid, where problem (23) is considered, with $(R_m)_{i,j}^{N_{ou}}$ as the right-hand side (in lieu of $(f_k)_{i,j}$), and with the same but *homogeneous* boundary conditions. (In other words, on the coarser grids, the *residual equation* is solved.) To do so, one has to provide an estimate of (λ) and (R_m) on consecutive grid levels. This is achieved by averaging their respective values over the *parent* cells as illustrated in the left scheme of Fig. 2a.

On the new grid level, a few outer iterations are performed, following the same methodology, to obtain an approximate solution and a residual. The projection process is repeated until the last grid level is reached. Then, from the coarser grid level, where an estimate solution for the residual equation has been obtained, it is first transferred to the previous grid level through a prolongation procedure and then used to correct the solution on that finer grid level. In the current implementation, this is achieved by summing the cell averaged solution at level k with the solution of its parent cell, as shown in Fig. 2b. When the solution has been prolonged onto level $k - 1$, a few outer iterations are performed (smoothing step) the process is repeated until the initial, fine, grid is reached.

5.3. Multigrid cycles

Starting from the original grid, the application of successive projections up to the coarsest grid level, followed by successive prolongations up to the starting grid, is referred to as a cycle. Different kinds of cycles may be used [41], according to the excursion path along the grid levels. For instance, the so-called W-cycles have been designed to improve the convergence rate of the multigrid method, and many other examples can be found in the literature. Since our objective here is simply to develop a multigrid methodology for stochastic diffusion equations, we have limited ourselves to the simplest case of the V-cycle as described above. Moreover, we use a constant number of Gauss–Seidel iterations, denoted N_{ou} , on every grid-level, after every projection or prolongation step.

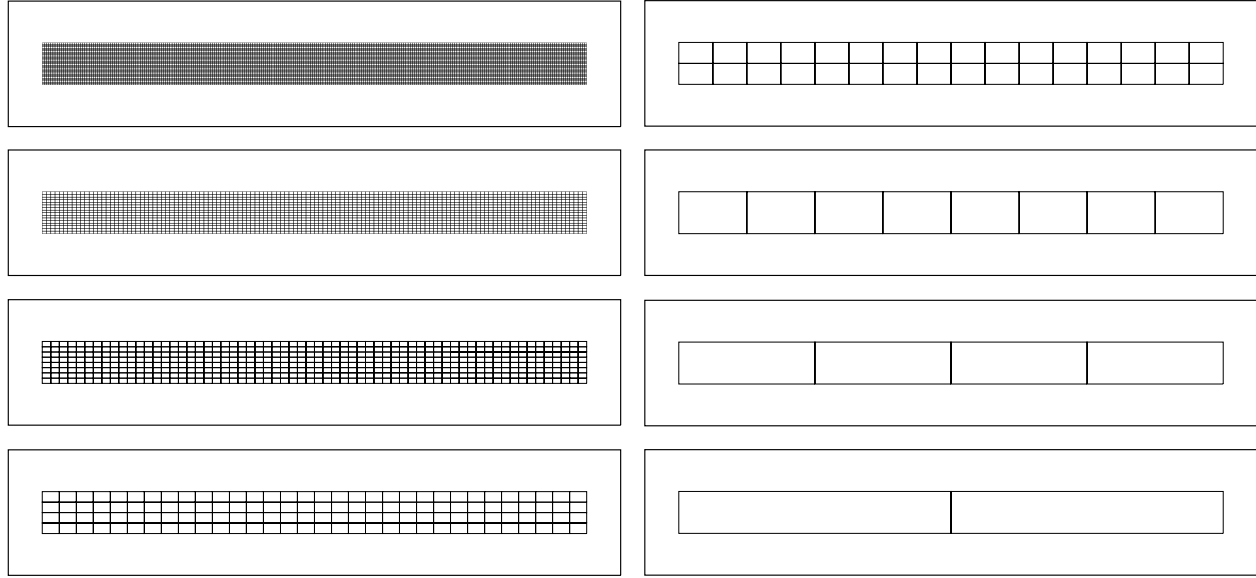


Fig. 1. Example of grid coarsening used for the multigrid method. The base grid consists of 32×256 cells (top left). The mesh is first coarsened by merging four (two in each direction) cells to form a coarser child cell. When the number of cells in one direction is odd, the coarsening process switches to 1D merging as in the last three grid levels.

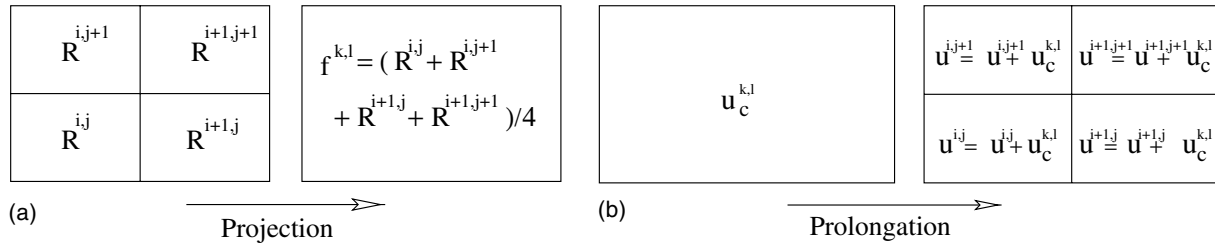


Fig. 2. Illustration of the (a) projection and (b) prolongation procedures to transfer data between two successive grid levels. In the projection step, the residual on a given grid is transferred to the next (coarser) grid level by spatial averaging. The same methodology is used to transfer the diffusivity data. For the prolongation of the solution from one grid level to the next (finer) one, simple addition is used.

5.4. Implementation of the multigrid scheme

Implementation of the MG scheme is now summarized as follows:

(1) Initialization:

- Determine spectral basis, compute and store the multiplication tensor \mathcal{M} .
- Compute the KL decomposition of the λ . (Alternatively the PC expansion of λ is imported (e.g. [8]) or set by the user.)
- Determine the system coefficients for all grid levels:

For $ig = 1, \dots, Ng$

- Determine the grid properties: $\Delta x^{ig} = 2^{ig-1} \Delta x$, $\Delta y^{ig} = 2^{ig-1} \Delta y$, $Nx^{ig} = Nx/2^{ig-1}$, $Ny^{ig} = Ny/2^{ig-1}$.
- Compute the cell averaged diffusion field $(\lambda_l)_{i,j}^{ig}$, for $i = 1, \dots, Nx^{ig}$, $j = 1, \dots, Ny^{ig}$

- Using Eqs. (21) and (22), determine the system coefficients $(C_l^k)_{i,j}^{ig}$, $(E_l)_{i,j}^{ig}$, $(W_l)_{i,j}^{ig}$, $(N_l)_{i,j}^{ig}$, and $(S_l)_{i,j}^{ig}$.
- Compute and store the modified system coefficients accounting for the boundary conditions: $(\tilde{C}_l^k)_{i,j}^{ig}$, $(\tilde{E}_l)_{i,j}^{ig}$, $(\tilde{W}_l)_{i,j}^{ig}$, $(\tilde{N}_l)_{i,j}^{ig}$, $(\tilde{S}_l)_{i,j}^{ig}$.

End of loop over ig

- Initialize solution.

(2) **Loop over time index n :**

- (a) Compute the right-hand side of system (23) on the first grid level: $(\tilde{f}_k^n)_{i,j}^{ig=1}$.
- (b) Initialize solution on the first grid level: $(\tilde{u}_k)_{i,j}^{ig=1} = (\tilde{u}_k^n)_{i,j}$.

(c) **Beginning of V-cycle**

For $ig = 1, \dots, Ng$ (coarsening)

- If $ig > 1$ then initialize the solution $(\tilde{u})^{ig}$ to zero.
- **Outer loop:**

For $ou = 1, \dots, Nou$

- **Loop over spatial indices**

For $i = 1, \dots, N_x^{ig}$

For $j = 1, \dots, N_y^{ig}$

Using Eq. (24), compute the right-hand side of Eq. (25).

Inner loop

For $in = 1, \dots, Nin$

Loop over mode index

For $k = 0, \dots, P$

Apply Eq. (26) to $(\tilde{u}_k)_{i,j}^{ig}$

End of loop over k

End of loop over in

End of loop over i, j

End of loop over ou

- If $ig < Ng$, then

- Compute the local residual $(R_k)_{i,j}^{ig}$ of Eq. (23) on the current grid level.
- Project the local residuals to compute the right-hand side of Eq. (23) at the next grid level $ig + 1$, i.e. determine $(\tilde{f}_k)_{i,j}^{ig+1}$.

End of loop over ig

For $ig = Ng - 1, \dots, 1$ (refinement)

- Update solution $(\tilde{u}_k)^{ig}$ through the prolongation of $(\tilde{u}_k)^{ig+1}$.

- **Outer loop:**

For $ou = 1, \dots, Nou$

- **Loop over spatial indices**

For $i = 1, \dots, N_x^{ig}$

For $j = 1, \dots, N_y^{ig}$

Using Eq. (24), compute the right-hand side of Eq. (25).

Inner loop

For $in = 1, \dots, Nin$

Loop over mode index

For $k = 0, \dots, P$

Apply Eq. (26) to $(\tilde{u}_k)_{i,j}^{ig}$

End of loop over k

End of loop over in

End of loop over i, j

End of loop over ou

End of loop over ig

Compute local residual $(R_k)_{i,j}$ of Eq. (23) on the first grid level. If one of the norms \mathcal{N}_l from Eq. (27) is greater than the prescribed threshold, then a new V-cycle is performed starting from (c).

(d) Determine the solution: $(\tilde{u}_k^{n+1})_{i,j} = (\tilde{u}_k^{ig=1})_{i,j}$, for $i = 1, \dots, Nx$, $j = 1, \dots, Ny$ and $k = 1, \dots, P$.

(3) **End of time loop**

6. Results

We now present test results that show the behavior and convergence properties of the multigrid method. For the test cases below, we set $\alpha = 0$ and study the stochastic diffusion in a square domain, with unit edge-length and with no source term ($s \equiv 0$). Deterministic boundary conditions are used with Dirichlet conditions on $x = 0$ (where $u = 1$) and $x = 1$ (where $u = 0$), and homogeneous Neumann boundary conditions for the $y = 0$ and $y = 1$ edges. As stated previously, the spatially dependent diffusivity field is modeled using a truncated KL expansion involving N modes. It is characterized by its variance, coefficient of variation, and correlation length. To analyze the performance of the scheme, we monitor the evolution of the maximum (over all the modes) of the L^2 -norms of the normalized residuals, more specifically the decay of the peak residual as the number of multigrid cycles increases.

6.1. Multigrid acceleration

6.1.1. Dependence on grid size

We start by examining the dependence of the convergence rate on the number of points involved in the spatial discretization. To this end, the COV of the diffusivity field is set to 0.1, with a normalized correlation length $L_c = 5$. A KL expansion with 5 modes is used (i.e. $N = 5$), together with a second-order PC expansion ($N_0 = 2$). With these parameters, $P = 20$ and so the total number of modes equals 21. The multigrid parameters are selected as follows: $N_{ou} = N_{in} = 3$ and $\omega = 1.5$. The computations are performed for the spatial discretizations of $Nx = Ny = 16, 32, 64$ and 128; the corresponding number of grid levels are $N_g = 4, 5, 6$ and 7. For each, the maximum normalized residual is plotted against cycle number in Fig. 3.

These results clearly show the quasi-independence of the convergence rate with respect to the spatial discretization. There is a very weak improvement in the convergence rate at the lower values of Nx and Ny , which may be attributed to the lack of resolution in the representation of the KL modes on the coarser meshes. This claim is supported by the observation that the convergence rate tends to be grid-size independent when Nx and Ny increase. The weak dependence of the convergence rate on the grid size also highlights the excellent scalability of the method concerning the spatial discretization, as the CPU time scales roughly as $Nx \times Ny$. Note that the relaxation parameter, ω , and number of inner and outer iterations, N_{ou} and N_{in} , have been selected based on systematic tests (not shown) to determine their optimal value. While further refinement of these parameters may be possible, these values will be kept the same for the remaining cases below, unless explicitly stated.

6.1.2. Effect of grid levels on MG acceleration

Fig. 4 shows the evolution of the peak normalized residual with the number of cycles for a fixed grid with $Nx = Ny = 32$. Results obtained for different numbers of grid levels in the V-cycles are shown, namely $N_g = 1, 2, 3, 4$ and 5.

The results clearly show the effect of MG acceleration with increasing number of grid levels. The setting $N_g = 1$ corresponds to the Gauss–Seidel iteration, applied to the initial system of equations with no coarsening. Thus, after the first V-cycle (that is $2N_{ou} = 6$ GS iterations) the short-scales in the residual (mostly related to the Dirichlet boundary conditions) have been reduced and the convergence rate falls

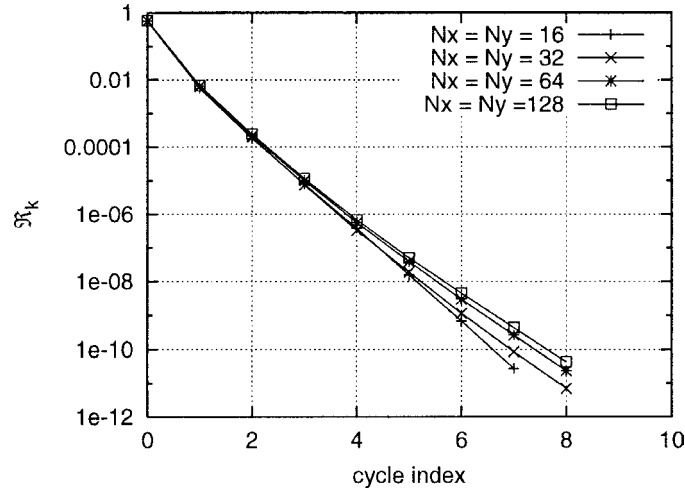


Fig. 3. Convergence of the iterative scheme for different spatial discretizations: $N_x = N_y = 16, 32, 64$ and 128 . The corresponding number of grid levels are $N_g = 4, 5, 6$ and 7 . $\text{COV} = 0.1$, $L_c = 5$, $N = 5$, $N_0 = 2$ ($P = 20$), $\omega = 1.5$, $N_{ou} = N_{in} = 3$.

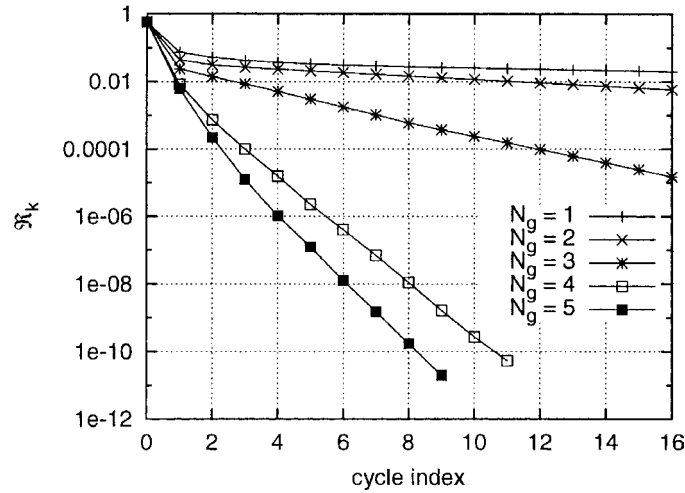


Fig. 4. Convergence of the iterative scheme for $N_x = N_y = 32$ and $N_g = 1, 2, 3, 4$ and 5 . $\text{COV} = 0.1$, $L_c = 1$, $N = 10$, $N_0 = 2$ ($P = 65$), $\omega = 1.5$, $N_{ou} = N_{in} = 3$.

dramatically. This clearly illustrates the lower convergence rate of the larger length scales. When the number of grid levels is increased to $N_g = 2$ the convergence rate is slightly improved, but the iterative method is still inefficient. In fact, the first significant improvement is reported for $N_g = 3$, where one observes a residual reduction factor per V-cycle of approximately 0.78. With $N_g = 4$, the convergence rate is much larger, as the residual reduction factor per V-cycle is approximately 0.2. As expected, the largest convergence rate is observed for $N_g = 5$, with a residual reduction factor close to 0.1. These tests show that the discretization parameters N_x and N_y should be selected, to the extent possible, so that the coarsest grid level has a minimum number of cells in each direction. Note, in particular, that the large improvement in convergence rate between $N_g = 3$ and $N_g = 5$ is achieved at a very low additional CPU cost, since the fourth and last grid levels only involve 16 and 4 cells respectively.

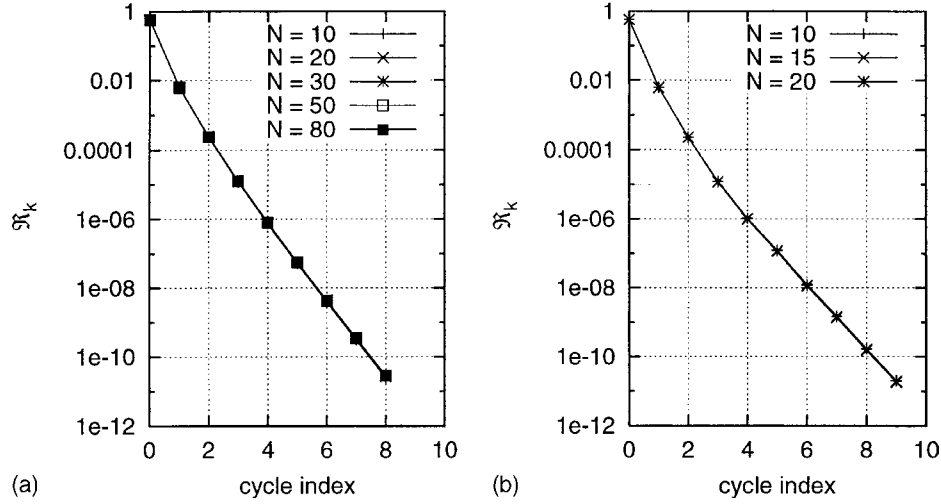


Fig. 5. Peak normalized residual versus cycle number: (a) first-order PC expansion with $N = 10, 20, 30, 50$ and 80 ; (b) second-order PC expansion with $N = 10$ ($P = 65$), 15 ($P = 135$) and 20 ($P = 230$). In both cases, $N_x = N_y = 32$, $L_c = 1$, $N_{in} = N_{ou} = 3$, and $\omega = 1.5$.

6.2. Influence of stochastic representation parameters

The behavior of the MG scheme is now investigated in terms of the stochastic representation parameters, namely the number, N , of KL modes used in the representation of the stochastic diffusivity field, and the order, N_0 , of the PC expansion. In the tests below, the spatial discretization parameters are held fixed, as are the over-relaxation parameter, $\omega = 1.5$, the number of grid levels, $Ng = 5$, and the number of iterations performed on each grid level, $N_{in} = N_{ou} = 3$. The coefficient of variation and correlation length are also held fixed, $COV = 0.1$ and $L_c = 1$, respectively.

6.2.1. Number of KL modes

In these tests, the impact of the number of modes retained in the KL expansion of the diffusivity field is investigated by varying N . Results are reported in Fig. 5, where the peak normalized residual is plotted against cycle number for (a) first-order PC expansion with N ranging from 10 to 80, and (b) second-order PC expansion with $N = 10, 15$ and 20 ($P = 65, 135$ and 230 , respectively). For both first- and second-order expansions, the evolution of the residual is independent of N , again showing the efficiency of the MG scheme. Note that in the present case one cannot infer from this behavior a linear relationship between N and the CPU time. The latter is in fact a strong function of the number of non-zero terms in \mathcal{M} , which depends on both N and N_0 . This contrasts with previous observation regarding scalability of the scheme with respect to the number of grid points.

6.2.2. Effect of PC expansion order on rate of convergence

The results of the previous section show a dependence of the convergence rate of the multigrid method on the order of the PC expansion. This dependence is further investigated by setting $N = 10$ and varying N_0 from 1 to 3; with $P = 10, 65$ and 285 , respectively. The convergence of the iterations for these cases is illustrated in Fig. 6, which depicts the behavior of the peak residual as the number of cycles increases.

The results indicate that the convergence rate decreases slightly as the order of the PC expansion increases. The residual reduction factor per cycle is about 0.09 for $N_0 = 1$ and approximately 0.2 for $N_0 = 3$. In light of the experiences above, it is evident that the present reduction in convergence rate is not due to the increase in number of modes P , but rather to the need for additional cycles in order to propagate the

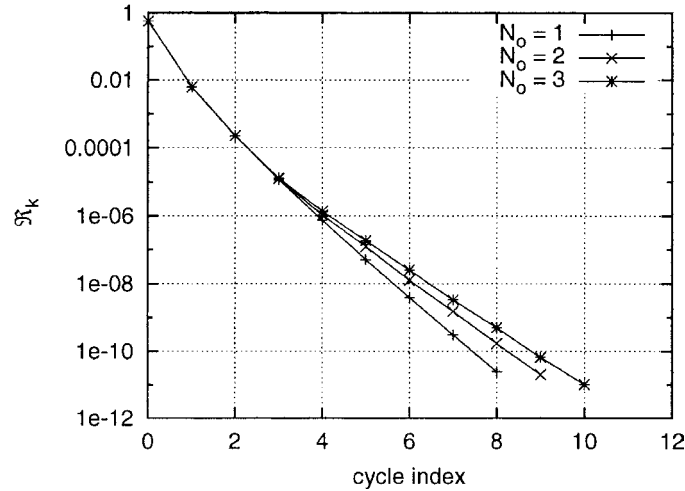


Fig. 6. Peak normalized residual versus cycle number for $N_0 = 1$ ($P = 10$), $N_0 = 2$ ($P = 65$), and $N_0 = 3$ ($P = 285$). In all cases, $N = 10$, $N_x = N_y = 32$, $L_c = 1$, $N_{in} = N_{ou} = 3$, and $\omega = 1.5$.

residual for coupled terms of different order. For the present examples, the convergence rate is still satisfactory for $N_0 = 3$. In situations requiring higher order expansions, however, further improvement may be required. This could be achieved for instance by blending the (spatial) MG concepts with a spectral (mode) coarsening procedure.

6.3. Effects of diffusivity field statistics

We now analyze the effects of the diffusivity field characteristics on the convergence rate, by varying its statistical parameters. We recall that the diffusivity is parametrized through its COV, which represents the normalized local statistical spread of the realizations about the expected value, and the correlation length, which accounts for the spatial variability of the process. The effects of these two parameters are analyzed separately below.

6.3.1. Effect of diffusivity variance

Tests on the effect of the variance of the diffusivity field are performed using $L_c = 1$, a KL expansion with $N = 25$, and PC expansion of first and second order ($P = 25$ and 350, respectively). A 32×32 computational grid is used and the MG parameters are as follows: $\omega = 1.5$, $N_{ou} = N_{in} = 3$ and $Ng = 5$. Results with different values of σ_λ are reported in Fig. 7.

The results show that, as expected, the convergence rate is strongly dependent on the variance of the diffusivity field. Actually, the highest convergence rate is achieved for the lowest values of COV ($\sigma_\lambda = 0.025$) where the residual is reduced with each MG cycle, by a factor of about 0.05 for $N_0 = 1$ (Fig. 7a) and approximately 0.06 for $N_0 = 2$ (Fig. 7b). Consistent with previous findings, for the same values of σ_λ (and COV) the second-order PC expansion exhibits slower convergence rate than the first-order scheme. Moreover, when COV increases, the convergence rate decreases for both the first- and second-order expansions, but the reduction is more substantial in the latter case. As noted previously, the diffusivity field should be positive at any point inside the domain. However, the KL expansion does not guarantee this constraint, and the probability that this constraint is violated increases as COV increases. In fact, for $\text{COV} \geq 0.4$ and $N_0 = 2$, the solver did not converge. In contrast, with a first-order expansion the MG iterations did converge for $\text{COV} = 0.4$, but with a very low convergence rate (not shown). It should be

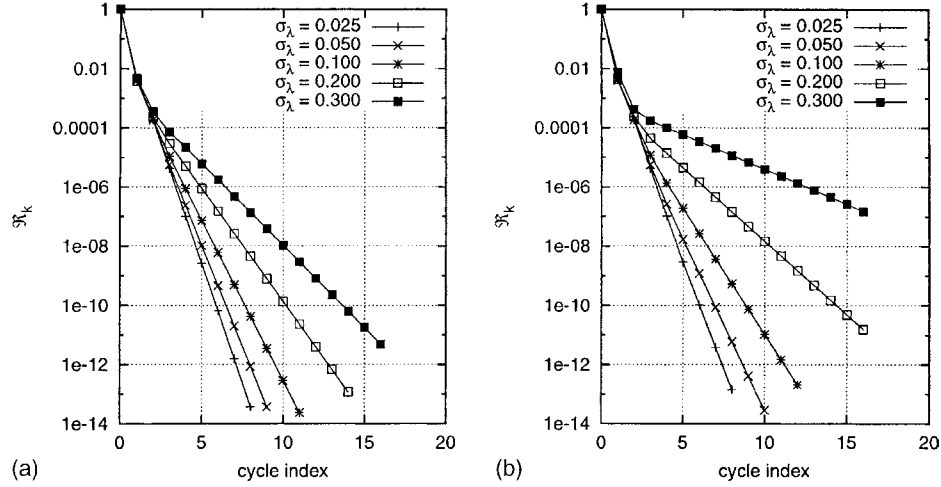


Fig. 7. Peak residual versus number of cycles for different values of σ_λ : (a) first-order PC expansion and (b) second-order PC expansion. In all cases, $L_c = 1$, $N = 25$, $\omega = 1.5$, $N_{out} = N_{in} = 3$, $Ng = 5$ and $Nx = Ny = 32$.

emphasized, however, that the deterioration of convergence rate with increasing COV is due to the extreme behavior of the corresponding problem, and therefore is not inherent to the present multigrid scheme.

6.3.2. Influence of the correlation length

The effect of the correlation length is analyzed in this section by performing computations with a fixed variance ($COV = 0.1$) but varying L_c . As illustrated in Fig. 8, as L_c decreases, the spectrum of λ broadens with higher amplitudes in the small scales. Since the variance is fixed, however, the “energy” content of the spectrum remains constant.

Fig. 9 shows the convergence rate of the MG iterations for different correlation lengths, $L_c = 0.25, 0.5, 1, 2$ and 5 . Plotted are results obtained using both first- and second-order PC expansions. The results show a weak dependence of the convergence rate on L_c , indicating that the MG method effectively maintains its good convergence properties even as small-scale fluctuations in λ increase. The weak dependence of the convergence rate on spatial lengthscales of λ has also been observed in deterministic simulations (not

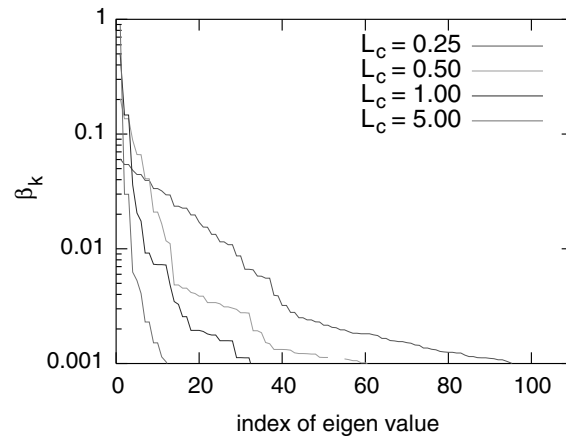


Fig. 8. Spectra of the eigenvalues, β_k , of the KL expansion for different correlation lengths $L_c = 0.25, 0.5, 1$ and 5 .

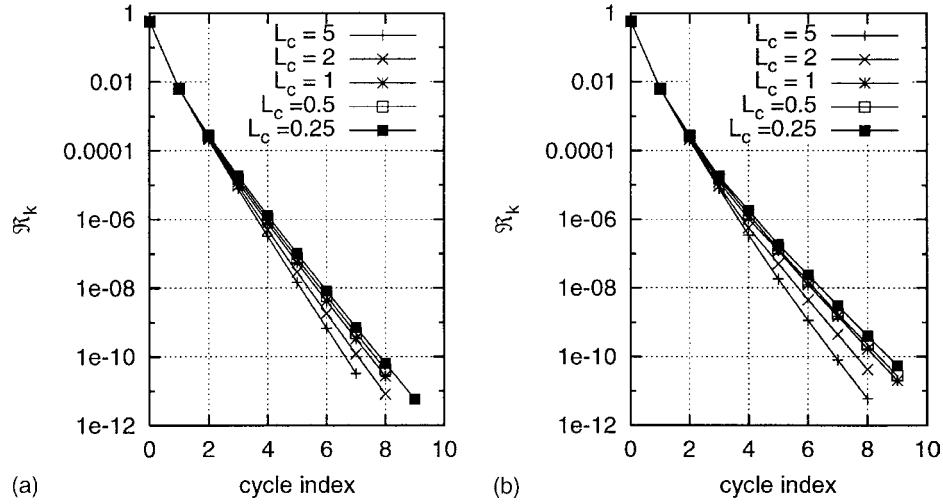


Fig. 9. Peak residual versus number of cycles for $N = 20$ KL modes and different values of L_c : (a) first-order PC expansion ($P = 20$); (b) second-order PC expansion ($P = 350$). In all cases, $\text{COV} = 0.1$, $N_{in} = N_{out} = 3$, $\omega = 1.5$ and $N_x = N_y = 32$.

shown). This shows that the extension of the MG scheme to stochastic problems does not adversely affect its effectiveness in dealing with spatially varying diffusivity. Closer analysis of the results in Fig. 9 also supports our previous observation that the convergence rate for first-order PC expansions is larger than for the second-order case, but differences are once again small.

As shown in Fig. 8, decreasing L_c results in a broader eigenvalue spectrum, which raises the question whether $N = 20$ KL modes is sufficient to capture all the relevant scales of λ . This question arises because truncation of the KL expansion removes the highest spatial frequencies, and leads to under-estimation of the variance. To verify that the near collapse of the curves in Fig. 9 with decreasing L_c is not due to such truncation, simulations were repeated using a first-order PC expansion and a higher number of KL modes, $N = 105$. The results (not shown) exhibit essentially the same convergence rate as with $N = 20$. This indicates that the truncation of the KL expansion does not affect the convergence rate of the multigrid solver.

6.4. Selection of multigrid parameters

The computational tests above were performed with fixed MG parameters, which enabled direct comparison between various cases and thus simplified the analysis. It is evident, however, that tuning these parameters can improve the efficiency of the method. For the test cases in the previous sections, selecting $\omega \in [1.2, 1.7]$ results in convergent iterations, but varying ω within this range affected the convergence rate. Specifically, for fixed tolerance on the peak residual (10^{-10}), the number of cycles needed to achieve this level varied between 3 and 5 cycles. Consequently, tests should generally be conducted in order to select the optimal ω value for the problem at hand. A similar optimization process should also be conducted for proper selection of the number of inner and outer iterations. Clearly, using a large number of outer iterations results in an inefficient method, since one does not want to perform a large number of outer iterations on the initial grid level. At the same time, a minimal number of outer iterations is required during prolongation in order to smooth the solution sufficiently before switching to the next grid level. Thus, N_{ou} should be carefully optimized. Meanwhile, N_{in} should be set to the minimum value above which the convergence rate starts to decrease.

Lastly, the efficiency of the multigrid procedure can also be drastically improved by designing cycles with a more complex structure than the simple V-cycle used in the present work. To illustrate the improvement

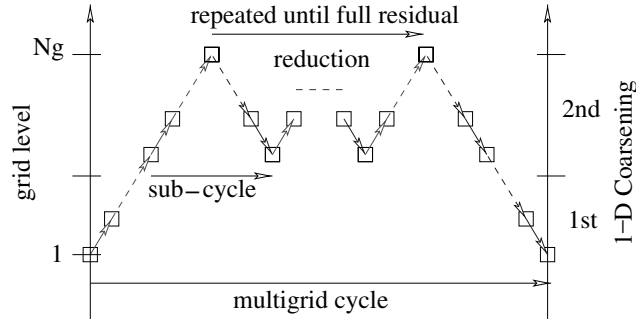


Fig. 10. Example of line-coarsening strategy for highly stretched grids. Instead of the usual V-cycle, the coarsening is first performed along the well resolved direction, and next in the second direction. Treatment (sub-cycles) of the second direction is repeated until the residual is reduced to the selected tolerance level.

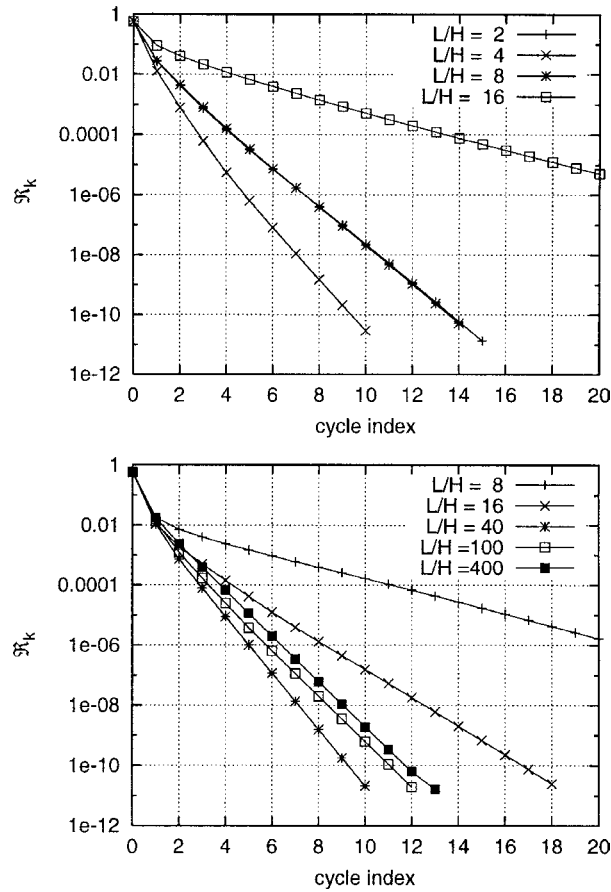


Fig. 11. Convergence rate of MG iterations: V-cycle approach (top) and line coarsening strategy (bottom). Curves are generated for solutions obtained in domains with different aspect ratio, L/H . In both sets of simulations, $N_x = 128$, $N_y = 32$, $N_{ou} = 3$, $N_{in} = 2$, $\omega = 1.5$, $N_0 = 2$ and $N = 3$. The stochastic diffusivity field has $L_c = L$ and $COV = 0.1$.

that can be achieved by adaptation of cycle structure, a line-coarsening strategy, designed for highly stretched grids and/or domains with high aspect ratios, is briefly outlined below. Assuming that $\Delta x \gg \Delta y$,

the strategy consists of (i) performing a 1D-coarsening along the y -direction only, which eventually leads to a quasi-1D problem in x ; (ii) applying a 1D MG approach in the x -direction, which is iterated until the overall tolerance level is reached; and (iii) performing a prolongation in the y -direction only. This cycle, whose structure is schematically illustrated in Fig. 10, is repeated until the residual on the original fine grid drops below the desired tolerance level.

In Fig. 11 we contrast the convergence rates of the MG scheme using the V-cycles and of the adapted MG scheme outlined above. In both cases, the number of grid cells is fixed, $N_x = 128$ and $N_y = 32$, but the aspect ratio, L/H , of the domain is varied. Note that the case $L/H = 4$ corresponds to a grid with square cells, i.e. $\Delta x = \Delta y$. For the V-cycle iterations, the results indicate that the convergence rate deteriorates as the cell aspect ratio increases. Meanwhile, with the line-coarsening strategy, the convergence rate improves as L/H is increased from 8 to 40; for higher aspect ratios, up to $L/H = 400$, the convergence rate decreases slightly, but remains at a satisfactory level. In contrast, for such high aspect ratios, the regular V-cycle iterations are quite inefficient.

7. Conclusions

A multigrid scheme for the simulation of steady and unsteady stochastic diffusion equations was developed, and computational tests were conducted to analyze its behavior. In particular, these tests show that:

- The MG scheme exhibits a fast rate of convergence and good scalability with respect to spatial resolution in a fixed domain.
- The convergence rate is independent of the number of stochastic dimensions as long as the variance of the diffusivity field is held fixed.
- The convergence rate drops slowly as the order of the PC expansion increases.
- The convergence rate deteriorates substantially as the variance of the stochastic diffusivity field becomes large, but satisfactory convergence rates are still observed for COV up to 0.2. On the other hand, the convergence rate decreases slightly as the correlation length of the stochastic diffusivity field is decreased.
- Selection of MG parameters and cycle structure can drastically affect the efficiency of the iterations. These parameters should therefore be carefully optimized.

Future work will aim at enhancing the present MG approach, particularly for situations involving large variance and high order PC expansions. An attractive approach that is currently being explored is based on exploiting the structure and sparsity of the stochastic system. This structure suggests a hierarchical iterative strategy [34], which has been successfully exploited in the context of stochastic finite elements. In particular, it appears that incorporation of such an approach into the present MG framework could lead to a substantial performance enhancement.

Acknowledgements

This work was supported by the Defense Advanced Research Projects Agency (DARPA) and the Air Force Research Laboratory, Air Force Material Command, USAF, under agreement number F30602-00-2-0612. The US government is authorized to reproduce and distribute reprints for Governmental purposes notwithstanding any copyright annotation thereon. Computations were performed at the National Center for Supercomputing Applications.

References

- [1] M. Abramowitz, L.A. Stegun, *Handbook of Mathematical Functions*, Dover, 1970.
- [2] I. Babuska, P. Chatzipantelidis, On solving elliptic stochastic partial differential equations, *Comput. Methods Appl. Mech. Engrg.* 191 (2002) 4093–4122.
- [3] I. Babuska, K.M. Liu, On solving stochastic initial-value differential equations, Technical report, TICAM Report 02-17, The University of Texas at Austin, 2002.
- [4] E. Bielewicz, J. Górski, Shells with random geometric imperfections simulation-based approach, *Int. J. Nonlinear Mech.* 37 (2002) 777–784.
- [5] R.H. Cameron, W.T. Martin, The orthogonal development of nonlinear functionals in series of fourier-hermite functionals, *Ann. Math.* 48 (1947) 385–392.
- [6] S.F. McCormick, *Multigrid Methods*, SIAM, 1987.
- [7] M.K. Deb, I.M. Babuska, J.T. Oden, Solution of stochastic partial differential equations using Galerkin finite element techniques, *Comput. Methods Appl. Mech. Engrg.* 190 (2001) 6359–6372.
- [8] B. Debusschere, H. Najm, A. Matta, O. Knio, R. Ghanem, O. Le Maître, Numerical simulation and quantitative uncertainty assessment of a reacting electrochemical microchannel, *Phys. Fluids* 15 (8) (2003) 2238–2250.
- [9] B. Debusschere, H. Najm, A. Matta, T. Shu, O. Knio, R. Ghanem, O. Le Maître, Uncertainty quantification in a reacting electrochemical microchannel flow model, in: 5th Int. Conf. on Mod. and Sim. of Microsystems, 2002.
- [10] O. Ditlevsen, N.J. Tarp-Johansen, Choice of input fields in stochastic finite-elements, *Probabilist. Engrg. Mech.* 14 (1999) 63–72.
- [11] C.A.J. Fletcher, *Computational Techniques for Fluid Dynamics*, vol. 1, Springer-Verlag, 1988.
- [12] R. Ghanem, Ingredients for a general purpose stochastic finite elements formulation, *Comput. Methods Appl. Mech. Engrg.* 168 (1999) 19–34.
- [13] R. Ghanem, The nonlinear gaussian spectrum of lognormal stochastic processes and variables, *ASME J. Appl. Mech.* 66 (1999) 964–973.
- [14] R. Ghanem, S. Dham, Stochastic finite element analysis for multiphase flow in heterogeneous porous media, *Transport Porous Med.* 32 (1998) 239–262.
- [15] R.G. Ghanem, Probabilistic characterization of transport in heterogeneous media, *Comput. Methods Appl. Mech. Engrg.* 158 (1998) 199–220.
- [16] R.G. Ghanem, P.D. Spanos, A spectral stochastic finite element formulation for reliability analysis, *J. Engrg. Mech. ASCE* 117 (1991) 2351–2372.
- [17] R.G. Ghanem, P.D. Spanos, *Stochastic Finite Elements: A Spectral Approach*, Springer Verlag, 1991.
- [18] H. Grudmann, H. Waubke, Non-linear stochastic dynamics of systems with random properties, a spectral approach combined with statistical linearization, *Int. J. Nonlinear Mech.* 31 (5) (1996) 619–630.
- [19] T.D. Hien, M. Kleiber, Stochastic finite element modelling in linear transient heat transfer, *Comput. Methods Appl. Mech. Engrg.* 144 (1997) 111–124.
- [20] H. Holden, B. Oksendal, J. Ubøe, T. Zhang, *Stochastic Partial Differential Equations*, Birkhauser, 1996.
- [21] M. Kaminski, T.D. Hien, Stochastic finite element modeling of transcient heat transfer in layered composites, *Int. Commun. Heat Mass* 26 (6) (1999) 801–810.
- [22] O.M. Knio, R.G. Ghanem, Polynomial Chaos product and moment formulas: A user utility, Technical report, Johns Hopkins University, 2001.
- [23] O.P. Le Maître, O.M. Knio, H.N. Najm, R.G. Ghanem, A stochastic projection method for fluid flow. I. Basic formulation, *J. Comput. Phys.* 173 (2001) 481–511.
- [24] O.P. Le Maître, M.T. Reagan, H.N. Najm, R.G. Ghanem, O.M. Knio, A stochastic projection method for fluid flow. II. Random process, *J. Comput. Phys.* 181 (2002) 9–44.
- [25] J.S. Liu, *Monte Carlo Strategies in Scientific Computing*, Springer, 2001.
- [26] N. Liu, B. Hu, Z.-W. Yu, Stochastic finite element method for random temperature in concrete structures, *Int. J. Solids Struct.* 38 (2001) 6965–6983.
- [27] M. Loève, *Probability Theory*, Springer, 1977.
- [28] H.G. Matthies, C.E. Brenner, C.G. Bucher, C.G. Scares, Uncertainties in probabilistic numerical analysis of structures and solids—stochastic finite-elements, *Struct. Saf.* 19 (3) (1997) 283–336.
- [29] H.G. Matthies, C.G. Bucher, Finite element for stochastic media problems, *Comput. Methods Appl. Mech. Engrg.* 168 (1999) 3–17.
- [30] H.G. Matthies, A. Keese, Multilevel solvers for the analysis of stochastic system, in: *First MIT Conference on Computational Fluid and Solid Mechanics*, Elsevier, 2001, pp. 1620–1622.
- [31] H.G. Matthies, A. Keese, Multilevel methods for stochastic systems, in: *Proceedings of the 2nd European Conference on Computational Mechanics*, Cracow, Poland, June 26, 2001.

- [32] J. Náprstek, Strongly non-linear stochastic response of a system with random initial imperfections, *Probabilist. Engrg. Mech.* 14 (1999) 141–148.
- [33] B.M. Nicola, B. Verlinden, A. Beuselinck, P. Jancsok, V. Quenon, N. Scheerlinck, P. Verbosen, J. de Baerdemaeker, Propagation of stochastic temperature fluctuations in refrigerated fruits, *Int. J. Refrig.* 22 (1999) 81–90.
- [34] M.F. Pellissetti, R.G. Ghanem, Iterative solution of systems of linear equations arising in the context of stochastic finite elements, *Adv. Engrg. Software* 31 (2000) 607–616.
- [35] R.F. Probstein, *Physicochemical Hydrodynamics*, Wiley, 1995.
- [36] G.I. Schuëller, Computational stochastic mechanics—recent advances, *Comput. Struct.* 79 (2001) 2225–2234.
- [37] A. Sluzalec, Random heat flow with phase change, *Int. J. Heat Mass Transfer* 43 (2000) 2303–2312.
- [38] A. Sluzalec, Stochastic finite element analysis of two-dimensional eddy current problems, *Appl. Math. Model.* 24 (2000) 401–406.
- [39] J. Stoer, R. Bulirsch, *Introduction to Numerical Analysis*, Springer, 1991.
- [40] T.G. Theting, Solving Wick-stochastic boundary value problems using a finite element method, *Stoch. Stoch. Rep.* 70 (2000) 241–270.
- [41] U. Trottenberg, C. Oosterlee, A. Schüller, *Multigrid*, Academic Press, 2001.
- [42] S. Wiener, The homogeneous chaos, *Amer. J. Math.* 60 (1938) 897–936.
- [43] D. Xiu, D. Lucor, G.E. Karniadakis, Modeling uncertainty in flow-structure interactions, in: *First MIT conference on Computational Fluid and Solid Mechanics*, Elsevier, 2001, pp. 1420–1423.

Protein labeling reactions in electrochemical microchannel flow: Numerical simulation and uncertainty propagation

Bert J. Debuschere^{a)} and Habib N. Najm^{b)}

Sandia National Labs, Livermore, California 94550

Alain Matta,^{c)} Omar M. Knio,^{d)} and Roger G. Ghanem^{e)}

The Johns Hopkins University, Baltimore, Maryland 21218

Olivier P. Le Maître^{f)}

Université d'Evry Val d'Essonne, Evry, France

(Received 30 October 2002; accepted 18 April 2003; published 30 June 2003)

This paper presents a model for two-dimensional electrochemical microchannel flow including the propagation of uncertainty from model parameters to the simulation results. For a detailed representation of electroosmotic and pressure-driven microchannel flow, the model considers the coupled momentum, species transport, and electrostatic field equations, including variable zeta potential. The chemistry model accounts for pH-dependent protein labeling reactions as well as detailed buffer electrochemistry in a mixed none-rate/equilibrium formulation. Uncertainty from the model parameters and boundary conditions is propagated to the model predictions using a pseudo-spectral stochastic formulation with polynomial chaos (PC) representations for parameters and field quantities. Using a Galerkin approach, the governing equations are reformulated into equations for the coefficients in the PC expansion. The implementation of the physical model with the stochastic uncertainty propagation is applied to protein-labeling in a homogeneous buffer, as well as in two-dimensional electrochemical microchannel flow. The results for the two-dimensional channel show strong distortion of sample profiles due to ion movement and consequent buffer disturbances. The uncertainty in these results is dominated by the uncertainty in the applied voltage across the channel. © 2003 American Institute of Physics. [DOI: 10.1063/1.1582857]

I. INTRODUCTION

Microchannel flows, involving electroosmotic flow of charged components in an electrolyte buffer, are generally characterized by strong coupling between multiple physical and chemical processes.¹ Numerical simulations for detailed studies of phenomena such as analyte dispersion therefore require accurate models for the fluid flow, species transport, chemical reactions, buffer equilibrium, protein amphoteric behavior, electrostatic field strength, wall layer, and many other processes.² Most of these processes are well understood and adequate models are generally available. Many simulations of microchannel flow can be found in the literature, with varying detail in the resolution of the ongoing physical processes.^{3–13} However, simulations that take into account the full range of coupled processes in microchannel flows are hard to find.

Further, the mathematical models for these physical processes generally require knowledge of several parameters such as species mobilities, viscosity, electrolyte dissociation constants, reaction rate parameters, and other physical and

environmental parameters. These parameters are typically not known exactly due to experimental measurement uncertainties and/or inherent variability. Consequently, computational predictions will have some uncertainty, associated with the uncertainties in the input parameters. In order to make valid comparisons between experimental and computational data, or to assess the reliability of computational predictions, a careful analysis of the uncertainty in the simulation results is required.

In the current work, a detailed model is developed of both electroosmotic and pressure-driven flow in a microchannel filled with an electrolyte buffer and model protein analyte samples. The construction considers the fully coupled momentum, species transport, and electrostatic field equations, including a model for the dependence of the zeta potential on pH and buffer molarity. A mixed none-rate, partial-equilibrium formulation is applied for the chemical reactions. In particular, “fast” electrolyte reactions are described by associated equilibrium constraints, while the remaining “slow” protein labeling reactions are modeled with none-rate kinetics.

To quantify the uncertainty in the model predictions, due to uncertainty in the input parameters, a stochastic uncertainty propagation method¹⁴ is applied. This method introduces a new stochastic dimension for each uncertain parameter, and uses polynomial chaos (PC) expansions¹⁵ to describe the dependence of model parameters and flow quan-

^{a)}Electronic mail: bjdebus@ca.sandia.gov

^{b)}Electronic mail: hnnajm@ca.sandia.gov

^{c)}Electronic mail: alan@mars.ce.jhu.edu

^{d)}Electronic mail: knio@jhu.edu

^{e)}Electronic mail: ghanem@jhu.edu

^{f)}Electronic mail: olm@iup.univ-evry.fr

tities on these dimensions. After introducing these PC representations into the governing equations, a Galerkin approach is used to determine evolution equations for the spectral mode strengths in the expansion. The resulting system is more complex than the corresponding deterministic model, requiring more computational effort. However, it is potentially more efficient than Monte Carlo (MC) simulations.¹⁶ Moreover, the pseudo-spectral PC approach readily provides sensitivity information and the contribution to the total uncertainty by each of the model parameters.

First we outline the formulation of the governing equations that constitute the deterministic system model. Next, we implement the stochastic uncertainty quantification method to reformulate these equations into evolution equations for the spectral mode strengths. We then proceed to the description of the numerical construction used to integrate the resulting set of equations, highlighting particular developments necessary for handling the coupled evolution of momentum, species, and the electrostatic field. The methodology is then applied to model protein labeling reactions in homogeneous systems as well as two-dimensional microchannel flows. The results illustrate the convergence of the construction as well as the propagation/growth of uncertainty in the simulations. The detailed physical model gives insight into important microfluidic sample dispersion mechanisms.

II. PHYSICAL MODEL FORMULATION

A. Momentum

The continuity and momentum equations for a two-dimensional flow field in the (x, y) plane, with uniform density and viscosity are given by¹⁷

$$\nabla \cdot \mathbf{u} = 0, \quad (1)$$

$$\frac{\partial \mathbf{u}}{\partial t} + \mathbf{u} \cdot \nabla \mathbf{u} = -\nabla p + \nu \nabla^2 \mathbf{u}, \quad (2)$$

where \mathbf{u} is the velocity, p is the pressure normalized by density, and ν is the kinematic viscosity.

The microchannel flows in this study are electroosmotically driven with an applied electrostatic field in the x direction. Assuming a double layer that is thin with respect to the channel size, the effect of wall electrostatic forces can be represented in terms of a wall slip velocity u_w , using the Helmholtz–Smoluchowski relationship¹⁷

$$u_w = \frac{\epsilon \zeta}{\mu} \nabla_t \phi_w, \quad (3)$$

where ϵ is the permittivity of the fluid, ζ is the zeta potential, ϕ_w is the electrostatic field potential at the wall, and μ is the dynamic viscosity. Since both the electrostatic field and the ζ potential depend on the fluid composition, Eq. (3) represents a major coupling between the flow velocity and the species transport.

The ζ potential is a function of the wall material and fluid characteristics.^{7,18} In this work, a relationship for ζ as a function of the local pH and buffer molarity was obtained from empirical data for the zeta potential of a fused silica capillary in an aqueous solution of KCl, as shown in Fig. 1.¹⁹

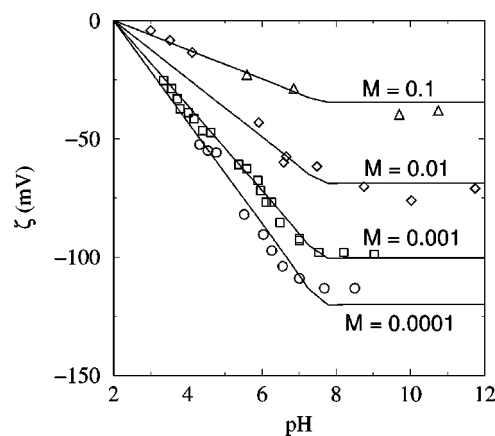


FIG. 1. Empirical data and curve fit for the ζ potential of a fused silica capillary vs pH in an aqueous solution of KCl at various molarities. Adapted with permission from Ref. 19, Copyright 1992 American Chemical Society.

These data were curve-fitted into the following relationship:

$$\begin{aligned} \zeta(\text{pH}, \mathcal{M}) = & \left\{ -(\text{pH} - 2) + \left(\frac{1}{2} + \frac{1}{2} \tanh(5(\text{pH} - 7.5)) \right) (\text{pH} - 7.6) \right\} \\ & \times (-2.7 \ln(\mathcal{M} + 2.3 \times 10^{-4})), \end{aligned} \quad (4)$$

where \mathcal{M} is the molarity of the KCl solution. The quantitative accuracy of this curve-fit is obviously limited to systems similar to the one considered in Ref. 19. However, Eq. (4) qualitatively gives the correct behavior of $\zeta(\text{pH}, \mathcal{M})$ for various other systems.^{7,18}

B. Species concentrations

A variety of species are considered in this work, ranging from model proteins and dyes in samples, to the ions of aqueous buffer solutions. The transport of these species is governed by¹⁷

$$\frac{\partial c_i}{\partial t} + \nabla \cdot [c_i(\mathbf{u} + \mathbf{u}_i^e)] = \nabla \cdot (D_i \nabla c_i) + \hat{w}_i, \quad (5)$$

where c_i is the concentration of species i , and D_i is the corresponding diffusivity. The electromigration velocity \mathbf{u}_i^e accounts for the electrophoretic movement of electrically charged species relative to the bulk flow. This velocity is given by¹⁷

$$\mathbf{u}_i^e = -\beta_i z_i F \nabla \phi, \quad (6)$$

where β_i is the electrophoretic mobility for species i , z_i is the charge number, F is the Faraday constant (9.648×10^4 C/mol), and ϕ is the electrostatic field potential. The term \hat{w}_i is a source term from the chemical and electrochemical reactions in which species i is involved. Note that for each species, the diffusivity D_i and the mobility β_i are coupled through the Nernst–Einstein equation¹⁷

$$D_i = RT\beta_i, \quad (7)$$

where R is the universal gas constant and T the temperature.

The integration of Eq. (5) is performed differently depending on the chemical time scales involved. In general,

electrolyte association and dissociation reaction rates are several orders of magnitude faster than electrophoretic phenomena¹ and typical sample-processing reactions. Thus, direct integration of fast reactions would impose severe time step restrictions. In order to avoid these difficulties, an equilibrium approach for the electrolyte reactions is implemented. For example, consider a weak acid HA, which dissociates according to



where

$$K_A \equiv \frac{[\text{H}^+][\text{A}^-]}{[\text{HA}]} \quad (9)$$

is the corresponding dissociation constant. Instead of integrating Eq. (5) for the concentrations of species HA and A⁻ individually, consider the combined concentration of both of these quantities $\theta_a = [\text{HA}] + [\text{A}^-]$. The source terms for [HA] and [A⁻] from the electrolyte reaction (8) cancel out in the θ_a transport equation, which is the sum of the transport equations for the two individual quantities,

$$\begin{aligned} \frac{\partial \theta_a}{\partial t} + \nabla \cdot [c_{\text{HA}}(\mathbf{u} + \mathbf{u}_{\text{HA}}^e) + c_{\text{A}^-}(\mathbf{u} + \mathbf{u}_{\text{A}^-}^e)] \\ = \nabla \cdot [D_{\text{HA}} \nabla c_{\text{HA}} + D_{\text{A}^-} \nabla c_{\text{A}^-}]. \end{aligned} \quad (10)$$

Therefore, barring any other chemical reactions involving these species, θ_a is a conserved quantity and can be integrated with Eq. (10) without a chemical source term.^{2,4,10} Note that if the chemical source terms for HA or A⁻ in Eq. (5) do include participation by reactions other than the HA buffer chemistry, e.g., by (typically slow) sample chemistry, then the utilization of θ_a is still advantageous in that it eliminates the fast electrolyte reactions, but in this case θ_a is no longer a conserved scalar. In either case, one arrives at a governing equation for θ_a , which does not include the fast reaction terms. Once θ_a is known, the concentrations of the individual components of the weak acid are obtained from

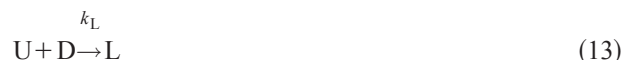
$$[\text{HA}] = \frac{[\text{H}^+]}{[\text{H}^+] + K_A} \theta_a \equiv \alpha_{\text{HA}} \times \theta_a, \quad (11)$$

$$[\text{A}^-] = \frac{K_A}{[\text{H}^+] + K_A} \theta_a \equiv \alpha_{\text{A}^-} \times \theta_a. \quad (12)$$

Note that this construction is equally useful for buffers with multiple dissociation states, where θ_a is the sum of concentrations of the weak acid and all of its dissociated states. Since the mobilities and diffusivities are generally different for the species that make up θ_a , the convection and diffusion terms in the transport equation for θ_a are calculated as the sum of the convection and diffusion for each species in θ_a . A similar approach holds for weak bases.

For strong acids and bases, which are fully dissociated in the solution, or for other species that do not take part in electrolyte dissociation and association reactions, Eq. (5) can be integrated directly. The model proteins and fluorescent dyes in this work are assumed to have a fixed charge, so their concentrations are integrated using Eq. (5), with an appropriate

nite-rate chemical source term. However, a complete ampholyte description for proteins can readily be formulated with a similar framework as is used for the weak acids and bases.^{2,20–22} In the simulations in this work, proteins are assumed to take part in a nite rate, irreversible labeling reaction of the form



with a pH-dependent reaction rate $k_L = k_L(\text{pH})$. In Eq. (13), U is the unlabeled protein, D the fluorescent dye, and L the labeled protein.

Since a thin double layer is assumed, the system is also assumed to satisfy the electroneutrality condition

$$\sum_i z_i c_i = 0 \quad (14)$$

everywhere in the domain. The concentrations of H⁺ and OH⁻ are obtained from this electroneutrality condition and the water dissociation constant

$$[\text{H}^+][\text{OH}^-] = K_w. \quad (15)$$

Note that the composition, and therefore also the total charge, of weak acids and bases in the system depends on the H⁺ concentration [see Eqs. (11) and (12) above]. The substitution of Eqs. (12) and (15) into the electroneutrality condition (14), in order to account for the dependence of [A⁻] and [OH⁻] on [H⁺], introduces nonlinear terms in this equation. For buffers with multiple dissociation states, even more nonlinear terms are introduced. Therefore, an iterative solution of the electroneutrality condition for [H⁺] is usually required.

C. Electrostatic field strength

Allowing for concentration field gradients, the electrostatic field potential, ϕ , is obtained from the current continuity constraint,¹⁷

$$\nabla \cdot (\sigma \nabla \phi) = -F \sum_i z_i \nabla \cdot (D_i \nabla c_i). \quad (16)$$

This equation is coupled to the species concentrations through the right-hand side (diffusion of charge) and the electrical conductivity σ of the solution

$$\sigma = F^2 \sum_i z_i^2 \beta_i c_i. \quad (17)$$

The electrostatic field strength is then obtained as $\mathbf{E} = -\nabla \phi$.

This completes the description of the key elements of the deterministic model formulation. We next outline the stochastic construction for uncertainty quantification, and its implementation in this model.

III. STOCHASTIC FORMULATION

To propagate uncertainty from the input parameters of the physical model, to the results of model simulations, we use a spectral stochastic formulation based on polynomial chaos (PC) expansions.^{14,15} For each uncertain parameter,

this technique introduces a new stochastic dimension ξ , where ξ is a random variable with a standard normal Gaussian probability density function (PDF). The parameter is then modeled as a random variable whose dependence on ξ is described using a spectral PC expansion. For example, the species diffusivity D is written as

$$D(\xi) = \sum_{k=0}^P D_k \Psi_k(\xi), \quad (18)$$

where the Ψ_k are the PC basis functions and the deterministic coefficients D_k are the spectral mode strengths. If the model has only one uncertain parameter, then the basis functions are the one-dimensional Hermite polynomials:

$$\Psi_0 = 1, \quad \Psi_1 = \xi, \quad \Psi_2 = \xi^2 - 1, \quad \Psi_3 = \xi^3 - 3\xi, \dots \quad (19)$$

In this case, P corresponds to the highest order polynomial used in the expansion. For a model with N uncertain parameters, an N -dimensional stochastic space is considered, and the Ψ_k are N -dimensional Hermite polynomials up to a specified order p in the Gaussian variables $\theta = \{\xi_1, \xi_2, \dots, \xi_N\}$,¹⁴ such that

$$D(\theta) = \sum_{k=0}^P D_k \Psi_k(\theta). \quad (20)$$

Note that in this case, the Gaussian variables ξ_1, \dots, ξ_N are assumed to be uncorrelated. The number of terms $(P+1)$ in the expansion corresponds to the number of polynomials with order less or equal to p . Higher order polynomial chaos basis functions increase the accuracy of the spectral representation, but add a lot more terms for problems with many stochastic dimensions.

The solution field variables, such as velocities, concentrations, and the electrostatic field potential are expanded similarly:

$$\mathbf{u}(\mathbf{x}, t; \theta) = \sum_{k=0}^P \mathbf{u}_k(\mathbf{x}, t) \Psi_k(\theta), \quad (21)$$

$$c(\mathbf{x}, t; \theta) = \sum_{k=0}^P c_k(\mathbf{x}, t) \Psi_k(\theta), \quad (22)$$

$$\phi(\mathbf{x}, t; \theta) = \sum_{k=0}^P \phi_k(\mathbf{x}, t) \Psi_k(\theta). \quad (23)$$

Using the orthogonality of the basis functions, the coefficients D_k , $\mathbf{u}_k(\mathbf{x}, t)$, $c_k(\mathbf{x}, t)$, and $\phi_k(\mathbf{x}, t)$ can be calculated by a projection operation onto the PC basis. Thus, for D_k

$$D_k = \frac{\langle \Psi_k D \rangle}{\langle \Psi_k^2 \rangle}, \quad (24)$$

where the expectation is defined as

$$\langle f \rangle = \frac{1}{(2\pi)^{N/2}} \int_{\mathbb{R}^N} f(\xi_1, \xi_2, \dots, \xi_N) \times \exp\left[-\frac{\sum_{i=1}^N \xi_i^2}{2}\right] d\xi_1 d\xi_2 \dots d\xi_N. \quad (25)$$

Note that the expectations $\langle \Psi_k \rangle = 0$ for $k > 0$. Therefore the zeroth-order spectral mode for each field quantity represents the mean field, whereas the higher order modes represent the variation, or uncertainty, around this mean. This is reflected in the calculation of the standard deviation σ of a quantity, as shown below for the concentration c :

$$\begin{aligned} \sigma_c^2 &= \langle (c - \langle c \rangle)^2 \rangle \\ &= \left\langle \left(\sum_{j=1}^P c_j \Psi_j \right) \left(\sum_{k=1}^P c_k \Psi_k \right) \right\rangle \\ &= \sum_{j=1}^P \sum_{k=1}^P c_j c_k \langle \Psi_j \Psi_k \rangle \\ &= \sum_{k=1}^P c_k^2 \langle \Psi_k^2 \rangle. \end{aligned} \quad (26)$$

To further interpret this, consider the example of a second-order PC expansion for the concentration c in the case of two uncertain parameters:

$$c = c_0 + c_1 \xi_1 + c_2 \xi_2 + c_3 (\xi_1^2 - 1) + c_4 \xi_1 \xi_2 + c_5 (\xi_2^2 - 1). \quad (27)$$

In Eq. (27), the ξ_1 dimension corresponds to the first uncertain parameter in the system, and ξ_2 corresponds to the second uncertain parameter. Substituting this expression into Eq. (26) and evaluating the $\langle \Psi_k^2 \rangle$, we obtain the following equation for the variance of c in this example:

$$\sigma_c^2 = c_1^2 + c_2^2 + 2c_3^2 + c_4^2 + 2c_5^2. \quad (28)$$

Grouping the terms that correspond to the same stochastic dimensions, it is possible to identify the contributions of individual parameters to this overall standard deviation:

$$\sigma_c^2 = \sigma_1^2 + \sigma_{12}^2 + \sigma_2^2, \quad (29)$$

$$\sigma_1 = \sqrt{c_1^2 + 2c_3^2}, \quad (30)$$

$$\sigma_{12} = \sqrt{c_4^2}, \quad (31)$$

$$\sigma_2 = \sqrt{c_2^2 + 2c_5^2}. \quad (32)$$

In these expressions, σ_1 and σ_2 represent the individual contributions of the first and second uncertain parameters, respectively, to the overall uncertainty in c . The term σ_{12} represents a coupled term involving the combined effect of the two parameters. This feature of the PC methodology is very powerful, as it allows identification of the major contributions to the uncertainty in the simulation output and model results.

After representing all model parameters and solution fields with PC expansions, those expansions are substituted into the transport equations for the deterministic quantities. Evolution equations for the unknown coefficients in the PC expansions are then obtained by a Galerkin approach. For example, consider the momentum equation. Substituting the appropriate PC expansions for velocities, pressure, and viscosity in Eq. (2), multiplying by Ψ_k , and taking the expectation gives^{23,24}

$$\begin{aligned} \frac{\partial \mathbf{u}_k}{\partial t} + \sum_{i=0}^P \sum_{j=0}^P C_{ijk} (\mathbf{u}_i \cdot \nabla) \mathbf{u}_j \\ = -\nabla p_k + \sum_{i=0}^P \sum_{j=0}^P C_{ijk} \nu_i \nabla^2 \mathbf{u}_j \end{aligned} \quad (33)$$

with $C_{ijk} \equiv \langle \Psi_i \Psi_j \Psi_k \rangle / \langle \Psi_k \Psi_k \rangle$. Similarly, the equations for the modes $c_{m,k}$ of the species concentration (with m the species index) become

$$\begin{aligned} \frac{\partial c_{m,k}}{\partial t} + \sum_{i=0}^P \sum_{j=0}^P C_{ijk} \nabla \cdot (c_{m,i} (\mathbf{u}_j + \mathbf{u}_{m,j}^e)) \\ = \sum_{i=0}^P \sum_{j=0}^P C_{ijk} \nabla \cdot (D_{m,i} \nabla c_{m,j}) + \hat{w}_{m,k}, \end{aligned} \quad (34)$$

where

$$\mathbf{u}_{m,j}^e = \frac{\langle \Psi_j \mathbf{u}^e \rangle}{\langle \Psi_j^2 \rangle} = \sum_{k=0}^P \sum_{i=0}^P C_{kij} \beta_k z F \nabla \phi_i, \quad (35)$$

$$\hat{w}_{m,k} = \frac{\langle \Psi_k \hat{w} \rangle}{\langle \Psi_k^2 \rangle}. \quad (36)$$

Equations (35) and (36) represent the pseudo-spectral projection of the electrophoretic velocities and the stochastic chemical source terms onto the ψ_k basis functions (see also Sec. IV F). Finally, the electrostatic field equation (16) becomes

$$\begin{aligned} \sum_{i=0}^P \sum_{j=0}^P C_{ijk} \nabla \cdot (\sigma_i \nabla \phi_j) \\ = -F \sum_m z_m \sum_{i=0}^P \sum_{j=0}^P C_{ijk} \nabla \cdot (D_{m,i} \nabla c_{m,j}). \end{aligned} \quad (37)$$

The modes σ_i of the electrical conductivity are obtained from

$$\sigma_i = F^2 \sum_m z_m^2 \sum_{j=0}^P \sum_{k=0}^P C_{jki} \beta_{m,j} c_{m,k}. \quad (38)$$

Equations (33), (34), and (37) each represent a set of $P+1$ coupled equations to be solved for the mode strengths u_k , $c_{m,k}$, and ϕ_k , $k=0, \dots, P$. With M species, the total number of equations to be solved is $(M+2)(P+1)$.

IV. IMPLEMENTATION

A. Data structure

As described in Sec. II B, species concentrations are integrated differently, based on whether or not they take part in equilibrium reactions. For instance, for components of weak acids or bases, which typically serve as buffers, only the combined concentration of all components is integrated directly. The total charge associated with the buffer components is required for the enforcement of the electroneutrality equation (14). For a given buffer, this total charge can be obtained from the total buffer concentration θ and $[H^+]$ through buffer-specific equations such as Eqs. (11) and (12).

To make the treatment of weak acids or bases as general as possible, separate objects are used in the current code to represent these components. Each object contains all the species properties for the weak acid or base it represents, as well as the dissociation constants for the electrolyte reactions between its species. Specific functions are also associated with each object to return the total charge or other information about the weak acid or base, given its total concentration and $[H^+]$. This way, different buffers can be included in the simulations by simply including different objects, without the need for specific code modifications.

B. Spatial discretization

The computational domain is discretized using a Cartesian mesh with uniform cell size Δx and Δy in the x and y direction, respectively. Vector fields, such as the velocity and the electrostatic field strength, are defined on the cell faces. Scalar fields, such as pressure and species concentrations, are defined at the cell centers. Spatial derivatives are discretized with second-order central differences.

C. Electroneutrality

As explained in Sec. II B, the individual concentrations of the buffer ions and $[H^+]$ are obtained from the electroneutrality condition (14). This results in a set of nonlinear algebraic relations between $P+1$ stochastic modes. This coupled nonlinear system of equations is iteratively solved at each point in the domain, using a Newton solver from the NITSOL package.²⁵ The solver uses an inexact Newton method with backtracking. Using the solution from the previous time step as initial guess, the convergence is generally very fast.

D. Electrostatic field strength

To obtain the electrostatic field potential ϕ , the set of $P+1$ equations (37) needs to be solved over the domain. Since these equations are coupled, an iterative solution method was developed, consisting of Gauss–Seidel iterations over the spatial dimensions in combination with SOR iterations over the stochastic dimensions. To accelerate the convergence speed, spatial coarsening with a multigrid approach is applied. The electrostatic field strength is computed in turn as the gradient of the electrostatic potential.

E. Time integration

The time integration algorithm in this work is based on a previously developed stochastic projection method for the momentum equations in low-Mach-number flow.²⁴ This momentum solver uses a time splitting approach in which the convection and diffusion terms are integrated in a first fractional step, and the continuity constraints are then enforced in a pressure projection step.²⁶ Since the continuity constraints [Eq. (1)] are decoupled in the stochastic dimension, this leads to a set of $P+1$ decoupled Poisson problems.

In the current work, this method is expanded to the integration of the coupled momentum and species transport equations, in combination with the electrostatic field solu-

tion. For brevity, the equations for the stochastic mode k of the species concentrations and the velocity can be written as

$$\frac{\partial c_k}{\partial t} = -Csp_k + Dsp_k + Ssp_k, \quad (39)$$

$$\frac{\partial \mathbf{u}_k}{\partial t} = -Cm_k + Dm_k - \nabla p_k \quad (40)$$

where Csp_k , Dsp_k , and Ssp_k represent the convection, diffusion, and chemical source terms in the species equation (34). Similarly, Cm_k and Dm_k represent the convection and diffusion terms in the momentum equation (33). Using the projection scheme for momentum, in combination with a Runge–Kutta (RK) time integration scheme, Eqs. (39) and (40) are discretized between t^n and the RK stage time level $t^{(s)} = t^n + \Delta t^{(s)}$ as

$$\begin{aligned} \frac{c_k^{(s)} - c_k^n}{\Delta t^{(s)}} &= -Csp_k^{(s-1)} + Dsp_k^{(s-1)} + Ssp_k^{(s-1)} \\ &\equiv \mathcal{Fsp}_k^{(s-1)}, \end{aligned} \quad (41)$$

$$\frac{\mathbf{u}_k^{(s),*} - \mathbf{u}_k^n}{\Delta t^{(s)}} = -Cm_k^{(s-1)} + Dm_k^{(s-1)} \equiv \mathcal{Fm}_k^{(s-1)}, \quad (42)$$

$$\frac{\mathbf{u}_k^{(s)} - \mathbf{u}_k^{(s),*}}{\Delta t^{(s)}} = -\nabla p_k^{(s)}, \quad (43)$$

where \mathcal{Fsp}_k and \mathcal{Fm}_k represent the full right-hand sides in the corresponding time integration steps. Equation (43) is the pressure correction step, which requires the pressure to be solved for first. The equation for pressure is obtained by substituting Eq. (43) into the stochastic form of the continuity equation for $\mathbf{u}^{(s)}$,

$$\nabla \cdot \mathbf{u}_k^{(s)} = 0 \quad (44)$$

resulting in the following set of Poisson equations:

$$\nabla^2 p_k^{(s)} = -\frac{1}{\Delta t^{(s)}} \nabla \cdot \mathbf{u}_k^{(s),*} \quad k=0, \dots, P. \quad (45)$$

As discussed in Ref. 24, these $P+1$ Poisson equations are decoupled; therefore, each can be solved individually using existing Poisson solvers for deterministic flow problems. In the current work, the same fast Fourier transform based flow solver is used as in Ref. 24.

The time integration of Eqs. (41) and (42) is performed using the four-stage, fourth order Runge–Kutta scheme (RK4),²⁷ which was selected because of its good stability for convection dominated problems. Keeping in mind the coupling between the equations, the computations during the subsequent stages of the RK4 integration over a time step Δt from time t^n to $t^{n+1} = t^n + \Delta t$ can be represented with the following pseudo-code. The superscripts (s) denote the Runge–Kutta stage number. For clarity, the subscripts for the mode strength k have been dropped.

Stage $s=1$; $t=t^n$.

Calculate the right hand sides in Eqs. (41) and (42) using the species concentrations, velocities and electrostatic field strength at time $t=t^n$:

- $\mathcal{Fsp}^{(1)} = \mathcal{Fsp}(c(t^n), \mathbf{u}(t^n), \mathbf{E}(t^n))$,
- $\mathcal{Fm}^{(1)} = \mathcal{Fm}(\mathbf{u}(t^n), u_w(t^n))$ where u_w is the electroosmotic wall velocity.

Stage $s=2,3,4$; $t=t^n + \Delta t^{(s)}$.

Update species concentrations to the current time level:

- $c^{(s)} = c(t^n) + \Delta t^{(s)} \mathcal{Fsp}^{(s-1)}$ for all directly integrated species.
- Solve electroneutrality constraint to obtain $[\text{H}^+]^{(s)}$.
- Update concentrations of weak acids and/or bases.

Update electrostatic field strength and velocity boundary conditions using the updated concentrations:

- $\mathbf{E}^{(s)} = \mathbf{E}(c^{(s)})$.
- $u_w^{(s)} = u_w(c^{(s)}, \mathbf{E}^{(s)})$.

Update velocities to the current time level:

- Update the velocities to their intermediate (*) values at the current time level: $\mathbf{u}^{(s),*} = \mathbf{u}(t^n) + \Delta t^{(s)} \mathcal{Fm}^{(s-1)}$.
- Apply the boundary conditions $u_w^{(s)}$ to the $\mathbf{u}^{(s),*}$ velocity field.
- Solve for pressure at this time level using Eq. (45): $p^{(s)} = p(\mathbf{u}^{(s),*})$.
- Apply the pressure correction to $\mathbf{u}^{(s),*}$ to obtain $\mathbf{u}^{(s)}$: $\mathbf{u}^{(s)} = \mathbf{u}^{(s),*} - \Delta t^{(s)} \nabla p^{(s)}$.

Calculate the new right hand sides in Eqs. (41) and (42) using the updated species concentrations, velocities, and electrostatic field strength:

- $\mathcal{Fsp}^{(s)} = \mathcal{Fsp}(c^{(s)}, \mathbf{u}^{(s)}, \mathbf{E}^{(s)})$,
- $\mathcal{Fm}^{(s)} = \mathcal{Fm}(\mathbf{u}^{(s)}, u_w^{(s)})$.

Final update to time $t^{n+1} = t^n + \Delta t$.

Update species concentrations to t^{n+1} :

- $c(t^{n+1}) = c(t^n) + \Delta t(\frac{1}{6}\mathcal{Fsp}^{(1)} + \frac{2}{6}\mathcal{Fsp}^{(2)} + \frac{2}{6}\mathcal{Fsp}^{(3)} + \frac{1}{6}\mathcal{Fsp}^{(4)})$ for all directly integrated species.
- Solve electroneutrality constraint to obtain $[\text{H}^+]$ at t^{n+1} .
- Update concentrations of weak acids and/or bases.

Update electrostatic field strength and velocity boundary conditions using the updated concentrations:

- $\mathbf{E}(t^{n+1}) = \mathbf{E}(c(t^{n+1}))$,
- $u_w(t^{n+1}) = u_w(c(t^{n+1}), \mathbf{E}(t^{n+1}))$.

Update velocities to t^{n+1} :

- Update the velocities to the intermediate (*) values at t^{n+1} : $\mathbf{u}^*(t^{n+1}) = \mathbf{u}(t^n) + \Delta t(\frac{1}{6}\mathcal{Fm}^{(1)} + \frac{2}{6}\mathcal{Fm}^{(2)} + \frac{2}{6}\mathcal{Fm}^{(3)} + \frac{1}{6}\mathcal{Fm}^{(4)})$.
- Apply the boundary conditions $u_w(t^{n+1})$ to the $\mathbf{u}^*(t^{n+1})$ velocity field.

- Solve for pressure at t^{n+1} using Eq. (45): $p(t^{n+1}) = p(\mathbf{u}^*(t^{n+1}))$.
- Apply the pressure correction to $\mathbf{u}^*(t^{n+1})$ to obtain $\mathbf{u}(t^{n+1})$: $\mathbf{u}(t^{n+1}) = \mathbf{u}^*(t^{n+1}) - \Delta t \nabla p(t^{n+1})$.

In the above integration scheme, the respective time steps $\Delta t^{(s)}$ of the Runge–Kutta stages $s=2, 3$, and 4 are given by $\frac{1}{2}\Delta t$, $\frac{1}{2}\Delta t$, and Δt .

F. Tools for stochastic operations: Uncertainty quantification toolkit

As explained in Sec. III, the governing equations for the spectral mode strengths of the field variables are obtained by substituting the PC expansions for those field variables in their original, deterministic governing equations. Instead of explicitly writing out these equations for the spectral mode strengths, it is also possible to retain the governing equations in their original form, but take into account during the implementation that all arithmetic needs to be performed on stochastic instead of deterministic variables.

To facilitate this approach, we developed an uncertainty quantification (UQ) toolkit which contains subroutines to perform most of the common operations on stochastic variables that are represented by PC expansions. Using this toolkit, many algorithms that were originally designed for deterministic problems can easily be converted for stochastic computations by merely replacing mathematical operators with calls to their stochastic equivalent. The details of some of these operations are explained in the following.

Aside from additions, one of the most common operations is the multiplication of two stochastic variables. Consider two stochastic variables, u and v , with the following PC representations:

$$u = \sum_{i=0}^P u_i \Psi_i, \quad (46)$$

$$v = \sum_{j=0}^P v_j \Psi_j. \quad (47)$$

We need to find the modes w_k in the PC representation of $w = uv$:

$$w = \sum_{k=0}^P w_k \Psi_k. \quad (48)$$

As mentioned before, these coefficients are obtained by using the orthogonality property of the PC basis functions:

$$w_k = \sum_{i=0}^P \sum_{j=0}^P C_{ijk} u_i v_j, \quad k=0, \dots, P \quad (49)$$

with

$$C_{ijk} \equiv \frac{\langle \Psi_i \Psi_j \Psi_k \rangle}{\langle \Psi_k^2 \rangle}. \quad (50)$$

Since the tensor C_{ijk} is a function of the PC basis functions only, it only needs to be calculated once during a preprocessing step and can then be stored for use throughout the com-

putations. The implementation of Eq. (49) also takes advantage of the fact that this tensor is sparse, reducing the amount of storage and CPU time needed.

A similar procedure could also be used to determine the PC expansion for the product of three stochastic variables $g = uvw$. This would give the spectral coefficients g_l as

$$g_l = \sum_{i=0}^P \sum_{j=0}^P \sum_{k=0}^P D_{ijkl} u_i v_j w_k, \quad l=0, \dots, P, \quad (51)$$

where

$$D_{ijkl} \equiv \frac{\langle \Psi_i \Psi_j \Psi_k \Psi_l \rangle}{\langle \Psi_l^2 \rangle}. \quad (52)$$

Instead of this pure spectral approach, however, a pseudo-spectral approach is used in this work to calculate products such as $g = uvw$ by repeated use of the regular product function. First the product uv is calculated with Eq. (49), and the result of this multiplication is multiplied in the same way with w to give the PC expansion for g . The advantage of this pseudo-spectral approach is that it does not require the evaluation and storage of the fourth-rank tensor D_{ijkl} , is more efficient, and is easy to generalize to products of any number of variables. Some aliasing errors are introduced though in this approach, but they were found to be negligible as long as the order of the PC expansions is chosen sufficiently high.

Another frequent operation is the calculation of the inverse of a stochastic quantity. To explain how this operation is implemented, consider again three stochastic variables, u , v , and w , with their respective PC expansions given by Eqs. (46)–(48). If we wish to calculate $u = w/v$, then this implies $w = uv$, which is given by Eq. (49). This equation, assuming the modes w_k and v_j are known, represents a system of $P+1$ linear equations in the unknown modes u_i . Since it is a sparse system of equations, it is solved efficiently in this work with a GMRES iterative solver, taken from the SLATEC library.²⁸

More challenging is the evaluation of nonpolynomial functions of stochastic variables such as the exponential, which will show up in the calculation of the protein labeling reaction rate with Eq. (56), or the logarithm in the calculation of pH. Currently, these operations are performed by expanding them in Taylor series around the mean of the argument. For example, the exponential of a stochastic quantity u , with a PC expansion given by Eq. (46), is computed as

$$e^u = e^{u_0} \left(1 + \sum_{n=1}^N \frac{d^n}{n!} \right), \quad (53)$$

where

$$d = u - u_0 = \sum_{i=1}^P u_i \Psi_i \quad (54)$$

is the stochastic part of u . The powers d^n are again calculated in a pseudo-spectral way with the product formula (49), as $d^n = d d^{n-1}$, with d^{n-1} known from the previous term in the Taylor series. The number of terms N in this truncated series is chosen adaptively to satisfy a given tolerance level.

The Taylor series approach works reasonably well as long as the uncertainties in the field variables are moderate and the probability density functions (PDFs) of those variables are not too skewed. For highly skewed PDFs, however, high order PC expansions are required to capture this stochastic information, and the evaluation of high power terms d''' in the Taylor series can become inaccurate. A new approach, based on integrations, is currently under development to alleviate this problem.

All the operations described above, among many others, have been implemented in the UQ toolkit library. The UQ toolkit greatly facilitates the development of stochastic solvers from scratch, as well as the conversion of existing deterministic routines into stochastic ones. A more general and effective approach would be to develop the capability to automatically convert existing deterministic programs to stochastic arithmetic. As an extension of the UQ toolkit methodology, this could conceptually be achieved by creating a new data type for variables represented with PC expansions, and then overloading operators to perform the proper stochastic operations on these variables where needed. Such an approach is outside the scope of this paper but will be explored elsewhere.

V. NUMERICAL RESULTS

A. Test system

This section presents some results of test problems illustrating the spatial and temporal convergence properties of the developed code. Figure 2 shows the geometry considered for these test problems, consisting of a rectangular microchannel in which a protein U and dye D react to form a labeled protein L. An external electrostatic potential is applied across the system to generate an electroosmotic flow in the x direction. The unlabeled protein U has a charge of $+1$ versus a charge of -1 for the dye D, so electrophoresis will move U forward and D backward, relative to the bulk flow. For all cases simulated in this work, an aqueous potassium phosphate (KH_2PO_4) buffer solution is considered. Therefore, the species in the solution are the proteins U and L, the dye D, the electrolytes H^+ , OH^- , K^+ as well as the components of phosphoric acid H_3PO_4 , H_2PO_4^- , HPO_4^{2-} , and PO_4^{3-} .

As mentioned in Sec. II B, the proteins in this solution are assumed to have a fixed charge and can therefore be integrated with Eq. (5) with a chemical reaction source term \hat{w}_i according to a model irreversible labeling reaction



The rate constant k_L in this reaction is pH dependent, given by the following:

$$k_L = k_L^0 + d_L e^{-(\text{pH} - \text{pH}_0)/\delta_{\text{pH}}}. \quad (56)$$

The Gaussian dependence of this relationship on pH is based on the shape of the measured pH-dependence of the rate of production of the high-fluorescence-efficiency species from the reaction of naphthalene-2,3-dicarboxaldehyde (NDA) with amino acids in the presence of CN^- .²⁹ Unless stated otherwise, the values for the reaction rate parameters are

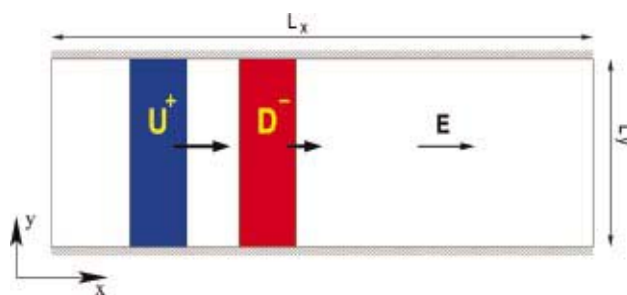


FIG. 2. (Color) Geometry for the numerical test problems: a plug of protein U and dye D are introduced in a rectangular microchannel and react to form a labeled protein L.

chosen in this work as $k_L^0 = 0.25 \times 10^6 \text{ mol}^{-1} \text{ l s}^{-1}$, $d_L = 2.15 \times 10^6 \text{ mol}^{-1} \text{ l s}^{-1}$, $\text{pH}_0 = 7.40$, and $\delta_{\text{pH}} = 0.85$. The chemical source terms used in Eq. (5) are correspondingly

$$\hat{w}_U = \hat{w}_D = -\hat{w}_L = -k_L[\text{U}][\text{D}]. \quad (57)$$

The concentration of the K^+ ion, which is fully dissociated and is a conserved quantity can also be integrated by Eq. (5) directly (without a source term). Phosphoric acid, however, is a weak acid and will dissociate according to the following electrolyte reactions:



where the K_i are the corresponding dissociation constants. As discussed in Sec. II B, an equilibrium formulation is used for these fast electrolyte reactions. Therefore, we consider the total concentration of this weak acid

$$\theta_a = [\text{H}_3\text{PO}_4] + [\text{H}_2\text{PO}_4^-] + [\text{HPO}_4^{2-}] + [\text{PO}_4^{3-}] \quad (61)$$

whose transport equation is obtained similarly to Eq. (10) by adding up the transport equations for all the components in θ_a so the dissociation reaction source terms disappear. The concentrations of the individual components of θ_a are then calculated as $c_i = \alpha_i \theta_a$, where the α_i are calculated from the equilibrium expressions for the dissociation reactions (58)–(60) and can be written as a function of $[\text{H}^+]$ and the dissociation constants only:

$$\alpha_{\text{H}_3\text{PO}_4} = \frac{[\text{H}^+]^3}{[\text{H}^+]^3 + K_1[\text{H}^+]^2 + K_1K_2[\text{H}^+] + K_1K_2K_3}, \quad (62)$$

$$\alpha_{\text{H}_2\text{PO}_4^-} = \frac{K_1[\text{H}^+]^2}{[\text{H}^+]^3 + K_1[\text{H}^+]^2 + K_1K_2[\text{H}^+] + K_1K_2K_3}, \quad (63)$$

$$\alpha_{\text{HPO}_4^{2-}} = \frac{K_1K_2[\text{H}^+]}{[\text{H}^+]^3 + K_1[\text{H}^+]^2 + K_1K_2[\text{H}^+] + K_1K_2K_3}, \quad (64)$$

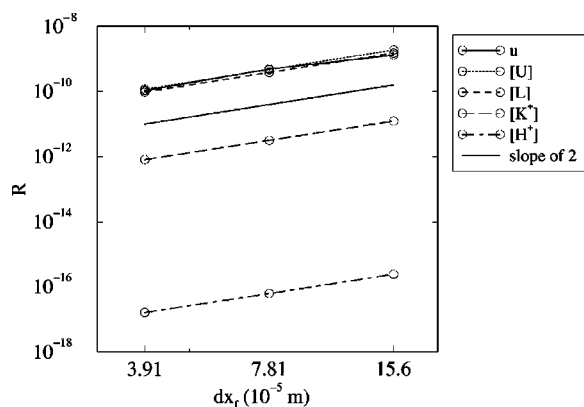


FIG. 3. L^2 norm of the difference between solutions on successive grids as a function of the grid spacing dx_f . The slope of the lines shows a second-order spatial convergence rate for various species concentrations as well as the streamwise velocity.

$$\alpha_{\text{PO}_4^{3-}} = \frac{K_1 K_2 K_3}{[H^+]^3 + K_1 [H^+]^2 + K_1 K_2 [H^+] + K_1 K_2 K_3} \quad (65)$$

As discussed in Sec. II A, Eq. (4) is used to model the dependence of the zeta potential on pH and buffer molarity. The concentration of the fully dissociated potassium ion, $[K^+]$, is used for the local buffer molarity \mathcal{M} along the walls. The temperature is assumed constant in this work, with all species properties and reaction rate constants evaluated at 298 K.

For the computations in this paper, all parameters and eld variables, were represented with third-order polynomial chaos expansions. The highest order stochastic modes in the expansions of the predicted eld variables were significantly lower than the lower order modes, indicating that the third-order expansions were sufficiently accurate.

B. Convergence with grid spacing

To test the spatial convergence rate of the code, simulations of the test case described above were run on a domain with $L_x = 1$ cm and $L_y = 0.25$ cm. The potassium phosphate buffer solution was initialized with a uniform concentration of 10^{-3} mol/l and a pH of 7.25. The unlabeled protein U and the dye D were initialized with a profile, Gaussian in x and uniform in y , both with a maximum concentration of 10^{-5} mol/l at $x = 4$ mm and a width of 1 mm. The labeled protein concentration was initialized to zero. The electrostatic potential difference ΔV between the inlet and exit of the domain was set to 10 V, creating an average eld strength of 0.01 kV/cm. An uncertainty of 1% was assumed in the mobilities of both U and D, in the labeling rate parameter pH_0 of Eq. (56), and in the potential difference ΔV . Using third order polynomial chaos expansions, these four uncertain parameters led to four stochastic dimensions with a total of $P + 1 = 35$ stochastic modes.

Four runs were performed, with uniform grid spacings in x and y doubling between each run, from 3.91×10^{-5} m in the nest grid to 3.13×10^{-4} m in the coarsest grid (corresponding, respectively, to 256×64 , 128×32 , 64×16 , and

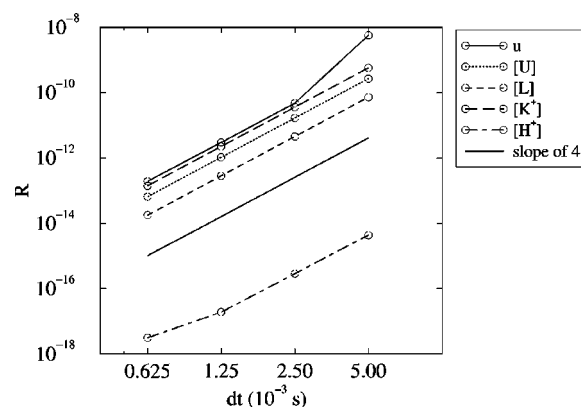


FIG. 4. L^2 norm of the difference between solutions at successive time steps as a function of the shorter time step dt . The slope of the lines shows a fourth-order temporal convergence rate for various species concentrations as well as the streamwise velocity.

32×8 cells in $x \times y$). Each run used the same time step of 10^{-4} s for a total of 200 time steps. Figure 3 shows the L^2 norm of the difference between the solutions for the streamwise velocity u as well as several species concentrations at successive grid spacings. To monitor the spatial convergence of the full stochastic solution, the L^2 norm was calculated over all points in space and all $P + 1$ stochastic modes. Clearly, the slope of the curves in Fig. 3 shows an overall second-order convergence rate with grid spacing, consistent with the spatial differencing scheme used.

C. Convergence with time step

The temporal convergence behavior of the code was studied with a similar test case as in the previous section. Referring to Fig. 2, the domain sizes were chosen as $L_x = 2$ cm and $L_y = 0.25$ cm. The buffer initialization was the same as in the previous case. For the unlabeled protein U and the dye D, however, the peak concentrations were raised to 10^{-4} mol/l, located at $x = 4$ mm and $x = 6$ mm, respectively. The electrostatic potential difference ΔV across the domain was set to 2000 V, giving an average eld strength of 1 kV/cm. A slightly higher uncertainty of 2% was assumed in the mobilities of both U and D, the parameters pH_0 and ΔV , as well as the bulk kinematic viscosity. These stochastic dimensions with third-order polynomial chaos expansions led to a total of $P + 1 = 56$ stochastic modes.

This test case was run for a total time of 0.5 s, with different time steps, ranging in factors of 2 from 6.25×10^{-4} s up to 1.00×10^{-2} s. In each case, the number of cells was 128×16 in $x \times y$. Figure 4 shows the L^2 norm of the difference between the solutions for the streamwise velocity u as well as several species concentrations at successive time steps. The fourth-order temporal convergence rate observed in Fig. 4 is consistent with the Runge–Kutta scheme used in the time integration.

VI. PROTEIN LABELING IN A HOMOGENEOUS BUFFER

To illustrate the stochastic uncertainty quantification methodology, this section describes protein labeling in a

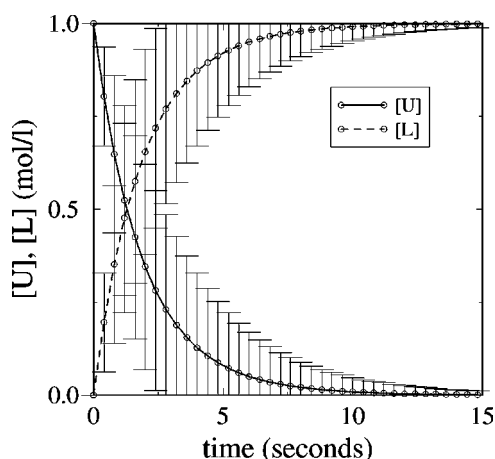


FIG. 5. Time evolution of U and L concentrations in a homogeneous protein labeling reaction. The uncertainty in these concentrations, due to a 1% uncertainty in the labeling reaction rate parameters, is indicated by $\pm 3\sigma$ “error bars.”

simple homogeneous system. Figure 5 shows the time evolution of the concentrations of the unlabeled and labeled protein in a homogeneous potassium phosphate buffer at a pH of 8.25. In this problem, the dye D was assumed to be present in abundance so that the source term for the labeled protein in Eq. (5) can be written as

$$\hat{w}_L = k_L[U]. \quad (66)$$

The same expression as before, Eq. (56), was used for the reaction rate, but with the following parameters: $k_L^0 = 0.25 \times 10^{-3} \text{ s}^{-1}$, $d_L = 2.15 \text{ s}^{-1}$, $\text{pH}_0 = 9.25$, and $\delta_{\text{pH}} = 0.85$. Both proteins U and L, as well as the dye D were assumed to have no charge, and therefore the buffer equilibrium and pH did not change with time. For this simulation, a standard deviation of 1% was assumed for all parameters in the rate expression (56), as well as for the electrolyte dissociation constants. Third order PC expansions were used.

The resulting uncertainty in the protein concentrations is indicated in Fig. 5 with “error bars” that span the $\pm 3\sigma$ range, where σ indicates the standard deviation. Clearly, uncertainty in the input parameters causes large uncertainties in the simulated concentrations. At the point where $[U] = 0.5$, a standard deviation of 1% in the parameter pH_0 is magnified about 16 times in the standard deviation of $[U]$.

Note that after about 3 s, the range of the $\pm 3\sigma$ “error bars” becomes so large that it seems to include concentrations for U that are negative, which is clearly not physically possible. However, the interval $\pm 3\sigma$ around the mean value properly represents the full range of possibilities for a certain variable only when its probability density function is Gaussian, and therefore symmetric. Figure 6 shows the probability density function of $[U]$, generated from its PC expansion at various points in time. When the mean value of $[U]$ is sufficiently far away from zero, this PDF has a Gaussian shape. However, for mean values of $[U]$ closer to zero, the PDF becomes narrower and more skewed. This predicted uncertainty properly reflects the physical system behavior where all unlabeled protein reacts away, but its concentration can not be negative.

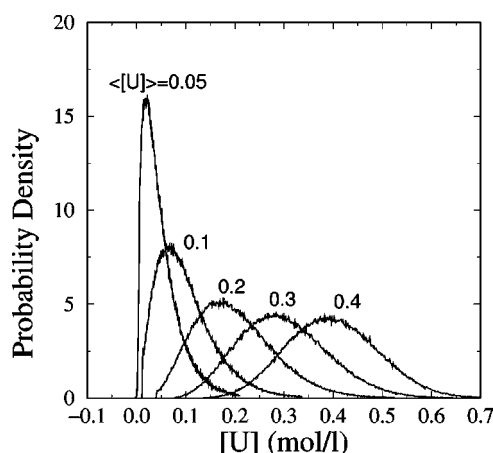


FIG. 6. PDF of the unlabeled protein concentration at different mean values. As the unlabeled protein reacts away, its PDF becomes narrower and more skewed.

VII. PROTEIN LABELING IN A TWO-DIMENSIONAL MICROCHANNEL

In this section, the simulation and uncertainty quantification code is used to tackle a more physically challenging problem of protein labeling in a two-dimensional microchannel. The problem setup is similar to the numerical test problems described in Sec. V. The labeling reaction is the same as Eq. (55) with the reaction rate k_L and the corresponding source terms as in Eqs. (56) and (57). Again, a charge of +1 is assumed for the unlabeled protein U and a charge of -1 for the dye D, resulting in a neutral labeled protein L.

Referring to Fig. 2, a microchannel was considered with a length $L_x = 1 \text{ cm}$ and a height $L_y = 1 \text{ mm}$. The potassium phosphate buffer solution was initialized with a uniform concentration of 10^{-3} mol/l and a pH of 7.25. The Gaussian profiles for the initial U and D concentrations had peak concentrations of 10^{-4} mol/l , located at $x = 2.5 \text{ mm}$ and $x = 4 \text{ mm}$, respectively, and a width in x of 0.75 mm. The electrostatic potential difference ΔV across the domain was set to 1000 V, giving an average field strength of 1 kV/cm. An uncertainty of 1% was assumed in the mobility of U, in the labeling rate parameter pH_0 , the dissociation constant K_2 , and the potential difference ΔV . Third-order polynomial chaos expansions were used in the computations with a total of 35 stochastic modes. The time step was set to $2 \times 10^{-4} \text{ s}$ and the domain was discretized with 512×32 cells in x and y .

Figure 7 shows a contour plot of the mean concentrations of the proteins and dye at $t = 0.12 \text{ s}$. At this point in time, the plugs of U and D have just met at $x \approx 4 \text{ mm}$, and labeled protein is generated at the interface. Note that the labeling reaction is fast compared to the electroosmotic and electrophoretic transport. Consequently, U and D react as soon as they meet, resulting in almost no overlap between the U and D profiles, and a sharp profile for L. Since L is neutral, it travels with the bulk convective velocity, which is the average of the total convective velocities of U and D. Therefore the peak value of L is always located at the interface of U and D, and since L is generated in that same area,

its peak concentration will keep increasing. At $t = 0.12$ s, the peak concentration for L is 1.3×10^{-4} mol/l, which is already higher than the peak concentrations of 9.4×10^{-5} mol/l for U and D.

The standard deviations in the concentrations of Fig. 7 are given in Fig. 8. The highest uncertainties appear in the reaction zone at the interface between U and D, with a maximum coefficient of variation of about 20% in the L concentration. Even though Fig. 8 only shows the overall uncertainty in the concentrations, a strong feature of the PC formalism is that the contributions of the uncertainty in individual parameters to this overall uncertainty can easily be retrieved, as explained in Sec. III. Figure 9, for example, shows the contributions from each of the four uncertain input parameters to the standard deviation of the L concentration, in the area around the reaction zone, at $y = 0.5$ mm. These contributions were obtained with a similar analysis as in Eqs. (27)–(32), but for the case of four stochastic dimensions and third-order PC expansions. The total standard deviation of $[L]$ is given by the curve labeled “all” in this figure. This overall standard deviation has a profile with a double peak, which for a single peak mean species profile, is characteristic of uncertainty caused by the convection velocity. When a single peak species profile is transported by an uncertain convection velocity, the uncertainty in the position of the peak at a given point in time will cause the most variability at the sides of the peak, where the profile has a steep slope in the x direction. At the top of the profile, there is no concentration gradient and uncertainties in peak position cause little uncertainty in the observed concentrations at that location.

As indicated by the curve labeled “ ΔV ,” the uncertainty in the applied electrostatic field potential has the most dominant contribution to the overall standard deviation. Since both the electroosmotic and electrophoretic velocities are directly proportional to ΔV , the uncertainty caused by this parameter naturally shows a double peak, characteristic of convection velocity uncertainty. Similarly, the parameter β_U affects the electrophoretic transport of the reactant U and its resulting contribution to the standard deviation of $[L]$ also has a double peak, albeit smaller than the ΔV contribution.

The contribution of parameter pH_0 also shows a double peak, but with its center located on the left side of the $[L]$ profile, where the gradient of $[L]$ in x is very steep. The steepness of the $[L]$ profile in that area is largely determined by the speed of the labeling reaction compared to the convection speed, with a faster reaction rate leading to a sharper increase in $[L]$. With the pH in this area between 7.0 and 7.1 (not shown), Eq. (56) predicts significant variability in k_L for changes in pH_0 . So the uncertainty in pH_0 mainly affects the slope of the $[L]$ profile on the left side, consistent with the observed contribution of parameter pH_0 in Fig. 9.

Figure 9 further shows more minor contributions, from the dissociation parameter K_2 and from the coupled terms. Even though their contribution is small in this case, those coupled terms are interesting from a theoretical point of view, as they represent coupled effects of independent parameters. In the current figure, those terms represent the sum of three different coupled effects: the coupled effect of ΔV and β_U , of ΔV and pH_0 , and of ΔV and K_2 .

As time goes on and the U and D plugs cross each other, nearly all U and D are consumed in the labeling reaction. At $t = 0.50$ s, only labeled protein L remains, with its mean concentration and standard deviation as shown in Fig. 10. The maximum mean concentration of L at this point in time is 2.4×10^{-4} mol/l in the center of the channel, and about 3.2×10^{-4} mol/l near the walls. So the L concentration is up to three times as large as the initial U and D concentrations. The standard deviation in L, as shown in the bottom plot of Fig. 10, is very large near the wall, with maximum values up to 10^{-4} mol/l and coefficients of variation up to 100%. Again, the standard deviation in $[L]$ exhibits the double peak near the centerline, which is characteristic of uncertainty caused by the convection velocity.

What is particularly significant though, is the major distortion of the L plug, as opposed to the straight profile observed at early times. This distortion is caused by the disturbance of the buffer electrolyte, in response to the movement and annihilation of the charged protein U and the dye D. To explain why this is physically happening, consider Fig. 11, which shows the mean and standard deviation of the electrical conductivity σ of the electrolyte solution at $t = 0.50$ s. Because two charged molecules are used up for every new labeled protein, the area around the L plug has a reduced concentration of ions, with a mean electrical conductivity of almost a third lower than in the undisturbed buffer. Upstream of the L plug, the electrical conductivity shows some smaller fluctuations, which stem from shifts in the buffer equilibrium. Since the buffer ions are primarily negatively charged, those disturbances travel slower than the labeled protein plug. The bottom plot of Fig. 11 shows that the highest uncertainties in the electrical conductivity are found around the L plug, near the center and especially at the walls.

The large spatial variations in the electrical conductivity in turn cause nonuniformities in the electrical field strength, as shown in Figs. 12 and 13. Near the L plug, the mean electrostatic field strength in the x direction reaches a value up to 40% higher than in the undisturbed flow. This increase strongly affects the local electroosmotic and electrophoretic velocities, causing an increased wall velocity, leading to the observed distortion of the L plug. The largest uncertainties are again found near the L plug, with maxima up to 10%. Even though the initial field strength in the y direction was zero, Fig. 13 shows that this y component is quite significant at $t = 0.50$ s. The magnitude of this field strength is up to 15% of the initial, streamwise electrostatic field strength for the mean value. Even though this y component does not affect the electroosmotic flow velocity directly, it does provide electrophoretic ion transport in the wall-normal direction, which can further distort sample profiles.

As indicated by Eq. (3), the electroosmotic wall velocity depends on both the local electrostatic field strength and ζ potential, which in turn depends on the pH and the buffer molarity, as modeled by Eq. (4). Since all these variables are disturbed by the charged protein movement and annihilation, the electroosmotic wall velocity varies in the streamwise direction. These wall velocity changes in turn cause pressure gradients and local recirculation zones, as indicated by the velocity fields in Figs. 14 and 15. Figure 14 shows the

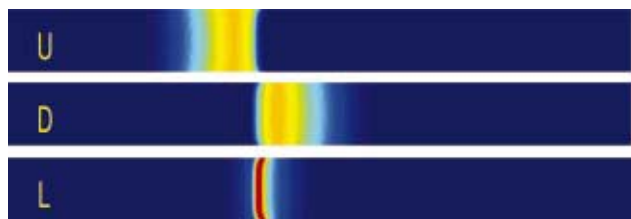


FIG. 7. (Color) Mean concentrations of proteins U, L, and dye D at $t = 0.12$ s. U and D just met and L is produced at their interface. The values of the contour levels go linearly from 0 (blue) to 1.3×10^{-4} mol/l (red). In this figure, as well as in all subsequent contour plots, the full physical domain is shown, from 0 to 1 cm in x and from 0 to 1 mm in y .

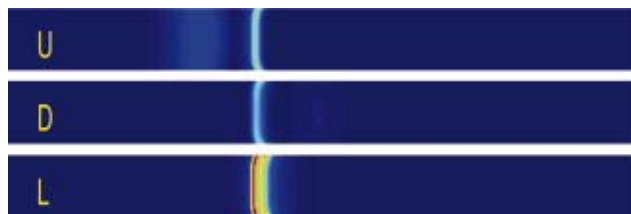


FIG. 8. (Color) Standard deviation of the protein and dye concentrations at $t = 0.12$ s. The values of the contour levels go linearly from 0 (blue) to 1.1×10^{-5} mol/l (red). The largest uncertainties are found in the reaction zone.

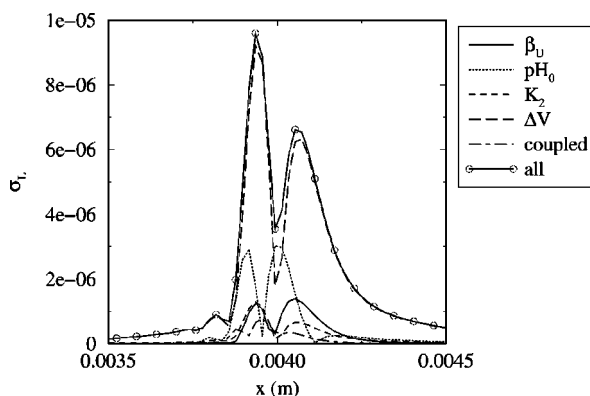


FIG. 9. Major contributions of individual input parameters to the overall standard deviation in $[L]$ in the area around the reaction zone at $t = 0.12$ s, $y = 0.5$ mm. The uncertainty in the applied voltage potential " ΔV " has the most dominant contribution to the overall standard deviation in $[L]$.



FIG. 10. (Color) Mean (top) and standard deviation (bottom) of the labeled protein concentration L at $t = 0.50$ s. The initially at profiles are now severely distorted. The values of the contour levels go linearly from 0 (blue) to 3.2×10^{-4} mol/l (red) in the top plot and from 0 (blue) to 10^{-4} mol/l (red) in the bottom plot.



FIG. 11. (Color) Mean (top) and standard deviation (bottom) of the electrical conductivity of the electrolyte solution at $t = 0.50$ s. Annihilation of ions in the labeling reaction results in a significantly lower mean electrical conductivity near the L plug. The values of the contour levels go linearly from 7.1×10^{-3} S/m (blue) to 1.3×10^{-2} S/m (red) in the top plot and from 0 (blue) to 1.5×10^{-3} S/m (red) in the bottom plot.



FIG. 12. (Color) Mean (top) and standard deviation (bottom) of the electrical field strength in the x direction at $t = 0.50$ s. Near the L plug, the mean streamwise electrical field strength is about 40% higher than in the undisturbed flow. The values of the contour levels go linearly from 91.4 kV/m (blue) to 146 kV/m (red) in the top plot and from 0.20 kV/m (blue) to 13 kV/m (red) in the bottom plot.



FIG. 13. (Color) Mean (top) and standard deviation (bottom) of the electrical field strength in the y direction at $t = 0.50$ s. The magnitude of the mean of this field strength is up to 15% of the initial field strength in the x direction. The values of the contour levels go linearly from -16.3 kV/m (blue) to 16.3 kV/m (red) in the top plot and from 0 (blue) to 5.8 kV/m (red) in the bottom plot.



FIG. 14. (Color) Mean (top) and standard deviation (bottom) of the streamwise velocity at $t = 0.50$ s. The local increase in the electroosmotic wall velocity leads to recirculation zones near the L plug. The largest uncertainties are found near the wall. The values of the contour levels go linearly from 6.8 mm/s (blue) to 9.1 mm/s (red) in the top plot and from 5.6×10^{-3} mm/s (blue) to 0.59 mm/s (red) in the bottom plot.

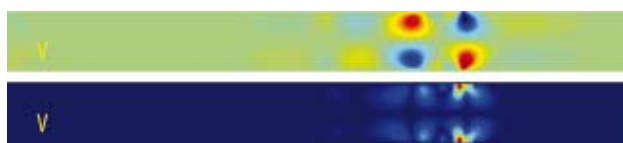


FIG. 15. (Color) Mean (top) and standard deviation (bottom) of the wall-normal velocity at $t = 0.50$ s. The mean of this velocity has a magnitude of up to 6% of the initial streamwise velocity. The values of the contour levels go linearly from -0.56 mm/s (blue) to 0.56 mm/s (red) in the top plot and from 0 (blue) to 0.26 mm/s (red) in the bottom plot.

streamwise velocity field, which has a mean wall velocity that is up to 20% higher near the L plug. The wall-normal velocity field shows positive and negative velocities near the L plug, with magnitudes up to 6% of the initial streamwise velocity.

Clearly, the recirculation zones in the flow field will distort initially at sample profiles. This increases the hydrodynamic dispersion, on top of the electrokinetic dispersion caused by nonuniformities in the electrophoretic transport.

VIII. CONCLUSIONS

In this paper, a detailed physical model for microchannel flows was presented to study protein labeling reactions in an electrolyte buffer. The model incorporates the coupled nature of momentum transport, species transport, and the electrostatic field as well as a full representation of the electrolyte buffer reactions and the dependence of the ζ potential on the local buffer properties. A stochastic uncertainty quantification method was developed to propagate uncertainty from the input parameters in the model to the simulation results, using polynomial chaos expansions for the uncertain model parameters and field variables.

Application of the model was illustrated in light of simulations of protein labeling reactions in homogeneous systems as well as two-dimensional electroosmotically driven microchannel flows. For the two-dimensional case, the simulation showed the impact of ion movement and subsequent buffer disturbances on the electrokinetic and hydrodynamic dispersion of sample plugs in the channel. The uncertainty in the results was primarily due to uncertainty in the applied voltage across the channel, with smaller contributions from the parameters in the labeling reaction rate as well as species properties.

Overall, the detailed physical model that was implemented in this work, allows the simulations of microchannel flows providing in-depth understanding of the transport and dispersion of protein sample plugs. In combination with this model, the stochastic uncertainty quantification method provides a powerful way to assess the impact of uncertain model input parameters on the uncertainty of the simulation results.

ACKNOWLEDGMENTS

This work was supported by the Defense Advanced Research Projects Agency (DARPA) and Air Force Research Laboratory, Air Force Materiel Command, USAF, under Agreement No. F30602-00-2-0612. The U.S. government is authorized to reproduce and distribute reprints for governmental purposes notwithstanding any copyright annotation thereon.

¹W. Thormann and R. Mosher, "Theory of electrophoretic transport and separations: The study of electrophoretic boundaries and fundamental separation principles by computer simulation," in *Advances of Electrophoresis*, edited by A. Chrambach, M. J. Dunn, and B. J. Radola (VCH, Weinheim, Germany, 1998), Vol. 2, pp. 45–108.

²G. Roberts, P. Rhodes, and R. Snyder, "Dispersion effects in capillary zone electrophoresis," *J. Chromatogr.* **480**, 35 (1989).

³M. Bier, O. Palusinski, R. Mosher, and D. Saville, "Electrophoresis:

Mathematical modeling and computer simulation," *Science* **219**, 1281 (1983).

⁴O. Palusinski, A. Graham, R. Mosher, M. Bier, and D. Saville, "Theory of electrophoretic separation. Part II: Construction of a numerical simulation scheme and its applications," *AIChE J.* **32**, 215 (1986).

⁵S. Ermakov and P. Righetti, "Computer simulation for capillary zone electrophoresis, a quantitative approach," *J. Chromatogr. A* **667**, 257 (1994).

⁶C. Shafer-Nielsen, "A computer model for time-based simulation of electrophoresis systems with freely defined initial and boundary conditions," *Electrophoresis* **16**, 1369 (1995).

⁷V. McGuffin and M. Tavares, "Computer assisted optimization of separations in capillary zone electrophoresis," *Anal. Chem.* **69**, 152 (1997).

⁸W. Thormann, C.-X. Zhang, J. Caslavská, P. Gebauer, and R. Mosher, "Modeling of the impact of ionic strength on the electroosmotic flow in capillary electrophoresis with uniform and discontinuous buffer systems," *Anal. Chem.* **70**, 549 (1998).

⁹N. Patankar and H. Hu, "Numerical simulation of electroosmotic flow," *Anal. Chem.* **70**, 1870 (1998).

¹⁰S. Ermakov, S. Jacobson, and J. Ramsey, "Computer simulations of electrokinetic transport in microfabricated channel structures," *Anal. Chem.* **70**, 4494 (1998).

¹¹S. Ermakov, S. Jacobson, and J. Ramsey, "Computer simulations of electrokinetic injection techniques in microfluidic devices," *Anal. Chem.* **72**, 3512 (2000).

¹²Q. Mao, J. Pawliszyn, and W. Thormann, "Dynamics of capillary isoelectric focusing in the absence of flow: High-resolution computer simulation and experiment validation with whole column optical imaging," *Anal. Chem.* **72**, 5493 (2000).

¹³V. Andreev, N. Pliss, and P. Righetti, "Computer simulation of affinity capillary electrophoresis," *Electrophoresis* **23**, 889 (2002).

¹⁴R. Ghanem and P. Spanos, *Stochastic Finite Elements: A Spectral Approach* (Springer, New York, 1991).

¹⁵N. Wiener, "The homogeneous chaos," *Am. J. Math.* **60**, 897 (1938).

¹⁶O. Le Maître, M. Reagan, H. Najm, R. Ghanem, and O. Knio, "A stochastic projection method for fluid flow II. Random process," *J. Comput. Phys.* **181**, 9 (2002).

¹⁷R. Probstein, *Physicochemical Hydrodynamics: An Introduction*, 2nd ed (Wiley, New York, 1994).

¹⁸Q.-H. Wan, "Effect of electroosmotic flow on the electrical conductivity of packed capillary columns," *J. Phys. Chem. B* **101**, 4860 (1997).

¹⁹P. Scales, F. Grieser, T. Healy, L. White, and D. Chan, "Electrokinetics of the silica-solution interface: A flat plate streaming potential study," *Langmuir* **8**, 965 (1992).

²⁰R. Mosher, D. Dewey, W. Thormann, D. Saville, and M. Bier, "Computer simulation and experiment validation of the electrophoretic behavior of proteins," *Anal. Chem.* **61**, 362 (1989).

²¹R. Mosher, P. Gebauer, and W. Thormann, "Computer simulation and experimental validation of the electrophoretic behavior of proteins. III. Use of titration data predicted by the protein's amino acid composition," *J. Chromatogr.* **638**, 155 (1993).

²²S. Ermakov, M. Zhukov, L. Capelli, and P. Righetti, "Artificial peak splitting in capillary electrophoresis. 2. Defocusing phenomena for ampholytes," *Anal. Chem.* **67**, 2957 (1995).

²³O. Le Maître, O. Knio, R. Ghanem, and H. Najm, "A stochastic projection method for microchannel flow," in *Proceedings of the Fourth International Conference on Modeling*, 2001, pp. 246–249.

²⁴O. Le Maître, O. Knio, H. Najm, and R. Ghanem, "A stochastic projection method for fluid flow I. Basic formulation," *J. Comput. Phys.* **1732**, 481 (2001).

²⁵M. Pernice and H. Walker, "NITSOL: A Newton iterative solver for nonlinear systems," *SIAM J. Sci. Comput. (USA)* **19**, 302 (1998).

²⁶A. Chorin, "A numerical method for solving incompressible viscous flow problems," *J. Comput. Phys.* **2**, 12 (1967).

²⁷E. Hairer, S. Nørsett, and G. Wanner, *Solving Ordinary Differential Equations I, Nonstiff Problems*, 2nd ed. (Springer, Berlin, 1992).

²⁸SLATEC common mathematical library, version 4.1, <http://www.netlib.org/slatec/>, 1993.

²⁹P. de Montigny, J. Stobaugh, R. Givens, R. Carlson, K. Srinivasachar, L. Sternson, and T. Higuchi, "Naphtalene-2,3-dicarboxaldehyde/cyanide ion: A rationally designed urogenic reagent for primary amines," *Anal. Chem.* **59**, 1096 (1987).

Computational Study of Band-Crossing Reactions

Alain Matta, Omar M. Knio, Roger G. Ghanem, Chua-Hua Chen, Juan G. Santiago, Bert Debusschere, and Habib N. Najm

Abstract—A numerical study of band-crossing reactions is conducted using a quasi-one-dimensional (1-D) computational model that accounts for species bulk advection, electromigration velocities, diffusion, and chemical reaction. The model is used to simulate chemical reactions between two initially distinct sample zones, referred to as “bands,” that cross each other due to differences in electromigration velocities. The reaction is described in terms of a single step, reversible mechanism involving two reactants and one product. A parametric study is first conducted of the behavior of the species profiles, and results are interpreted in terms of the Damköhler number and of the ratios of the electromigration velocities of the reactant and product. Computed results are then used to explore the possibility of extracting forward and backward reaction rates based on time resolved observation of integral moments of species concentrations. In particular, it is shown that in the case of fast reactions, robust estimates can be obtained for high forward rates, but that small reverse rates may not be accurately observed. [934]

Index Terms—Binding kinetics, electrochemical processes, electrophoretic band crossing, microfluidics, on-chip analysis.

I. INTRODUCTION

MICROFLUIDIC devices have been successfully applied to the analysis of chemical and biological systems. These systems provide many advantages over the conventional biochemical lab analysis, including improved speed and reproducibility, greatly reduced reagent consumption and fabrication cost [1]. Microfluidic devices have in particular been used to quantify a variety of physical parameters [2], including measurements of molecular diffusion coefficients [3], enzyme reaction kinetics [4], [5], and fluid viscosity [6]. Other applications include immunoassays [7]–[9], DNA analysis [10], cell manipulation [11], and capillary electrophoresis [12].

One important class of microfluidic applications concerns kinetic measurements, which provide concise rate expressions that can be used to predict yield, optimize designs, and to provide insight into relevant molecular processes. For example, Hadd *et al.* [4] describe on-chip enzyme assay of

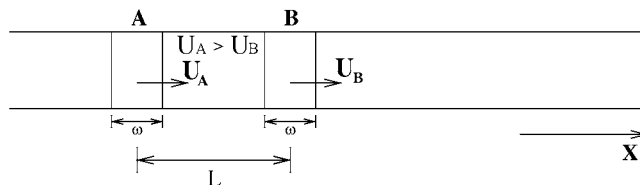


Fig. 1. Schematic illustration of band-crossing reactions, showing the initial structure of reactant bands A and B.

beta-galactosidase [4]. Their work clearly showed that the utility of these devices can be extended from the concept of only performing separations to the idea of integrating a complete analysis system. Reagent mixing and transport were accurately controlled by electrokinetic means. Enzyme reaction kinetics were obtained by altering the substrate concentration and measuring the product concentration. Similarly, Chiem *et al.* [8] demonstrated an integrated immunoreactor with electrophoretic separation for serum theophylline determination. In this work, all operations required by the immunoassay like mixing, incubation, separation and detection were automated on the chip.

An important challenge in the design of high throughput microfluidic systems concerns the relatively low diffusion rates of many species of interest, particularly macromolecules. Specifically, since characteristic lengthscales are small, the flow is laminar and mixing is generally diffusion-limited, requiring large times for substantial progress of chemical reactions. Consequently, various efforts have been directed at enhancing mixing rates in microfluid devices [13], [15]. Multilamina and splitting techniques are common examples of mixer designs. Mixing induced by lateral transport [13], [14] and electrokinetic instability [15] have also been recently reported.

One attractive alternative to diffusion-controlled reaction is electrophoretically mediated microanalysis (EMMA) [16], [17], which we also refer to as the on-chip electrophoretic band-crossing system [18]. As schematically illustrated in Fig. 1, the setup consists of the simultaneous introduction of two reactive species having different electrophoretic mobilities into a microchannel. The flow is then driven electrokinetically so that the species with the higher electromigration velocity will cross and eventually overtake the one having slower electromigration velocity. Thus, the mixing times are controlled by differences in electromigration velocities, and this distinguishes the present technique from approaches based on fluid stirring, where mixing times are diffusion limited. Since the reactant bands have small width and the electromigration-limited mixing rates are high, this enables rapid observations of fast reactions. The band crossing technique is particularly useful in situations where the fluorescent signal strength of a reaction

Manuscript received September 22, 2002; revised October 1, 2003. This work was supported by the Defense Advanced Research Projects Agency (DARPA) and Air Force Research Laboratory, Air Force Materiel Command, USAF, under agreement F30602-00-2-0612. The U.S. government is authorized to reproduce and distribute reprints for Governmental purposes notwithstanding any copyright annotation thereon. Computations were performed at the National Center for Supercomputer Applications. Subject Editor A. J. Ricco.

A. Matta, O. M. Knio, and R. G. Ghanem are with the Department of Mechanical Engineering, The Johns Hopkins University Baltimore, MD 21218 USA (e-mail: knio@jhu.edu).

C.-H. Chen and J. G. Santiago are with Stanford University Stanford, CA 94305 USA.

B. Debusschere and H. N. Najm are with Sandia National Laboratories, Livermore, CA 94550 USA.

Digital Object Identifier 10.1109/JMEMS.2004.825315

product is low, and a substantial amount of reactants is consequently required for a successful experiment. This in contrast rapid mixing schemes which rely on thin lamination of reactant streams in order to minimize diffusion times [19].

Mathematical [17], [20], [21] and computational [22], [23] models describing the behavior of the EMMA experiments are now well established. The present work builds on prior results by 1) conducting a systematic analysis on the role of various operating parameters such as electromigration velocities, reaction rates and initial concentrations, 2) exploiting the results to establish essential trends and to express these trends in terms of a reduced set of dimensionless parameters, and 3) applying the computations to explore the possibility of extracting kinetic rate constants based on measurements of species concentration profiles. As outlined in Section II, we rely on a quasi-one-dimensional (1-D) model that accounts for species advection and electromigration, reaction and diffusion. Brief dimensional arguments are then introduced in Section III in order to characterize specific flow conditions. Section IV highlights selected results from a detailed parametric study of the effects of reaction rates, differences in electromigration velocities and initial concentrations. An analysis of extraction rate methodologies on basis of integral moments of concentration profiles is then presented in Section V. Major conclusions are summarized in Section VI.

II. FORMULATION AND NUMERICAL SCHEME

As mentioned in the introduction, we rely on a quasi-1-D, advection-diffusion-reaction design model. The formulation reflects the idealized situation of a dilute solution evolving in a uniform, electrokinetically driven plug flow, and thus inherently ignores dispersive effects that may arise due to unwanted external pressure differences, spatial variation in wall mobility, or spatial variations in electrical conductivity. We consider the evolution of three chemically interacting species using a first-order, finite-rate, reversible reaction of the form



with a chemical rate term given by

$$R_A = R_B = -R_C = -k_f c_A c_B + k_r c_C \quad (2)$$

where the R denotes the rate of production, k_f and k_r denote the forward and backward rates, respectively. The indexes A and B denote the reactants while C refers to the reaction product.

Under the idealized conditions outlined above, the conservation equations for the three reacting species can be expressed as [23]

$$\frac{\partial c_i}{\partial t} + u_i \frac{\partial c_i}{\partial x} = D_i \frac{\partial^2 c_i}{\partial x^2} + R_i, \quad i = A, B, C \quad (3)$$

where c_i , u_i and D_i denote the molar concentration, electromigration velocity, and mass diffusivity of species i , respectively.

In the computations presented in Section IV, (3) is simulated using a finite difference scheme that is based on a cell-centered discretization of the concentration fields on a fine, uniform mesh of cell size Δx . Spatial derivatives are approximated

using a second-order, centered-difference discretization, and the discrete equations are advanced in time using the second-order Adams–Bashforth scheme. Inflow/outflow conditions are used at the left/right domain boundaries.

III. SCALE ANALYSIS

While the dimensional form of the governing equations is used in the simulations, a brief scale analysis is conducted in this section in order to characterize the solutions. As mentioned earlier, the present study is motivated by a desire to determine rates of reaction in a dilute solution involving proteins having low molecular diffusion coefficients. Thus, molecular diffusion effects are expected to be small, so that the rates of reaction are dominated by electrokinetic and chemical time scales. (For the presently considered regime, diffusion time scales are smaller than crossing time scales by at least three orders of magnitude.) Below, we provide estimates of these time scales, the ratio of which yields a Damköhler number.

A. Electrophoretic Crossing Time Scale

Let w denote the initial widths of species A and B (see Fig. 1). The relevant time scale for band crossing may be estimated from

$$t_{cr} \equiv \frac{w}{\Delta u_{AB}} \quad (4)$$

where $\Delta u_{AB} = u_A - u_B > 0$. The convention we have adopted is that species A with electromigration velocity u_A , is the faster migrating species, which overtakes species B having electromigration velocity u_B .

B. Chemical Time Scale

In order to derive a suitable chemical time scale, we will assume for the moment that the crossing time is fast and consequently consider that the two bands are brought together instantaneously. Thus, we focus on a quasi-0D problem where the initial mixture relaxes to equilibrium. In this limiting case, the relevant concentrations are the initial peak concentrations c_A^0 and c_B^0 .

An exact solution to this pure chemical problem can be derived. Since this solution suggests an interesting diagnostic approach, a few details are provided. We use subscripts $\{1,2,3\}$ to denote species $\{A,B,C\}$. In the absence of transport, the governing equation for concentration reduces to

$$\frac{dc_1}{dt} = -k_f c_1 c_2 + k_r c_3. \quad (5)$$

Let $\delta(t)$ denote the amount of reactants consumed by the reaction over the interval $[0, t]$, and Δ denote the steady-state or equilibrium value of δ ; we have

$$c_1(t) = c_1^0 - \delta(t), \quad c_2(t) = c_2^0 - \delta(t), \quad c_3(t) = c_3^0 + \delta(t) \quad (6)$$

Substitution of (6) into (5) yields

$$\frac{d\delta}{dt} = k_f c_1^0 c_2^0 - k_r c_3^0 - \delta [k_f (c_1^0 + c_2^0) + k_r] + k_f \delta^2. \quad (7)$$

We will later discuss how (7) may be used to diagnose band-crossing data.

At steady state, we have $d\delta/dt = 0$, which gives

$$a\delta^2 - b\delta + c = 0 \quad (8)$$

where $a \equiv k_f$, $b \equiv k_f(c_1^0 + c_2^0) + k_r$, and $c \equiv k_f c_1^0 c_2^0 - k_r c_3^0$. The solution is given by

$$\Delta = \frac{b - \sqrt{b^2 - 4ac}}{2a}. \quad (9)$$

Letting $q(t) = \Delta - \delta(t)$, we have

$$-\frac{1}{2a\Delta - b} \frac{dq}{q} + \frac{a}{2a\Delta - b} \frac{dq}{aq - (2a\Delta - b)} = -dt \quad (10)$$

with initial condition $q(0) = \Delta$. The exact solution is given by

$$q(t) = \frac{\gamma}{a - \theta \exp(-\gamma t)} \quad (11)$$

where $\gamma \equiv 2a\Delta - b = -\sqrt{b^2 - 4ac}$ and $\theta \equiv (b - a\Delta)/\Delta$. As expected, q vanishes at steady-state since $\gamma < 0$, and this is reflected in (11) above.

This suggests that an appropriate timescale, τ , for the reaction is such that $q(\tau) = \Delta/e$, which gives

$$\tau = -\frac{1}{\gamma} \ln \left[\frac{a\Delta - e\gamma}{\theta\Delta} \right]. \quad (12)$$

Note that τ depends on the initial concentrations c_1^0 , c_2^0 and, if initially present, c_3^0 .

Also note that the above definition of τ differs from the usual definition of the chemical time scale based on the eigenvalues of J , the Jacobian of the chemical source term. For the present reaction mechanism, we have

$$J \equiv \frac{\partial R_i}{\partial c_j} = \begin{bmatrix} -k_f c_2 & -k_f c_1 & k_r \\ -k_f c_2 & -k_f c_1 & k_r \\ k_f c_2 & k_f c_1 & -k_r \end{bmatrix} \quad (13)$$

J has a single nonvanishing eigenvalue $\lambda = -k_f(c_1 + c_2) - k_r$, giving the following timescale:

$$\tau' = \frac{1}{|\lambda|} = \frac{1}{k_f(c_1 + c_2) + k_r} \quad (14)$$

which, unlike τ , does not depend on the initial concentration of the product, c_3^0 . However, one can readily verify that for conditions near equilibrium, τ and τ' coincide; this agreement was in fact behind the selection of the $1/e$ decay rate in Δ . In the analysis below, we will exclusively rely on the chemical time scale definition in (12), as it accounts for the overall nonlinear behavior of the system.

C. Damköhler Number

The estimates above enable us to define a Damköhler number

$$\text{Da} \equiv \frac{t_{\text{cr}}}{\tau} \quad (15)$$

In order to control Da one can either alter the initial concentration levels (i.e., control τ), or change the electromigration velocity (i.e., control t_{cr}). The latter can be achieved either by changing the electric field strength or, to the extent possible, by

altering w and/or the mobility of individual species. Note, however, that the possibility of experimentally controlling τ and t_{cr} is subject to constraints that limit the range of electromigration velocities and the range of concentration values. For t_{cr} , the primary restriction comes from a limitation on the electric field, which should not be so high as to cause significant Joule heating. For τ , one needs to ensure that the concentration remains high enough to fall within detection limits, but not so high as to require a highly concentrated initial mixture.

IV. BEHAVIOR OF SOLUTIONS

A detailed parametric study was conducted of the effects of electromigration velocities, rate parameters, and initial reactant concentrations. The effects of electromigration velocity were analyzed by systematically varying u_A . For each value of u_A , a two-parameter family of solutions was considered, by setting $u_B = \alpha u_A$ and $u_C = \beta u_A$. The parameter α was varied independently, and for each α , five values of β were considered: 1) $\beta = 0$, where the electromigration velocity of the product vanishes, 2) $\beta = \alpha/2$, i.e., the electromigration velocity of the product (u_C) is half that of the slower reactant (u_B), 3) $\beta = \alpha$, where $u_C = u_B$, 4) $\beta = (1 + \alpha)/2$, where $u_C = (u_A + u_B)/2$, and 5) $\beta = 1$, where $u_C = u_A$. Meanwhile, the initial concentrations of the reactants and the values of the rate constants were also systematically varied. In all cases, the width of the initial reactant bands, w , was held fixed, with concentration profiles described by sixth-order Gaussian profiles of the form

$$c_i^0(\xi) = C_i^0 \exp\left(-\frac{\xi_i^6}{w^6}\right), \quad i = A, B$$

where C^0 is the initial peak concentration and ξ is a shifted spatial variable centered at the peak. The high-order Gaussian was selected because it mimics a top-hat profile with smooth tails, as can be appreciated from the results below. In all cases, $w = 50 \mu\text{m}$, the diffusivity $D = 3 \times 10^{-10} \text{ m}^2/\text{s}$, the initial product concentration vanishes identically (i.e., $c_C^0 = 0$), and the computational domain is 3-mm long. A systematic study was also conducted of the effect of the discretization parameters. This study showed that for range of parameters of interest, a fine mesh with $\Delta x = 0.2 \mu\text{m}$ and a time step $\Delta t = 10 \mu\text{s}$ were sufficient for accurate predictions. These values are used in the computations presented below.

Selected cases from the detailed parametric study are presented in this section. As summarized in Table I, we focus our attention on six cases. In cases 1–4, the electromigration velocity of the reactants is held fixed, while that of the products is varied. Thus, as shown in the table, the Damköhler number and α are held fixed, respectively $\text{Da} = 33$ and $\alpha = 0.25$, while β is varied. In case 5, α is increased to 0.5, resulting in a higher Damköhler number $\text{Da} = 49$. In case 6, the initial peak concentration of the reactants is reduced, leading to a lower Damköhler number $\text{Da} = 2$.

Fig. 2 depicts the evolution of the reactants' concentration profiles for case 1 (see Table I). The results illustrate how the two bands approach each other in the early stage of the computation. Due to weak molecular diffusion effects, before the two bands overlap, there is little change in the peak concentration of

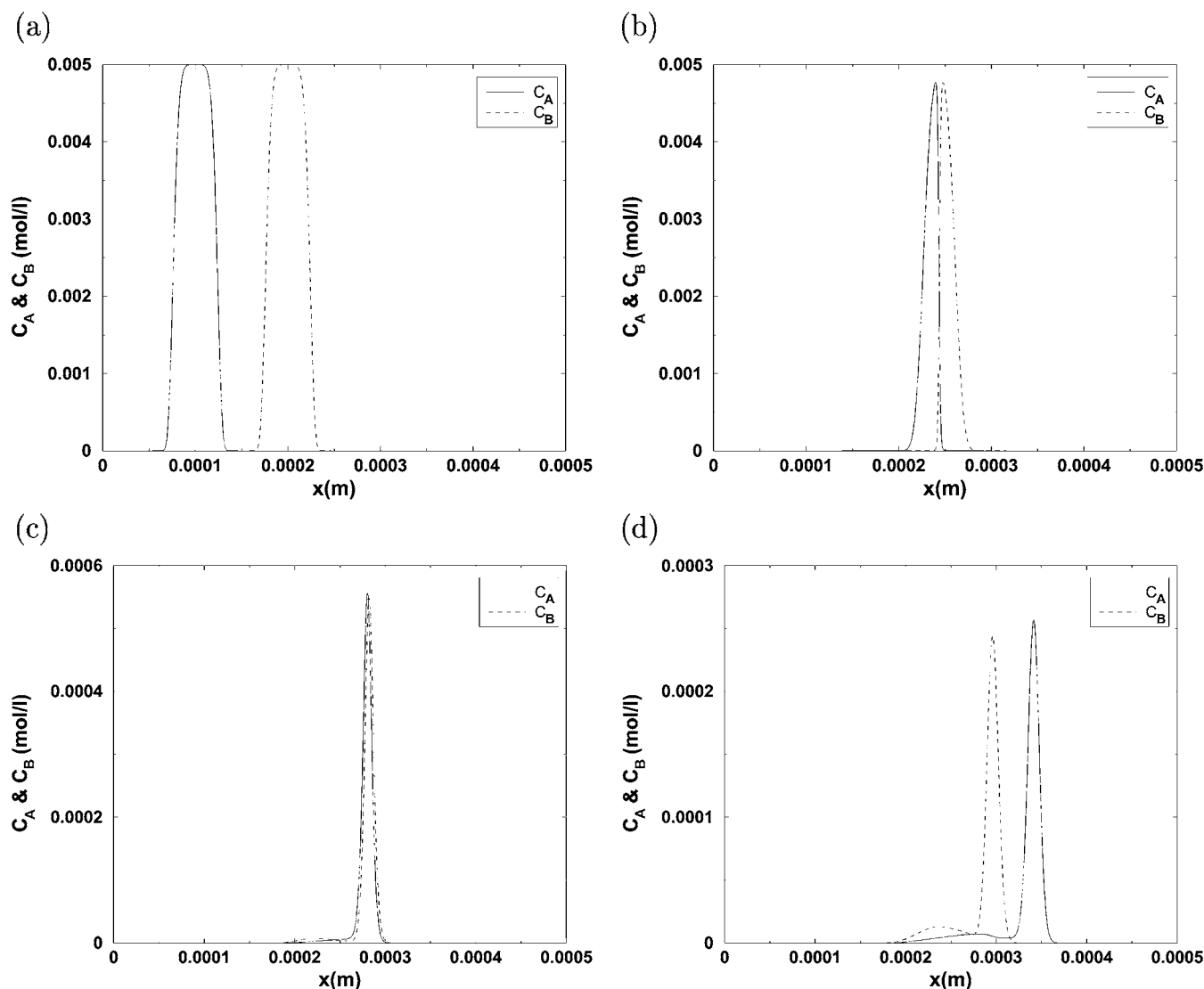


Fig. 2. Instantaneous profiles of C_A and C_B for case 1. Plots are generated at times (a) $t = 0$, (b) $t = 50$ ms, (c) $t = 70$ ms, and (d) $t = 90$ ms.

TABLE I

SELECTED INPUT CASES. SHOWN ARE VALUES OF THE ELECTROMIGRATION VELOCITIES (mm/s), INITIAL REACTANT CONCENTRATIONS (mM), FORWARD REACTION RATE ($M^{-1}s^{-1}$), AND BACKWARD REACTION RATE (s^{-1}). ALSO SHOWN ARE THE DIMENSIONLESS PARAMETERS α AND β AS WELL AS THE DAMKÖHLER NUMBER, Da

Case	u_A	u_B	u_C	C_A^0	C_B^0	k_f	k_r	α	β	Da
1	3	0.75	0	5.	5.	4×10^5	0.1	0.25	0	33
2	3	0.75	0.375	5.	5.	4×10^5	0.1	0.25	0.125	33
3	3	0.75	0.75	5.	5.	4×10^5	0.1	0.25	0.25	33
4	3	0.75	1.875	5.	5.	4×10^5	0.1	0.25	0.625	33
5	3	1.5	1.5	5.	5.	4×10^5	0.1	0.5	0.5	49
6	3	0.75	0.75	0.25	0.25	4×10^5	0.1	0.25	0.25	2

A and B. For these conditions, the peak concentrations of A and B decrease rapidly when the two bands overlap, and by the time the bands separate, the peak concentrations drop by approximately a factor of 20. As shown in Fig. 2(d), after separation the reactant profiles are no longer symmetric and slight differences in the peak concentrations of A and B can be observed. The profiles exhibit a double hump structure with a strong primary peak that leads a weak local maximum. The behavior of

the reactants concentration profiles for cases 2–4 was found to be qualitatively similar to that of Case 1; the corresponding plots are consequently omitted.

Fig. 3 shows instantaneous profiles of C_A and C_B for case 5. As shown in Table I, for this case, β has been increased to 0.5, which results in an increased crossing time scale and, consequently, a larger Damköhler number. The results indicate the profiles of C_A and C_B behave in a qualitatively similar fashion as in case 1 (Fig. 2). However, for case 5, there is an even more substantial reduction in the peak values of C_A and C_B , which drop by approximately a factor of 30 during the crossing. As further discussed below, this suggests that the overall rate of progress of the reaction is larger as Da increases.

As shown in Table I, the electromigration velocities for case 6 are the same as in case 3, but the initial concentrations of A and B have been reduced by a factor of 20. This results in a significant drop in the Damköhler number, from Da = 33 in case 3 to Da = 2 in case 6. Instantaneous profiles of C_A and C_B for case 6 are plotted in Fig. 4, using the same time intervals as in Fig. 2. The plots show that for case 6, the behavior of the reactants' profiles differs significantly from that of the

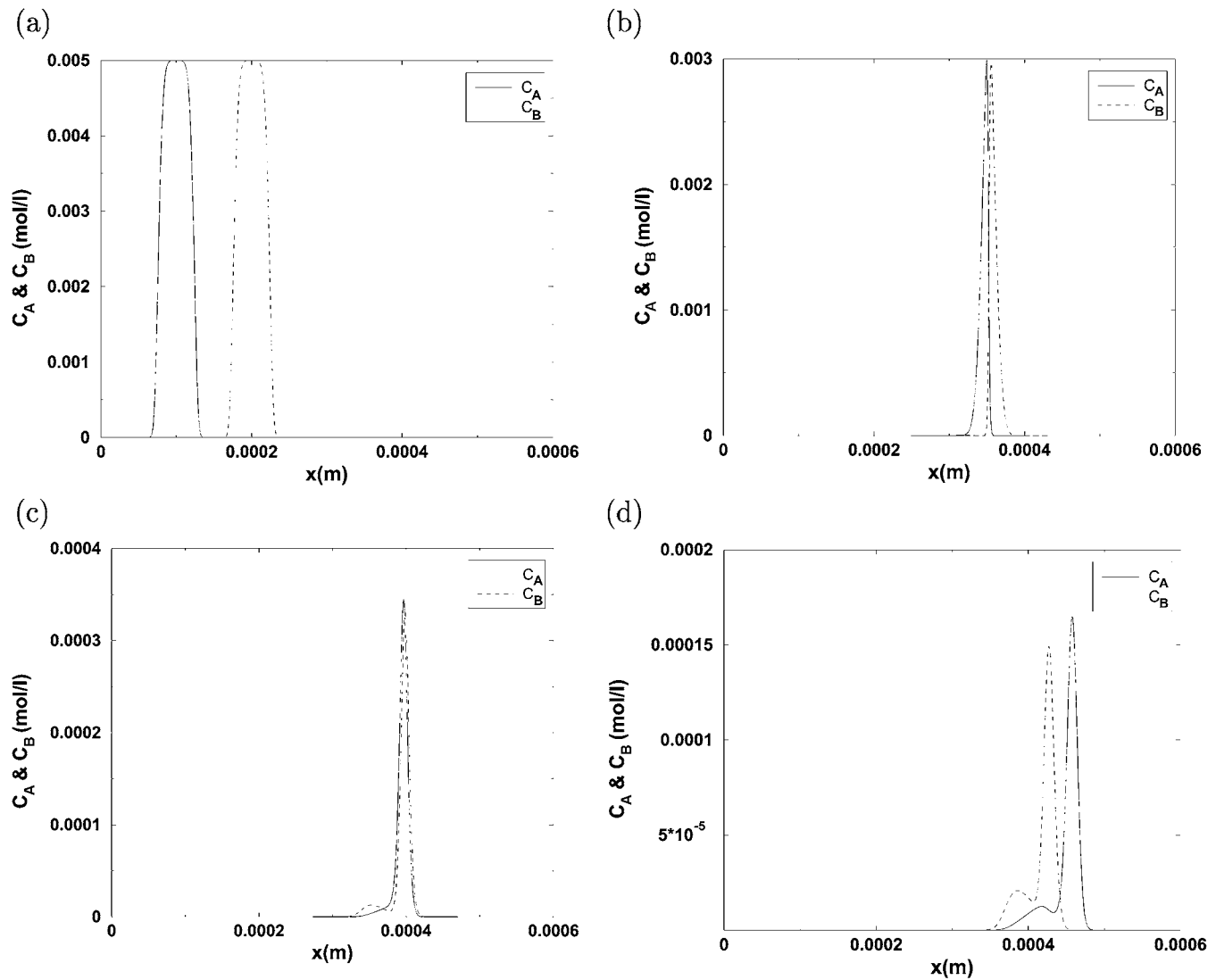


Fig. 3. Instantaneous profiles of C_A and C_B for case 5. Plots are generated at times (a) $t = 0$, (b) $t = 90$ ms, (c) $t = 110$ ms, and (d) $t = 130$ ms.

previous cases. Specifically, the concentration profiles develop a weak asymmetry and, unlike the profiles in Figs. 2 and 3, do not exhibit a secondary trailing peak. An additional distinctive feature is the prolonged coexistence of C_A and C_B during the crossing [see Fig. 4(b)]. As expected, for this reduced value of Da , the drop in the peak concentrations of A and B is rather weak, approximately a factor of 3.

The effects of electromigration velocities and Damköhler number can also be observed in Fig. 5(a)–(f), which depicts the evolution of product concentration profiles for cases 1–6, respectively. As shown in Table I, for cases 1–4, Da and the electromigration velocities of the reactants are held fixed, while u_C is systematically varied by increasing α . For $\alpha = 0$, u_C vanishes so that the product concentration profiles does not propagate. As shown in Fig. 5(a), at the beginning of band crossing ($t = 50$ ms) the product concentration profile exhibits a sharp leading front, followed by a smoothly decaying tail. As the reaction proceeds, the leading front becomes smoother, eventually giving the profile a nearly symmetric shape. For the present case ($u_C = 0$), the product concentration profile has an appreciably smaller peak and larger width than the initial reactants' profile.

A similar behavior is observed in Fig. 5(b), which depicts the evolution of c_C for case 2, where $u_C = u_B/2$. However, one can observe that for this case the final profile has smaller width and higher peak than in case 1. Furthermore, unlike case 1, the C_C profile is no longer stationary, but translates to the right with the product electromigration velocity u_C .

The trends noted above can also be observed for case 3, where $u_C = u_B$. In particular, as shown in Fig. 5(c), the product concentration profile for case 3 has slightly larger peak and is slightly thinner than in the previous cases. In particular, for case 3 the peak product concentration following the band crossing is close to that of the initial reactants profiles.

When u_C is equal to the average of u_A and u_B (case 4), a peculiar behavior is observed. As shown in Fig. 5(d), a very narrow profile with a pronounced peak is observed. Note that the peak concentration is more than 4 times higher than initial peak of the reactants profiles. Thus, in the present situation the product tends to accumulate at a single spatial position that moves with the average velocity of the reactants. We finally note that, if u_C is increased further then the presently observed "focusing" effect is greatly diminished. In these cases, i.e. $u_C > (u_A + u_B)/2$, the product concentration resembles

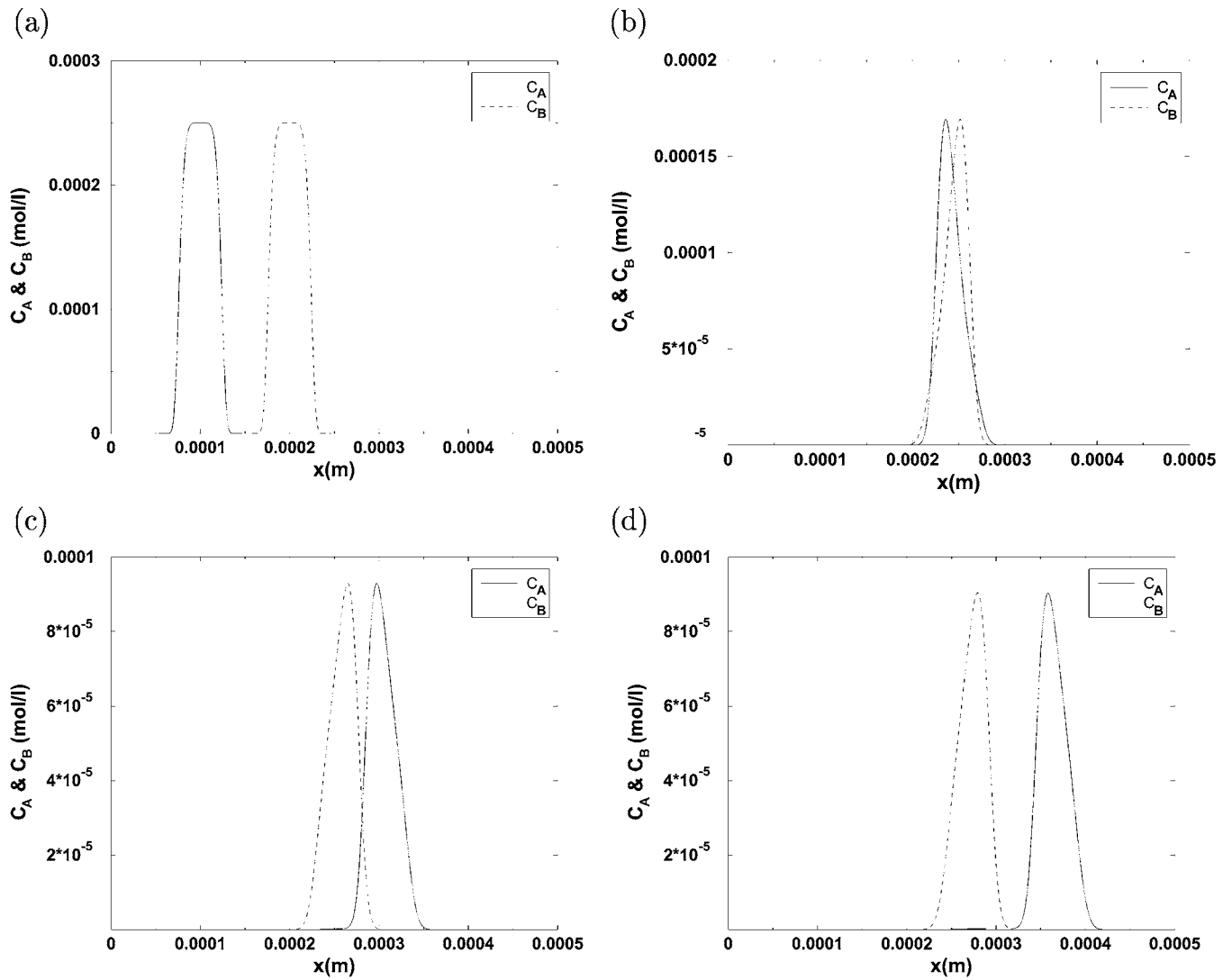


Fig. 4. Instantaneous profiles of C_A and C_B for case 6. Plots are generated at times (a) $t = 0$, (b) $t = 50$ ms, (c) $t = 70$ ms, and (d) $t = 90$ ms.

those in Fig. (5a)–(c); the corresponding results are therefore omitted.

Fig. 5(e) shows instantaneous product concentration profiles for case 5. Compared with case 3, in case 5 the velocities u_B and u_C have been doubled. This results in a longer crossing time scale and consequently a larger Damköhler number. As can be seen in Fig. 5(c) and (e), however, these changes appear to have little impact on the shape of the product concentration profiles. While interaction times evidently differ, in both cases the profiles develop similar widths and peak values.

Finally, concentration profiles for case 6 are shown in Fig. 5(f). As shown in Table I, the electromigration velocities are identical in cases 3 and 6, but the initial reactants concentrations are substantially lower in case 6. As a result, in the latter case the Damköhler number is significantly lower. The reduction in Damköhler number appears to have little impact on the shape of the profiles, but does have a noticeable effect on the rate of progress of the reaction. Specifically, in case 3 the peak product concentration is nearly equal to the initial reactants' peak, while the peak product concentration in case 6 is noticeably lower.

The above results indicate that the behavior of the concentration profiles can be essentially characterized by the Damköhler number, and by the ratio of the electromigration velocity of the product with respect to the mean of the reactants electromigration velocities. The trends with these two parameters, briefly illustrated above for selected cases, were in fact observed for a wide range of electromigration velocities, rate constants, and initial concentrations.

In order to briefly illustrate the above claims, we compute two measures that characterize the progress of the reaction: a global measure \mathcal{G} defined by

$$\mathcal{G} \equiv \max_t \frac{\int c_C dx}{\int c_A^0 dx} \quad (16)$$

and a local measure \mathcal{P} given by

$$\mathcal{P} \equiv \max_t \frac{c_C^{\max}(t)}{c_A^{\max}(t=0)}. \quad (17)$$

Here, c_A^{\max} and c_C^{\max} denote the peak instantaneous values of the concentrations of A and C, respectively. Note that \mathcal{G}

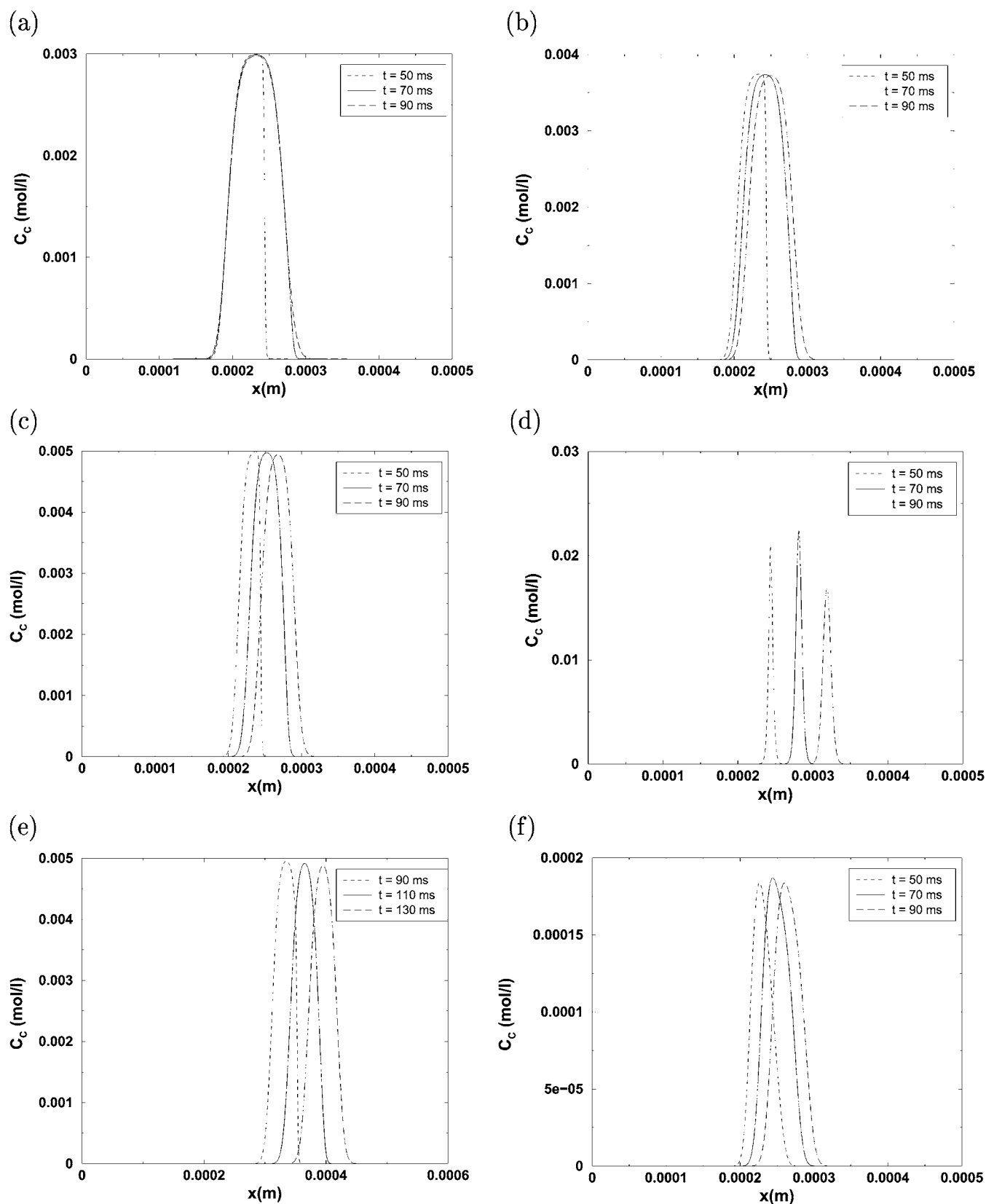


Fig. 5. Instantaneous profiles of C_C for cases (a) 1, (b) 2, (c) 3, (d) 4, (e) 5, and (f) 6.

can be interpreted as “chemical conversion efficiency” since it corresponds to the peak fraction of moles of A that are converted into moles of C by the chemical reaction. On the other hand, \mathcal{P} corresponds to the peak spatial product concentration

normalized by the initial peak of the concentration profile of A. Thus, it reflects the tendency of the peak product concentration to be larger or smaller than the initial peak of the reactants.

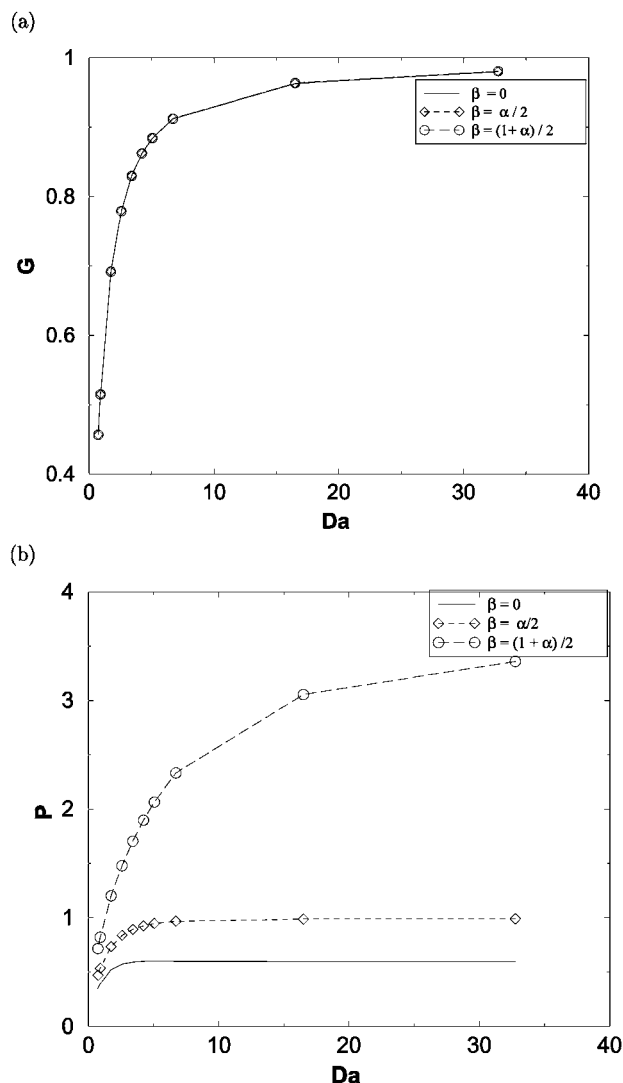


Fig. 6. Dependence of \mathcal{G} (top) and \mathcal{P} (bottom) on Da . Different curves are generated for cases with $\beta = 0$, $\alpha/2$, and $(1 + \alpha)/2$.

Fig. 6(a) shows the dependence of \mathcal{G} on the Damköhler number. Plotted are curves generated for $\beta = 0$, $\alpha/2$ and $(1 + \alpha)/2$, and for Damköhler numbers in the range $1 \leq Da \leq 33$. The figure shows that the three \mathcal{G} versus Da curves collapse onto each other, supporting the earlier claim that the overall conversion of reactants into products is governed by the Damköhler number, and is essentially independent of the ratios of electromigration velocities. Note that the curves for \mathcal{G} are monotonically increasing, from about 45% at low Da to about 98% at higher Da . Thus, as observed earlier, consumption of the reactants increases with increasing Damköhler numbers.

Meanwhile, as shown in Fig. 6(b), distinct \mathcal{P} versus Da curves are obtained for each value of β . For all three values of β , the curves increase monotonically with Da . For $\beta = 0$ and $\alpha/2$, the curves saturate for $Da > 10$, while for $\beta = (1 + \alpha)/2$ substantial variation is observed throughout the range considered. The largest values of \mathcal{P} are achieved when $\beta = (1 + \alpha)/2$, i.e. when the product electromigration velocity is equal to the average of the electromigration velocities of the reactants. In particular, for this value of β , \mathcal{P} is substantially larger than unity at high Da ;

this indicates that in this regime the peak product concentration is several times larger than the peak reactant concentration.

We finally note that the results in Fig. 6 are consistent with earlier observations of the behavior of the concentration profiles, and their dependence on relevant parameters. In addition, the results enable us to generalize previously observed trends to a wider range of operating conditions.

V. ESTIMATION OF RATE CONSTANTS

We now explore the possibility of extracting reaction rates from the evolution of concentration profiles. This exercise is motivated by optical measurements of species concentrations, which give spatial profiles at selected time intervals [24]. In many cases, the impact of experimental noise may be reduced by analyzing moments of the profile instead of local values. In this section, we examine two different means for exploiting such integral measures. In the first approach (see Section V-A), concentration profiles of both reactants and of the product are assumed available. A different scenario is considered in Section V-B, which involves interrupting the electric field once the bands overlap. For this scenario, an alternative means of estimating chemical rate constants is considered which only assumes that the reactants' concentration profiles are measured.

A. Multiple Measurements

When the concentrations of both reactants and of the product are simultaneously measured, a simple approach can be implemented to deduce the reaction rates. Specifically, by integrating (3) over the domain or, in the case of experimental measurements, over a sufficiently wide window, the transport (convection, electromigration and diffusion) terms drop out, and one obtains

$$I_1(t) \equiv \frac{d}{dt} \int c_1 = -k_f \int c_1 c_2 + k_r \int c_3. \quad (18)$$

If the signals for $I_1(t)$, $\int c_1 c_2$ and $\int c_3$ are available, then one can perform a straightforward least-squares regression of the form

$$I = -A \int c_1 c_2 + B \int c_3 \quad (19)$$

to determine unknown coefficients A and B . These can be immediately identified with k_f and k_r . In particular, based on the computed results for case 3 we obtain $A = 3.99 \times 10^5$ and $B = 0.088$. These values are in very good agreement with the rate parameters used as input. Similar experience was observed for other cases considered; the corresponding results are therefore omitted.

B. Interrupted Flow Experiment

In many situations, simultaneous measurement of all three species concentrations is either not possible or excessively difficult. In this section, we explore the possibility of deducing reaction rates with fewer experimental signals. Specifically, we consider what we call an “interrupted flow” experiment, which consists of first driving the reactants so that they overlap and then suddenly switching off the electrokinetic pumping (see also

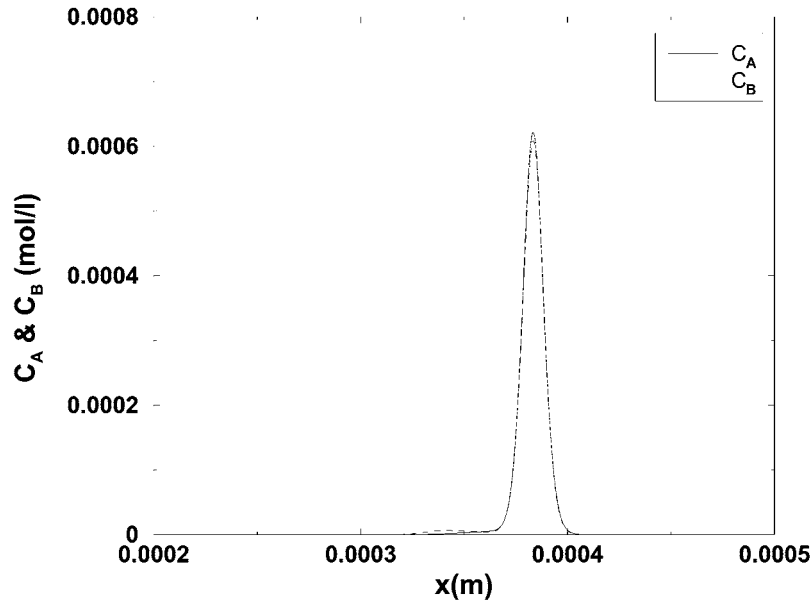


Fig. 7. Profiles of reactants concentration at the time the flow is interrupted.

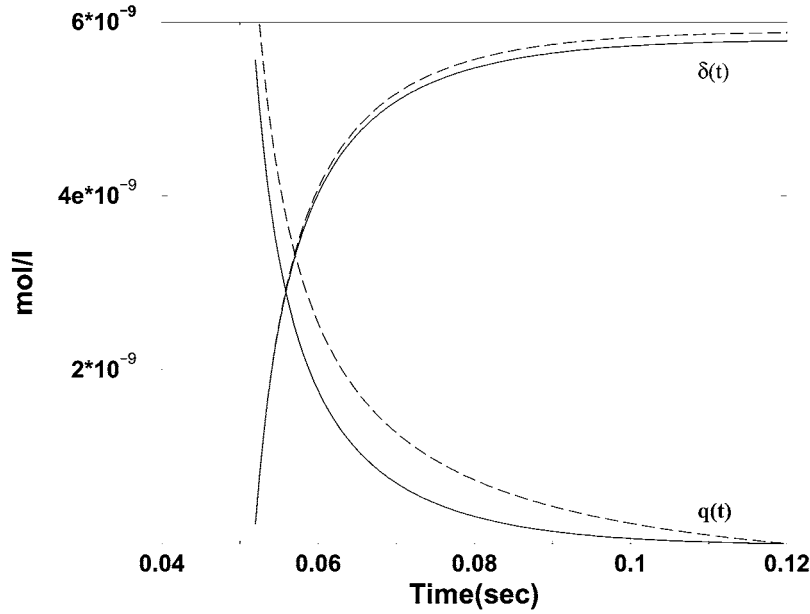


Fig. 8. Comparison of analytical (dashed) and numerical (solid) results for $\delta(t)$ and $q(t)$.

[16], [17]). The advantage of this approach is that, in the parameter regime of interest, once the flow is interrupted, the evolution of the concentration fields is primarily dominated by the reaction and only weakly affected by diffusion. The assumptions will be verified based on simulation results below.

The simulation conditions are the same as those in the previous section. However, once the reactants overlap, all velocities are suddenly switched to zero. The reactant concentration profiles at the time the flow is interrupted are shown in Fig. 7. This mimics the sudden interruption of the electric field since, due to the very low Reynolds number and the absence of a driving pressure gradient, the bulk velocity decays rapidly to zero.

We start by examining the effects of diffusion on the evolution of the concentration field. In Fig. 8, we contrast the computed values of $\delta(t)$ and $q(t)$ at the location of the peak reactant concentration (see Fig. 7) to the analytical solution for a purely

reactive system [see (11)]. The results show that the two predictions are in reasonably close agreement, indicating that for the present set of conditions diffusion has a small effect on the evolution of \bar{q} and $\bar{\delta}$ throughout the decay period.

Combined with the weak effect of diffusion, the absence of advective or electromigration effects then offers the following possibility of extracting the reaction rates. From (7) we have

$$\frac{d\delta}{dt} = k_f c_1^0 c_2^0 - k_r c_3^0 - \delta [k_f (c_1^0 + c_2^0) + k_r] + k_f \delta^2. \quad (20)$$

Integrating over a fixed, sufficiently large window, we have:

$$\int \frac{d\delta}{dt} dx = -k_r \int \delta dx + k_f \int [\delta^2 - (c_1^0 + c_2^0) \delta] dx + \int [k_f c_1^0 c_2^0 - k_r c_3^0] dx \quad (21)$$

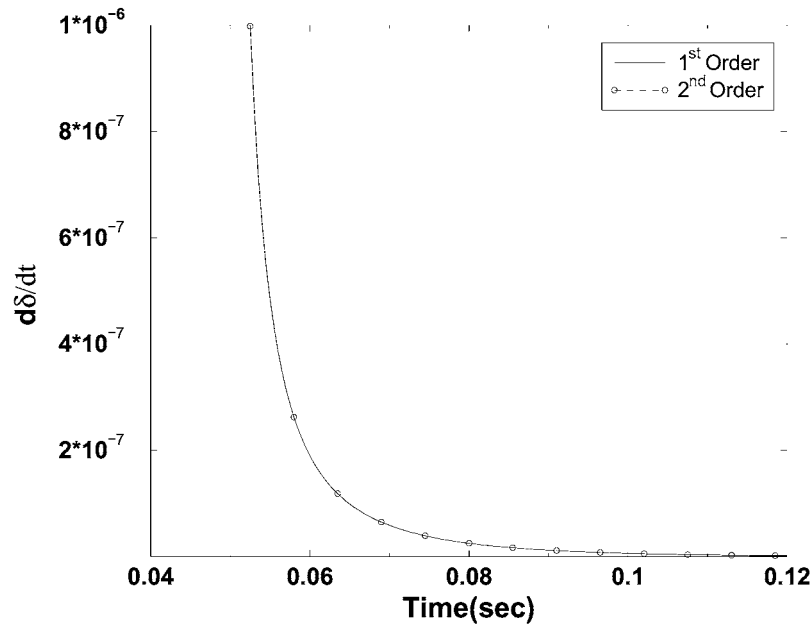


Fig. 9. Evolution of $(d\bar{\delta}/dt)$ using first and second-order approximations. The time step used in the finite difference formulae corresponds to that of the simulations, i.e., $\Delta t = 10^{-5}$ s.

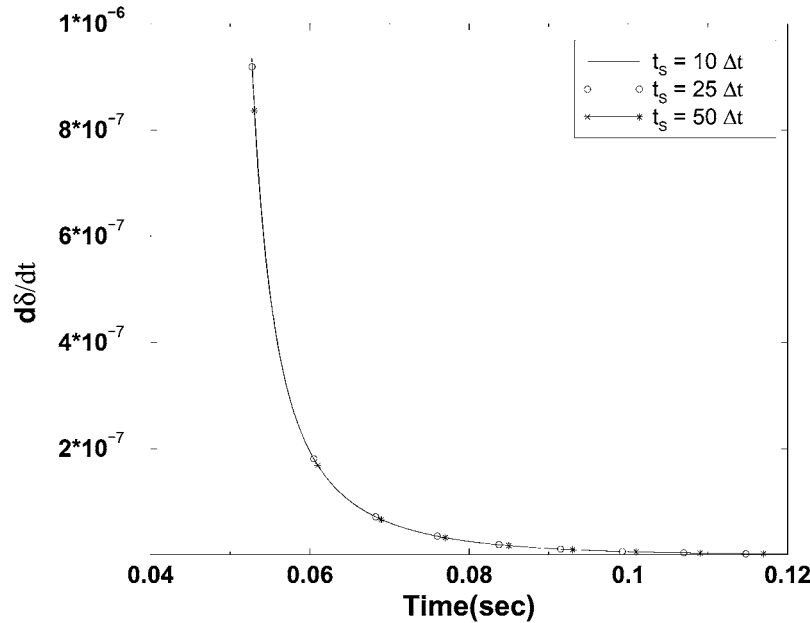


Fig. 10. Evolution of $(d\bar{\delta}/dt)$ using a second-order approximation. The time step used in the finite difference formula corresponds to the length of the sampling interval, t_s . We use $t_s = 10\Delta t$, $25\Delta t$ and $50\Delta t$.

which can be rewritten as

$$\frac{d\bar{\delta}}{dt} = -A\bar{\delta} + B \int [\delta^2 - (c_1^0 + c_2^0) \delta] dx + C \quad (22)$$

where $\bar{\delta} \equiv \int \delta dx$. Thus, if time resolved measurements evolution of one reactant concentration are performed, and the “initial” concentration of the other reactant is also measured, one can determine the coefficients A , B , and C by linear regression (least-squares) from the data. Comparing (21) and (22), one can immediately identify the coefficients A and B with the backward rate and forward rate, respectively.

TABLE II
LEAST-SQUARES INTERPOLATION RESULTS USING THE ANALYTICAL SOLUTION FOR A PURELY REACTIVE SYSTEM

Coefficients	$t_s = 50\Delta t$	$t_s = 25\Delta t$
A	0.1002	0.1000
B	4.0000×10^5	4.0000×10^5
C	4.3363×10^{-6}	4.3363×10^{-6}

Note, however, that unlike the approach of the previous section, the present approach is only approximate, and its success hinges on situations where Da is not so large that the reactants are consumed very quickly (see Fig. 6), before one can inter-

TABLE III

LEAST-SQUARES INTERPOLATION RESULTS FOR DIFFERENT SAMPLING TIMES t_s USING THE COMPUTED SOLUTIONS. SHOWN ARE RESULTS OBTAINED WHEN MOLECULAR DIFFUSION ACCOUNTED FOR ($D \neq 0$) AND WHEN IT IS IGNORED ($D = 0$). IN THE PRESENT CASE, ESTIMATES OF $d\bar{\delta}/dt$ ARE OBTAINED FROM A CENTERED DIFFERENCE APPROXIMATION USING THE COMPUTATIONAL TIME STEP Δt

Coefficients	$D = 0$			$D \neq 0$		
	$t_s = 50\Delta t$	$t_s = 25\Delta t$	$t_s = 10\Delta t$	$t_s = 50\Delta t$	$t_s = 25\Delta t$	$t_s = 10\Delta t$
A	0.1012	0.1011	0.1023	0.275	0.2712	0.2676
B	4.0000×10^5	4.0000×10^5	3.9999×10^5	3.9963×10^5	3.9964×10^5	3.9965×10^5
C	1.2970×10^{-6}	1.2970×10^{-6}	1.2970×10^{-6}	1.2969×10^{-6}	1.2969×10^{-6}	1.2969×10^{-6}

TABLE IV

LEAST-SQUARES INTERPOLATION RESULTS FOR DIFFERENT SAMPLING TIMES t_s USING THE COMPUTED SOLUTIONS. SHOWN ARE RESULTS OBTAINED WHEN MOLECULAR DIFFUSION ACCOUNTED FOR ($D \neq 0$) AND WHEN IT IS IGNORED ($D = 0$). IN THE PRESENT CASE, ESTIMATES OF $d\bar{\delta}/dt$ ARE OBTAINED FROM A CENTERED DIFFERENCE APPROXIMATION USING THE SAMPLING TIME t_s

Coefficients	$D = 0$			$D \neq 0$		
	$t_s = 50\Delta t$	$t_s = 25\Delta t$	$t_s = 10\Delta t$	$t_s = 50\Delta t$	$t_s = 25\Delta t$	$t_s = 10\Delta t$
A	3.7046	1.0067	0.2532	3.9915	1.2094	0.4247
B	3.8619×10^5	3.9661×10^5	3.9944×10^5	3.8537×10^5	3.9613×10^5	3.9908×10^5
C	1.2732×10^{-6}	1.2913×10^{-6}	1.2961×10^{-6}	1.2719×10^{-6}	1.2909×10^{-6}	1.2960×10^{-6}

rupt the flow. Also, note that if pointwise, time-resolved measurements are sufficiently accurate, the regression analysis can be performed on (20) directly. In this case pointwise measurement of only a single reactant concentration is needed, with the coefficient of δ^2 providing k_f . This latter possibility, however, is not explored in the present study.

The evolution of $d\bar{\delta}/dt$ is shown in Figs. 9 and 10. In Fig. 9, we rely on first- and second-order formulas for evaluating the derivative, and in both cases the time step corresponds to that used in the computations. In Fig. 10, we rely only on a second-order approximation, with a sampling time step t_s that is significantly larger than that used in the computations. This mimics actual experiments, where sampling at very high frequencies may neither be possible nor desirable. As shown in the figures, in all cases $d\bar{\delta}/dt$ is well approximated.

The least-squares procedure is tested using the analytical solution for a purely reactive system at different sampling time intervals. As shown in Table II the interpolated coefficients match the actual input parameters $k_f = 4 \times 10^5$ and $k_r = 0.1$. Note, however, that at the larger sampling interval very small errors appear in the estimate of k_r , even though the exact solution is used as input to the regression. These weak errors reflect the amplification of round-off errors due to the stiffness of the linear equation system. As further discussed below, the impact of this stiffness is substantially more pronounced when numerical results are used, especially when molecular diffusion effects are accounted for.

We now apply the regression analysis directly to the output of the computations. The analysis is conducted in two versions. In the first version, we simply switch off the electric field, as outlined above. In the second, both diffusion and electromigration are interrupted. Comparison of the two sets of results thus enables us to directly assess the role of diffusion on the extrapolated rates.

As shown in (22), the present analysis requires estimates of $d\bar{\delta}/dt$. In the results below, these estimates are obtained using a second-order centered-difference formula. In the results shown

in Table III, this approximation is performed within the simulations, using the computational time step $\Delta t = 10 \mu s$. The sampling time, t_s , denotes the time interval between neighboring points in the least-squares procedure. Thus, in Table III, the derivative $d\bar{\delta}/dt$ is estimated using a finer time step than the sampling time t_s . In Table IV, this exercise is repeated with $d\bar{\delta}/dt$ estimated from the sampled data, i.e., using a time step equal to the sampling time t_s . This latter case mimics more closely the experimental analysis, as data between neighboring points is not available.

Examination of the results in Tables III and IV indicates that:

- 1) There is better agreement between the estimated and input/known values ($k_f = 4 \times 10^5$, $k_r = 0.1$) of the reaction rates for the case where the derivative $d\bar{\delta}/dt$ is estimated based on the computational time step. Thus, for fixed t_s , the agreement between the estimated and input values deteriorates when the derivative is estimated on a wider time interval.
- 2) Kinetic rate estimates obtained with molecular diffusion ignored are in better agreement with the input values than estimates obtained in the diffusive cases. This indicates that even though diffusion may have weak a effect on the absolute values of concentration, it still has a substantial effect on the least-squares predictions, especially at large sampling intervals.
- 3) The extrapolated backward rate is highly sensitive to the presence of diffusion and to the sampling interval t_s . Except for small t_s and negligible diffusion, the interrupted flow approach proposed here does not seem to be a practical method of estimating the backward rate, k_r . The high-sensitivity of the estimated values of k_r can be traced to the stiffness of the equation system, which leads to an ill-conditioned matrix.
- 4) In contrast, the extrapolated values of k_f are much more robust, and provide reasonable estimates of the forward rate. In particular, for all cases analyzed, the estimated value of k_r differs by less than 4% from the input value.

VI. CONCLUSION

A numerical study of band-crossing reactions was conducted using a quasi-1-D computational model. The model accounts for the evolution of species concentrations due to bulk advection, electromigration, diffusion and chemical reaction. The latter is described using a single step, reversible mechanism involving two reactants and one product. Attention is focused on a fast reaction between initially unmixed bands.

A parametric study of the behavior of the species profiles during the crossing was performed. Simulation results were interpreted in terms of the Damköhler number and of the ratios of the electromigration velocities of the reactant and product. As expected, the results indicate that the overall consumption of the reactants increases as the Damköhler number increases. The results also indicate that the structure of the concentration profile is strongly dependent on the differences of electromigration velocities. In particular, when the product electromigration velocity is equal to the average of the reactants electromigration velocities, the product concentration exhibits a thin profile with peak values significantly higher than the initial reactants' concentrations. This stacking effect may provide a useful means of sample preconcentration based on reaction rates and mobilities, and for enhancing the sensitivity of a variety of on-chip assays. For higher or lower velocity, the product concentration profiles are spatially wider and exhibit significantly lower peak values.

The simulations were then used to explore the possibility of extracting forward and backward rates based on time resolved observation of integral moments of species concentrations. When signals of all three species are observed, a robust extraction procedure can be implemented, which results in excellent estimates of the forward and reverse rates. The simulations are also used to investigate interrupted flow experiments where only the reactants' concentrations are measured. In these situations, an approximate analysis can be applied to extract reaction rate parameters. Results indicate that in the case of fast forward reaction this approach yields robust estimates of the forward rate constant, but that the reverse rate parameter is not accurately predicted.

REFERENCES

- [1] L. Bousse, C. Cohen, T. Nikiforov, A. Chow, A. R. Kopf-Sill, R. Dubrow, and J. W. Parce, "Electrokinetically controlled microfluidic analysis systems," *Annu. Rev. Biophys. Biomol. Struct.*, vol. 29, pp. 155–181, 2000.
- [2] P. Yager, *Basic Microfluidic Concepts*, 2001.
- [3] A. E. Kamholz, B. H. Weigl, B. A. Finlayson, and P. Yager, "Quantitative analysis of molecular interaction in a microfluidic channel: the t-tensor," *Anal. Chem.*, vol. 71, pp. 5340–5347, 1999.
- [4] A. G. Hadd, D. E. Raymond, J. W. Halliwell, S. C. Jacobson, and J. M. Ramsey, "Microchip device for performing enzyme assays," *Anal. Chem.*, vol. 69, pp. 3407–3412, 1997.
- [5] A. G. Hadd, S. C. Jacobson, and J. M. Ramsey, "Microfluidic assays of acetylcholinesterase inhibitors," *Anal. Chem.*, vol. 71, pp. 5206–5212, 1999.
- [6] P. Galambos, PhD thesis, Department of Mechanical Engineering, University of Washington, Seattle, WA, 1998.
- [7] N. Chiem and D. J. Harrison, "Microchip-based capillary electrophoresis for immunoassays: analysis of monoclonal antibodies and theophylline," *Anal. Chem.*, vol. 69, pp. 373–378, 1997.
- [8] —, "Microchip systems for immunoassay: an integrated immunoreactor with electrophoretic separation for serum theophylline determination," *Clin. Chem.*, vol. 44, pp. 591–598, 1998.

- [9] B. K. Lance, D. Schmalzing, A. T. Todd, and M. Fuchs, "Microchip electrophoretic immunoassay for serum cortisol," *Anal. Chem.*, vol. 68, pp. 18–22, 1996.
- [10] G. B. Lee, S. H. Chen, G. R. Huang, W. C. Sung, and Y. H. Lin, "Micro-fabricated plastic chips by hot embossing methods and their applications for dna separations and detection," *Sens. Actuators, Chem. B*, vol. 75, pp. 142–148, 2001.
- [11] I. K. Glaskow *et al.*, "Handling individual mammalian embryos using microfluidics," *IEEE Trans. Biomed. Eng.*, vol. 48, pp. 570–578, 2001.
- [12] J. Kameoka, H. G. Craighead, H. W. Zhang, and J. A. Helton, "A polymeric microfluidic chip for ce/ms determination of small molecules," *Anal. Chem.*, vol. 73, pp. 1935–1941, 2001.
- [13] T. J. Johnson, D. Ross, and L. E. Locascio, "Rapid microfluidic mixing," *Anal. Chem.*, vol. 74, pp. 45–51, 2002.
- [14] B. He, B. J. Burke, X. Zhang, R. Zhang, and F. E. Regnier, "A picoliter-volume mixer for microfluidic analysis systems," *Anal. Chem.*, vol. 73, pp. 1942–1947, 2001.
- [15] M. H. Oddy, J. G. Santiago, and J. C. Mikkelsen, "Electrokinetic instability micromixing," *Anal. Chem.*, vol. 73, pp. 5822–5832, 2001.
- [16] J. Jianmin Bao and F. E. Fred E. Regnier, "Ultramicro enzyme assays in a capillary electrophoretic system," *J. Chromatogr.*, vol. 608, pp. 217–224, 1992.
- [17] B. J. Bryan J. Harmon, D. H. Dale H. Patterson, and F. E. Fred E. Regnier, "Mathematical treatment of electrophoretically mediated microanalysis," *Anal. Chem.*, vol. 65, pp. 2655–2662, 1993.
- [18] C. H. Chen, J. C. Mikkelsen, and J. G. Santiago, "Electrophoretic band crossing for measurements of biomolecular binding kinetics," presented at the 2000 International Forum on Biochip Technologies, Beijing, China.
- [19] J. B. Knight, A. Vishwanath, J. P. Brody, and R. H. Austin, "Hydrodynamic focusing on a silicon chip: mixing nanoliters in microseconds," *Phys. Rev. Lett.*, vol. 80, pp. 3863–3866, 1998.
- [20] B. J. Harmon, I. Leesong, and F. E. Regnier, "Selectivity in electrophoretically mediated microanalysis by control of product detection time," *Anal. Chem.*, vol. 66, pp. 3797–3805, 1994.
- [21] —, "Moving boundary electrophoretically mediated microanalysis," *J. Chromatogr. A*, vol. 726, pp. 193–204, 1996.
- [22] D. H. Dale H. Patterson, B. J. Bryan J. Harmon, and F. E. Fred E. Regnier, "Dynamic modeling of electrophoretically mediated microanalysis," *J. Chromatogr. A*, vol. 732, pp. 119–132, 1996.
- [23] V. P. Andreev and N. S. Pliss, "Computer simulation of electroinjection analysis and electrophoretically mediated microanalysis commensurable concentrations of sample and reagent," *J. Chromatogr. A*, vol. 845, pp. 227–236, 1999.
- [24] S. Devasenathipathy and J. G. Santiago, "Electrokinetic flow diagnostics," in *Micro- and Nano-Scale Diagnostic Techniques*. New York: Springer, 2002.



Alain Matta received the B.E. degree in civil engineering from the Lebanese American University, Lebanon, in 2000 and the M.S. degree in civil engineering from the Johns Hopkins University (JHU), Baltimore, MD, in 2003. He is currently working toward the Ph.D. degree in the Department of Civil Engineering at JHU.

His research focuses on stochastic modeling of microfluidic systems.



Omar M. Knio received the Ph.D. degree in mechanical engineering from the Massachusetts Institute of Technology (MIT), Cambridge, in 1990.

He is Professor of Mechanical Engineering at the Johns Hopkins University (JHU), Baltimore, MD. He held a Postdoctoral Associate position at MIT, before joining the Mechanical Engineering Faculty at JHU in 1991. His research interests include computational fluid mechanics, oceanic and atmospheric flows, turbulent flow, physical acoustics, chemically reacting flow, energetic materials, microfluidic devices, dynamical systems, as well as asymptotic and stochastic techniques.



Roger G. Ghanem received both the Master's and Ph.D. degrees from Rice University, Houston, TX.

He is Professor of Civil Engineering at the Johns Hopkins University (JHU), Baltimore, MD, where he specializes in the area of computational stochastic mechanics on which has authored numerous publications.



Bert Debusschere received the M.S. and Ph.D. degrees in mechanical engineering from the University of Wisconsin—Madison in 1995 and 2001, respectively, and the B.S. degree in mechanical engineering from the Katholieke Universiteit Leuven, Belgium, in 1994.

He is a Research Associate at Sandia National Laboratories, Livermore, CA. His research interests include simulation of turbulent scalar transport, microfluidic flow phenomena, and stochastic uncertainty quantification.



Chuan-Hua Chen received the B.S. degree in mechanics from Beijing University, China, and the M.S. degree in mechanical engineering from Stanford University, Stanford, CA. He is currently working toward the Ph.D. degree and is a Research Assistant at the Stanford Microfluidics Laboratory, where his research involves electrokinetic microsystems. He has published on electroosmotic micropumps, bioreaction kinetics, and electrokinetic flow instabilities.



Juan G. Santiago received the Ph.D. degree in mechanical engineering from the University of Illinois at Urbana-Champaign (UIUC).

He was a Senior Member of the Technical Staff at the Aerospace Corporation from 1995 to 1997, where his work included the development of flow diagnostics for micronozzles. He was then a Research Scientist at UIUC's Beckman Institute from 1997 to 1998, where he studied the performance of scaled down bioanalytical microfluidic systems. Since 1998, he has been an Assistant Professor of

Mechanical Engineering at Stanford University, Stanford, CA, where he specializes in microscale fluid mechanics, microscale optical flow diagnostics, and microfluidic system design. His research includes the investigation of transport phenomena and optimization of systems involving microscale fluid pumping, electrophoretic injections and separations, sample concentration methods, and rapid micromixing processes. The applications of this research include microfabricated bioanalytical systems for drug discovery and bioweapon detection. He is the Director of the Stanford Microfluidics Laboratory.



Habib N. Najm received the M.S. and Ph.D. degrees in mechanical engineering from the Massachusetts Institute of Technology (MIT), Cambridge, in 1986 and 1989, respectively, and the B.E. degree in mechanical engineering from the American University of Beirut in 1983.

He is a Principal Member of the Technical Staff at Sandia National Laboratories in Livermore, CA. Before joining Sandia in 1993, he worked with the Semiconductor Process Design Center at Texas Instruments, on the development of sensors and control in semiconductor processing, and on design studies of thermo-fluid systems in semiconductor process technology. His group at the Sandia Combustion Research Facility is involved in a range of computational reacting flow research funded by the U.S. Department of Energy, Basic Energy Sciences/Chemical Sciences Division and the DOE SciDAC Computational Chemistry program. This work spans the development of algorithms for time integration and uncertainty quantification, distributed high-performance component software implementations, and computational studies of reacting flow with detailed hydrocarbon kinetics. The group also works on DARPA-funded research focused on detailed modeling and uncertainty quantification in electrochemical microfluid systems. He is coauthor of over 30 archival journal articles and four U.S. patents.